Quantum Information Processing with Superconducting Circuits and High Q Cavities

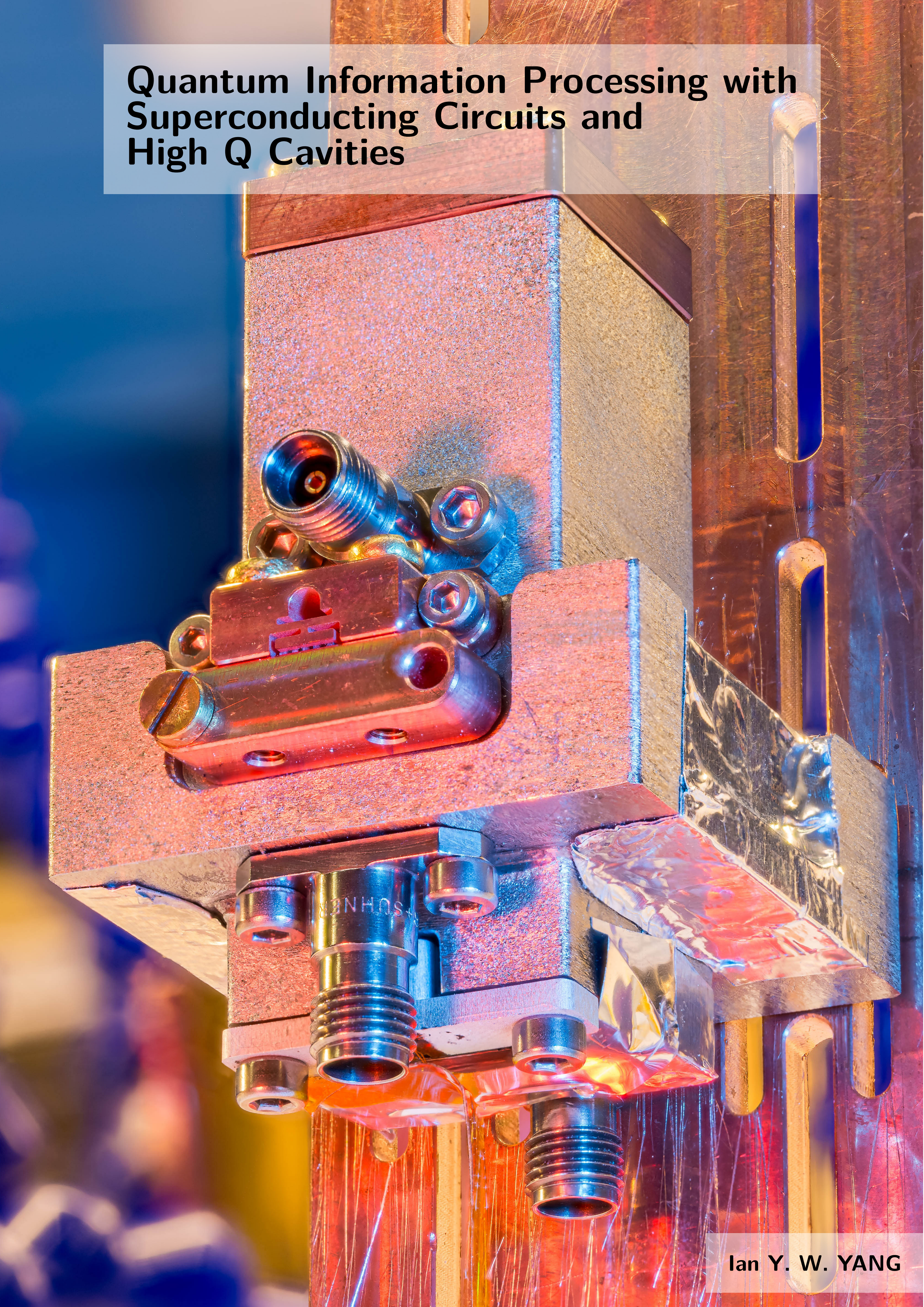

Ian Y. W. YANG

universität innsbruck

Quantum Information Processing with Superconducting Circuits and High Q Cavities

Ian Y. W. Yang, 11940581

Innsbruck, February 2024

Dissertation

submitted to the Faculty of Mathematics, Computer Science and Physics of the University of Innsbruck in partial fulfilment of the requirements for the academic degree

Doctor of Philosophy

Doctor of Philosophy – Doctoral Program in Physics

Main Supervisor: Univ. Prof. Dr. Gerhard Kirchmair

Institute of Experimental Physics

Co-supervisor: Univ. Prof. Dr. Oriol Romero-Isart

Institute of Theoretical Physics

Faculty of Mathematics, Computer Science and Physics

Abstract

Within the field of superconducting circuits, bosonic qubits have emerged as an exciting avenue for research. As compared to qubits, the higher lifetimes and larger Hilbert space inherent to bosonic modes serve as an ideal playground to explore new quantum protocols for physics experiments. In this thesis, I outline a platform that couples superconducting qubits to a high coherence bosonic mode.

I developed additional experimental capabilities and expanded the library of experimental tools in the Kirchmair lab. The two main new features are a new generation of magnetic flux hose that allows for the threading of magnetic flux into a 3D superconducting cavity and a modular 3D Purcell filter with an integrated SMA pin for driving and readout. With this platform, I realised three main experiments.

First, I performed a closed-looped optimisation on a bosonic mode. I showed that it was possible to use a proxy measurement as feedback to the optimisation routine instead of the traditionally resource-intensive state tomography approach. The proxy measurement focused on the important features of the prepared state, such as the interference fringes and Gaussian distributions in a Schrödinger cat state. I report an overall increase in the preparation of the state characterised by a figure of merit increase from 0.50 to 0.74. While the optimisation was carried out on a cat state in a circuit quantum electrodynamics (QED) platform, the novel and general method can also be used to prepare many other complex states and can be adapted to other platforms.

Second, I generated a quantum superposition of a thermal state. Thermal states are highly mixed states with low purity. The experimental results demonstrate that thermal states, up to a mean thermal photon number of eight, a purity of 0.062 and a mode temperature of 1.8 K, which is sixty times hotter than its physical temperature, can still be used to form quantum states. Such hot cat states are a resource for quantum computation and quantum meteorology and can also be realised in other bosonic systems, such as levitated optomechanical setups. The existence of hot cat states shows that reaching the ground state is not a strict condition for quantum features. Importantly, it is coherent dynamics and not purity that determines the "quantum-ness" of a state. While the experiment was limited by instrument power, fundamentally the theoretical results do not place a fundamental limit on how hot the initial thermal state can be.

Finally, I demonstrate a proof of principle experiment to realise a flexible multi-qubit gate. This method uses the high Q cavity as a quantum bus to apply conditional qubit operations. The main strength of this novel gate comes from its flexibility to apply any target unitary needed. One of the most exciting applications of such a gate is the quantum switch gate. A superposition of the order of quantum gates is a novel method that opens new research areas for exploration and improvement such as quantum causality, quantum communication, quantum computation, and quantum error mitigation experiments.

Contents

CHAPTER 1

Introduction

A famous thought experiment in the field of quantum physics is Schrödinger's cat [1]. In the 1935 thought experiment, a cat is placed in a box with a jar of poison and a radioactive atom. The poison is then released if the radioactive atom decays. As radioactive decay is a quantum phenomenon, to an observer outside of the box, the atom is in a superposition of decayed and not decayed at the same time. The superposition of the atom becomes entangled with the cat being dead and alive at the same time. This thought experiment demonstrated the quantum property of entanglement between the state of the atom and the state of the cat. Analogous to the entangled Schrödinger cat state, quantum superposition states also have special quantum properties. Since the thought experiment, many experiments in varied platforms have demonstrated the creation and measurement of Schrödinger cat states using coherent states in a bosonic mode as the cat [2–4]. These experiments and many others use the quantum properties of entanglement and superposition to demonstrate the non-intuitive ways of the quantum world. This has led to an increasing interest in using these properties to gain an advantage over classical computers.

The huge potential of quantum computers in tackling computational problems that are classically prohibitive has driven research in the quantum computing field. Such problems are called bound quantum polynomial (BQP) time problems and have wide-ranging implications. Notable examples include breaking RSA encryption with Shor's algorithm [5], finding solutions to optimisation problems such as the travelling salesman problem [6] or simulation in quantum chemistry [7]. The basis of quantum computers is qubits, whose quantum properties give the "quantum advantage". Superconducting circuits have been one of the promising platforms to realise such qubits. This comes from the complementary-metal-oxide-semiconductor (CMOS) like fabrication techniques for the scalability and engineerability of the circuits. The combination of different elements gives rise to engineerable Hamiltonians in the field of circuit quantum electrodynamics (QED).

The increasing attention on quantum computers with superconducting circuits is also evident in the billions of dollars being invested by big tech companies and governments [8]. The impressive roadmaps and big promises from the likes of Google [9], IBM [10], Amazon [11] and many more brought ever-growing attention to the progress of the field. Even on the academic front in the superconducting circuits field, larger research groups such as those from Yale University, MIT Lincoln labs or ETH Zurich have grown and are pushing the boundaries of the circuit QED field. Many startup companies like Rigetti [12], Alice and Bob [13], and Oxford Quantum Circuits have also spawned from research groups, each having their expertise area in this highly competitive market. Aside from the quantum physics research front, a growing support industry of hardware companies has risen around the quantum computing field. These include Quantum Machines, Zurich Instruments, Qblox or Delft Circuits that handle a wide range of hardware, from measurement and control instruments to cryogenic input drive lines. These large research groups and bigger companies have led the way in terms of progress of increasing qubit lifetimes, and improvements in software and hardware used in the experiments. Thus, the role of smaller research groups has to be redefined and must find a niche area in this ever-changing field.

Within the field of superconducting circuits, bosonic qubits have emerged as a compelling avenue. There have been many exciting experimental results from hardware-efficient bosonic quantum error correction [14, 15], to the quantum simulation of the vibrational modes of a molecule [16] and even gates between two bosonic modes [17]. Improving understanding and control of such bosonic modes are thus of great importance.

In the Kirchmair lab, one research direction has been in the field of coupling superconducting qubits to high coherence cavities (Fig. 1.1). The cavities have long lifetimes and high quality factors and are also known as high Q cavities. Such a setup allows us to manipulate the quantum systems and perform fundamental science research on a smaller scale. I built a flexible platform that couples qubits to a bosonic mode. This platform has been designed with the consideration of the flexibility of different experimental requirements. I demonstrate the optical control of a bosonic mode (chapter 5), the superposition of classical states (chapter 6), and a flexible multi-qubit gate (chapter 7).

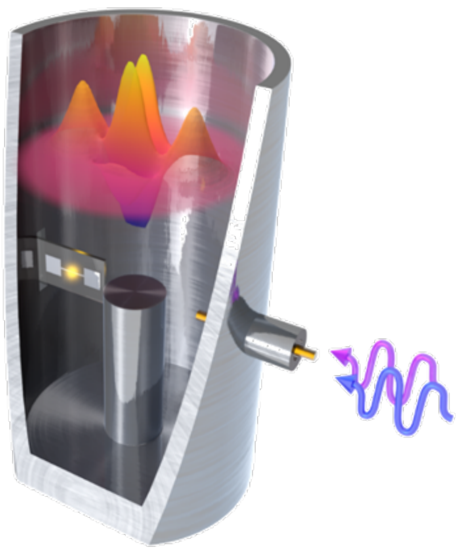

Figure 1.1: Artistic drawing of high Q post cavity coupled to a qubit. Also shown is a Wigner function of a Schrödinger cat state. Drawing done by Dr. Mathieu L. Juan.

1.1 Overview of thesis

The thesis is divided into four main parts.

Part 1: Concept and Characterisation. In the first part, I introduce the theoretical concepts and characterisation measurements required to understand the superconducting circuits field and experiments later. In chapter 2, I cover the theory used in quantum information processing and the platform used to realise the qubits. Chapter 3 introduces the design, simulation, fabrication and setup process used in the lab. Chapter 4 elaborates on the circuit QED toolbox and demonstrates the basic measurements done to characterise the setup. I show the progress made in improving the existing platform used in the Kirchmair lab. In particular, this includes the first measurements of two prototype devices. A new generation of magnetic flux hose was used to thread magnetic fields into a superconducting cavity and a modular 3D Purcell filter with an integrated SMA pin.

Part 2: Quantum Superpositions. In the next part (Chapter 5), I demonstrate different ways to form a Schrödinger cat state in a bosonic mode. This includes the first main experiment where closed-looped optimisation is done on a bosonic mode with an infinite Hilbert space.

Part 3: Quantum Superpositions of Thermal States. In chapter 6, the methods described in part 2 are used to generate a quantum superposition of a classical state. The results are closer to the original Schrödinger's thought experiment, the cat — a hot and out-of-equilibrium system — is prepared in a superposition of two mixed states dominated by classical fluctuations [1].

Part 4: Flexible Multi-qubit Gate. In the last experiment, shown in chapter 7, I demonstrate a proof of principle experiment to realise a flexible multi-qubit gate. This method uses the high Q cavity as a quantum bus to effectively perform flexible conditional qubit operations.

Finally in chapter 8, I conclude and give my thoughts on the applications of the experimental results and outlook on anticipated results.

1.2 Work not covered in this thesis

Being part of an experimental group, I had the honour of helping out with many other projects such as the setting up of a new lab space in the Kirchmair group. These projects are beyond the scope of the thesis, but I would like to briefly mention one here.

The project utilises the non-linear dispersion of a waveguide to focus microwave pulses to individually address spatially separated qubits. Maximilian Zanner and Romain Albert headed this project in the lab. My small part was in assisting in the qubit fabrication process. In a non-linear dispersion medium, such as above the cut-off frequency of a waveguide, pulses at different frequencies will have different group velocities. This results in the dispersion of a microwave pulse [18]. The non-linear dispersion enables to spatially focus a microwave pulse onto a qubit [19]. The efforts led to a paper in the publication process [20].

CHAPTER 2

Theory

This chapter serves as a theoretical framework to discuss the research conducted in the later chapters. Parts of the chapter can also be found in many textbooks [21–23], reviews and theses including [24–28]. The first section begins with the theoretical concepts of quantum information processing. Next, I cover the platform to realise such quantum systems, superconducting circuits and the experimental toolbox of circuit Quantum Electrodynamics (cQED). Finally in Sec. 2.3, I discuss the question of manipulation and control of a quantum system.

2.1 Quantum Information Processing

2.1.1 Qubits and Qubit States

In classical digital computers, the basic unit is the binary digit (bit). Each bit can only hold one of two different values (0 or 1). In contrast, quantum bits (qubits) can hold any linear combination of the two states. Mathematically, the state of the qubit $|\psi\rangle$ can be represented by a vector in a 2-dimensional Hilbert space

$$|\psi\rangle = \alpha\,|0\rangle + \beta\,|1\rangle\,. \tag{2.1}$$

The complex coefficients α and β represent the probability of finding the qubit in state $|0\rangle$ or $|1\rangle$ in a classical measurement. The probability to find a quantum state $|\psi\rangle$ in some state $|\phi\rangle$ is given by

$$P_\phi = |\langle\phi|\psi\rangle|^2\,. \tag{2.2}$$

In addition to the probabilistic property in quantum mechanics, classical systems also have stochasticity. A quantum state that can be expressed as a state vector is called a pure state. A pure state can also be a coherent superposition of some basis states. Conversely, quantum states that are a statistical ensemble of pure states are known as mixed states. It is important to distinguish between coherent superpositions and an incoherent mixture. A useful mathematical tool is the density matrix ρ [21, 29]. For a pure state in Eq. (2.1),

$$\rho = |\psi\rangle\,\langle\psi| = \begin{pmatrix} |\alpha|^2 & \alpha\beta^* \\ \alpha^*\beta & |\beta|^2 \end{pmatrix}.$$

The diagonal terms represent the population of the quantum state and the off-diagonal terms represent coherences of a qubit. For mixed states, the statistical mixture is represented by $\rho = \sum_i P_i |\psi_i\rangle \langle\psi_i|$, where P_i are the classical probabilities of the different quantum states $|\psi_i\rangle$. In such cases, the purity, $\mathcal{P}$, is used to measure how much a state is mixed

$$\mathcal{P} = \mathrm{Tr}\{\rho^2\}. \tag{2.3}$$

It is important to note that in many real physical realisations of the qubit, the actual quantum system has multiple excitation levels and is not a true two-level system. This key difference is often an avenue for experimental difficulties but can also lead to potential advantages. The concept of two levels of the qubit can be extended to even higher levels giving a qudit [30].

A useful visualisation tool for the evolution and transformation of the qubit state is the Bloch vector on the Bloch sphere [21, 31]. Eq. (2.1) can be written as

$$|\psi\rangle = \cos\frac{\theta}{2}|0\rangle + e^{i\phi}\sin\frac{\theta}{2}|1\rangle \tag{2.4}$$

where $\theta \in [0;\pi]$ and $\phi \in [0;2\pi]$ are the polar and azimuthal angles on the Bloch sphere. The quantum state is visualised as a Bloch vector pointing in the direction given by the spherical coordinates. Pure states have unit length on the Bloch sphere while mixed states will have a length smaller than the radius of the Bloch sphere.

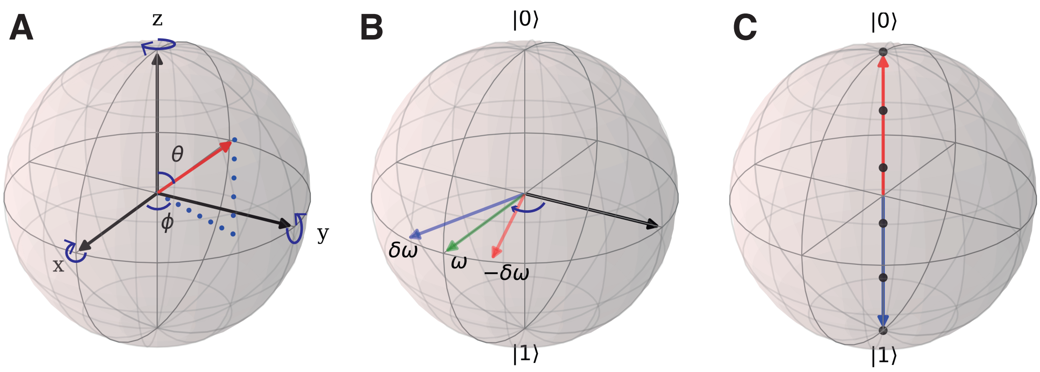

Figure 2.1: Bloch sphere examples. (**A**) The Bloch sphere is a useful visualisation tool to represent a qubit state. The Bloch vector is a state with azimuthal angle, ϕ, and polar angle θ. Operations are rotations about the relevant axis. (**B**) The natural evolution of a qubit state is a rotation about the z-axis at a rate of the frequency of the qubit ω. Stochastic variations of the qubit frequency, $\delta\omega$, will cause a variation of the qubit rotation rate and thus over multiple iterations, the Bloch vectors have a spread in the angle ϕ. (**C**) Decay of the qubit state. An initially excited qubit will decay over time to the ground state. This is through energy relaxation where the qubit loses information to its surrounding environment.

2.1.2 Time Dynamics of Quantum systems

Manipulation and control of a quantum state is an essential ingredient in experiments. The natural evolution of quantum states follow the Time Dependent Schrödinger equation [22]

$$\begin{aligned} i\hbar\frac{d\left|\psi\right\rangle}{dt} &= \hat{H}(t)\left|\psi\right\rangle, \\ \left|\psi(t)\right\rangle &= \hat{U}(t)\left|\psi(t=0)\right\rangle \\ &= e^{-i\frac{E_i}{\hbar}t}\left|\psi(t=0)\right\rangle = \sum_i c_i e^{-i\omega_i t}\left|\phi_i\right\rangle, \end{aligned} \tag{2.5}$$

where the third equation follows for states that are an eigenstate given by $\hat{H}\left|\psi\right\rangle = E\left|\psi\right\rangle = \hbar\omega\left|\psi\right\rangle$. The third equation shows the state will undergo a phase evolution at a rate $e^{-i\omega_i t}$. For superpositions of initial states $\left|\phi_i\right\rangle$, the quantum state can be decomposed into a linear mix of the eigenstates weighted by the initial amplitudes c_i and will each evolve according to the eigenstate's energy.

To realise operators on quantum systems, we can consider the effect of turning on a Hamiltonian for $\hat{H}(t)$ a length of time which results in an operator $\hat{U}(t)$ acting on the quantum state. A common set of operators on a qubit state are the $\hat{R}_X$, $\hat{R}_Y$ and $\hat{R}_Z$ rotation

$$\hat{R}_X(\theta) = e^{-i\frac{\theta\hat{\sigma}_x}{2}} = \begin{pmatrix} \cos\frac{\theta}{2} & -i\sin\frac{\theta}{2} \\ -i\sin\frac{\theta}{2} & \cos\frac{\theta}{2} \end{pmatrix}, \tag{2.6}$$

$$\hat{R}_Y(\theta) = e^{-i\frac{\theta\hat{\sigma}_y}{2}} = \begin{pmatrix} \cos\frac{\theta}{2} & \sin\frac{\theta}{2} \\ \sin\frac{\theta}{2} & \cos\frac{\theta}{2} \end{pmatrix}, \tag{2.7}$$

$$\hat{R}_Z(\theta) = e^{-i\frac{\theta\hat{\sigma}_z}{2}} = \begin{pmatrix} e^{-i\frac{\theta}{2}} & 0 \\ 0 & e^{-i\frac{\theta}{2}} \end{pmatrix}. \tag{2.8}$$

A rotation about any axis $\hat{n} = (n_x, n_y, n_z)$ is given by: $\hat{R}_{\hat{n}}(\theta) = e^{-i\frac{\theta\hat{n}}{2}} = \cos\frac{\theta}{2}\mathbb{I} - i\sin\frac{\theta}{2}(n_x\hat{\sigma}_X + n_y\hat{\sigma}_Y + n_z\hat{\sigma}_Z)$. These rotation matrices are often written in the Pauli matrix basis. The Pauli matrix often appears naturally in many Hamiltonians and are used as gate operations on qubits. Some common rotations are shown in table 2.1.

Operation	Rotation Matrix	Matrix
$\hat{X}(\pi)$	$i\hat{R}_X(\pi)$	$\begin{pmatrix} 0 & 1 \\ 1 & 0 \end{pmatrix}$
$\hat{X}(\pm\frac{\pi}{2})$	$e^{\pm i\pi/4}\hat{R}_X(\frac{\pi}{2})$	$\frac{e^{\pm i\pi/4}}{\sqrt{2}}\begin{pmatrix} 1 & \mp i \\ \mp i & 1 \end{pmatrix}$
$\hat{Y}(\pi)$	$i\hat{R}_X(\pi)$	$\begin{pmatrix} 0 & -i \\ i & 0 \end{pmatrix}$
$\hat{Y}(\pm\frac{\pi}{2})$	$e^{\pm i\pi/4}\hat{R}_Y(\frac{\pi}{2})$	$\frac{e^{\pm i\pi/4}}{\sqrt{2}}\begin{pmatrix} 1 & \mp 1 \\ \pm 1 & 1 \end{pmatrix}$

Table 2.1: Rotation matrix of commonly used single qubit rotations.

These operations differ from the respective rotation matrix by a phase factor. For single qubit systems or global rotations, this global phase is not important and is often neglected.

However, it is crucial to remember such factors when dealing with rotations on a subset of a quantum element in the system.

Equivalently, operations on density matrices can be written as $\rho(t) = \hat{U}(t)\rho(t=0)\hat{U}^\dagger(t)$.

Operations and evolution of the Bloch vector can be viewed as rotations about the relevant axis as seen in Fig. 2.1A. As a static offset in energy does not influence the dynamics, we can define the ground state energy $E_{|0\rangle} = 0$. Quantum states with a $|1\rangle$ component will have that component evolve at $e^{-i\omega t}$, where $\omega = E_{|1\rangle} - E_{|0\rangle}$. On the Bloch sphere, this corresponds to an azimuthal rotation about the z-axis as seen in Fig. 2.1B.

The final piece of manipulation of a quantum system is measurement. In quantum mechanics, a measurement operator, $\hat{M}$, is defined as the projection of the quantum state into an eigenstate of the measurement operator $|m\rangle\langle m|$. For example, a measurement operator $|1\rangle\langle 1|$ acting on a quantum state Eq. (2.1) will give $M|\psi\rangle = |1\rangle$ with probability $|\beta|^2$. The expected value of a measurement observable on an ensemble average is

$$\langle\hat{M}\rangle = \langle\psi|\hat{M}|\psi\rangle = \mathrm{Tr}\{\rho\hat{M}\}. \tag{2.9}$$

In realistic experiments, an initially pure qubit state can decohere. This occurs through environmental energy loss, thermal excitation or other sources of noise. Information on the quantum state is lost and any further processing on it will become meaningless. Decoherence is the loss of a quantum state over time and is described by two processes: energy relaxation over a time scale T_1 or dephasing over a time scale of T_2^*.

Energy relaxation occurs when the qubit decays into the ground state and loses all state and phase information. This can occur due to noise at the qubit frequency or coupling with the surrounding lossy environment. On the Bloch sphere, the Bloch vector will evolve towards the North pole, the $|0\rangle$ state, as seen in Fig. 2.1C.

Conversely, dephasing events are characterised by the loss of a well-defined phase on the Bloch sphere. This can be seen as moving towards the center of the Bloch sphere. Dephasing occurs due to stochastic shifts in the qubit frequency or reference drive source that lead to a variation in qubit evolution (Fig. 2.1B). Over many iterations, the Bloch vector will point in different directions on the plane. The ensemble average of the qubit state is a Bloch vector with a smaller length. The qubit lifetime T_1 and coherence time T_2 can be related via a pure dephasing time T_ϕ

$$\frac{1}{T_2^*} = \frac{2}{T_1} + \frac{1}{T_\phi}. \tag{2.10}$$

2.1.3 Bosonic Modes

As compared to the two-level qubit system, the quantum harmonic oscillator (QHO) is an infinite-level system. Similar to classical harmonic oscillators, QHO can be used to describe many real-world scenarios such as vibrations in a phonon lattice or molecular bonds to experimental setups such as mechanical cantilevers or LC resonators. These bosonic modes are governed by the Hamiltonian:

$$\hat{H} = \hbar\omega \left(\hat{a}^\dagger \hat{a} + \frac{1}{2} \right) \tag{2.11}$$

where $\hat{a}^\dagger$ and $\hat{a}$ are the creation and annihilation operators and $\hbar\omega$ is the energy difference between energy levels. [1]

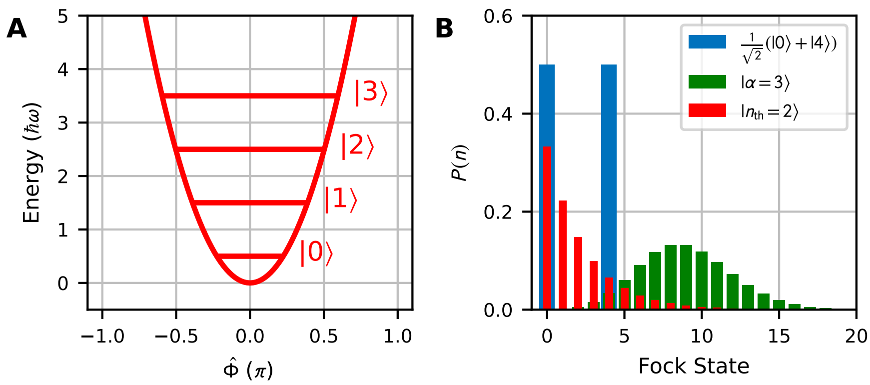

Figure 2.2: Quantum harmonic oscillator (QHO) energy levels and examples of Fock state distributions. (**A**) The QHO is a very common system with a parabolic potential well. The energy levels are equally spaced by $\hbar\omega$. (**B**) Examples of different bosonic states are represented in the Fock basis. In blue, an equal superposition of the ground and fourth Fock state. In green, the photon number distribution of a coherent state with a mean of 9 photons. Finally, in red, a thermal state with a mean of two photons in the bosonic mode.

Fock states and Thermal States

A common basis state to use for the quantum system is the photon number basis. This is known as the Fock basis

$$|\psi\rangle = \sum_{n=0}^{\infty} c_n |n\rangle \tag{2.12}$$

with probability amplitudes c_n. The number operator is $\hat{n} = \hat{a}^\dagger \hat{a}$ with eigenstates given as Fock states $|n\rangle$ and corresponding eigenvalue n. In Fig. 2.2B, the Fock state distribution of a thermal state with mean photon number $n_{\text{th}} = 2$ is plotted (red).

[1] Similar to the qubit states, we often drop the zero point energy $\frac{1}{2}\hbar\omega$.

An important operator on the QHOs is the parity operator

$$\hat{\Pi} = (-1)^n. \tag{2.13}$$

This operator is useful during state reconstruction of the bosonic mode and is also used in quantum error correction codes. For example, in the binomial code, logical states have the same parity. Thus, an error such as the loss of a photon is detectable without destroying any superposition of the logical states [32].

In realistic experiments, bosonic modes will have some loss rate κ. The loss rate will scale with each fock state: $\kappa_n = n\kappa$. For a state with n photons, each photon can independently decay. Thus, the overall Fock state has a reduced lifetime by a factor n [33, 34].

Another important bosonic state is the thermal state. Such states are a generalisation of classical thermodynamics in the language of quantum mechanics. Thermal states are often considered to be classical states as the photon number distribution follows Boltzmann statistics [22]. They can be described by a density matrix with Boltzmann factors $\frac{\hbar\omega}{k_B T}$

$$\begin{aligned}
\rho(n_{\mathrm{th}}) &= \left(1 - \exp\left(-\frac{\hbar\omega}{k_B T}\right)\right) \sum_{n=0}^{\infty} \exp\left(-\frac{n\hbar\omega}{k_B T}\right) |n\rangle && (2.14)\\
&= n_{\mathrm{th}} \sum_{n=0}^{\infty} \exp\left(-(n+1)\frac{\hbar\omega}{k_B T}\right) |n\rangle && (2.15)\\
n_{\mathrm{th}} &= \frac{1}{\exp\left(\frac{\hbar\omega}{k_B T}\right) - 1} && (2.16)
\end{aligned}$$

where n_{th} is the mean number of photons in the bosonic mode with mode frequency ω, $\hbar$ is the reduced Planck constant, k_{B} is the Boltzmann constant and mode occupation temperature T. The photon number probability distribution follows a thermal distribution

$$P(n_{\mathrm{th}}, n) = \frac{n_{\mathrm{th}}^n}{(n_{\mathrm{th}}+1)^{n+1}}. \tag{2.17}$$

This is a super-Poisson distribution as the variance of the distribution is greater than the mean of the distribution, $\Delta n^2 = \langle n\rangle + \langle n\rangle^2 > \langle n\rangle$. Due to the classical fluctuations of photon number, the quantum state has a reduced purity given by

$$\mathcal{P} = \frac{1}{2n_{\mathrm{th}} + 1}. \tag{2.18}$$

While it is not immediately obvious that such classical thermal states can still show quantum properties, in chapter 6, a coherent superposition of thermal states is shown. This was done using only coherent dynamics and without changing the entropy of the system by cooling or measurement.

Coherent States

Due to the equal energy spacing of the harmonic oscillator, if a classical drive is applied to a QHO, the quantum state would start to occupy higher energy levels depending on the strength of the drive. The resulting state is called a coherent state. Coherent states have evolution dynamics that resemble a classical harmonic oscillator and have the minimum Heisenberg-limited quantum fluctuations [22, 35]. The coherent state written in the Fock basis is

$$|\alpha\rangle = e^{-\frac{|\alpha|^2}{2}} \sum_{n=0}^{\infty} \frac{\alpha^n}{\sqrt{n!}} |n\rangle \tag{2.19}$$

where α relates to the amplitude and phase of the drive. The coherent state is an eigenstate of the annihilation operator $\hat{a}|\alpha\rangle = \alpha|\alpha\rangle$. Coherent states have a photon number distribution

$$P_\alpha(n) = |\langle n|\alpha\rangle|^2 = e^{-|\alpha|^2} \frac{|\alpha|^{2n}}{n!} \tag{2.20}$$

which is a Poissonion distribution with standard deviation $\Delta n = \bar{n}$, for a mean number of photons $\bar{n} = |\alpha|^2$.

The evolution of coherent states with time is only a change of the phase of α

$$\begin{aligned} |\alpha(t)\rangle &= e^{-\frac{|\alpha|^2}{2}} \sum_n \frac{\alpha^n e^{-i(\omega(n+\frac{1}{2}))t}}{\sqrt{n!}} |n\rangle \\ &= e^{-i\omega t/2} e^{-\frac{|\alpha|^2}{2}} \sum_n \frac{(\alpha e^{-i\omega t})^n}{\sqrt{n!}} |n\rangle \\ &\equiv |\alpha e^{-i\omega t}\rangle . \end{aligned} \tag{2.21}$$

The global phase factor $e^{-i\omega t/2}$ is due to the non-zero ground state energy and can be neglected. Similarly, for a mode with an energy loss rate κ, a coherent state will decay as: $|\alpha(t)\rangle = |\alpha(t_0)e^{-\frac{\kappa}{2}t}\rangle$.

The classical drive on a harmonic oscillator can be written as a unitary operation called the displacement operator

$$\hat{D}(\alpha) = e^{\alpha\hat{a}^\dagger - \alpha^*\hat{a}} \tag{2.22}$$

$$\hat{D}(\alpha)|0\rangle = |\alpha\rangle \tag{2.23}$$

Similar to the Fock basis, an arbitrary bosonic mode can be represented by a distribution of coherent states. The set of coherent states is an overcomplete basis that can represent any state in the QHO [24]. The basis change moves from the discrete Fock basis to a continuous variable (CV) system. Some quantum error correction codes [36] use this CV basis as the logical states. As an experimentalist, it is enlightening to view quantum circuit protocols from these two equivalent bases.

2.1.4 Visualising Continuous Variable Systems

To fully describe a given quantum state, we need to perform quantum state tomography. Quantum state tomography is a method to reconstruct a given quantum state using measurements on an ensemble of the input quantum state.

For the two-level qubit, this involves measurements along x, y and z axes to reconstruct the general qubit state. The different bases are required to reveal differences between a classical mixture or a quantum superposition of states [37]. However, the infinite Hilbert space of bosonic modes requires a different measurement method.

Similar to the qubit, bosonic modes can also have correlations between different bosonic states. A mathematical tool used to study such quantum features for bosonic modes is the Wigner function [38]. The Wigner function $W(\beta)$, where β is a complex-valued phase space location in the coherent state basis and $W(\beta)$ is real-valued, is a complete representation of the state of a bosonic quantum-mechanical system. It is a probability distribution as the function is normalised, $\int W(\beta)d^2\beta = 1$. However, the probability distribution can take negative values which have no classical analogue and reveal the quantum nature of a state. The Wigner function can be written as [39]

$$W(\beta) = \frac{2}{\pi}\mathrm{Tr}\left\{\hat{D}(\beta)\hat{\Pi}\hat{D}^\dagger(\beta)\rho\right\}. \tag{2.24}$$

This is equivalent to doing a displaced parity measurement over the entire phase space of the bosonic mode.

Another equivalent description of the bosonic mode is the generalised Husimi-Q function. The generalised Husimi-Q_n measurement gives the probability of finding n photons at a given point in phase space. The two functions are related by

$$Q_n(\beta) = \frac{1}{\pi}\mathrm{Tr}\left\{\langle n|\hat{D}^\dagger(\beta)\rho\hat{D}(\beta)|n\rangle\right\}, \tag{2.25}$$

$$W(\beta) = \sum_{n=0}^{\infty}(-1)^n Q_n(\beta). \tag{2.26}$$

The Wigner function can be calculated by taking the difference between the even and odd photon probabilities. Similar to viewing the bosonic mode with a different basis, some experimental setups would naturally prefer one measurement method or the other to reconstruct the bosonic quantum state.

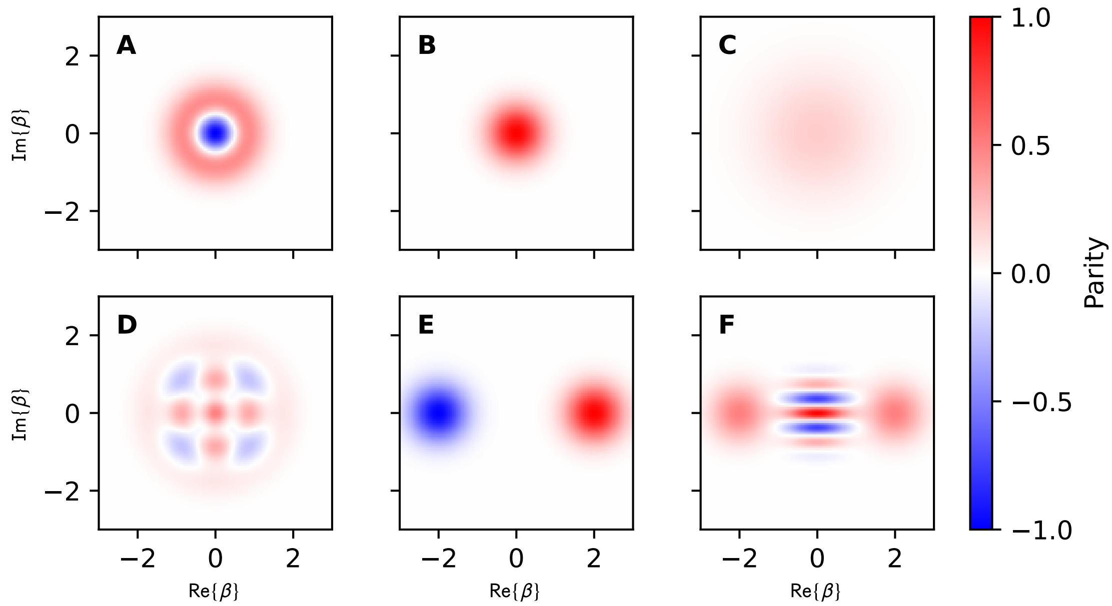

Figure 2.3: Examples of Wigner distribution of different bosonic states. (**A**) A Fock state with a single photon $|1\rangle$. It is useful to note that the parity of the state at $P(\beta = 0) = -1$. (**B**) The ground state of the cavity is plotted. The parity of the state at $P(\beta = 0) = 1$ and the ground state has a standard deviation of $\frac{1}{2}$. (**C**) Thermal state with a mean of two photons in the bosonic mode. Compared to the ground state, the thermal state has a bigger phase space extent that scales as $1/(n_{\text{th}})$ and a smaller parity and purity value (**D**) An equal superposition of the $|0\rangle$ and $|4\rangle$ Fock state is plotted. This state is also one of the logical states used in the binomial code [40]. (**E**) An entangled cat with state $|\psi\rangle = \frac{1}{\sqrt{2}}(|e, -\alpha\rangle + |g, \alpha\rangle)$. Here, the parity of the $|-\alpha\rangle$ coherent state is flipped to reflect the experimental method used to measure parity shown in Sec. 4.3.1. The qubit in the $|e\rangle$ state will have an opposite mapping of the parity value. (**F**) Wigner Function of a Schrödinger cat state $\frac{1}{\sqrt{2}}(|\alpha\rangle + |-\alpha\rangle))$

In Fig. 2.3, examples of Wigner functions of several bosonic states are plotted. Comparing Fig. 2.3A and Fig. 2.3B, we see that fock states have a well-defined photon number but the phase is undefined. Conversely, the coherent states have a well-defined phase up to the Heisenberg uncertainty but have a distribution of photon numbers.

Behind every QHO, we have a physical Hamiltonian that is expressed in some conjugate position $\hat{x}$ and conjugate momentum $\hat{p}$ coordinates. These are then expressed in terms of the raising and lowering operator $\hat{a}^\dagger$ and $\hat{a}$ with some zero point fluctuation. This is shown explicitly for the LC resonator case in Sec. 2.2.1. It is important to note that the zero-point fluctuation is not uniquely defined. Different normalisations can lead to different axis scaling factors between the generalised coordinate space $W(x, p)$ and expressing in terms of the coherent states $W(\beta)$. However, this is merely a scaling factor and does not change the underlying physics. In Fig. 2.3B, the ground state has a standard deviation of 1/2. This is due to a choice of the normalisation $\hat{X} = \frac{1}{2}(\hat{a}^\dagger + \hat{a})$ (see appendix A.2 for a detailed explanation).

2.1.5 Schrödinger Cat States

In the original Schrödinger cat state thought experiment [1], a cat is placed in a box with a jar of poison and a radioactive atom. Depending on the decay state of the atom, the poison is released and the cat is killed. In this experiment, the cat state is entangled with the decay state of an atom. This experiment highlights the quantum properties of entanglement between classical and quantum objects.

The quantum state of the system can be written as: $|\psi\rangle = |\mathrm{atom}, \mathrm{cat}\rangle \propto |\mathrm{nodecay}, \mathrm{alive}\rangle + |\mathrm{decay}, \mathrm{dead}\rangle$. As shown in Fig. 2.3E, with a qubit and a bosonic mode, this is equivalent to $|\mathrm{qubit}, \mathrm{bosonicmode}\rangle \propto |0, \alpha\rangle + |1, -\alpha\rangle$. By measuring the qubit state in $|0\rangle$ or $|1\rangle$ will also project the bosonic mode to $|\alpha\rangle$ or $|-\alpha\rangle$ respectively. In this case, the qubit and the bosonic modes are entangled.

Analogous to the Schrödinger cat state, the bosonic mode can also be in a superposition of two coherent states. In Fig. 2.3F, the bosonic mode is in the state $|\psi\rangle \propto |\alpha\rangle + |-\alpha\rangle$. The qubit is disentangled from the bosonic mode and we see fringes between the two bosonic states in the Wigner function. These negativities reveal the quantum nature of the bosonic state. To distinguish between the entangled Schrödinger cat states, these superposition states are sometimes called cat states.

In chapter 5, I show methods to generate cat states with the superconducting circuits platform. In chapter 6, I demonstrate the generation of hot Schrödinger cat states by creating a coherent superposition of thermal states.

2.2 Superconducting circuits

Superconducting circuits are a promising platform for realising well-controlled quantum systems for quantum information processing, quantum optics and quantum simulation experiments. While every platform has its advantages and drawbacks, superconducting circuits have two main advantages. Firstly, the samples can be fabricated with methods used in the existing complementary-metal-oxide-semiconductor (CMOS) industry. This compatibility allows for ease of scalability and design of many circuit elements. Secondly, using different circuit elements, we can build engineered Hamiltonians with a wide range of parameters. A detailed review of superconductors can be found in [41, 42].

Superconductors are non-dissipative materials where currents can flow without any electrical resistance. In superconducting materials, electrons pair up via phonon interactions with the lattice to form Cooper pairs. These Cooper pairs experience no resistance while carrying the charge through the material. The electric field mode of such superconductors can be used as storage for quantum information.

These circuit elements can have large dipole strengths which gives strong coupling and interaction energies in the Hamiltonian. These interactions can be used to protect and control the quantum system. With such a coupled system, we have access to the rich circuit Quantum Electrodynamics (cQED) toolbox.

2.2.1 LC resonators

The simplest circuit is made up of a capacitor and inductor in parallel (Fig. 2.4A). Analogous to the mechanical pendulum, the energy oscillates between the electrical energy in the capacitor C which can be associated with "kinetic energy" and the magnetic energy in the inductor L associated with "potential energy" (Fig. 2.4B).

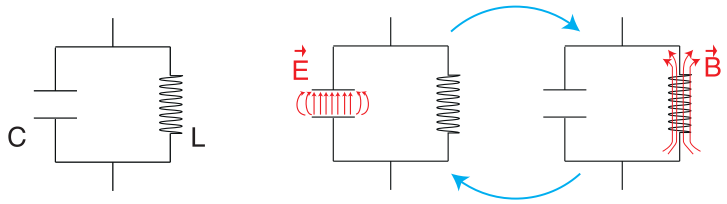

Figure 2.4: Schematic of an LC circuit. The parallel inductor L and capacitor C make a harmonic oscillator. In this system, the oscillations are between the electric field stored in the capacitors and the magnetic field in the coil.

To derive the Hamiltonian of the system, we consider the energy associated with the mode and the inductor and capacitor current relationships [43]

$$E(t) = \int_{-\infty}^{t} I(\tau)V(\tau)d\tau \tag{2.27}$$

$$I_C = C\frac{dV_C}{dt} \tag{2.28}$$

$$I_L = \frac{1}{L}\int_{-\infty}^{t} V_L(\tau)d\tau. \tag{2.29}$$

The circuit is then considered at different nodes. A node is a region between two circuit elements that are connected by ideal wires. Expressing these equations in terms of a node fluxes $\Phi(t) = \int_{-\infty}^{t} V(\tau)d\tau$ and node charges $Q(t) = \int_{-\infty}^{t} I(\tau)d\tau$. We can write the Lagrangian $\mathcal{L}$ of the system and thus the Hamiltonian H as

$$\mathcal{L} = \frac{C\dot{\Phi}^2}{2} - \frac{\Phi^2}{2L} \tag{2.30}$$

$$H = \frac{Q^2}{2C} + \frac{\Phi^2}{2L}. \tag{2.31}$$

We consider the system in terms of the photon excitation numbers. Writing the Hamiltonian can be written with photon number formalism by "second quantisation" of the flux $\hat{\Phi}$ and charge $\hat{Q}$. We introduce creation $\hat{a}^\dagger$ and annihilation $\hat{a}$ operators

$$\hat{\Phi} = \Phi_{\text{ZPF}}(\hat{a}^\dagger + \hat{a}) \tag{2.32}$$

$$\hat{Q} = iQ_{\text{ZPF}}(\hat{a}^\dagger - \hat{a}) \tag{2.33}$$

where zero point fluctuations of flux and charge are $\Phi_{\text{ZPF}} = \sqrt{\frac{\hbar Z}{2}}$ and $Q_{\text{ZPF}} = \sqrt{\frac{\hbar}{2Z}}$. The characteristic impedance of the circuit mode is $Z = \sqrt{\frac{L}{C}}$. Doing the expansion of the Hamiltonian, we arrive at the same QHO equation Eq. (2.11), with mode frequency $\omega = \frac{1}{\sqrt{LC}}$.

2.2.2 Josephson Junctions, Transmons and SQUIDs

Quantum harmonic oscillators have a linear energy level separation. This leads to unwanted transitions to higher excited states that leave the computational subspace when the system is coherently driven. A solution is to build a non-linear system with anharmonicity, meaning that the transition frequency from the state $|0\rangle$ to $|1\rangle$ (ω_{01}) and that from $|1\rangle$ to $|2\rangle$ (ω_{12}) are sufficiently different. In superconducting circuits, such non-linear systems, are created from Josephson junctions.

The junctions are made by sandwiching an insulating layer (an oxide) between two superconducting layers (aluminium) (Fig. 2.5A). The insulating layer acts as a potential barrier for the Cooper pairs to tunnel through. This results in a relation between the tunnelling current and phase across the Josephson junction known as the Josephson relations [44, 45]

$$I = I_c \sin(\phi) \tag{2.34}$$

$$\frac{d\phi}{dt} = \frac{2eV}{\hbar} \tag{2.35}$$

where I_C, ϕ and V are the critical current, phase difference and potential difference across the junction. The voltage and current across the junction are given by taking the time derivative of Eq. (2.34) and the time integral of Eq. (2.35)

$$V = \frac{\Phi_0}{2\pi} \frac{1}{I_C \cos\phi} \dot{I} = L_J \dot{I} \tag{2.36}$$

$$I = I_C \sin \frac{2\pi V}{\Phi_0} t + \delta_0 \tag{2.37}$$

where $\Phi_0 = \frac{h}{2e}$ is the magnetic flux quantum and $L_J = \frac{\Phi_0}{2\pi} \frac{1}{I_C \cos\phi}$ is a non-linear inductance of the Josephson junction and δ_0 is some offset phase which can be neglected. The

Hamiltonian of the Josephson junction can be given by calculating the energy due to the tunnelling of the Cooper pairs and the capacitance of the Josephson junction

$$H = \int IV\, dt + U_C \tag{2.38}$$

$$= \int I_C \sin\phi(t) \frac{\hbar}{2e}\frac{d\phi}{dt} dt + \frac{1}{2}\frac{Q^2}{C_J} \tag{2.39}$$

$$= -E_J \cos\phi + 4E_C N^2 \tag{2.40}$$

where we have used $Q = N \times 2e$ for an excess of N Cooper pairs with charge $2e$ on one side of the junction. The Josephson energy $E_J = \frac{\Phi_0 I_C}{2\pi}$ is the characteristic coupling energy and charging energy $E_C = \frac{e^2}{2C_J}$ is the energy needed to transfer one electron across the junction. Equation 2.40 has a constant energy offset after the integration which can be neglected. Thus, we can view the Josephson junction as a capacitor in parallel with a non-linear inductor (Fig. 2.5B) which results in a energy levels in a cosine potential (Fig. 2.5C).

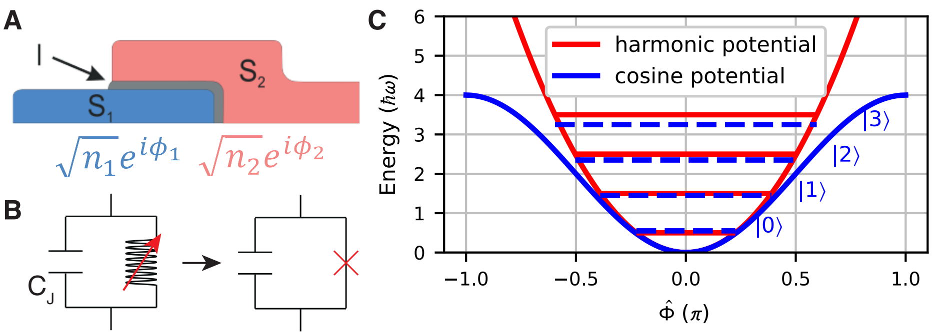

Figure 2.5: Josephson Junction schematic, circuit and energy levels. (**A**) The Josephson junction is made out of a superconductor-insulator-superconductor (SIS) sandwich. The superconducting islands will have a macroscopic phase difference which results in a non-linear inductance. Figure taken from [46]. (**B**) Electrical circuit representation of the SIS junction. (**C**) The cosine potential from the junction inductance results in an anharmonic potential with different energy level spacings.

Similar to the QHO, we can introduce occupation number formalism by quantising the phase ϕ and number N operators to arrive at the Cooper pair box Hamiltonian [47]

$$\hat{H}_{\mathrm{CPB}} = 4E_C\hat{N}^2 - E_J \cos\hat{\phi}. \tag{2.41}$$

Transmon regime

For the Hamiltonian Eq. (2.41), small fluctuations of charge number N will cause large changes in the energy level [48, 49]. This is known as charge noise. To circumvent this problem, the qubits are designed to be in the so-called transmon regime [50] such that $\frac{E_J}{E_C} \gg 1$. These qubits have already shown coherence times that are orders of magnitude larger than single qubit gate times, $T_2^*/t_{\text{gate}} \approx 10^5$ [51].

Drawing parallels to an LC harmonic circuit, the first term in Eq. (2.41) represents the kinetic energy of the "particle" and the second term represents a cosine potential well. Thus, the energy levels have different gaps because of this non-linear junction inductance L_J.

In this limit, the "particle" is confined towards the minimum of the cosine potential[2] and thus we can expand the cosine term: $\cos\phi \approx 1 - \frac{1}{2}\phi^2 + \frac{1}{4!}\phi^4 + O(\phi^4)$. Introducing creation and annihilation operators for the qubit

$$\hat{\phi} = \phi_{\text{ZPF}}(\hat{a}^\dagger + \hat{a}) \tag{2.42}$$

$$\hat{N} = iN_{\text{ZPF}}(\hat{a}^\dagger - \hat{a}) \tag{2.43}$$

where $\phi_{\text{ZPF}} = \sqrt[4]{\frac{2E_C}{E_J}}$ and $N_{\text{ZPF}} = \frac{1}{2}\sqrt[4]{\frac{E_J}{2E_C}}$ are the respective zero point fluctuations. Using the rotating wave approximation (RWA), where non-energy conserving and fast oscillation terms, such as $\hat{a}^\dagger\hat{a}^\dagger$ are removed. These fast oscillation terms average to zero over one oscillation period, leaving the slower rotating terms $\hat{a}^\dagger\hat{a}$ that determines the dynamics. The transmon Hamiltonian is

$$\hat{H} = \hbar\omega_q\hat{a}^\dagger a - \frac{\alpha}{2}\hat{a}^\dagger\hat{a}^\dagger\hat{a}\hat{a} \tag{2.44}$$

$$\hbar\omega_q = \sqrt{8E_JE_C} - E_C \tag{2.45}$$

where the frequency of the qubit is ω_q and the anharmonicity of the qubit is $\alpha = E_C$. The anharmonicity between energy levels sets the speed and selectivity of qubit operations. Fast qubit gates will have a broad frequency spectrum. This combined with a small anharmonicity, will lead to leakage to higher excited states. The default operating regimes are $E_C \approx 100 - 400\,\text{MHz}$ and $\frac{E_J}{E_C} \approx 20 - 200$ with higher transmon ratio meaning a qubit localised in the cosine potential well but lower selectivity in the qubit transition frequency [50].

The transmon qubit allows us to build artificial atoms with various parameters. Such systems are also easily extended to qudit algorithms with each successive energy level being different from the previous [30].

[2] One should note that this can be broken during a measurement process that causes the qubit to be excited out of the potential well and lead to excessive measurement-induced dephasing [52].

2.2.3 Circuit QED

There are two methods to obtain the Hamiltonian that describes the coupling of two elements (resonators or qubits) in a system. The first method describes the coupling of a qubit to a cavity in a semi-classical treatment of the system. The Hamiltonian obtained is known as the Jaynes-Cumming (JC) Hamiltonian [53] and will be explained in this section. Alternatively, the system Hamiltonian can also be derived via the linearisation of the system into the dressed frequencies and calculating the coupling between the modes. This is known as black box quantisation and is shown in Sec. 3.2.3.

The JC Hamiltonian describes an atom interacting with a bosonic mode [53]. This can also be used to describe our transmons as artificial atoms and resonators as QHO. This is a semi-classical method by taking the quantum nature of the atom interacting with a classical electric field from the bosonic mode.

The electric field from a mode can be written as $\mathbf{E}(\hat{c}^\dagger + \hat{c})$. Thus, the dipole interaction of the qubit mode, $\mathbf{d}(\hat{q}^\dagger + \hat{q})$, with the bosonic electric field $\mathbf{E}(\hat{c}^\dagger + \hat{c})$ is

$$\begin{aligned} \hat{H}_{\mathrm{JC-interaction}} &= \mathbf{E} \cdot \mathbf{d}(\hat{c}^\dagger + \hat{c})(\hat{q}^\dagger + \hat{q}) && (2.46) \\ &\approx \hbar g(\hat{c}^\dagger \hat{q} + \hat{c}\hat{q}^\dagger) && (2.47) \end{aligned}$$

where the coupling strength $\hbar g$ is proportional to the inner product of the electric field of the qubit and bosonic mode and the specific transition matrix between the qubit and bosonic energy levels. For superconducting circuits, we can design large dipole lengths leading to strong coupling strengths of $g/2\pi \approx 100 - 600\,\mathrm{MHz}$ with small loss rates $\gamma \ll 1\,\mathrm{MHz}$.

In the regime where the coupling strengths are smaller than individual element frequencies, $g \ll \omega_c, \omega_q$, we can use the RWA to arrive at the second equation which describes the interaction between the bosonic mode and the qubit. For a simplified two-level qubit, the eigenfrequencies for a coupled state $|\mathrm{qubit}, \mathrm{cavity}\rangle = |\pm, n\rangle$ are

$$\omega_{n,\pm} = n\omega_c \pm \frac{\hbar}{2}\sqrt{\Delta^2 + \Omega_n^2} \tag{2.48}$$

where $\Delta = \omega_c - \omega_q$ is the detuning between the modes and $\Omega_n = 2g\sqrt{n+1}$ is the Rabi frequency of the system for a specific cavity transition level. Near resonances, the frequencies will have an avoided crossing feature and experience vacuum Rabi oscillations between the two eigenstates. In this interaction regime, the two modes are highly hybridised and we can only call them "cavity-like" and "qubit-like" modes. An example of the feature is shown in Fig. 2.6 where a gap between the qubit and cavity frequency opens up. If the two modes are not coupled, the cavity and qubit frequencies will follow the dashed green and black lines respectively. The avoided crossing feature is used to determine the coupling strength g in simulations Sec. 3.2.1.

The vacuum Rabi oscillations result in excitation swapping from one mode to another and can be used as a two qubit gate [54]. The excitation swapping can be observed when we tune a qubit near another mode. Firstly, the far-detuned qubit is tuned near the resonance of a cavity and the system is allowed to evolve for a delay time. After which the qubit is tuned far away from resonance, the final population of the qubit is then a function of the delay time.

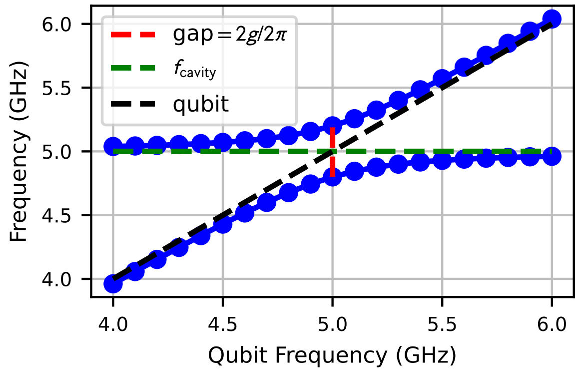

Figure 2.6: Calculated eigenfrequencies on avoided crossing feature. Away from the avoided crossing, we see the cavity mode at 5GHz. As the qubit is tuned near to the cavity frequency, we see a splitting of the two frequencies due to the hybridisation of the two modes. In this regime of $\Delta/2\pi = f_{\mathrm{cavity}} - f_{\mathrm{qubit}} = \pm g/2\pi$, the modes are only "cavity-like" and "qubit-like". For this calculation, $g/2\pi = 200\,\mathrm{MHz}$.

Strong Dispersive Limit

In the strong dispersive limit, the detuning between coupled modes is much greater than their coupling strength, $\Delta \gg g$. Using pertubation theory, we can derive the dispersive Hamiltonian via a unitary transformation of the JC Hamiltonian [28]

$$\hat{H}_{\mathrm{dispersive}} = \hbar\tilde{\omega}_c \hat{c}^\dagger \hat{c} + \hbar\tilde{\omega}_q \hat{q}^\dagger \hat{q} - \chi \hat{c}^\dagger \hat{c} \hat{q}^\dagger \hat{q} - \frac{\alpha}{2}\hat{q}^\dagger \hat{q}^\dagger \hat{q}\hat{q} \tag{2.49}$$

$$\hat{H}_{\mathrm{resonator-shifted}} = (\hbar\tilde{\omega}_c - \chi \hat{q}^\dagger \hat{q})\hat{c}^\dagger \hat{c} + \hbar\tilde{\omega}_q \hat{q}^\dagger \hat{q} - \frac{\alpha}{2}\hat{q}^\dagger \hat{q}^\dagger \hat{q}\hat{q} \tag{2.50}$$

$$\hat{H}_{\mathrm{qubit-shifted}} = \hbar\tilde{\omega}_c \hat{c}^\dagger \hat{c} + (\hbar\tilde{\omega}_q - \chi \hat{c}^\dagger \hat{c})\hat{q}^\dagger \hat{q} - \frac{\alpha}{2}\hat{q}^\dagger \hat{q}^\dagger \hat{q}\hat{q} \tag{2.51}$$

where the dressed frequencies of the qubit $\tilde{\omega}_q$ and resonator $\tilde{\omega}_c$ are renormalised due to a Lamb shift induced by the vacuum Rabi interactions. Importantly, the resonator frequency is shifted by χ for each excitation $\hat{q}^\dagger \hat{q}$ of the qubit mode as seen in Eq. (2.50). Alternatively, the qubit frequency is shifted by χ for each photon $\hat{c}^\dagger \hat{c}$ in the cavity. The two ways of viewing the dispersive Hamiltonian is shown in Fig. 2.7.

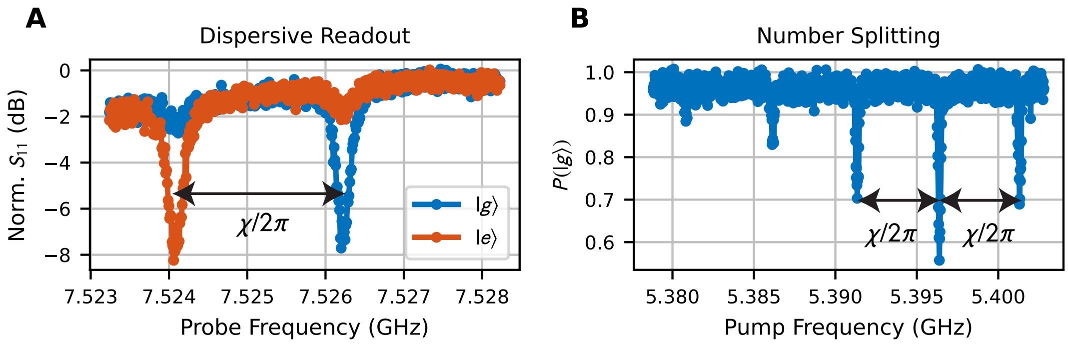

Figure 2.7: Dispersive readout and number splitting view of the dispersive Hamiltonian. (**A**) Dispersive readout where the qubit state shifts the readout resonator by $\chi/2\pi$. Thus, readout resonator reflection measurements will show different frequency values. (**B**) Each photon in the resonator will shift the qubit frequency by $\chi/2\pi$. Thus, qubit spectroscopy will show a distribution of qubit frequencies according to the cavity photon number state.

By determining the frequency of the cavity, the state of the qubit can be inferred. This is known as dispersive readout, in which the qubit state is inferred by coupling the qubit to a low Q resonator and letting the photons of the readout resonator leak into its environment (the measurement device). The dressed frequencies and dispersive interaction are given by [28]

$$\tilde{\omega}_c = \omega_c - \frac{g^2}{\Delta - \frac{E_C}{\hbar}} \tag{2.52}$$

$$\tilde{\omega}_q = \omega_q + \frac{g^2}{\Delta} \tag{2.53}$$

$$\chi = 2\frac{g^2}{\Delta}\frac{1}{1 - \frac{\Delta}{E_C}} \tag{2.54}$$

where $\tilde{\omega}_{\mathrm{c,q}}$ and $\omega_{\mathrm{c,q}}$ are the dressed and bare frequencies of the cavity and the qubit respectively.

Considering, the JC Hamiltonian and the coupling strength of the bosonic mode to the qubit $g_n \propto 2g\sqrt{n}$. To be in the dispersive limit for all occupied levels, we need to stay below the limit where $g_n < \Delta$. This gives an upper bound of the critical number of photons in the cavity mode $n_{\mathrm{crit}} = (\Delta/2g)^2$.

As mentioned in the beginning, the dispersive Hamiltonian can also be derived by considering the dressed modes of the system. In this view, each mode induces a current flow through each junction. From the Josephson relation Eq. (2.34), we can relate the phase across the junction being the sum of the contributions from the different modes, $\hat{\phi}\sum_i \phi^i_{\mathrm{ZPF}}(\hat{i}^\dagger + \hat{i})$. This is shown in Sec. 3.2.3.

2.2.4 SQUIDs and Flux Tuning

The transmon qubits considered are fixed-frequency qubits. To allow for in-situ tuning of qubit frequencies, two Josephson junctions are placed in parallel, producing a DC Superconducting Quantum Interference Device (SQUID) [55]. This geometry allows for the Josephson energy to be adjusted by a magnetic flux through the SQUID loop

$$E_J^{\mathrm{SQUID}}(\Phi) = 2E_J^{\Sigma}\left|\cos\left(\pi\frac{\Phi_{\mathrm{loop}}}{\Phi_0}\right)\right|^2\sqrt{1+\alpha_I^2\tan^2\left(\pi\frac{\Phi_{\mathrm{loop}}}{\Phi_0}\right)} \tag{2.55}$$

where $E_J^{\Sigma} = E_J^1 + E_J^2$ is the sum of the individual Josephson junctions, Φ_{loop} is the magnetic flux through the SQUID loop and α_I is the asymmetry factor between the junction inductances, or equivalently, the ratio of junction sizes. Examples of SQUID frequency tuneability with different asymmetry factors are plotted in Fig. 2.8. By tuning the qubit frequency, we can also tune the strength of the dispersive interaction χ between the modes.

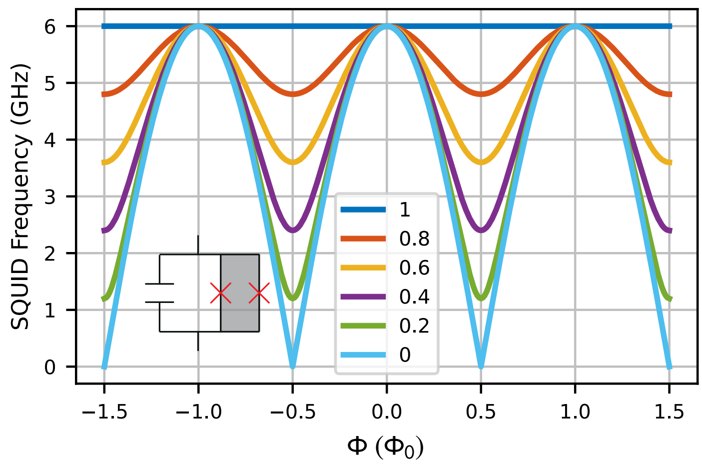

Figure 2.8: SQUID frequencies with threaded flux. A SQUID element is made by placing two Josephson junctions in parallel. **Inset**: circuit representation of the SQUID element. By threading a magnetic flux through the loop created by the Josephson junctions (grey area), we can tune in-situ the SQUID frequency. The degree of tuneability can be adjusted by the relative Josephson energies of the individual junctions (denoted by the different colours in the legend). Due to stochastic fabrication processes, we have $d > 0.1$.

While SQUIDs allow the fine in-situ tuning of the qubit frequency, this extra control knob comes at a cost. The qubit is exposed to flux noise which will cause variations in the qubit frequency and cause a faster dephasing rate. To avoid excessive dephasing, extra care needs to be considered in filtering such flux bias lines.

For full qubit frequency range tuneability, these flux bias lines must deliver at least a full flux quantum. For fast qubit frequency tuning, we might need to account for the response of the coil loops and thus might need as much as $5\Phi_0$. This can be done by scaling up the SQUID loop size or increasing the current in the flux bias line. However, the former is undesirable as the additional dephasing rate with flux will grow as a function of SQUID loop size [56]. The latter is limited by the amount of current we can put into the cryostat before the experiment warms up. Thus, the flux bias lines need to be as efficient as possible. In Sec. 3.5, I describe the fabrication of a new generation of flux hoses that allows magnetic fields to be guided into a superconducting 3D cavity.

2.2.5 Purcell Decay and Filters

For dispersive readout, we drive the readout resonator with photons and measure its response. The rate of the resonator photons leaking out is the linewidth of the cavity κ. For a high measurement fidelity, we want the total measurement time to be much faster than the lifetime of the qubit. Thus, one might assume that we want as large a κ as possible.

However, the dispersive coupling between the qubit and low Q readout resonator will provide a decay channel for the qubit [57]. The Purcell effect is the enhancement of the spontaneous decay of an atom when the cavity and atom are on resonance. In our case, our artificial atoms have large dipole moments and will naturally have strong couplings to their environment. The qubit is limited by a decay rate of [58]

$$\Gamma_{\text{Purcell}} = \kappa \left(\frac{g}{\Delta} \right)^2 \tag{2.56}$$

where κ is the decay rate of the resonator, g and Δ is the coupling strength and detuning between the resonator and qubit. The $\frac{g}{\Delta}^2$ factor comes from the Lorentzian shape of the resonator. Thus, to suppress the Purcell rate of the qubit, we need to decrease the qubit resonator coupling, increase the detuning between the qubit and the resonator, reduce the energy damping rate of the resonator or change the Lorentzian shape of the resonator.

However, the first three methods lead to longer readout times. This ultimately reduces readout fidelity due to the finite lifetime of the qubit. For fast readout of the resonator, we desire a large κ for faster leakage of resonator photons and a strong coupling between the qubit and readout resonator $\chi \approx \frac{g^2}{\Delta}$. But this comes at a cost of increased Purcell decay of the qubit. Thus, there is a balance between these competing requirements. It has been shown that the optimal readout is when $\kappa = \chi$ [59, 60].

In the dispersive limit, the large detunings between the qubit and the resonator provide an opportunity to break the trade-off between fast readout and protection. This is done with Purcell filters that suppress the qubit frequencies in the measurement line. Some methods are shown in Fig. 2.9. These methods work by reducing the transmission probability into the environment at the qubit frequency.

Firstly, another resonator can be coupled to the qubit. The two qubit-resonator decay paths destructively interfere at the measurement line. This can be seen as adding a notch filter at the qubit frequency in the spectrum [61]. Alternatively, a bandpass filter can be added that only allows the transmission of frequencies around the readout resonator [62–64]. Or if possible, the experiment can be placed in a waveguide that suppresses transmission below the waveguide cut-off frequency. The cut-off of the waveguide will protect the qubit from decaying to its environment [65].

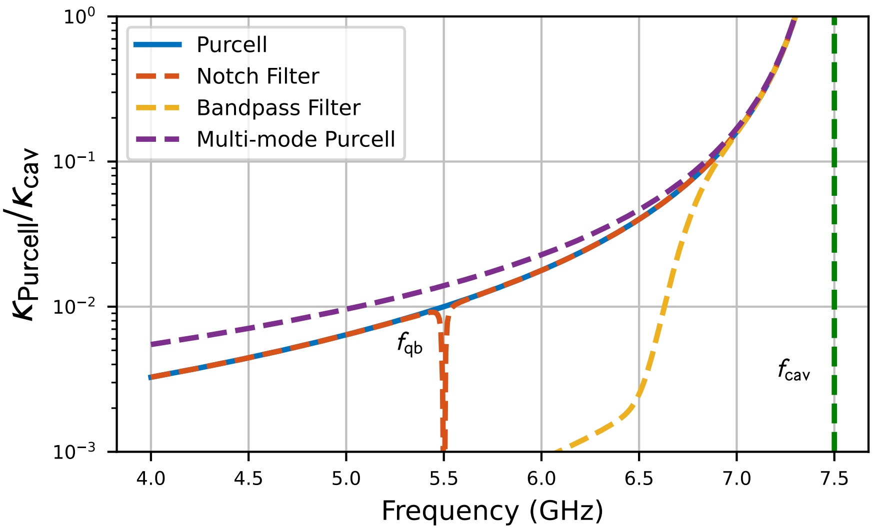

Figure 2.9: Comparision of decay rates of the qubit for different setups. Due to the coupling to the readout cavity, the qubit will have a Purcell rate given by the blue line. Accounting for higher modes of the cavity, the multi-mode Purcell effect (purple dashed line) results in an even lower limit of the maximum qubit T_1 time. Different methods show the Purcell protection from a notch filter at the qubit frequency (red dashed line) and a bandpass filter that only allows the transmission near the cavity frequencies (yellow dashed line). The notch filter can be achieved by a simple addition of another resonator and provides Purcell protection at a specific qubit frequency (in this example, at 5.5 GHz). Conversely, the bandpass filter is more complicated to design but provides Purcell protection for a range of qubit frequencies (in this example, below 6 GHz). Not shown are methods such as using a waveguide, careful positioning of the readout pin or a saturable filter.

A passive Purcell protection method works by placing the measurement pin at the node of the electric field of the qubit mode. At such a location, the qubit electric field is not able to excite a mode in the coaxial measurement line and thus the decay is suppressed [66].

While these methods have been shown to beat the readout trade-off problem, for control lines used to address both the qubit and cavity modes, Purcell filters introduce a qubit control problem. In the ideal case, complete suppression of the coupling between the measurement line and qubit mode leads to sacrificing control of the qubit. Experimentally, this means more power is needed in qubit signals or a separate qubit control line is required. Saturable or non-linear Purcell filters have been suggested to overcome this limitation [67, 68].

In Sec. 3.6, I describe the fabrication of a modular bandpass Purcell filter that is integrated into a coupling pin for 3D cavity architectures.

2.3 Quantum Control

To perform operations on the quantum systems, the relevant qubit or cavity mode d has to be coupled to an external drive $\mathbf{E}$. For superconducting circuits, the drive is a microwave drive at frequency ω_d introduced by an external coupling pin. This adds another term in the Hamiltonian $\mathbf{d} \cdot \mathbf{E}(t)(\hat{a}^\dagger e^{-i\omega_d t} + \hat{a} e^{i\omega_d t})$. For cavity modes, such on-resonant classical drives are described by the displacement operator

$$\hat{U}_{\text{cavity control}} = e^{-i\frac{1}{\hbar}\mathbf{E}(t)(\hat{a}^\dagger + a)t} \propto \hat{D}(\mathbf{E}(t)t). \tag{2.57}$$

By turning on a drive $\mathbf{E}(t)$ for a certain time t, we can apply a displacement on the cavity. The phase of the drive will also determine the phase of the displacement.

For qubit modes with sufficiently large anharmonicities, we can consider the simplified picture of a two-level system and reduce the drive operators $\hat{a}^\dagger \to \hat{\sigma}_+$ and $\hat{a} \to \hat{\sigma}_-$. By doing a frame transformation $\tilde{\hat{H}}_\text{d} = \hat{U}(t)\hat{H}_\text{d}\hat{U}^\dagger - i\hbar\hat{U}(t)\frac{\partial \hat{U}^\dagger}{\partial t}$ into the rotating frame of the drive and performing the rotating wave approximation, the drive Hamiltonian is

$$\tilde{\hat{H}}_\text{d} \propto E(t)(\cos\omega_q t\hat{\sigma}_y - \sin\omega_q t\hat{\sigma}_x). \tag{2.58}$$

The electric field applied can be written as: $E(\omega, t, \phi) = V(t)(\cos\phi\sin\omega_d t + \sin\phi\cos\omega_d t)$. Considering this drive, Eq. (2.58) is

$$\begin{aligned}\tilde{\hat{H}}_\text{d} &\propto V(t)(\cos\phi\sin\omega_d t + \sin\phi\cos\omega_d t)(\cos\omega_q t\hat{\sigma}_y - \sin\omega_q t\hat{\sigma}_x) && (2.59)\\ &\approx -\frac{1}{2}V(t)(\cos(\Delta t + \phi)\hat{\sigma}_x) + \sin(\Delta t + \phi)\hat{\sigma}_y) && (2.60)\end{aligned}$$

where $\Delta = \omega_q - \omega_d$ and we have used the RWA for the second equation. Thus, for on-resonance pulses, the Hamiltonian is

$$\tilde{\hat{H}}_\text{d} = -\frac{\Omega}{2}(I\hat{\sigma}_x + Q\hat{\sigma}_y) \tag{2.61}$$

for some Rabi frequency Ω that is determined by the overlap between the electric field of the drive and the mode, and the qubit level transition matrix element. Here, we have adopted the electrical engineers' definition for the "in-phase" $I = \cos\phi$ and "out-of-phase" $Q = \sin\phi$ components. By changing the drive phase, we can apply $\hat{\sigma}_X$ or $\hat{\sigma}_Y$ operations giving us universal control on the qubit. $\hat{\sigma}_Z$ rotations can be done by changing the frame of the drive by changing the phase ϕ. The probability of finding the qubit in the excited state for a drive with Rabi frequency Ω and detuning Δ is [31]

$$P(e) = \frac{\Omega^2}{\Omega^2 + \Delta^2}\sin^2\left(\frac{\sqrt{\Omega^2 + \Delta^2}}{2}\right)t. \tag{2.62}$$

By changing the amplitude of the pulse or the length of the pulse we can Rabi flop the qubit from the ground to the excited state. For off-resonant pulses, the qubit is not fully flipped to the excited state [3].

[3]Due to the multi-level nature of the transmon, a drive will also induce AC Stark shifts that change the frequency of the mode. For the case $\Delta \gg \Omega$, the AC Stark shift is approximated by Shift $\approx \frac{\Omega^2}{\Delta}$ [69, 70].

2.3.1 Conditional Qubit Control

The number splitting Hamiltonian Eq. (2.51) allows for conditional qubit control. Since the qubit frequency is shifted by χ for each photon in the cavity, we can apply selective pulses on the different number split qubit peaks, by shaping the spectral content of the pulse. As illustrated in Fig. 2.10, this is done by defining a Gaussian pulse with a certain linewidth σ_t. The linewidth of the Fourier transform of the Gaussian is then given by $\sigma_f = 1/(2\pi\sigma_t)$ (green dashed line).

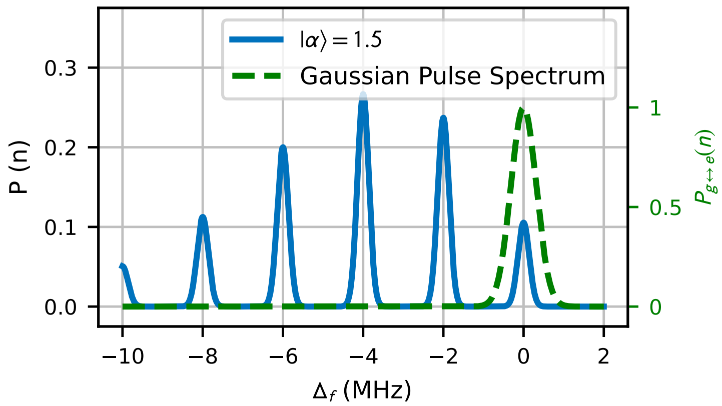

Figure 2.10: Calculated qubit spectroscopy of a number split qubit and frequency spectrum of a cavity photon number selective Gaussian pulse. In this setup, a qubit is coupled to a cavity in the strong dispersive regime. Due to the cavity photon state, the qubit frequency is split into many peaks that correspond to the cavity photon number Here, $\alpha = 1.5$. By choosing the spectrum of our qubit pulse (green dashed line), we can perform operations that affect the qubit at certain frequencies. As these frequencies correspond to the cavity photon state, this is effectively a qubit operation conditioned on the number of photons in the cavity.

By choosing a longer pulse length $\frac{1}{2\pi\sigma_t} < \chi/2\pi$, the pulse will be selective on one number of qubit peaks. This allows qubit operations condition on the number of photons in the cavity. This can be extended to playing a multi-frequency pulse conditional on an even or odd number of photons in the cavity.

2.3.2 Two qubit operations

For more complex algorithms, multi-qubit operations are required. There are many possible schemes of realising operations between two qubits. A good summary can be found in [28].

These gates can then be transformed into any two qubit unitary by the addition of other single-qubit unitaries. Each gate has its own advantages and drawbacks, but in general requires purpose-built hardware and have limited flexibility in applying any target unitary.

Beyond the fixed-design two qubit gates, a scheme to implement a flexible controlled unitary was proposed by Friis et al [71]. The scheme uses qubits that are coupled via a high coherence cavity acting as a quantum bus. The multi-qubit gate is realised by mapping the state of one qubit onto the cavity and playing operations on the second qubit conditioned on the cavity states. Effectively, this is a controlled operation between the two qubits with the cavity acting as a quantum bus.

In chapter 7, I explain a proof-of-principle experiment that demonstrates the realisation of a modular, flexible multi-qubit gate protocol.

2.3.3 Quantum Optimal Control

The generation of high-fidelity quantum states and multi-qubit gate operations is a fundamental requirement for quantum physics experiments. With the ability to do displacements on the cavity and conditional or unconditional rotations on the qubit, we have full universal control of the quantum system and can produce any target state. However, in reality, we need to consider imperfections in the system that limit the fidelity of the operation. These include decoherence, experimental limitations of qubit pulses, stochastic variations of Hamiltonian parameters, and unknown transfer functions of the qubit and cavity pulse.

Fidelity is a measure of the distance between two states or two gates. When preparing a final state $|\psi_{\text{final}}\rangle$ from an initial state $|\psi_{\text{initial}}\rangle$ using a unitary $\hat{U}$, the state fidelity with the target state $|\psi_{\text{target}}\rangle$ is

$$\mathcal{F}_{\text{st}} = \left|\langle\psi_{\text{target}}|\hat{U}|\psi_{\text{initial}}\rangle\right|^2 = \left|\langle\psi_{\text{target}}|\psi_{\text{final}}\rangle\right|^2 . \tag{2.63}$$

Similarly, the gate fidelity of a unitary $\hat{U}$ with $\hat{U}_{\text{target}}$ is

$$\mathcal{F}_{\text{g}} = \frac{1}{N}\sum_{i}^{N}\left|\langle\psi_i|\hat{U}^\dagger\hat{U}_{\text{ideal}}|\psi_i\rangle\right|^2 \tag{2.64}$$

$$= \frac{1}{N}\sum_{i}^{N}\left|\langle\psi_{\text{final},i}|\psi_{\text{target},i}\rangle\right|^2, \tag{2.65}$$

where $\hat{U}_{\text{ideal}}$ is the ideal state of the target unitary for an input state $|\psi_i\rangle$, and the sum is over all possible input states N. Fidelities are often described in the context of quantum channels and more information can be found in [21, 38].

One can see that optimising a gate is more difficult as the set of all possible input states needs to be considered. For single qubit unitaries, this entails measuring the overlap between the final state and the ideal output state when the gate $\hat{U}$ is applied to the 6 cardinal states on the Bloch sphere. For example, the gate fidelity of a pulse that realises the $\hat{X}$ operation needs to include the following terms $\mathcal{F}(\hat{U}) = \frac{1}{6}(\left|\langle 1|\hat{U}|0\rangle\right|^2 + \left|\langle 0|\hat{U}|1\rangle\right|^2 + \left|\langle +|\hat{U}|+\rangle\right|^2 + \left|\langle -|\hat{U}|-\rangle\right|^2 + \left|\langle -i|\hat{U}|i\rangle\right|^2 + \left|\langle i|\hat{U}|-i\rangle\right|^2)$. For two qubit unitaries, the set of all possible input states is much larger and grows with the number of qubits n as 6^n [72].

Quantum Optimal Control (QOC) is a toolbox to design pulses to improve quantum operations by dynamically changing the control fields. A good overview of the QOC field can be found in [73, 74]. The unitary between some initial state and target state need not be only discrete cavity displacements and qubit rotations. Instead, we can consider a "continuous" quantum trajectory. This is done by shaping the pulses applied to the quantum system to dictate the evolution of the system. The optimal unitary $\hat{U}_{\text{QOC}}$ is defined as

$$|\psi_{\text{final}}\rangle = \hat{U}_{\text{QOC}}(t, \mathbf{E}(t))\,|\psi_{\text{initial}}\rangle \tag{2.66}$$

$$\hat{U}_{\text{QOC}}(t, \mathbf{E}) = Te^{-\int_0^T \hat{H}_{\text{drive}} dt}. \tag{2.67}$$

where $\mathbf{E}(t)$ is the control fields for each quantum system (qubit and high Q cavity), T is the total time of the drive Hamiltonian $\hat{H}_{\text{drive}}$.

Open-Loop Optimisation

In open-loop optimal control, the quantum system is first characterised and then numerically simulated. Pulses are applied to the simulated system and the fidelity is maximised.

In the language of computer science, the optimisation problem is to maximise or minimise an objective function, some fidelity $\mathcal{F}$, that is given by some cost function under some constraint functions

$$\max_{\mathbf{E}} \mathcal{F}(\mathbf{E}) - \sum_i \lambda_i g_i(\mathbf{E}).$$

where λ_i is the associated multiplier (weight) for a particular constraint function $g_i(\mathbf{E})$. Constraint functions are used to guide the optimisation towards desired experimental needs, such as a constraint on the maximum pulse voltage or bandwidth of the pulses applied.

In appendix B, the open-loop optimisation problem is outlined with examples of constraint functions used and a brief explanation of the different search routines. One notable search method is gradient descent [75] in which parameters are changed and the direction of search in the parameter space is guided by the gradient of the objective function with respect to the change in the control field.

Closed-Loop Optimisation

Most experiments are guided by Hamiltonians containing terms that are either neglected in corresponding models or imperfectly characterised. Stochastic variations of the Hamiltonian or in the instrument setup exacerbate these imperfections. A method that aims to mitigate these problems is called closed-loop optimisation.

Closed-loop optimisation works by giving the final state of the operation as feedback to the optimisation routine. A larger fidelity rewards the routine in a method similar to a reinforcement learning algorithm. The main advantage compared to open-loop optimisation is this feedback mechanism back into the optimisation routine. The optimiser can iterate over a few control parameters to learn about the objective function "landscape". Then based on the search method, find the next iteration of pulses to apply to find the optimal control pulses.

If the repetition rate of experiments is fast, this feedback method can help find optimised pulses quickly. However, measuring the state or gate fidelity of a quantum process is computationally expensive, especially for a high number of qubits. This problem is even worse for bosonic modes. The infinite Hilbert space of the bosonic mode requires measurements across the entire phase space for full-state reconstruction.

However, a carefully chosen figure of merit (FOM) can approximate the final state fidelity. Two examples of choices for a FOM are

$$\mathrm{FOM} = \frac{\sum_i W_{\mathrm{data}}(i)}{\sum_i W_{\mathrm{ideal}}(i)}, \tag{2.68}$$

$$\mathrm{FOM} = \frac{\sum_i W_{\mathrm{ideal}}(i) W_{\mathrm{data}}(i)}{\sum_i |W_{\mathrm{ideal}}(i)|^2} \tag{2.69}$$

where the sum is over some chosen distribution of points over the bosonic mode Wigner function. The first FOM puts equal weights on all distribution points, while the second FOM has more emphasis on the parts of the Wigner function with larger values. Depending on the desired target state, one can extend this idea by a prefactor k on the sample points that should be weighted heavier.

In my work, we collaborated with Dr. Marco Rossignolo and Dr. Phila Rembold from the group of Prof. Simone Montangero at the University of Padova. A QOC protocol was used, known as dressed Chopped Randomised Basis (dCRAB) [76, 77] algorithm. In the dCRAB algorithm, the optimal pulses are defined over some basis and the coefficients in the basis are optimised. The algorithm then changes the basis in which the optimal pulses are defined and the optimisation is continued in the new basis. This way, a global maximum or minimum in the objective function can be found without the need to search a large control parameter search space.

In Sec. 5.4, a proof of principle experiment demonstrates an improvement of state preparation fidelity of a cat state. This was done in a closed-looped optimisation routine without full-state reconstruction. This method applies to any platform and can also be used for more complex bosonic states [78, 79].

CHAPTER 3

Experimental Platform

"a little quantum physics"

Apart from the superconducting circuits and quantum physics field, the physical realisation of the experiment covers many different areas. We operate in the radio frequency (RF) regime, which uses many proven classical methods to design and simulate our electrical circuits. Many RF instruments can also be commercially bought and directly used. Likewise, cryogenic systems have become increasingly automated. The fabrication of the samples uses nano- and micro-fabrication techniques adapted from the complementary-metal-oxide-semiconductor (CMOS) industry. Finally, machining and polishing methods are used to build the cavities and mounting clamps. The work of an experimentalist is to then integrate these different fields according to the needs of each experiment to do a "little quantum physics".

Information in this chapter will briefly cover these many different aspects of the experimental setup. I had the fortunate opportunity to expand the Kirchmair lab to a new space and set up a new cryostat. This allowed me to learn more about the finer details of the instruments behind the experiments. A full in-depth description of each section can be expanded to cover a chapter on its own, as can be found in many good textbooks and theses [18, 80–83]. However, the goal of this chapter is to outline the working principles used for the measurements presented in this thesis and the rules of thumb for the experimental design.

The experimental setup consists of qubits coupled to a high coherence cavity with individual readout resonators. These cavities have long lifetimes and high quality factors and are also known as high Q cavities. The high Q cavity acts as a quantum information storage mode or a quantum bus between qubits. The qubits provide the non-linearity and quantum properties required for the experiment. The individual readout resonators are for qubit state measurements. Finally, the transmons can be embedded in a loop forming a SQUID for in-situ qubit frequency tuning. The platform shown in Fig. 3.1 was built to accommodate the different requirements of various experiments.

In the first section, I discuss the design of qubits and resonators. Next, I cover how the specific geometries are simulated in a finite-element simulation. Section 3.3 and 3.4 cover the fabrication and treatment of the qubits and cavities in the cleanroom and mechanical workshop. In Sec. 3.6 and Sec. 3.5, I briefly cover the fabrication and design of our Purcell filter and flux hose setup. Finally, Sec. 3.7 and Sec. 3.8 cover the cryogenic and microwave setups used to reach the superconducting temperatures required for the experiments.

Figure 3.1: Picture of the experiment setup which consists of a high Q cavity coupled to qubits. Each qubit is also coupled to an individual readout resonator. Included in the setup are 3D modular Purcell filters that replace the conventional SMA pin and a new generation flux hose design to introduce magnetic flux tuning. Photo taken by David Jordan.

3.1 Design

A great benefit of superconducting circuits is the ability to design a wide range of Hamiltonian parameters. By combining different circuit elements (inductors, capacitors and junctions) and different coupling methods (inductive or capacitive), we can build artificial atoms catered to the experimental needs.

It is important to remember that in the realisations of the LC resonators, the resonators are rarely single mode and have higher-order modes at double or triple the frequency. Depending on the specific design and mode structure, these modes can also have unwanted coupling to a qubit or the environment leading to additional Purcell decay of the qubit [58].

3.1.1 "2D" Resonators and Qubits

A type of resonator used in 3D architectures of superconducting circuits is the microstrip resonator design. This design is a strip of superconducting material patterned on a sapphire or silicon substrate. The length of the strip is $L \approx \lambda/2$ with the specific geometry of the strip affecting the self-inductance and capacitance. A ground plane is added on the backside of the substrate leading to a small, compact design. Such structures are called "2D" in the sense that the sheets of metal are patterned on a substrate. However, in the designs used in the thesis, the ground plane is not on the back of the substrate but on the surrounding walls around the structure. Thus, the field of such microstrip modes lives in a 3D space (Fig. 3.2A).

Due to the extended structure of the microstrip, the resonators are not lumped-element structures resulting in a modified inductance and capacitance. The frequency and mode distribution of the structures are found in electrostatic finite element simulations.

Although these structures are operating in a superconducting, and thus dissipationless, state, in practice there is some dissipation due to imperfections in the fabrication process or unwanted coupling to a lossy environment. These lead to resistive losses. A useful metric is the quality factor

$$Q = \omega \frac{\text{Total Energy Stored}}{\text{Total Power Dissipated}} = \frac{\omega}{\kappa} = \omega(2T_1). \tag{3.1}$$

The quality factor or linewidth can be further divided into internal losses and external losses $1/Q_{\text{total}} = 1/Q_{\text{internal}} + 1/Q_{\text{external}}$. External losses are by design, and are the coupling between our measurement devices and the resonator mode. 2D designs will experience higher internal loss as the electric field is contained in a dielectric substrate. These substrates can contain substrate or surface defects in 2D samples.

Transmons are made by connecting large capacitive pads with a Josephson junction. The capacitor pads form the large capacitance needed for the transmon limit and the Josephson junction provides the non-linearity for the addressability of the qubit. The connection link is made as small as possible to reduce the linear inductance of the transmon.

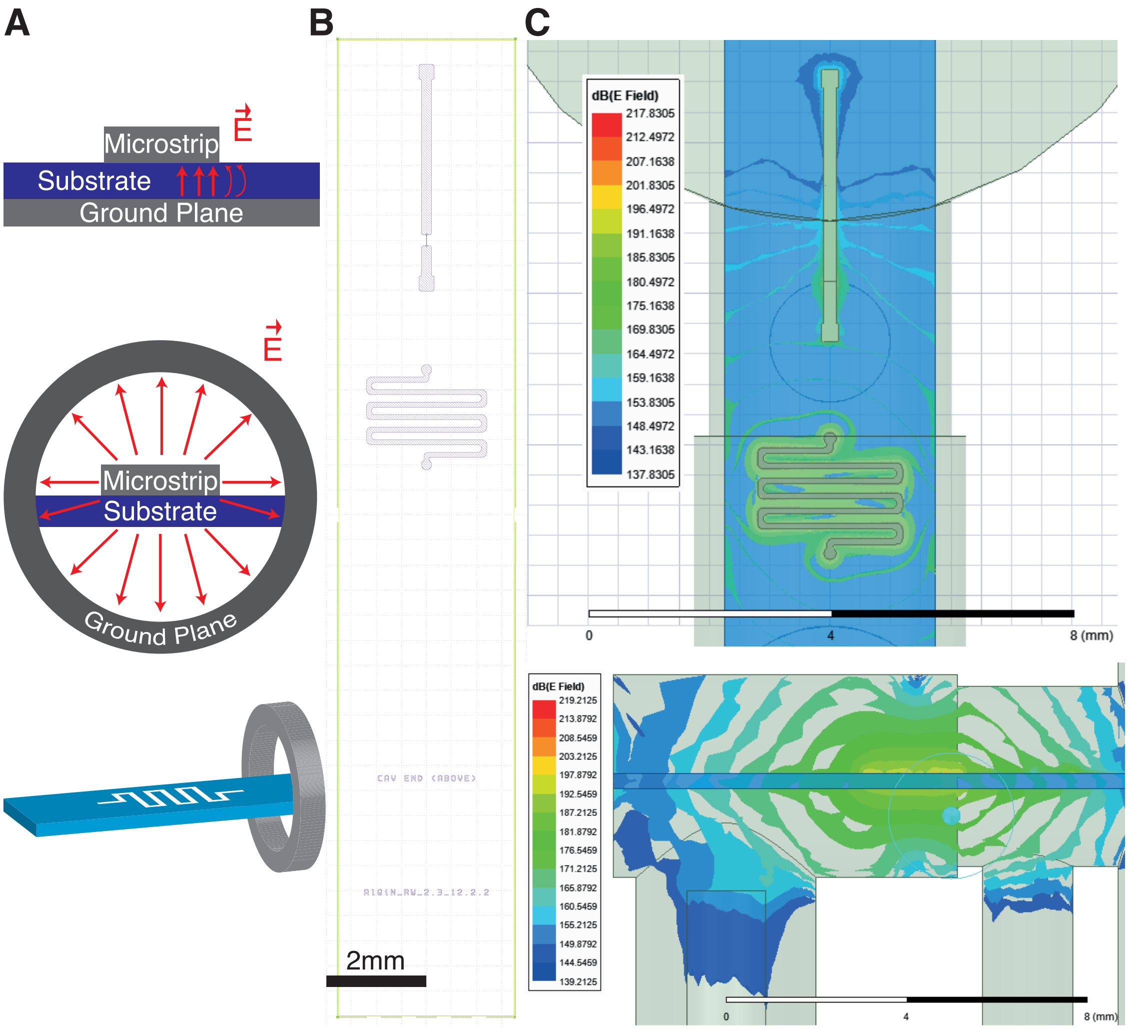

Figure 3.2: Schematic, design and simulation of microstrip. (**A**) Electric fields (red lines) from microstrip design. Dimensions are not to scale. (Top) The typical 2D microstrip design consists of a metallic plane on top of a substrate and a ground plane on the bottom. The electric fields are between these two metal sheets and the design has a small compact form factor. (Centre and bottom) In the "3D" microstrip designs used here, the central microstrip is placed on the substrate and the chip is placed into a superconducting tunnel. The electric fields are then between the central metallic plane and the surrounding walls. (**B**) Design of qubit and microstrip resonator. The resonator is the meandering structure whose length and shape determine the resonance frequency of the resonator. At the top of the chip, there is a design for a qubit which is a Josephson junction connecting two capacitor pads. At the bottom of the chip, there is space left for the copper clamps holding the sample chip. (**C**) Top and side view of HFSS eigenmode simulations of the microstrip mode of the resonator in a tunnel. The ground plane is not in the substrate but in the surrounding cavity walls around the structure. Thus, the field of such a microstrip mode lives in a 3D space. In these simulations, hybridisation with the qubit mode is seen from the electric fields also overlapping with the qubit structure.

3.1.2 High Q cavities

The electric field mode of 2D resonators has additional losses due to the presence of the substrate. Surface defects at the substrate-metal and substrate-vacuum interface will limit the quality factor of the resonator mode. A way to circumvent this problem is with 3D cavities where the electric field is mainly in the vacuum. This results in a lower participation ratio in the lossy areas and thus the cavity mode has much higher internal quality factors [84]. The first 3D cavities were cuboid blocks with the length, width and height of the cavity determining the mode frequency [85].

The cavities are mainly made from a block of metal in a subtractive process[1]. This means a cut through the cavity halves is needed. Such a cut will introduce a seam which is an area for imperfections. The electric field mode which induces a current flow across such seams will lead to resistive losses. These seam losses can be reduced by choosing the cut of the cavity to be parallel with the current flow direction or providing a better seal with indium wire bonding [86]. Another method to reduce seam losses is through the usage of electron beam welds shown in Tesla cavities [87, 88]. Good sources for the discussion of various loss mechanisms can be found in [60, 89]. Some designs avoid the seams entirely which allows for higher quality factors. Some examples are post cavities [90] or flute cavities [91].

In the Kirchmair lab, we use coaxial $\lambda/4$ post cavities [92], which combines the concepts of a coaxial transmission line and a circular waveguide section at the top (Fig. 3.3). These cavities can be made by a subtractive process from one block of metal and thus the current of the cavity mode can flow without going through any seams. The radius of the inner to outer conductor is chosen $\frac{a}{b} = \frac{1}{3}$, which reduces surface resistance losses [82].

The coaxial part forms a post which is short-circuited at the bottom and open at the top. The height of the post approximately determines the frequency of the mode $l = \frac{\lambda}{4}$. The effective length is altered due to the capacitive loading of the circular waveguide. This effect can be accounted for by eigenmode simulation of the designed structure.

The circular waveguide is designed with a cutoff frequency much higher than the frequency of the cavity mode. This leads to exponential suppression of any leakage of the cavity mode. The propagation constant of the waveguide is $\beta = \sqrt{(\frac{2\pi}{\lambda})^2 - (\frac{p_{01}}{b})^2}$, where $p_{01} = 2.405$ is the first root of the Bessel function J_0. The electric field strength will thus decrease by $\mathbf{E} \propto e^{-2\beta L}$. Choosing a length L such that the electric field is attenuated to a factor 10^{-9} will thus allow for a high coherence mode with quality factors limited by $Q \approx 10^9$.

[1] As 3D metal printing processes are being developed, one can consider such an additive fabrication process. However, we will need to etch the surface of the structure after machining which is difficult for an enclosed cavity.

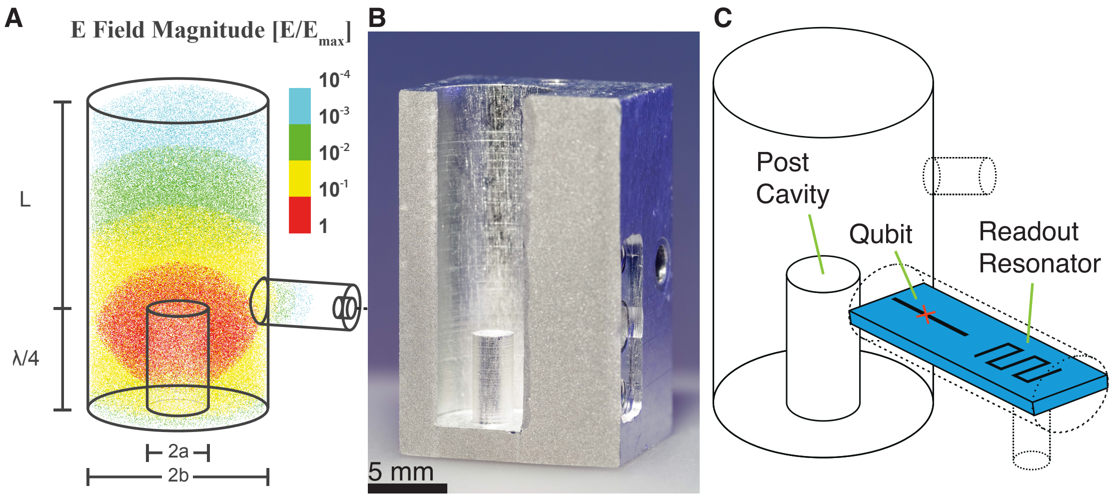

Figure 3.3: Schematics and picture of the high Q post cavity design. (**A**) Electric field distribution of the cavity mode. The length $\lambda/4$ determines the frequency of the cavity, radius a and b are chosen to have a ratio of $1:3$. The length of the waveguide section is made long enough to ensure no decay of the cavity field through the waveguide. Figure taken from [92]. (**B**) Cut through an aluminium post cavity. Photo taken by David Jordan and Markus Knabl. Figure taken from [93]. (**C**) Schematic of post cavity coupled to a qubit and a readout resonator on the substrate. The overlap between the cavity field and the qubit mode determines the dipole interaction and coupling between the two elements.

3.2 Simulation

Being able to calculate the final Hamiltonian from complex circuits is a classical problem [2]. On top of the complex structure of inductors, capacitors and resistors, the non-linearity of the Josephson junctions can further complicate the calculation. Fortunately, there are many methods which decompose a general circuit network into an equivalent impedance function that we can easily quantise. Here, we use the Foster Theorem [94], which decomposes the circuit into parallel LC modes. Such modes are the normal modes of the system which also allows the derivation of the coupling terms between the different modes. Finally, to achieve our final Hamiltonian, we perturbatively add the non-linearity of the transmon. This method is called black-box quantisation (BBQ) [95] and is also covered in detail in [82, 96].

There are two other noteworthy methods of calculating the final Hamiltonian. Firstly, by writing out the different nodes of the system and the capacitive coupling between each node, one can do an electrostatic simulation to obtain the cross-capacitance matrix. The different terms in the Hamiltonian are then a function of the different elements in the

[2] Calculating the final Hamiltonian from very complicated circuits used to be on University physics examinations. A point that some Professors like to repeatedly mention on the convenience of the tools that we have available today.

matrix. This method is known as the method of nodes and is nicely covered in [97]. Such electrostatic simulations are faster but are not as accurate. For large geometries, the non-lumped-element nature of the structure will complicate the actual circuit model used. Another approach is using the energy participation ratios of the different modes [98]. This method quantifies how much the different elements contribute to the mode energy. The final Hamiltonian terms can then be calculated via such ratios.

In this section, I will outline the simulation process of a single junction coupled to cavity modes and extend the explanation to a case of two junctions coupled via a cavity mode. For simplicity and speed, the simulations are done with infinite conductance, meaning that there are no losses. After simulations, the 3D cavity models were drawn in Solidworks, a 3D CAD modelling software used by the mechanical workshop at IQOQI.

The simulations were done with finite-element modelling (FEM). FEM is a mathematical tool that solves partial differential equations numerically. The model is split into finite-element sizes and solves the boundary-value problem within each element. A complex geometry can then be discretised in space (known as meshes) and we can obtain the admittance of the system. For circuits, the partial differential equations are the Maxwell equations and the boundary conditions are the conductance and charges on the surfaces. In particular, the High Frequency Structure Simulator (HFSS) tool in the ANSYS software and the SONNET software were used.

3.2.1 HFSS Simulations

After drawing a particular experimental geometry, the first step is to simulate the eigenmodes of the system. The Josephson junction is included by adding a lumped element with a defined junction capacitance and inductance.

Coupling between the qubit and resonator modes can be calculated by sweeping the junction inductance, and thus the qubit frequency. For each coupled mode, we will see an avoided crossing between the resonator and qubit. Eigenmode simulation results of a qubit coupled to a High Q cavity and readout resonator are shown in Fig. 3.4.

Equation 2.52 is used to obtain the coupling strength g. For an initial guess, a simple polynomial fit can be used. The coupling strength g obtained from fitting with a polynomial and the correct equation is usually within error bars of each other.

The exact geometric parameters often need to be refined after a few iterations of the full simulation process. One should also take into account fabrication and mounting considerations. For example, a small line width might provide the required capacitance for qubit anharmonicity. However, a long, thin structure has a large aspect ratio and is difficult to consistently fabricate in the cleanroom.

In 3D structures, structural and space limitations should be considered. High-purity aluminium is used for 3D cavities. This material is considered very soft and needs at least $1-2\,\mathrm{mm}$ wall thickness to be structurally sound. The samples are also placed inside superconducting and magnetic shields. Thus, sufficient space must be provided to allow for SMA flanges and the tightening of SMA cables.

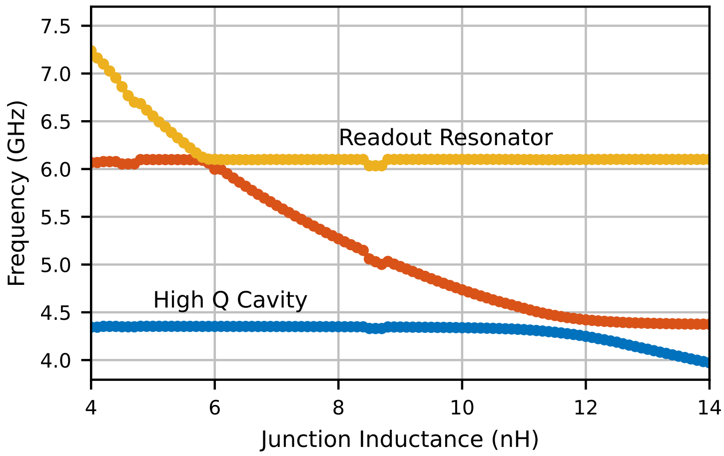

Figure 3.4: HFSS eigenmode simulation results with a sweep in qubit inductance for a specific geometry. The eigenmodes of the system are obtained with simulation. By sweeping the parameters of the simulation, in this case, the qubit junction inductance, we will change the frequency of the relevant mode. When the mode crosses any other normal mode, for each coupled mode we will observe a gap opening up with an avoided crossing feature (Fig. 2.6) that can be fitted to obtain the coupling between the modes g. Results anomalies around 5 nH and 8.5 nH are due to simulation inaccuracies from the fast and rough simulation sweep parameters. The convergence of the simulation on slightly different frequency values in this region does not affect the accuracy of the estimation of coupling values.

After the eigenmode simulations, the next type of simulation is Driven Modal. In this simulation, we add lumped ports to represent the qubit mode and measure the frequency response (impedance or admittance) from each port. It is also possible to define wave ports to simulate SMA coupling pins or waveguide ports to measure the coupling between modes and the external environment. Each mode's characteristic impedance is used to predict the designed Hamiltonian.

3.2.2 Foster equivalent circuits

In Foster's theorem, a circuit is described by an equivalent circuit made up of parallel LC oscillators [94]. This is equivalent to diagonalising a linearised system of coupled harmonic oscillators. Given such a circuit, we can write the admittance of m modes as

$$Y(\omega) = \sum_m \frac{1}{i\omega_m L_m} + i\omega C_m = \sum_m \frac{1 - \omega^2 L_m C_m}{i\omega L_m}. \tag{3.2}$$

The admittance will have a zero-crossing at resonant frequencies $\omega_m = \frac{1}{\sqrt{L_m C_m}}$. Near the resonance, we can approximate $\omega = \omega_m + \Delta\omega \to \omega^2 \approx \omega_m^2 + 2\omega_m \Delta_m + O(\Delta\omega)$, resulting in the admittance

$$Y(\omega_m + \Delta\omega) = \sum_m \frac{-2\Delta\omega}{i\omega_m^2 L_m} = \sum_m i2\Delta\omega C_m. \tag{3.3}$$

Therefore, by taking the gradient of the imaginary part of the admittance, we can calculate each mode's capacitance, inductance and characteristic impedance

$$\omega_m = \frac{1}{\sqrt{L_m C_m}}, \tag{3.4}$$

$$C_m = \frac{1}{2}\left(\frac{\partial(\mathrm{Im}\{Y\})}{\partial\omega}\right)_{\omega_m}, \tag{3.5}$$

$$L_m = \frac{1}{\omega_m^2 C_m}, \tag{3.6}$$

$$Z_m = \sqrt{\frac{L_m}{C_m}}. \tag{3.7}$$

The imaginary part of the admittance for a qubit coupled to a cavity mode is plotted in Fig. 3.5. The bare, uncoupled cavity frequency at $\omega_{\mathrm{cav}} = f_{\mathrm{cav}}/2\pi$ will shift to its dressed frequency, $\tilde{\omega}_{\mathrm{cav}} = \tilde{f}_{\mathrm{cav}}/2\pi$. The simulation results allows us to obtain the Hamiltonian $\hat{H} = \sum_m \hbar\omega_m(\hat{m}^\dagger\hat{m} + \frac{1}{2})$, which is in terms of the linearised coupled modes. The coupling between the modes is implicit in the dressed frequencies of the circuit.

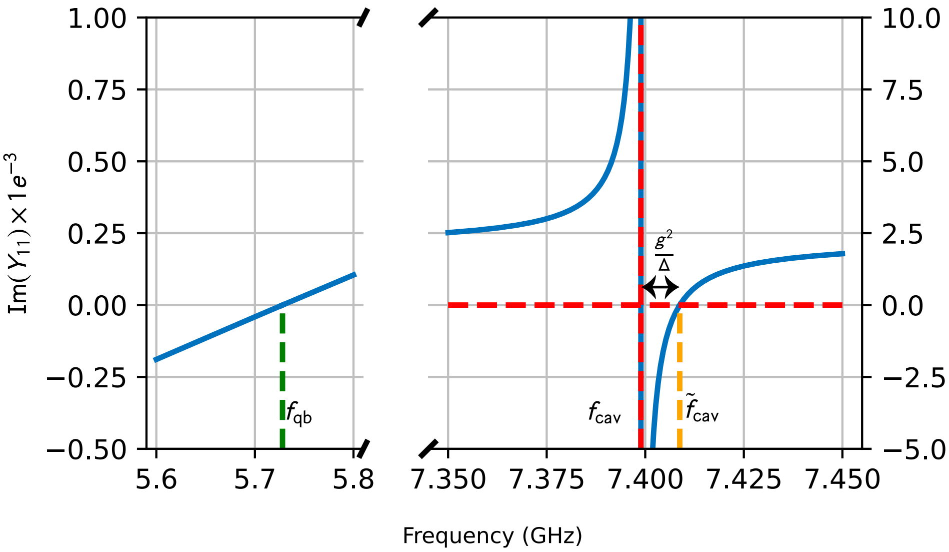

Figure 3.5: Calculated imaginary part of admittance from a qubit port for a qubit coupled to a cavity mode. For each coupled mode, we have a pole in the admittance and an additional zero crossing. The zero crossing, pole and gradient can be used to determine the parameters of the coupled modes. Here, we see the dressed qubit mode at frequency $f_{\mathrm{qb}} \approx 5.73\,\mathrm{GHz}$ (green line). The qubit is coupled to a cavity at the dressed frequency $\tilde{f}_{\mathrm{cav}} \approx 7.41\,\mathrm{GHz}$ (orange line) and a bare frequency at $f_{\mathrm{cav}} \approx 7.4\,\mathrm{GHz}$ (vertical red line). The gap between f_{cav} and $\tilde{f}_{\mathrm{cav}}$ is approximately the coupling strength and detuning between the qubit and the cavity, g^2/Δ.

3.2.3 Black Box Quantisation

To obtain the full Hamiltonian parameters of the circuit, we introduce the non-linearity from the Josephson junction. Recalling the LC Hamiltonian Eq. (2.30), the flux and charge operators Eq. (2.32), we perturbatively add the anharmonic part of the Hamiltonian $\hat{H}_{\mathrm{NL}}$

$$\hat{H} = \sum_m \hbar\omega_m \left(\hat{m}^\dagger \hat{m} + \frac{1}{2}\right) + \sum_i \hat{H}_{NL-JJ} \tag{3.8}$$

$$= \sum_m \hbar\omega_m \left(\hat{m}^\dagger \hat{m} + \frac{1}{2}\right) - \sum_i E_{Ji} \left[\cos\hat{\phi}_i - (1 + \frac{1}{2}\hat{\phi}_i^2)\right] \tag{3.9}$$

where we have m modes including the i junctions. The minus terms in the bracket after $\cos\hat{\phi}_i$ are already accounted for in the harmonic part of the oscillator. Using Kirchoff's law, the current through each junction is the sum of currents due to each mode. From the Josephson relations Eq. (2.34), we can write this as a phase through the junction due to each mode

$$\hat{\phi}_i = \sum_m \phi_{\mathrm{ZPF,m}}(\hat{m}^\dagger + \hat{m}) \tag{3.10}$$

where each mode's zero point fluctuation is given by $\phi_{\mathrm{ZPF,m}} = \sqrt{\frac{\hbar Z_m}{2}}$. $\hat{m}^\dagger$ and $\hat{m}$ are the creation and annihilation operators respectively. We can then expand the $\cos\hat{\phi}_i = 1 - \frac{1}{2}\hat{\phi}_i^2 + \frac{1}{4!}\hat{\phi}_i^4 - \frac{1}{6!}\hat{\phi}_i^6 ... + (-1)^n \frac{1}{2n!}\hat{\phi}_i^{2n} + ...$ Note that the phase operator here is a dimensionless normalised operator flux operator: $\hat{\phi} = \frac{\hat{\Phi}}{\phi_0}$, where we have the reduced flux quantum $\phi_0 = \frac{\hbar}{2e}$. This constant was initially absorbed into the operator coefficients in Eq. (2.32).

In the expansion of the $\hat{\phi}_i^n$ terms, using the RWA, we can drop many non-energy conversing terms such as $\hat{m}^\dagger \hat{m}^\dagger$. An important choice must be made in writing the operators in normal order ($\hat{m}^\dagger \hat{m}^\dagger \hat{m}\hat{m}$) or in terms of the number operator ($(\hat{m}^\dagger \hat{m})^2$). The difference is due to the commutation relation $[\hat{m}, \hat{m}^\dagger] = 1$ that will cause higher order terms to affect lower order terms. Here, I use the former notation.

1 cavity, 1 qubit

Consider the simplest setup of a qubit coupled to a single mode of a cavity. The phase through the junction is

$$\hat{\phi} = \hat{\phi}_c + \hat{\phi}_q = \phi_c(\hat{c}^\dagger + \hat{c}) + \phi_q(\hat{q}^\dagger + \hat{q}). \tag{3.11}$$

We can expand the cosine term and compare the Hamiltonian to the dispersive Hamiltonian up to the same order. The expansion is explicitly shown in appendix C.

$$\begin{aligned}\hat{H}_{\mathrm{1cavity,\ 1qubit}} = {} & \hbar\omega_c + \hbar\omega_q \\ & - \chi_{qc}\hat{q}^\dagger\hat{q}\hat{c}^\dagger\hat{c} - \frac{K_q}{2}\hat{q}^\dagger\hat{q}^\dagger\hat{q}\hat{q} - \frac{K_c}{2}\hat{c}^\dagger\hat{c}^\dagger\hat{c}\hat{c} \\ & + \frac{\chi_{qqc}}{2}\hat{q}^\dagger\hat{q}^\dagger\hat{q}\hat{q}\hat{c}^\dagger\hat{c} + \frac{\chi_{qcc}}{2}\hat{q}^\dagger\hat{q}^\dagger\hat{q}\hat{q}\hat{c}^\dagger\hat{c} + \frac{K_c'}{6}\hat{c}^\dagger\hat{c}^\dagger\hat{c}^\dagger\hat{c}\hat{c}\hat{c} + \frac{K_q'}{6}\hat{q}^\dagger\hat{q}^\dagger\hat{q}^\dagger\hat{q}\hat{q}\hat{q}\end{aligned} \tag{3.12}$$

where χ_{qc} is same dispersive shift in the dispersive Hamiltonian Eq. (2.49). K_c is the inherited non-linearity of the cavity, known as the self-Kerr. χ_{qcc} is the cavity photon number enhanced dispersive shift $(\chi_{qc} + \frac{\chi_{qcc}}{2}\hat{c}^\dagger\hat{c})\hat{c}^\dagger\hat{c}\hat{q}^\dagger\hat{q}$ or the qubit-enhanced cavity Kerr $(K_c + \frac{\chi_{qcc}}{2}\hat{q}^\dagger\hat{q})\hat{c}^\dagger\hat{c}^\dagger\hat{c}\hat{c}$. Lastly, neglected here is the shift from bare frequencies ω_c and ω_q to dressed frequencies $\tilde{\omega}_c$ and $\tilde{\omega}_q$ due to Lamb shift.

We neglect the K'_q and χ_{qqc} terms as the qubit is rarely excited to the second excited state. Thus to simplify the notation, we often write χ_{qc} as χ and χ_{qcc} as χ'. The choice of coefficients in this Hamiltonian is chosen to represent measured values. In the experiment, the difference between the transition frequencies of the cavity from $|0\rangle$ to $|1\rangle$ will be K and the difference between $|1\rangle$ and $|2\rangle$ will be $K - K'$ and similarly for the qubit peaks. Although, one must be careful in experiments if the peaks observed are due to a two photon process with frequency $2\omega_{\text{peak}} = 2\omega_c - K_c$ or a transition between the first and second excited state $\omega_{\text{peak}} = \omega_c - K$.

By comparing the different Hamiltonian coefficients, we obtain the relations to first-order

$$K_m = \frac{E_J}{2\phi_0^4}\phi_m^4, \tag{3.13}$$

$$\chi_{qc} = \frac{E_J}{\phi_0^4}\phi_q^2\phi_c^2 = \sqrt{2K_qK_c}, \tag{3.14}$$

$$K'_m = \frac{E_J}{6\phi_0^6}\phi_m^6, \tag{3.15}$$

$$\chi_{qcc} = \frac{E_J}{\phi_0^6}\phi_q^2\phi_c^4. \tag{3.16}$$

Due to the introduction of the non-linear junction, all coupled modes will inherit some non-linearity K_m. Such relations also show the relative scaling factors between the different Hamiltonian parameters, $\frac{\chi'}{\chi} = \frac{\phi_c^2}{\phi_0^2}$. One can see that the transmon ratio appears via the qubit anharmonicity, $K_q = E_C = \frac{E_J}{2\phi_0^4}\phi_q^4$. Thus, the term $\frac{E_J}{E_C} = \frac{2\phi_0^4}{\phi_q^4}$ is large.

Another important thing to note is the relative scale of $\frac{\chi_{qcc}}{K_c/2} = 4\frac{\phi_q^2}{\phi_0^2} = 4\sqrt{\frac{2}{E_J/E_C}} \approx 0.4-1.4$. If the qubit is excited, the self-Kerr of the cavity is enhanced by a noticeable amount. We can view this as the anharmonicity of the qubit being much larger than that of the cavity. The situation is made worse if the qubit frequency is above that of the cavity, the negative anharmonicity of the transmon means the excited states are closer to the transition frequency of the cavity resulting in possible overlap between the cavity frequency and higher level transitions of the qubit.

2 cavities, 1 qubit

In some experiments, we have a qubit coupled to two cavities. One cavity acts as a high Q storage for quantum information and another as a low Q resonator that allows for fast readout of the qubit state.

The flux operator over the junction is then $\hat{\phi} = \hat{\phi}_c + \hat{\phi}_q + \hat{\phi}_r$. Doing the same expansion, we find the similar terms $\hat{\phi}^4 \approx \sum_m \hat{\phi}_m^4 + 6\hat{\phi}_c^2\hat{\phi}_q^2 + 6\hat{\phi}_r^2\hat{\phi}_q^2 + 6\hat{\phi}_c^2\hat{\phi}_r^2$. The first 3 terms in the summation represent the anharmonicity of each mode and follow the 1 cavity and 1 qubit case. Likewise, the next 3 terms represent the pairwise coupling term between each of the modes. The additional term can be written as

$$\hat{\phi}_c^2\hat{\phi}_r^2 \approx \phi_c^2\phi_r^2\hat{c}^\dagger\hat{c}\hat{r}^\dagger\hat{r} \tag{3.17}$$

$$\hat{H}_{\text{cross-Kerr}} = \chi_{cr}\hat{c}^\dagger\hat{c}\hat{r}^\dagger\hat{r} \tag{3.18}$$

$$\chi_{cr} = \frac{E_J}{\phi_0^4}\phi_c^2\phi_q^2 = \frac{\chi_{cq}\chi_{rq}}{2K_q} \tag{3.19}$$

where χ_{cr} is the cross Kerr between the cavity and resonator through the qubit mode.

1 cavity, 2 qubits

For multiple junctions, there are two complications. Firstly, we need to determine the relative current flows induced by the different modes on each of the junctions. Specifically for the junctions, this means determining if the current across a junction induces an in-phase or out-of-phase current flow in the other junctions. This can be determined by the sign of the admittance matrix from each qubit port at each junction mode. Alternatively, we can examine the mode structure of each qubit mode and deduce the relative current flows in the other qubit modes.

Secondly, we need to expand the Hamiltonian for multiple junctions. In the case of 2 qubits coupled in phase with a cavity, Eq. (3.8) becomes

$$\hat{H}_{\text{NL}} = -E_{J1}\left(\cos\hat{\phi}_1 - (1 + \frac{1}{2}\hat{\phi}_1^2)\right) - E_{J1}\left(\cos\hat{\phi}_2 - (1 + \frac{1}{2}\hat{\phi}_2^2)\right) \tag{3.20}$$

$$\hat{\phi}_r = \phi_{1r}(\hat{q}_1^\dagger + \hat{q}_1) + \phi_{2r}(\hat{q}_2^\dagger + \hat{q}_2) + \phi_{cr}(\hat{c}^\dagger + \hat{c}) \tag{3.21}$$

$$\phi_{mr} = \sqrt{\frac{\hbar Z_{mr}}{2}} \tag{3.22}$$

$$Z_{mr} = \sqrt{\frac{L_{mr}}{C_{mr}}} = \frac{1}{\omega_m C_{mr}} \tag{3.23}$$

$$C_{mr} = \frac{1}{2}\left(\frac{\partial(\text{Im}\{Y_{mr}\})}{\partial\omega}\right)_{\omega_m} \tag{3.24}$$

where the flux operator is defined with respect to each qubit reference port r. The characteristic impedances and zero point fluctuations of each mode m are likewise changed for each port r given by ϕ_{mr}. Expanding the fourth-order term gives: $\hat{\phi}^4 = \sum_r(\hat{\phi}_r^4) =$

$\sum_r(\sum_m(\hat{\phi}^4_{mr}) + 6\hat{\phi}^2_{1r}\hat{\phi}^2_{cr} + 6\hat{\phi}^2_{2r}\hat{\phi}^2_{cr} + +6\hat{\phi}^2_{1r}\hat{\phi}^2_{2r})$. Comparing the Hamiltonian to that of a one cavity and two qubit quantum system, we can derive the coefficients with

$$\begin{aligned}
\hat{H}_{\text{1cavity, 2qubits}} = &\hbar\omega_{q_1}\hat{q}_1^\dagger\hat{q}_1 + \hbar\omega_{q_2}\hat{q}_2^\dagger\hat{q}_2 + \hbar\omega_c\hat{c}^\dagger\hat{c} \\
&- \frac{1}{4}\left(\frac{E_{J1}}{\phi_0^4}\phi_{11}^4 + \frac{E_{J2}}{\phi_0^4}\phi_{12}^4\right)\hat{q}_1^\dagger\hat{q}_1^\dagger\hat{q}_1\hat{q}_1 \\
&- \frac{1}{4}\left(\frac{E_{J1}}{\phi_0^4}\phi_{21}^4 + \frac{E_{J2}}{\phi_0^4}\phi_{22}^4\right)\hat{q}_2^\dagger\hat{q}_2^\dagger\hat{q}_2\hat{q}_2 \\
&- \frac{1}{4}\left(\frac{E_{J1}}{\phi_0^4}\phi_{c1}^4 + \frac{E_{J2}}{\phi_0^4}\phi_{c2}^4\right)\hat{c}^\dagger\hat{c}^\dagger\hat{c}\hat{c} \\
&- \left(\frac{E_{J1}}{\phi_0^4}\phi_{11}^2\phi_{c1}^2 + \frac{E_{J2}}{\phi_0^4}\phi_{12}^2\phi_{c2}^2\right)\hat{q}_1^\dagger\hat{q}_1\hat{c}^\dagger\hat{c} \\
&- \left(\frac{E_{J1}}{\phi_0^4}\phi_{21}^2\phi_{c1}^2 + \frac{E_{J2}}{\phi_0^4}\phi_{22}^2\phi_{c2}^2\right)\hat{q}_2^\dagger\hat{q}_2\hat{c}^\dagger\hat{c} \\
&- \left(\frac{E_{J1}}{\phi_0^4}\phi_{11}^2\phi_{21}^2 + \frac{E_{J2}}{\phi_0^4}\phi_{12}^2\phi_{22}^2\right)\hat{q}_1^\dagger\hat{q}_1\hat{q}_2^\dagger\hat{q}_2.
\end{aligned} \tag{3.25}$$

An additional term that arises is $\chi_{q_1q_2} = \frac{E_{J1}}{\phi_0^4}\phi_{11}^2\phi_{21}^2 + \frac{E_{J2}}{\phi_0^4}\phi_{12}^2\phi_{22}^2$ is the capacitive coupling between both qubits. This term also includes the dispersive cavity mediated coupling $\chi_{q_1q_2,\text{cavity mediated}} = \chi_{q_1c}\chi_{q_2c}\left(\frac{1}{\Delta_{q_1c}} + \frac{1}{\Delta_{q_2c}}\right)$. Repeating the calculation for a Rabi Hamiltonian with 2 qubits with a cavity-mediated coupling, we obtain the on-resonance coupling strength $J_{q_1q_2,eff} = \frac{g_{q_1c}g_{q_2c}}{2}\left(\frac{1}{\Delta_{q_1c}} + \frac{1}{\Delta_{q_2c}}\right)$ [99].

Comparision between Simulation and Experiment

Using the techniques mentioned in this section, we can simulate the expected experimental values for a given design. Table 3.1 summarises the results from the simulation and experiment.

One should note that there will always be some level of error arising from simulation or experimental implementation inaccuracies.

On the simulation side, it may be hard to simulate the small features on the admittance response of the curve. For example, in the case of small qubit-qubit coupling, it is easy to miss the pole in the qubit admittance curve. However, the fact that the features in the admittance response of the qubit are small, means that there is a steep gradient at the zero-crossing. Thus, this results in a small value of ϕ_{12} and ϕ_{21} and the correction terms are thus small. By neglecting, the calculated simulation values are a lower bound. The Hamiltonian parameters will increase depending on the size of $\frac{E_{J2}\phi_{12}^2}{E_{J1}\phi_{11}^2}$ or $\frac{E_{J1}\phi_{21}^2}{E_{J2}\phi_{22}^2}$.

On the experiment side, a source of inaccuracy is the clamping of the qubit chip. Currently, this is done by eye and can vary in position by 0.2 mm. This uncertainty will affect the coupling between the qubit and the high Q cavity. Thus, the anticipated dispersive shift χ_{qc} might defer from the designed value.

Parameter	Simulation	Experiment
f_{q1} (GHz)	5.700	5.731
f_{q2} (GHz)	6.175	6.229
f_c (GHz)	4.347	4.520
$K_{q1}/2\pi$ (MHz)	166	175
$K_{q2}/2\pi$ (MHz)	148	130
$K_c/2\pi$ (kHz)	2.95	1.14
$\chi_{q1c}/2\pi$ (MHz)	1.198	1.270
$\chi_{q2c}/2\pi$ (MHz)	0.687	0.408
$\chi_{q1q2}/2\pi$ (kHz) (calculated)	1.1	0.7

Table 3.1: Comparison between BBQ simulation and measured experimental results. In the experiment, Qubit 2 was an asymmetric SQUID and the reported parameters are for the low sweet spot. In the simulation, due to the small coupling between both qubits, it is difficult to simulate the relevant features in the admittance response of the terms ϕ_{12} and ϕ_{21}. Thus, the reported simulation values are a lower bound. For the qubit-qubit coupling, in both the simulation and experiment, the cavity-mediated interaction is used as a lower bound.

Rules of Thumb

When designing a new experiment, the number of parameters to vary are numerous and it can be overwhelming to know where to start. Here, I outline of the design process and rules of thumb to help the simulation process.

Before starting, it is important to understand what is simpler to consistently fabricate in the cleanroom or machine in the mechanical workshop. For 3D cavities, we should know the material and space limitations that the mechanical workshop or external companies can do. This will eliminate the need to repeat the simulations should the fabrication process be too difficult. From a design process perspective, it is also helpful to first build a quick and simple prototype of the final experiment. From the desired Hamiltonian, we can start the simulation process in ANSYS.

1. Draw out the model with driven modal simulation type.

    - This includes fine mesh sizes and any possible 2D readout resonators.
    - For the qubit modes, lumped ports and lumped RLC elements to represent the Josephson junction.
    - The junction will have around $5-10\,\text{fF}$ and $1-10\,\text{nH}$.

2. Duplicate the simulation model and change it to eigenmodal solution type.

    - The lumped ports can be made as a non-model object.

- Any additional 2D structures such as the readout resonator can also be made a non-model object as well.
- This is done to link the two geometries of the different simulation types to not affect the simulated capacitance of the qubit pads.

3. Do fast eigenmode simulations to obtain the mode frequencies and coupling strength g between qubit and cavity modes and fix the geometry of the experimental design.

   - The 3D experiment geometry is first fixed and limited to fabrication limitations.
   - Next, the qubit position and dipole lengths are fixed to obtain the correct coupling strength g.
   - Tapered lead qubit designs can help reduce surface loss [100].
   - With the coupling strength, we can calculate the rough qubit and cavity detuning needed to obtain the desired dispersive interaction χ (by changing the junction inductance).

4. For each mode of interest, we can do a driven modal simulation around the mode frequency.

   - It is faster to first do quick interpolation simulations and BBQ to obtain rough parameters.
   - The qubit anharmonicity can then be corrected by changing the qubit pad widths (affecting mainly the self-capacitance and not the coupling strength as much).

5. Next, we include any additional 2D readout resonators needed and repeat steps 2 to 4 for the 2D structures without changing the structure of the cavity and qubit.

6. Finally, we can include any coupling pins and simulate the external coupling factors.

   - The external coupling factors for each mode can be calculated by doing a circle fit of the reflection parameters [101].
   - For the circle fit, it is important to remove any lumped ports as these ports are 50Ω in a reflection measurement.
   - An additional weakly coupled qubit pin can be used to simulate the losses in a qubit. This allows the loss in the qubit to be controllable and makes it easier to find and fit mode resonances.
   - An alternative method to check for Purcell decay is to simulate and reduce the transmission between the qubit port and external coupling pin [66].

The simulations were done to an accuracy of 5%. In most experimental labs, there is not a well-optimised, established fabrication and assembly process specific to every experiment design. Thus, inaccuracies arising from fabrication, etching or assembly will add to the inaccuracy between designed parameters and measured parameters. In such cases, it is faster to design around established recipes and use in-situ tuning or experimental parameters sweet spots that can account for such imperfections. From a design process perspective, this is trading time taken to optimise fabrication recipes with time spent on increasing experimental complexity.

3.3 Qubit Fabrication

After finalising a design, the qubit design was drawn with gdspy and fabricated in the Quanten-Nano-Zentrum Tirol (QNZT) cleanroom in the University of Innsbruck and IQOQI Innsbruck. The Josephson junctions were made of aluminium through a double-angle shadow evaporation process with an oxidation step between the deposition layers. For the qubit antenna pads, both aluminium and tantalum were tested.

Electron-beam (e-beam) lithography was done with a Raith eLINE Plus 30 kV. The maximum voltage affects the amount of electron scattering and will eventually affect the resolution size that can be accurately exposed. The design will have two length scales. One for big structures such as the antenna pads that are written with a bigger write-field 1 mm and aperture. The smaller scale structures are written with higher accuracy with a write-field of 200 μm and smaller aperture size. Within this write-field, the smaller structures are limited to a 180 μm size to allow room for overlap structures to ensure good contact of different structures between adjacent write-fields. The Josephson junction can then be written with higher accuracy and the antennas can be written faster with the bigger aperture size.

3.3.1 Fabrication Parameters

The Josephson junction is a sandwich of aluminium-aluminium oxide-aluminium. At room temperature, the insulating aluminium oxide layer forms a resistive element. The normal state resistance R_n can be related to the critical current I_c and thus Josephson energy E_J via the Ambegaokar-Baratoff formula [102]

$$I_c R_n = \frac{\pi}{2e}\Delta(T)\tanh\frac{\Delta(T)}{2k_B T} \approx \frac{\pi\Delta_c(0)}{2e} \tag{3.26}$$

where $\Delta(T)$ is the superconducting energy gap at a temperature T. At temperatures much smaller than the critical temperature T_c, the relation can be approximated to the second equation where $\Delta_c(0) \approx 180\,\mu$eV for aluminium. An established process will have fabricated a range of junctions to relate the measured room temperature resistance to qubit frequencies. The room temperature resistance of qubit junctions is usually in the range of a few kΩ. With the junction critical current I_c and a designed qubit capacitance E_c, Eq. (2.45) can be used to calculate the estimated qubit frequency. An additional benefit for 3D architectures is the post-selection. The fabricated qubit with parameters closest to the desired value can be selected for the experiment. A standard design of qubits used in my experiments is shown in Fig. 3.6.

In addition to the inductance, the two aluminium layers will have a junction capacitance given by $C_J = \epsilon_0\epsilon_{r,AlOx}\frac{A_J}{t}$, for a dielectric constant of aluminium oxide $\epsilon_{r,AlOx} \approx 10$ [84, 103] and barrier thickness $t \approx 2$ nm [104]. In my samples, the junction size used is $A_J \approx 150\,\text{nm} \times 150\,\text{nm}$ with junction capacitance is around $5 - 10$ fF.

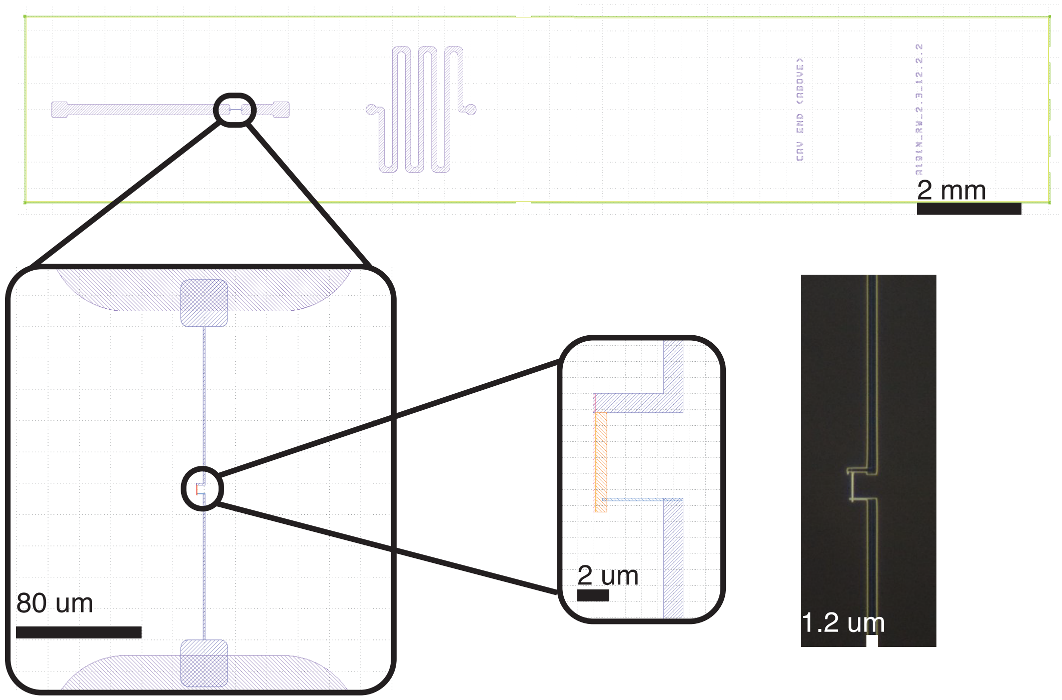

Figure 3.6: Design of a qubit and resonator and optical picture of a Josephson Junction. Different colours represent different dose factors for the e-beam lithography. (Bottom right) Dark field image from an optical microscope of the fabricated Josephson junction before the liftoff process.

The desired junction inductance can be reached by changing the designed junction size and oxidation parameters. $R_n \propto \frac{(p_{\text{ox}} t_{\text{ox}})^\gamma}{A_J}$, where t_{ox} and p_{ox} is the oxidation time and pressure, A_J is the size of the junction and γ is the proportionality constant. In my fabrication recipe and design, I find $\gamma \approx \sqrt{2}$. Junctions with larger sizes have a small fabrication spread [105]. However, smaller junctions lead to a smaller probability of adverse surface defects in the Josephson junction [106].

As the junctions are very small capacitors, care must be taken during the probing process. Ionisers and humidifiers are turned on to prevent a build-up of a potential difference across the junction[3]. Also, the probing needles are first shorted by an external connection. The needles are then placed in contact with the qubit pads before the external short is removed. The junction resistance is then measured in series with a $11\,\text{k}\Omega$ resistor.

An important point of the fabricated junctions is the effect of junction ageing. Over time, the oxide layer between the aluminium pads will grow and change in structure leading to a larger resistance [107]. This process is sped up through thermal cycling in the cryostat and saturates at approximately 10% higher value than the post-fabricated value.

[3]I have noticed that in the cold, dry Innsbruck winter months when experimentalists are more prone to wearing electrostatic inducing clothes, qubits are more prone to blowing up.

3.3.2 Aluminium

The fabrication process was established by Dr. Maximillian Zanner after the QNZT was opened in 2018 [83]. Below is a summary of the adapted process with an additional laser dicing step. The detailed fabrication recipe is provided in appendix D.1.

The fabrication process starts with a sapphire c-plane(001) from Crystec (Kyocera) with thickness 330 μm and diameter 50.8 mm. Sapphire was used as it has low dielectric losses [108, 109]. The wafers were piranha cleaned in a 3 : 1 ratio of $H_2SO_4 : H_2O_2$ for 5 min. They were rinsed in deionised (DI) water, dried and a bilayer resist was spun on top (1 μm MMA (8.5) EL13 and 0.3 μm of 950 PMMA A4). We place the designs in the centre of the wafer to avoid imperfect resist spinning thickness, wafer handling and clamping areas. The resist layer thickness was measured with the ellipsometry method using a SmartSE Ellipsometer.

As the sapphire is not conducting, a small gold layer is sputtered before the electron-beam lithography step. The gold layer will prevent the build-up of electron charge on the dielectric surface. The bottom resist layer is more sensitive to the lithography process. Low exposure doses will result in an overhang structure that is used for the double-angle junction evaporation process. After lithography, the gold layer is removed in a solution of potassium iodide and DI water. The sample is developed in a 6°C bath of 3 : 1 solution of isopropyl alcohol (IPA) and DI water.

The wafer is transferred to a Plassys MEB550S electron-beam evaporator and pumped overnight. The long pumping time is to decrease the water content and other gaseous impurities in the chamber. Before any process begins, the chamber undergoes titanium gettering of gas and any resist residues are cleaned by a weak oxygen and argon plasma. In the next step, two layers of aluminium (25 nm and 50 nm) were evaporated onto the sample with a controlled oxidation step (5 mbar for 5.5 min) carried out between the deposition of the two aluminium layers. The thicker second layer allows the layer to climb the bottom junction pad to give good contact of the second junction pad with the oxide layer. It has been shown that a choice of the different layer thicknesses and lengths will help in trapping quasiparticles [110].

Subsequently, the qubit chip was laser-diced. Finally, the resist layer and excess metal were lifted off. The laser dicing step is done via laser ablation of the sapphire material. This inevitably will have some material being thrown around the wafer. The sapphire cut quality can be improved by starting the cut away from the intended chip cut line. Also, such defects can be mitigated by a protective resist layer with an extra lithography and development step at the laser marks to prevent resist burn-in. The method used here is to do the lift-off after laser-dicing which provides the same protection cover. This step however prevents the probing of the junctions before dicing and reuse of the sapphire wafer in the case of fabrication anomalies.

3.3.3 Tantalum

Other than aluminium, tantalum and niobium can be used as superconducting materials [111]. Tantalum and niobium have a higher critical temperature which leads to a bigger superconducting gap and a smaller quasiparticle population. Furthermore, tantalum and niobium can be more aggressively cleaned with piranha during the fabrication process which reduces surface defects. However niobium oxide is a lossy superconductor, tantalum oxide has better superconducting properties and using tantalum as a material for antenna pads has led to higher qubit lifetimes [112]. The difficulty of using a double-angle shadow evaporation process for tantalum or niobium prevents the full replacement of the aluminium material. Thus, the Josephson junction is still made up of aluminium. The detailed fabrication recipe is adapted from [111] and is produced in appendix D.2. Work on adapting the recipe was done with Dr. Maximilian Zanner and Dr. Christian Schneider, with preliminary results on the coherence times of the qubits found in [83].

The process involves 550 μm sapphire wafers which were sputtered with a 200 nm layer of tantalum by the company STAR Cryoelectronics. The wafers are first solvent-cleaned and then a negative resist (600 nm of MaN 2403) is spun on top for an etching process. The structures are written via e-beam lithography. A negative resist process will allow the formation of cross-linked polymers where the electron beam hits the structure. The wafer is developed with Ma-D 525 and post-baked at 100°C to strengthen its resistance against the etching process and give better edge roughness during the etching process. Only the areas that were exposed to the electron beam will have a cross-linked polymer structure that is strong enough to resist the etching process.

The sample is placed in a Sentech ICP SI 500 which first does a soft oxygen cleaning to remove any resist residues. The areas of exposed tantalum are etched via a CF_4 process. Finally, the sample can be piranha cleaned to remove the leftover resist organics and the sample can be used for a double-angle aluminium shadow evaporation process.

3.4 High Q Cavities Fabrication

To achieve a long lifetime for quantum information storage, seamless 3D cavities were made. The design has a post length of 14.8 mm, an inner radius of 2 mm and an outer radius of 6.2 mm, giving a bare cavity frequency of approximately 4.5 GHz. The tunnel for the qubit chip has a diameter of 4 mm, which is a compromise between cavity mode leakage into the tunnel and qubit capacitance to the ground. The qubit chip is 1.2 mm below the top of the post to maximise the coupling between the qubit and the high Q cavity mode. Due to the high dielectric constant of the sapphire chip, there is a "concentration" effect of the high Q cavity mode in the sapphire dielectric. Thus, mistakes in the height of the chip will not change the coupling between the two modes significantly. It should be noted that in my experimental design, the presence of the sapphire dielectric will shift the resonance frequency of the high Q cavity down by approximately 10 MHz per sapphire chip. The Solidworks design of the cavity is shown in Fig. 3.7 with structures for the qubit, flux hose and Purcell filter clamps.

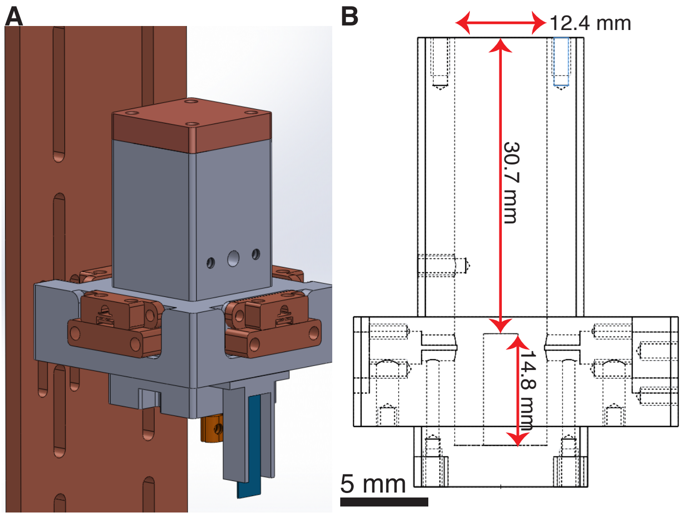

Figure 3.7: Solidworks design of high Q cavity. Design of (**A**) the full cavity setup in Solidworks and (**B**) the side view of the internal structure of the cavity. The important features are the height of the post (14.8 mm) which sets the resonance frequency of the cavity, the diameter (12.4 mm) and the length of the waveguide section (30.7 mm) which minimises the decay of the cavity mode. Not shown here is the diameter of the qubit tunnel (4 mm) which affects the coupling between the qubit and the cavity modes. Copper clamps that thermalise the cavity and the sample. The lid at the top is to block stray infrared photons. At the bottom, there are mounts for the flux hose and a Purcell filter.

For the cavity, two materials, aluminium and niobium, were used. Starting with a metal block, bigger holes are first milled away. Next, a negative of the cavity is made for an electrode in a plunger erosion electric discharge machining (EDM) process. This process involves putting a high voltage on an electrode that erodes the material by large electrical discharges. As compared to conventional milling, EDM allows for more complex shapes and larger aspect ratios to be formed. EDM requires a longer time and multiple electrode negatives have to be made as this process also damages the electrode.

Since any machining will inevitably damage the surface of the material, we etch away these surface defects by removing $\approx 150\,\mu$m of material in a buffer chemical process [60, 113]. This will produce a smooth surface that reduces losses in the cavity. The etching process involves strong acid and is very exothermic. The reaction rate doubles every 10°C. Thus, the solution must be temperature controlled to be relatively cold or the etching process will have a thermal runaway. The reaction also produces a lot of gas bubbles. Thus, the etchant flow must be fast to prevent undesirable streaking on the surface and non-uniform etching. Any screw threads must also be protected as the etchant will erode the threads and cause problems during mounting.

In the next part, I describe the specifics of the fabrication and etching process for both materials.

3.4.1 Aluminium

The high Q cavities were machined in the mechanical workshop at IQOQI Innsbruck. As high-purity aluminium is a soft material, the cavities were designed with a minimum thickness of 1 mm. After machining, we polish the surface with two rounds of Transene etchant in a double-walled beaker. The two rounds of etchant are needed to refresh the reactants in the solution. The beaker is temperature-controlled via an external heat controller. Transene etchant type A is a solution of $(55-65\%)$ phosphoric acid, $(1-5\%)$ nitric acid and $(3-5\%)$ acetic acid. The screw threads were protected with aluminium screws that were used as sacrificial material. The detailed etching recipe is produced in appendix D.4.

3.4.2 Niobium

In the Kirchmair lab, we also used high-purity niobium cavities [92]. Niobium gives benefits such as higher critical temperature and magnetic field. As niobium is a much harder material than aluminium, greater care is necessary. The milling process requires titanium drill bits. The EDM process also used multiple copies of a tungsten alloy electrode.

Due to the chemical resistance of niobium, the buffer chemical process is more dangerous. The cavity was etched with collaborators at the Institute of Science and Technology, Austria in Klosterneuburg with the group of Prof Johannes Fink. The detailed etching recipe is produced in appendix D.5.

This process involved an etching solution of $1:1:1$ (49%) hydrofluoric (HF), (69.5%) nitric (HNO_3) and (85%) phosphoric acid (H_3PO_4) for one hour at 5°C. After which, (H_3PO_4) is slowly added to reach a ratio of $1:1:2$ for another hour of polishing. The niobium cavity is then rinsed heavily with DI water. In the etching process, we found that cooling the cavity before etching was essential to prevent thermal runaway.

To prevent excessive heating of the solution, the cavity was also cooled down to 5°C before starting the etching process. The screw threads were protected with a PDMS photoresist.

Unfortunately, niobium cavities will start to grow an oxide layer over time. This niobium pentaoxide layer has lossy superconducting properties. Thus after a certain amount of time in ambient pressure, we need to consider the removal of the oxide layer. On 2D co-planar waveguide structures, a study on the oxide layer saturation showed that the oxide layer was saturated after 200 hours in atmospheric pressure [114]. Fortunately, the 3D geometry of the post cavity is forgiving as the participation ratio of the oxide layer is small and thus can still have high-quality factors. We had one cavity left in the ambient atmosphere for 6 months which still had a quality factor of 0.5 million [92]. However, one must also consider the effect of the oxide layer on qubits. To combat the regrowth of the oxide layer, there are some proposals to coat the layer with a good superconductor such as NbSn [115].

3.5 Flux Hoses

To allow for in-situ tuning of the qubit frequencies, we need to be able to thread magnetic flux through a SQUID loop. For 2D geometries, on-chip flux bias lines can be used to introduce the tuning magnetic field [116]. However, such lines complicate the fabrication process and can capacitively couple to the qubit becoming an additional loss channel. For qubits enclosed in a superconducting 3D cavity, introducing a magnetic field is difficult due to the Meissner effect [117]. To circumvent this problem, the Kirchmair lab uses flux hoses [118, 119]. These hoses guide the magnetic field lines in and out of the cavity so that flux quantisation is not broken. Here, I introduce a new design that improves the ease of fabrication and assembly of such hoses. Work in this section was done with Desislava, Stefan, Vasilisa and Lucien from the lab with help on the magnetostatics simulations from Dr. Natanael Bort-Soldevila [120].

The first generation flux hose design consisted of alternating layers of μ-metal and aluminium shells that guided magnetic fields inside a superconducting 3D cavity. With this hose design, fast flux control ($< 100\,\mathrm{ns}$) has been demonstrated. However, the design had many parts that made it difficult. The long physical distance between the coil and SQUID loop heavily attenuated the magnetic field. Normal metal at the connector assembly leads to a resistive load near the flux hose that could heat up. Thus larger coil currents were problematic. Finally, the outermost superconducting shell had to be embedded with the superconducting cavity to reduce the losses of the cavity.

In a new generation design, the flux hose is made from a single solid superconducting piece with a small slit and a central hole (Fig. 3.8). A coil can then be embedded into the superconducting body that shields the qubit from any potential losses from the coil. Currents in the coil will then try to induce magnetic fields in the superconducting body. However, due to the Meissner effect, this will cause shielding currents on the surface to counteract the added magnetic field. These shielding currents will then create a magnetic field in the inner hole of the superconductor that we can use to tune our SQUID.

This new design enables better integration into our 3D cavity. The flux hose was made from aluminium and is cut by wire EDM that enables the small feature size of a $200\,\mu\mathrm{m}$ slit across a $15\,\mathrm{mm}$ length. The coil can be wound much closer to the SQUID loop and is almost surrounded by superconducting material that shields the qubit from additional decay channels. The slit allows for arbitrary magnetic fields in the superconducting hole. After the hose is fabricated, a superconducting wire is wound around the end and secured with stycast 2850.

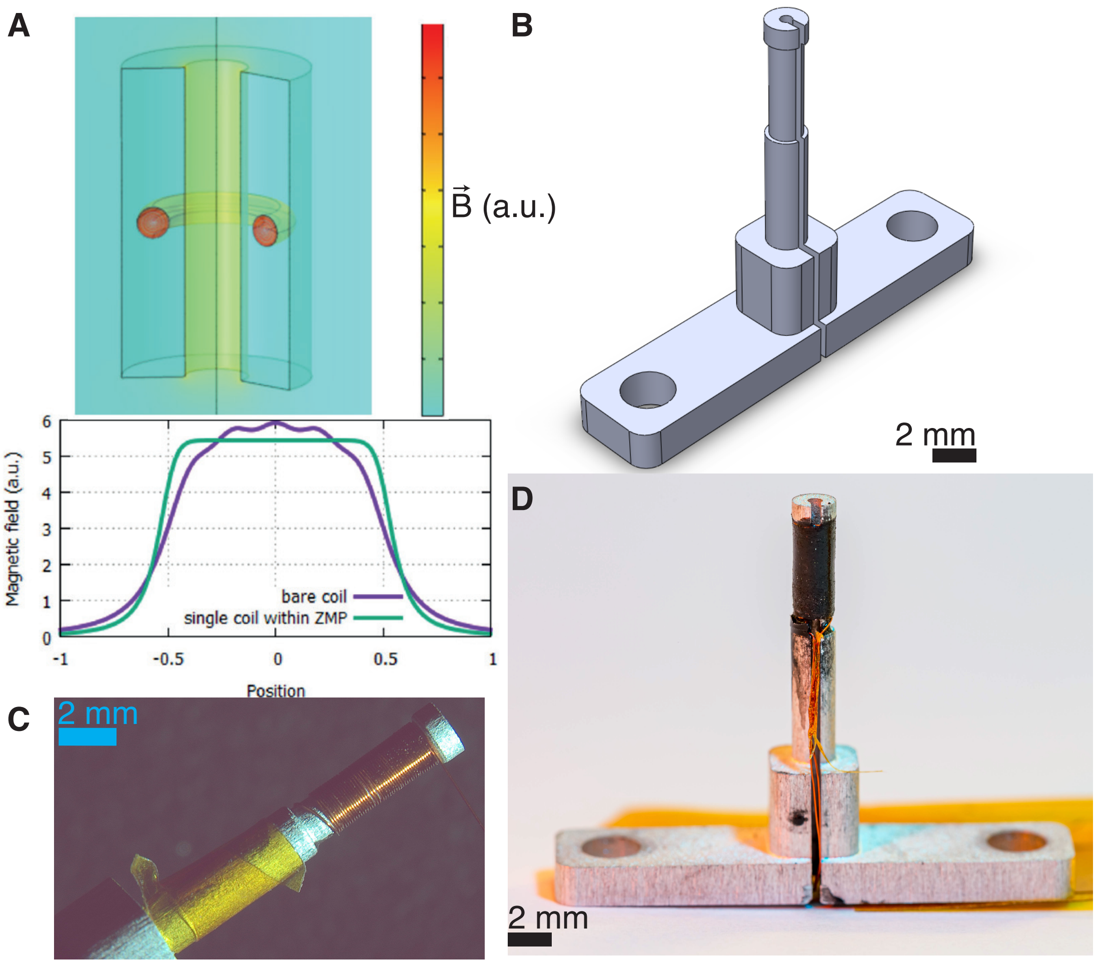

Figure 3.8: New generation design of flux hoses. (**A**) (Top) Simulation of a coil embedded in a hollow superconducting cylinder and (Bottom) linecut of the magnetic field generated by a five-loop bare coil (not pictured) and a single coil embedded within a zero-magnetic permeability material. When there is a current in the coil, shielding currents in the superconductor will produce a field in the hole of the cylinder. This field can be used to thread a magnetic field into a superconducting cavity. Figure from [120]. (**B**) SolidWorks drawing of a new generation of superconducting flux hose. The slit is made from wire electro-discharge machining and allows for arbitrary magnetic fields in the superconducting hole. The body is inserted into a superconducting hole and (**C**) the superconducting wire is wound around the slot with a smaller diameter. Picture from an optical microscope. (**D**) Assembled flux hose. The coil is secured with stycast 2850. Picture taken by David Jordan.

3.6 Purcell Filters

To include Purcell filters in the setup, a design of a modular bandpass filter for 3D architectures was made. Work in this section was done with many collaborators in the lab including Stefan, Desislava, Lucien and our external collaborators Dr. Arman Alizadeh in the group of Prof. Iman Mirzai, who worked on the design and simulation process.

The filters have a microstrip design with one end having an extended pin that will couple to the readout resonator and can replace the SMA pin (Fig. 3.9). The gap and width of each line determine the coupling and resonance frequency of the structure. The 3D modular design allows us to integrate the Purcell filter into the coupling pin and still gives the flexibility of redesigning and changing the qubit chips without the need to replace the Purcell filter. By using bandpass filters as the Purcell filter, the qubit frequency can be changed without the need to redesign the filter and allow for an in-situ tuning of a qubit that remains Purcell-protected.

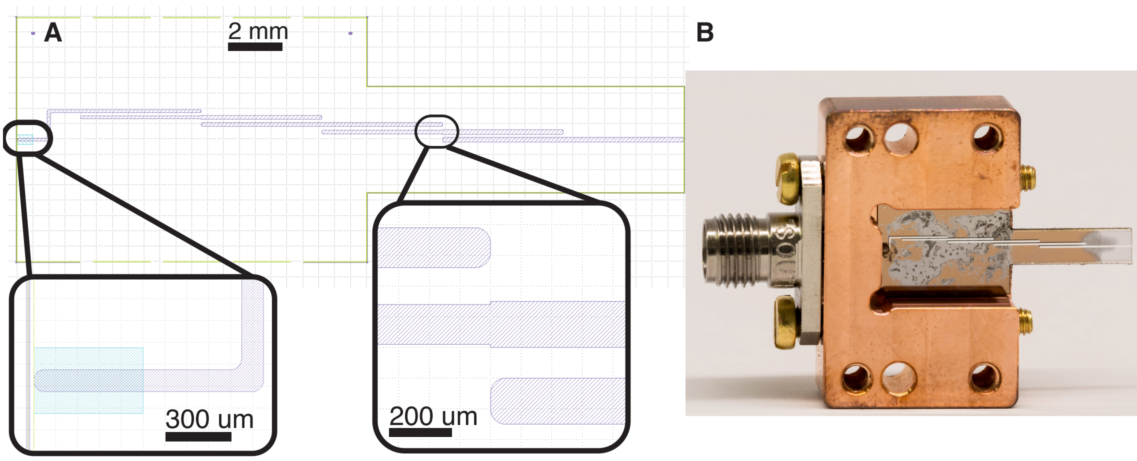

Figure 3.9: Purcell filter design and prototype device. (**A**) Design of Purcell filter which will be soldered to an SMA pin (bottom left) and on the other end, the extension of the microstrip structure serves as a 3D pin that couples to the cavity. The gap between and width of the microstrip structures determines the coupling and resonance of the mode. (**B**) Picture of mounted prototype Purcell filter design. The backside is soldered onto the ground plane. Picture taken by David Jordan.

The bandpass filter was designed with network synthesis methods [18, 121] and is formed by capacitively coupling small superconducting $\lambda/2$ microstrips. By optimising the width and gap size between the resonators, we can design a bandpass filter with network synthesis methods. This particular design is a 5^{th} order Chebyshev filter and is optimised for bandpass transmission flatness and compactness. The final design can be simulated with ANSYS HFSS for the coupling strength to the readout resonator or with Sonnet to simulate the transmission properties of the bandpass filter. The prototype filters were made with SMA pins on both sides to allow for faster feedback on the design process. A big difficulty in the design process was to integrate the 3D coupling pin into the structure. This led to an impedance matching problem which required a redesign of the filter structure.

The Purcell filters were fabricated with an optical lithography process. Optical lithography is a faster process and could be used due to the larger structures on the chip that reduce the fabrication resolution requirements. To improve ease of assembly, the wafer is first metalised on the backside with gold to allow for soldering to the sample box. The top layer is fabricated with aluminium and gold contact pads for soldering to an SMA pin. With the laser dicer, we can dice out part of the sapphire that will protrude into the qubit tunnel to act as a coupling pin to the readout resonator. The backside metalisation of the wafer was removed for the protrusion. In future iterations, niobium will be used for backside metalisation to reduce losses and sputtered with a hard mask layer. The fabrication recipe was developed by Stefan Oleschko and is reproduced in appendix D.3.

A prototype Purcell filter was made with SMA ports on both ends. A transmission measurement (red) of the prototype filter is plotted in Fig. 3.10 with a reference measurement (blue) with a through cable.

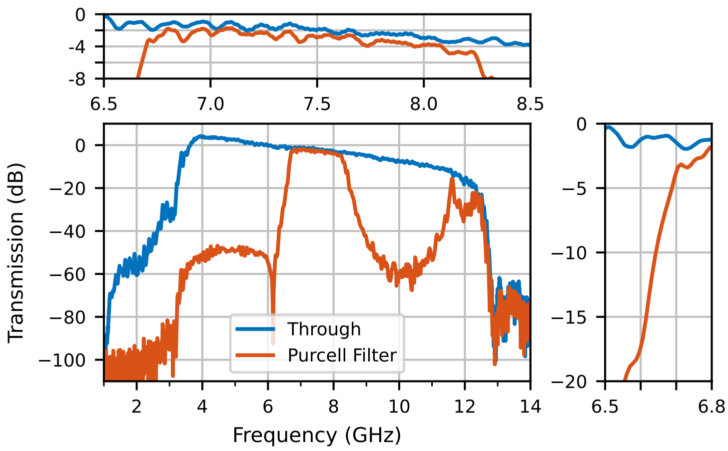

Figure 3.10: Transmission measurement of a prototype filter design with SMA ports on both ends. The red line is a measurement through the prototype Purcell filter while the blue line is a reference measurement through a cable. The insets are zoomed-in measurements to show the loss profile in the bandwidth of the filter and the transmission slope near the cut-off frequency.

3.7 Cryogenic setup

To reach superconducting temperatures and small levels of quasiparticle excitation, we need to cool the experiment down below the critical temperature of the superconductor to $T_C/4$. However, this is not enough as we also require that the thermal energy of the mode is much smaller than any transition frequencies $k_B T \ll \hbar\omega$. This way, through dissipation into the cold environment, the quantum system can be initialised into the ground state.

The experiments were conducted in a Triton DU7-200 Cryofree dilution refrigerator system (Fig. 3.11A) with a schematic of the cooling system shown in Fig. 3.11B. Operation in such a cryogenic environment poses its own challenges. In appendix E, I outline the operating principle of the cryostat and the heat load considerations on each operating temperature plate. The experiments are mounted on the bottom "base" plate that is at a physical temperature of 20 mK.

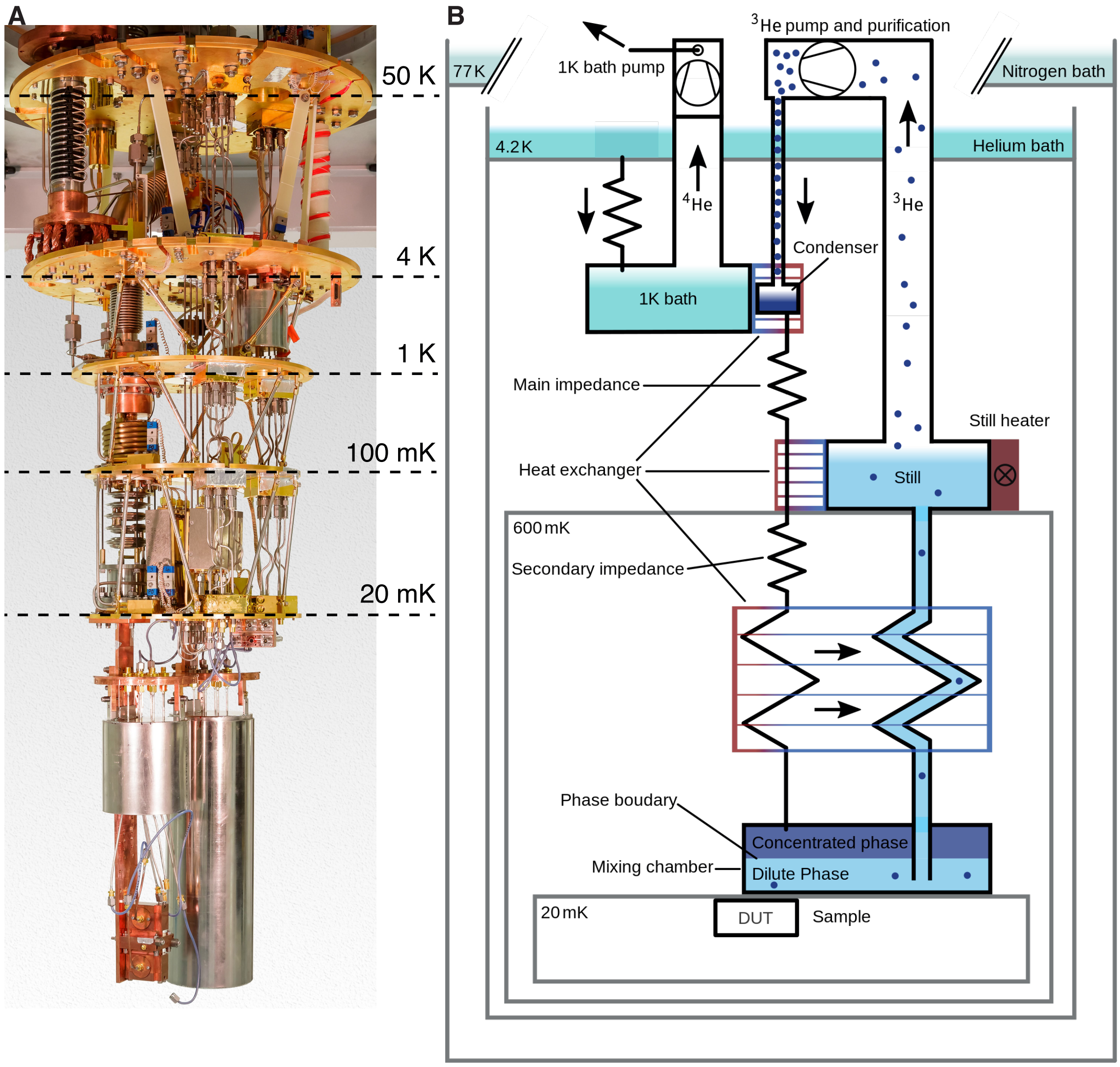

Figure 3.11: Working principle of the cryostat. (**A**) Picture of the cryostat dilution refrigerator. The different plates operate at different temperatures and provide different cooling powers. Picture taken by David Jordan. (**B**) Schematic of the cryostat. The cryostat has two cooling systems, a pulse tube at the 4K plate and a ^{3}He/^{4}He mixture at the base plate. Figure from [122].

3.7.1 Cryogenic Wiring

The experiment on the base plate has a physical temperature of approximately 20 mK. However, the experiment must be connected to some control drive lines and measurement output lines. These lines are connected to higher temperatures and will introduce additional thermal noise to the experiment.

For electrical circuits, this is the Johnson-Nyquist noise [123, 124]. The voltage noise power spectral density from a resistor R at temperature T is [125]

$$S_{VV}(\omega, R, T) = 4R\hbar\omega n_{\text{th}}(\omega, T) \tag{3.27}$$

$$n_{\text{th}}(T) = \frac{1}{e^{\frac{\hbar\omega}{k_B T}} - 1} \tag{3.28}$$

where $n_{\text{th}}(\omega, T)$ is the mean number of thermal photons. Without any attenuation, the residual mean thermal photon number at 7 GHz is 904 photons. Fluctuations of cavity photon number will cause the qubit frequency to shift through the dispersive interaction resulting in additional dephasing of the qubit. In the strong dispersive limit, the dephasing rate is [126]

$$\Gamma_{\phi,\text{th}} \approx \frac{n_{\text{th}}\kappa\chi^2}{\chi^2 + \kappa^2} = \frac{n_{\text{th}}}{1 + \frac{\kappa^2}{\chi^2}}\kappa. \tag{3.29}$$

Thus, we need to add attenuators to reduce this flux of thermal photons into the cavity. The effective thermal photon number is then given by

$$n_{\text{th,eff}} = \sum_{i}^{\text{(plates)}} A_i n_{\text{th}}(T_i) \tag{3.30}$$

$$T_{\text{eff}}(\omega) \approx \frac{\hbar\omega}{k_B \ln\left(1/n_{\text{th,eff}} + 1\right)} \tag{3.31}$$

where $A(i)$ is the total power attenuation factor from each plate to the base plate of the cryostat ($A_{\text{W}} = 10^{A_{\text{dB}}/10}$). T_{eff} is the effective mode temperature of the cavity and can be approximated by inverting the Bose-Einstein relation. This is an approximation as the different thermal contributions from the attenuators lead to a distribution that is not thermal anymore.

In addition to the thermal noise from the drive lines, the output lines will also contribute to the thermal noise. The main noise source on the output lines is from the high electron mobility transistor (HEMT) amplifiers at the 4 K stage. Unlike the input lines, we should not attenuate the output signal coming from the experiment. Thus, cryogenic isolators are used which allow the transmission of the signal from the experiment, but attenuate the thermal noise from the amplifier. For the output lines, isolation from 4 K noise of $40 - 60$ dB at the base plate will only result in a total of ≈ 0.095 nW of additional heat load on the base plate. Depending on the cavity external coupling rate, this translates to $\approx 10^{-3}$ to 10^{-5} residual thermal photons in the cavity.

The output RF line material has two sections: from the isolators to the 4 K stage, they are made from a niobium-titanium alloy that becomes superconducting. After the HEMTs, a copper-nickel alloy is used to connect the HEMTs to the room temperature plate. While copper has better transmission properties, it is thermally conducting. This will give too much heat load to the bottom plates. Thus, a copper-nickel alloy is used as a compromise between steel and copper. Additionally, the attenuation from the copper-nickel alloy does not significantly degrade the signal-to-noise ratio as this is after the first stage amplification from the HEMT [46].

The input lines are made from stainless steel inner and outer conductors. Stainless steel is a poor thermal conductor and is cheaper than the copper-nickel alloy. However, stainless steel will have a higher transmission loss which is acceptable for input lines. The assembled lines will also need to have a bend to account for thermal contraction during the cool-down of the cryostat.

The main heat load on each plate is due to the thermal conduction through each line. This is calculated in detail in appendix E.1. For 20 input lines and 4 output lines used in the cryostat here, we can assume the heat load on each plate of the cryostat is small compared to the cooling power.

The important quantity that affects our experiment is the residual thermal photons. Table 3.2 shows the contribution of the different stages and attenuation to the residual thermal photons in the cavity. At each plate, the attenuator will attenuate the thermal noise from above and also add thermal noise from its physical temperature. Depending on the subsequent attenuation below each plate, each plate's thermal noise contribution from its temperature can be calculated. The last row shows the sum of all the contributions from each plate and is the residual cavity photon number. For example, we can see that in the standard attenuation of $20-10-20$dB configuration, the highest contribution to the cavity thermal photon number is the 4 K plate, thus it would make sense to add additional attenuators after the 4 K plate. In these calculations, the cavity is at a frequency of 7 GHz.

Plate	Input Line Attenuation (4 K, 100 mK, Base)			Output Line Isolation	
	20-10-20	20-10-30	20 - 0 - 40	40	60
300 K	$9e^{-3}$	$0.9e^{-3}$	$0.9e^{-3}$	-	-
50 K	$1.5e^{-3}$	$0.15e^{-3}$	$0.15e^{-3}$	-	-
4 K	$11e^{-3}$	$1.1e^{-3}$	$1.1e^{-3}$	$1.1e^{-3}$	$11e^{-6}$
1 K	$2.5e^{-3}$	$0.25e^{-3}$	$0.25e^{-3}$	$0.25e^{-3}$	$2.5e^{-6}$
100 mK	$0.36e^{-3}$	$0.036e^{-3}$	$3.6e^{-6}$	-	$36e^{-9}$
20 mK	$51e^{-9}$	$51e^{-9}$	$51e^{-9}$	$51e^{-9}$	$51e^{-9}$
Residual n_{th}	0.025	0.0025	0.0024	0.0014	$14e^{-6}$

Table 3.2: Table showing the contributions of the residual thermal photons to the experiment on the base plate for different line configurations in units of dB. Each contribution considers the total attenuation after each plate. The last row shows the sum of the different contributions from all the plates and is the residual cavity photon number. Depending on the relative input and output coupling strength of the cavity, the residual thermal noise will be somewhere between the chosen input line and output line configuration. For these calculations, the cavity frequency is 7 GHz.

For a reflection configuration, only one cavity port is taken into account. The thermal photon flux from the input line and output line add up. An experiment in transmission will have a thermal equilibrium between the input line reservoir and output line reservoir determined by the ratio of the input and output coupling of the cavity. For a qubit coupled to a cavity with $n_{\mathrm{th}} = 0.02$ and optimal readout parameters of $\chi/2\pi = \kappa/2\pi = 1\,\mathrm{MHz}$, the thermal dephasing limit is $T_{\phi,\mathrm{th}} = 1/\Gamma_{\phi,\mathrm{th}} \approx 100\,\mu\mathrm{s}$. For a T_1 of $20\,\mu\mathrm{s}$, this will limit the maximum T_2^* to $35\,\mu\mathrm{s}$. Thus, it is important to make sure the thermal population in the cavity is as low as possible.

It is also important to consider the maximum heat load on each attenuator. Too much power dissipated at a certain resistor will cause the resistor to heat up and emit larger thermal radiation than the physical temperature of the plate. Although attenuators are properly thermally anchored, the inner conductor is still separated by some dielectric and will not be as efficiently cooled. Some wiring schemes include directional couplers which do not dissipate the signal [125]. Instead, the attenuation comes from the coupling coefficient from the input port to the output port. Most of the signal is routed back up to upper plates with larger cooling power.

From Eq. (3.29), one can see that, depending on the quality factor of the cavity $Q = \frac{1}{\kappa}$ and the coupling to the qubit χ, the additional thermal dephasing rate is different. Also, with low κ, we need much higher drive powers which would then negate the benefits coming from attenuating the thermal noise. Thus, there are two sets of attenuation for different cavity coupling quality factors.

Finally, care must be taken for DC bias lines. Ground loops through the SMA cables or power supplies can cause large fluctuations of currents in the flux bias lines leading to unstable qubit frequencies. A magnetic field change in the ground loops will generate circulating currents. If there is a cable which goes in the cryostat in proximity to these currents, an induced current will be guided inside the cryostat. More details about adverse effects and avoiding DC ground loops can be found in [25].

3.7.2 Cryogenic Filtering and Shielding and Packaging

In addition to the attenuation and isolation of thermal noise, we include filtering to reduce microwave noise. Bandpass filters on the drive line help to reduce noise fluctuations at higher drive harmonics or cross-talk between the different elements.

Most of these microwave components are rated only to 12 GHz or in the case of SMA connectors 18 GHz. Above these frequencies, the connectors or whole components can be transparent to infrared photons. Infrared photons can leak into the experiment and cause additional losses by exciting quasiparticles across the superconducting gap [127]. Thus, infrared filters are added in the form of Eccosorb filters. These are home-built dissipative low-pass filters with high attenuation up to the infrared regime. The filters should be placed as close to the experiment as possible. After the filter, we have to use light-tight cables and shields to prevent the leakage of infrared photons into the experiment.

The samples are placed in a μ-metal shield which sits in a superconducting shield to protect the experiment against stray magnetic fields. The shield is filled with eccosorb foam for absorption of any stray infrared photons and is surrounded by copper to have good thermal contact with the base of the fridge.

The sample chips and cavity are thermalised by copper clamps. To increase the efficiency of cooling, it is best to limit the number of separate mounting bodies as each interface will cause a reduction in the cooling efficiency. At cryogenic temperatures, thermalisation between two bodies is not determined by pressure but by the force applied between them [128, 129]. The qubit chip has an additional aluminium sheet with a small slit between the chip and copper clamp. The small aluminium sheet is to shield the qubit mode from the non-superconducting copper clamp. The small slit was made with a wire EDM.

3.8 Microwave setup

To apply gates on the qubits or cavities, we need to generate fast microwave pulses at the frequency of the respective quantum element. Such pulses can be as short as 10 ns in duration and have any pulse envelope shape. While there are some instruments capable of direct synthesis of the pulses, these instruments are still expensive for research labs.

To form any pulse shape, we use arbitrary waveform generators (AWG), with a sampling rate of at least 1 Gsample/s. However, most AWGs only have a limited bandwidth up to $(100 - 1000\,\mathrm{MHz})$. To up-convert the intermediate frequency (IF) signal from the AWG to the relevant quantum element frequency, mixers are used. Mixers are microwave devices that are used together with an additional local oscillator (LO) to output a radio frequency (RF) signal that is the product of the two. The output of a mixer is

$$\begin{aligned} v_{\mathrm{RF}}(t) &= K v_{\mathrm{LO}}(t) v_{\mathrm{IF}}(t) = K\cos(\omega_{\mathrm{LO}} t) V_{\mathrm{pulse}}(t)\cos(\omega_{\mathrm{IF}} t) \\ &= \frac{K}{2} V_{\mathrm{pulse}}(t)\left[\cos((\omega_{\mathrm{LO}} - \omega_{\mathrm{IF}})t) + \cos((\omega_{\mathrm{LO}} + \omega_{\mathrm{IF}})t)\right] \end{aligned} \tag{3.32}$$

where K is some voltage conversion loss in the IQ mixer. Depending on the specific mixer device, K is approximately $6 - 9\,\mathrm{dB}$ of loss. The output RF contains two frequencies $\omega_{\mathrm{RF}} = \omega_{\mathrm{LO}} \pm \omega_{\mathrm{IF}}$ called the left and right sideband.

Mixers are inherently non-linear devices and thus have higher order sidebands. Imperfections in each mixer device will also result in some LO leakage or phase and amplitude differences between the two sideband frequencies. Fortunately, there is a whole field of microwave engineering that can account for and calibrate out such imperfections to produce a clean RF signal. Here, I describe two such methods, In-phase and Quadrature (IQ) mixing and Double SuperHeterodyne (DSH) mixing. Details on pulse mixing and the IQ calibration routine are found in [26] with more theoretical details found in [80, 81].

In addition to the mixers used, it is crucial to have fast microwave switches after any IQ mixer and amplifier. This is especially important for IQ mixing, where the calibration in the presence of an IF signal is very different to the case without an IF signal. Thus, the LO leakage when there is no pulse being played might be large and must be attenuated with a fast switch. In the case where more RF power is needed, low-noise amplifiers can be used. It is also important to place amplifiers before any switch to prevent sending amplified thermal noise to the experiment. Small attenuators are placed before and after the amplifiers to protect the amplifier from damage.

3.8.1 IQ Mixing

IQ mixers are a four-port device designed to produce high suppression of unwanted sidebands. IQ mixers are made up of two balanced mixers and two hybrids. The LO signal is split with the first hybrid into two signals with a π phase difference and used to drive the two mixers. I and Q signals are used to drive the IF port of the mixers (Fig. 3.12A). The output of the two mixers is then combined with the second hybrid to produce the RF signal. The resulting RF signal is given by

$$V_{\mathrm{RF}}(t) = I(t)\cos(\omega_{\mathrm{LO}}t) + Q(t)\sin(\omega_{\mathrm{LO}}t) \tag{3.33}$$

Considering the general case of $I(t) = I_0(t)\cos(\omega_{\mathrm{IF}}t + \phi_{\mathrm{I}})$ and $Q(t) = Q_0(t)\cos(\omega_{\mathrm{IF}}t + \phi_{\mathrm{Q}})$, where $I_0(t)$ and $Q_0(t)$ are the pulse envelope. We can simplify the equation to

$$\begin{aligned} V_{\mathrm{RF}}(t) = {} & \frac{I_0(t)}{2}\left[\cos\left((\omega_{\mathrm{LO}}+\omega_{\mathrm{IF}})t + \phi_{\mathrm{I}}\right) + \cos\left((\omega_{\mathrm{LO}}-\omega_{\mathrm{IF}})t - \phi_{\mathrm{I}}\right)\right] \\ & + \frac{Q_0(t)}{2}\left[\sin\left((\omega_{\mathrm{LO}}+\omega_{\mathrm{IF}})t + \phi_{\mathrm{Q}}\right) + \sin\left((\omega_{\mathrm{LO}}-\omega_{\mathrm{IF}})t - \phi_{\mathrm{Q}}\right)\right]. \end{aligned} \tag{3.34}$$

By choosing $I_0(t) = Q_0(t)$ and the right conditions for ϕ_I and ϕ_Q, we can select the desired frequency and phase for the RF output. It is for this reason that qubit $\hat{\sigma}_x$ or cavity $\hat{D}(\mathrm{Re}\{\beta\})$ operations are called I pulses, while qubit $\hat{\sigma}_y$ or cavity $\hat{D}(\mathrm{Im}\{\beta\})$ operations are also known as Q pulses. The two terminologies are used interchangeably, as is the case in this thesis. In particular, table 3.3 states the matching conditions.

ϕ_{I}	ϕ_{Q}	$V_{\mathrm{RF}}(t)$
0	$\frac{\pi}{2}$	$I_0(t)\cos((\omega_{\mathrm{LO}}+\omega_{\mathrm{IF}})t)$
$\frac{\pi}{2}$	π	$-I_0(t)\sin((\omega_{\mathrm{LO}}+\omega_{\mathrm{IF}})t)$
0	$-\frac{\pi}{2}$	$I_0(t)\cos((\omega_{\mathrm{LO}}-\omega_{\mathrm{IF}})t)$
$\frac{\pi}{2}$	0	$I_0(t)\sin((\omega_{\mathrm{LO}}-\omega_{\mathrm{IF}})t)$

Table 3.3: IQ mixer calibration conditions. By choosing the right phase relation and adjusting for imperfect DC offsets, the output of the IQ mixer can calibrated to the left ($\omega_{\mathrm{LO}} - \omega_{\mathrm{IF}}$) or right sideband ($\omega_{\mathrm{LO}} + \omega_{\mathrm{IF}}$) frequencies.

Imperfections in the IQ mixer will lead to leakage of the LO tone. Furthermore, nonlinearities of the mixer will lead to the generation of higher-order sidebands. We can calibrate the LO leakage by adjusting the DC offset on both the I and Q ports. Imperfect sideband calibration can be tuned by calibrating the amplitude ratio and phase difference between the I and Q ports of the AWG. This is captured by a correction matrix that is applied to the pulses as they are played.

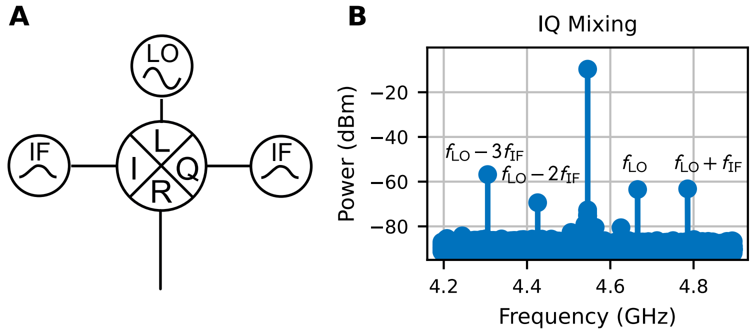

Figure 3.12: IQ mixing circuit and calibrated spectrum. (**A**) IQ mixing circuit. The IQ mixer is made up of two balanced mixers with two IF channels. (**B**) Spectrum analyser measurement of a calibrated IQ mixing circuit. The unwanted sideband suppression should reach $> 40\,\mathrm{dB}$. The highest unwanted sideband will come from higher-order harmonics that can not be calibrated. The IQ mixing circuits should be recalibrated if the pulse frequency is changed by $\approx 10\,\mathrm{MHz}$ or the pulse amplitude is changed by $\approx 0.1\,\mathrm{V}$.

The calibration is sensitive to instrument temperature, frequency and power and should be recalibrated every $\approx 10\,\mathrm{MHz}$ or $\approx 0.1\,\mathrm{V}$. IQ calibration will fluctuate but can achieve at least $40\,\mathrm{dB}$ suppression between the wanted sideband and unwanted tones (Fig. 3.12B). The highest unwanted sideband is the second order term $\omega_{\mathrm{LO}} \pm 2\omega_{\mathrm{IF}}$ which cannot be calibrated out for an IQ mixer with only two ports. Thus, for transmons, it is better to use the left sideband (LSB) for the qubit frequency. The anharmonicity of the transmon will mean the transition frequency for driving $|e\rangle$ to $|f\rangle$ is lower than the qubit drive frequency. Thus, the highest unwanted sideband tones near $\omega_{\mathrm{qb}} - \alpha$ will cause AC Starck shift or leakage out of the qubit computational subspace.

In some cases, the AWG signal needs to be attenuated for proper calibration. This can be due to the nonlinearities of the mixer or the voltage step size of the AWG. For example, the OPX AWG from Quantum Machines has a maximum voltage of $0.4\,\mathrm{V}$ with a 16-bit resolution DAC. This means the AWG has a voltage step size of $\frac{0.4}{2^{16-1}} \approx 12\,\mu\mathrm{V}$. By attenuating the IF signal first, this effectively decreases the step size and we can finely tune the calibration of the unwanted sidebands. The signal can be amplified afterwards to reach the required power levels.

For IQ calibration, some of the signal is routed via a directional coupler to a spectrum analyser. Signals from multiple mixing channels are combined with a power combiner. An important property of the combiner is to ensure that there is good isolation of the different ports in the power combiner. Leakage through the power combiner will result in unwanted pulses driving the experiment through other input paths.

3.8.2 DSH Mixing

Double-super-heterodyne (DSH) mixing is an alternative method to produce fast pulses at the desired frequency [80, 130]. Instead of calibrating out the unwanted peaks, DSH mixing uses a narrow bandpass filter and two mixing stages to produce a clean RF signal. The circuit is shown in Fig. 3.13A.

The first mixer stage produces frequencies at ω_{LO1}, $\omega_{\mathrm{LO1}} + n\omega_{\mathrm{IF}}$, where n is the sideband order. A narrow band pass filter is chosen with a bandwidth smaller than IF such that only one of the sidebands is transmitted. Only one sideband is chosen, here the LSB at $\omega_{\mathrm{LO1}} - \omega_{\mathrm{IF}}$, and the rest are filtered out with a narrow bandpass filter (Fig. 3.13B). The output frequencies of the second stage are ω_{LO2}, $\omega_{\mathrm{LO2}} + m(\omega_{\mathrm{LO1}} - \omega_{\mathrm{IF}})$. These frequency spacing of the signals is much further apart as compared to IQ mixing and can be easily filtered out with a low pass filter.

The IF is chosen such that it is larger than the bandwidth of the central bandpass filter. For good suppression of unwanted sidebands, the filter should have a fast dropoff. We operate with the passband at a high frequency and a down-mixing second stage to the desired RF output. This method will reduce image frequencies that are close to the RF output. For fast frequency changes, the bandwidth of the central bandpass filter will set the fast dynamic range. The AWG can quickly change the IF and the tone will still be well calibrated. Other desired RF frequencies can be reached by changing the frequency of LO2.

With a good bandpass filter, the DSH method will have a larger suppression of $\approx 60\,\mathrm{dB}$ between the wanted and unwanted sidebands (Fig. 3.13C). The main benefit of DSH is that no mixer calibration is needed across a large range of frequencies. This method also allows a comb of calibrated frequencies to be played simultaneously. This is useful if we want to play qubit pulses on even or odd cavity photon peaks (Fig. 3.13D). In terms of instruments, DSH uses one less AWG channel and one more LO.

However, there are some drawbacks to DSH. The main issue is that if the AWG does not have real-time phase control, we cannot play simultaneous I and Q pulses to the experiment. Furthermore, the two mixer stages will have larger losses and require a larger microwave amplifier in the setup. Lastly, we have to be careful with image frequencies produced in the setup.

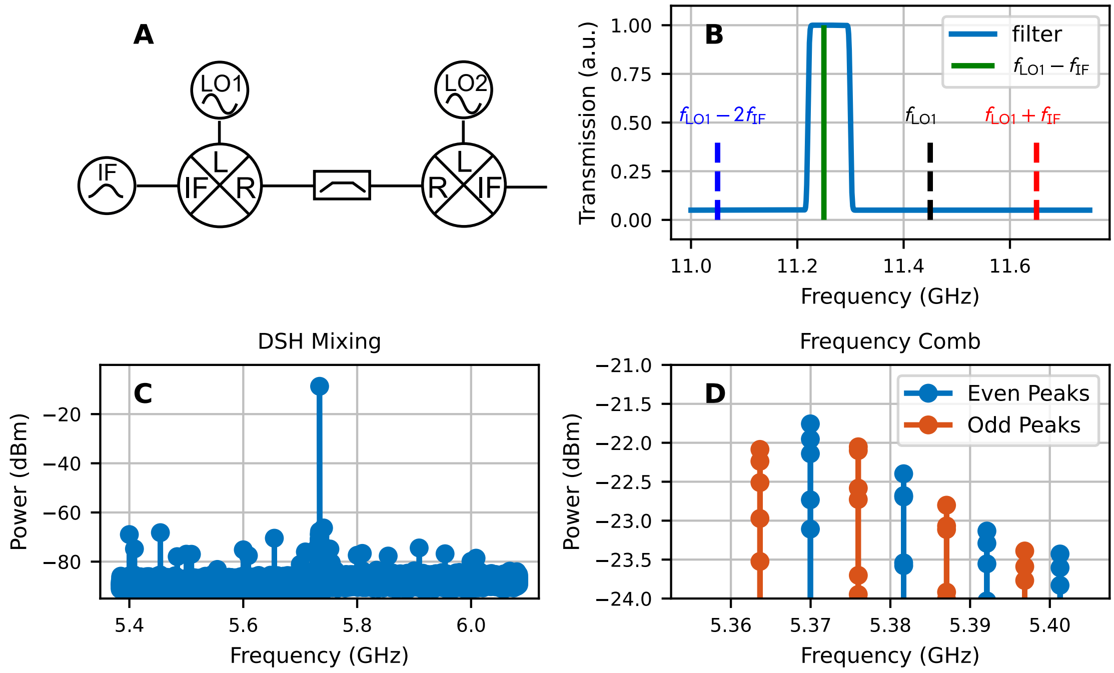

Figure 3.13: Double superheterodyne (DSH) working principle. (**A**) DSH mixing circuit. This circuit uses two single-sideband mixers with a narrow bandpass filter. (**B**) Spectrum after the first narrow bandpass filter. The unwanted sidebands are filtered out by the bandpass filter. (**C**) Spectrum analyser measurement of a tone produced by DSH mixing. The unwanted sideband suppression is $> 60\,\text{dB}$. The dynamic range of DSH mixing is determined by the frequency range of LO2 and the bandwidth of the central bandpass filter. (**D**) Zoomed in on the transmission spectrum of the frequency comb from a DSH setup. A huge benefit of DSH mixing is the ability to play a frequency comb that is well-calibrated. This is useful for playing selective pulses on the even or odd cavity photon qubit peaks. Here, the differences in amplitude are due to variations in line attenuation at different frequencies. The amplitudes are individually calibrated by selective Rabi pulses on the qubit peaks split by cavity photon numbers.

3.8.3 Microwave Readout

These mixing schemes work in both up and down conversion. However one must check the specific mixer model as certain models have image filters or diodes that will only allow the mixer to operate in one direction.

For readout signals, IQ mixing was used to up-convert the IF tones to the readout frequency. This avoids additional signal loss in the down-conversion process. The scheme shown in Fig. 3.14 uses a heterodyne setup that splits the LO of the readout to drive both the up-conversion IQ mixer and the down-conversion single-sideband mixer. This sets the LO as the phase reference. The IF signal can then be demodulated into the in-phase and out-of-phase components to determine the amplitude and phase response of the readout tone.

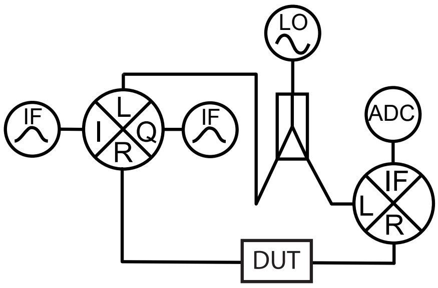

Figure 3.14: Readout with IQ mixing circuit. The LO is split to both the up-mixing and down-mixing side to allow for a phase reference between the probing signal and readout signal. The probing signal is then sent to the device under test (DUT) and the readout signal is digitised. Due to the dispersive interaction between the qubit and the readout resonator, the amplitude and phase of the readout signal will be dependent on the qubit state.

3.9 Experimental Setup Summary

The following is a summary of the instrument and wiring setup used in the experiments in the thesis. The schematic is shown in Fig. 3.15 which includes an additional pump line for a quantum-limited parametric amplifier.

The input drive lines for the qubit and readout resonator are attenuated by 20 dB at the 4 K plate and 10 dB at the still plate. At the base plate, the input signal is filtered by a K&L DC − 12 GHz low pass filter and then attenuated by a 20 dB Quantum Microwave thermalised cryogenic directional coupler followed by a Quantum Microwave thermalised cryogenic 20 dB attenuator and filtered by microtronics 4 − 8 GHz bandpass filter. The input signal for the high coherence cavity is attenuated and filtered similarly, except for the base plate where a 10 dB thermalised cryogenic attenuator is used instead.

The experiment was done in reflection with a Quinstar double junction 4−8 GHz circulator. Before and after the setup, the input and output signals pass through a home-built eccosorb filter.

The output signal is filtered via a microtronics 6 − 10 GHz bandpass filter, before passing through a quantum-limited parametric amplifier. The experiment is isolated from thermal noise in the parametric amplifier pump line by 60 dB at the base plate and 20 dB at the 4 K plate. The output signal is then filtered by a K&L filter which is connected to two Quinstar isolators giving 40 dB isolation. The signal is amplified at the 4 K plate by HEMT amplifiers and again with room temperature amplifiers outside of the refrigerator before being down-converted and digitised.

For shielding, the samples are placed in a light-tight μ-metal shield which sits in a superconducting shield to protect the experiment against stray magnetic fields. Copper mounts are used to thermalise the shield and experiment. Inside the shields, eccosorb foam surrounds the experiment to absorb any stray infrared photons.

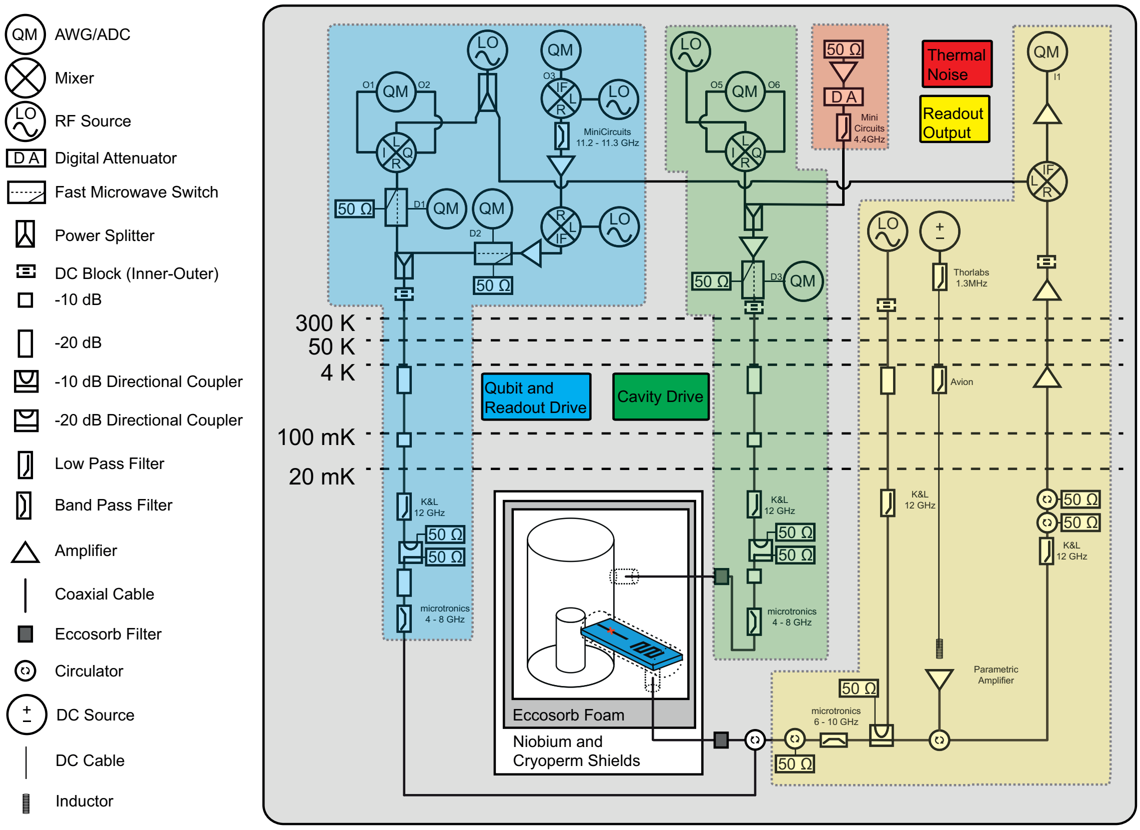

Figure 3.15: Full experimental wiring. The schematic includes microwave circuits at room temperature and cryogenic attenuation and filtering. Figure from supplementary material in [131].

The pulses for the high Q cavity and readout resonator with IQ mixing using a Marki microwave IQ mixer. The qubit pulses were up-mixed through a DSH setup employing two LOs and two MiniCircuits single side-band mixers. These pulse generation setups also incorporated various amplifiers, filters, alternators, and home-built fast microwave switches to achieve effective suppression of unwanted mixing products and minimise leakage of LO signals. The signal from the cryostat was down-mixed using the same readout LO and further amplified before being digitised.

Specifically, the AWG and ADC used was the Operator X (OPX1) from Quantum Machines. In later iterations of the experiments, an upgraded version (OPX+) was used with the Octave that included an integrated IQ mixing circuit. The additional LOs were from Valon RF Technologies.

CHAPTER 4

Experimental Characterisation

In this chapter, I outline the measurement methods used to characterise the Hamiltonian of the experiment. There are a plethora of measurement methods to get the same Hamiltonian parameters [24, 96, 103]. These can be classified into two broad categories. The first is the frequency domain, where we sweep the frequency of a probe or pump tone. The second is time domain measurements, where the response of the system is measured over time. Here I present a summary of characterisation experiments used and my thoughts on carrying out experiments in different situations.

In practice, instruments or experimental systems may not perform flawlessly. Thus, experiments such as null checks are crucial to differentiate measurement artefacts that arise due to imperfections. In research labs, we might also be limited in the number of available instruments. Thus, I believe it is useful to have a comprehensive understanding of multiple methods for measuring the same Hamiltonian. This redundancy serves as a valuable cross-check with various instruments in the troubleshooting process.

In the first section, I present the fast continuous wave (CW) measurements to characterise the readout resonator and check the status of the qubit. In Sec. 4.2, I outline the experiments done to characterise the qubit. Section 4.3 explains the measurements to characterise the high Q cavity mode. Finally, in the last section, I describe the method of creating single Fock states in the high Q cavity. Also, in appendix F, I include a diagnostic toolbox that includes other experiments that can be used for troubleshooting or fine-tuning of experiment parameters.

4.1 Readout Resonator CW Measurements

The first set of measurements is done with a Vector Network Analyser (VNA). VNAs measure the coherent complex scattering parameters of the experiment. To measure the readout resonator, we use the VNA S_{21} measurement which sends a pulse on port 1 of the VNA and measures its response at port 2. VNAs have a large dynamic range in power and frequency and thus can be used to quickly find the resonator frequencies.

VNAs can be set with a frequency range, number of frequency points and an associated intermediate frequency (IF) bandwidth that samples around each frequency point. Averages are then taken over each sweep and the final measurement is shown. For initial checks, it is visually faster to watch measurements happen with a higher IF bandwidth.

We can recognise patterns in the measurement results before the full measurement is finished. However, for doing bigger measurement maps where we are not actively monitoring the measurement, it is faster to do fewer frequency points with a lower IF and fewer number of averages. This is because most VNAs are designed such that it would do a full sweep in frequency first and then average on top of each frequency point with subsequent sweeps. This will take extra time when the VNA switches between the start and the stop probe frequency.

Power Spectroscopy The first measurement is a power spectroscopy with a VNA. At high powers, all qubits and other two-level systems become saturated. Thus, we will see the bare resonator frequency. At lower probe powers, for a coupled qubit that is alive, the resonator will become non-linear and start to shift to the dressed frequencies Fig. 4.1A. For this reason, we often interchange the terms used for the dressed and bare frequencies with low-power and high-power frequencies of the resonator. With the simulated coupling strength g and anharmonicity E_c, the difference between the dressed frequency and the bare frequency can be used to determine the qubit frequency with Eq. (2.52), $\omega_r' - \omega_r = -\frac{g^2}{\omega_q - \omega_r - E_c/h}$.

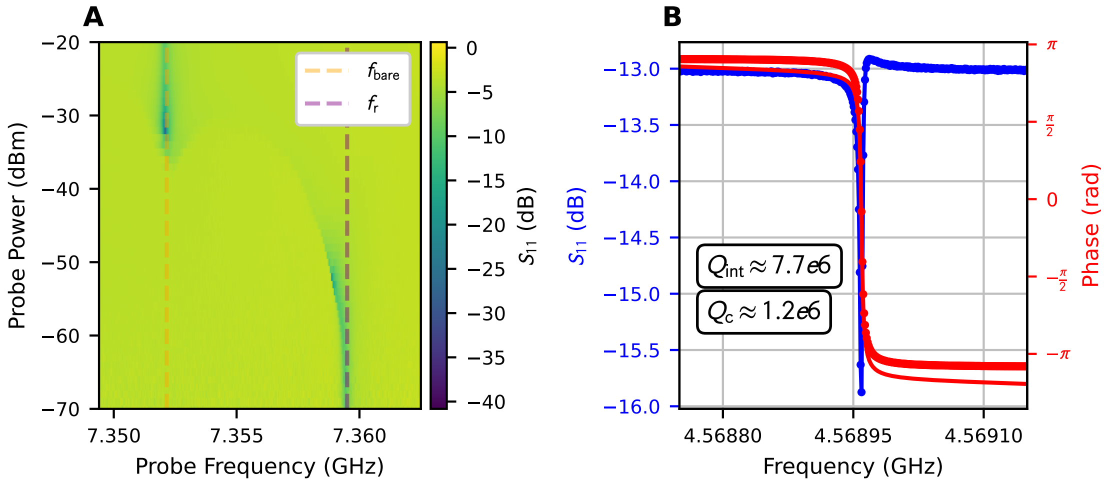

Figure 4.1: Readout resonator CW measurements.(**A**) Power Spectroscopy of a readout resonator coupled to the qubit. At high probe powers, the qubit is saturated or excited beyond the Josephson junction potential well [52]. This results in the readout resonator moving towards the bare frequency. At lower powers, the coupling between the resonator will become non-linear and shift towards the dressed frequency. This measurement map is done with a Vector Network Analyser and is the first measurement that determines if a qubit survived the mounting process. (**B**) For setups with the reflection configuration, a circle fit of the reflected signal allows the extraction of the quality factors of the cavity [101].

These measurements can be done while the fridge is still cooling down, after reaching a base temperature $\approx 100\,\mathrm{mK}$. The cavities are already superconducting and readout frequencies can be determined. These measurements will not reflect the true line widths of the resonators but allow for easier determination of frequencies in a new setup.

For experiments in reflection or hanger configuration, we can determine the internal loss rates and external coupling rates. This is done through a circle-fit routine [101] (Fig. 4.1B). For a resonator in reflection with frequency f_r

$$S_{11}(f) = \frac{2Q_{\mathrm{tot}}/Q_{\mathrm{c}}}{1 - 2iQ_{\mathrm{tot}}\frac{f-f_{\mathrm{r}}}{f_{\mathrm{r}}}} - 1 \tag{4.1}$$

where Q_{tot} is the total quality factor due to Q_{int} internal losses and Q_{c} external coupling. For accuracy in the fit routine, the experiment should have a coupling ratio of $\frac{Q_{\mathrm{int}}}{Q_{\mathrm{c}}} \approx 0.01 - 100$, with the optimal case being critically coupled, $Q_{\mathrm{int}} \approx Q_{\mathrm{c}}$. [1].

It is often difficult to estimate the final Q_{int} *a priori*. For better fitting of the different quality factors, it is better to be in the under-coupled regime $Q_{\mathrm{int}} < Q_{\mathrm{c}}$. By estimating the power sent to the resonator at the experiment, we can also determine the number of photons used in the readout with $\langle n_{\mathrm{photons}} \rangle = \frac{2}{\hbar\omega}\frac{Q_{\mathrm{tot}}^2}{Q_{\mathrm{c}}}P_{\mathrm{in}}$, where the P_{in} is the input power in W.

An important distinction between such a measurement and a true reflection measurement is the use of the circulator in the cryostat. The measurement is still a transmission configuration as the signal travels on separate input or output lines. Leakage through the circulator can cause an interference between the leakage signal and the signal from the experiment known as Fano-interference [132]. This will affect the shape of the resonance and cause inaccuracies in the determination of the different quality factors. This adverse effect can be mitigated by being in the under-coupled regime.

As we increase the number of photons used in the readout, we see the linewidth of the resonator changing [133, 134]. Thus, to determine the internal loss rate of the resonator, the power must be reduced such that there is roughly an average of 1 photon in the readout. The power level for a single photon in the cavity depends on the coupling quality factor but is approximately $-130\,\mathrm{dBm}$ at the base plate. In most cases, the external coupling will not change with frequency or power, thus to help with the fitting program, a faster measurement at high powers can be used to determine the external quality factor first.

[1] Another measurement method to determine the different coupling constants is via a spectrum analyser. Using the time traces of the response of the cavity to a pulse, we can fit the different decays [92] shown in appendix F.3

Flux Tuning For resonators with a SQUID, we can check the tuneability of the qubit via the readout resonator. By tuning the qubit frequency, the dressed frequency of the readout resonator will also shift. Thus, we can already determine the current needed for changing the flux by a Φ_0. Higher-frequency sweet spots in the readout resonator will correspond to low-frequency sweep spots in the SQUID. We can also use Eq. (2.48) to fit any avoided crossings to determine the coupling between the resonator and SQUID.

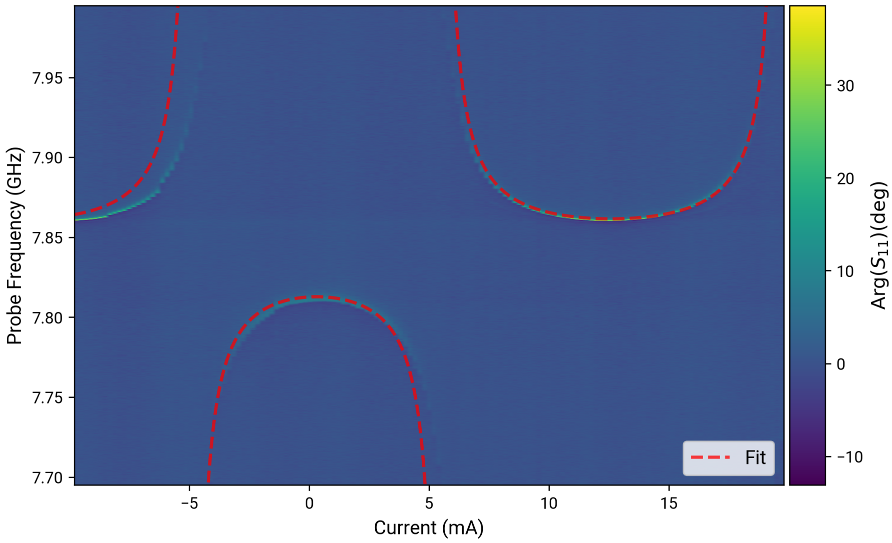

Figure 4.2: Readout resonator flux map. A readout resonator is coupled to a SQUID which is coupled to a flux hose. By changing the current in the coil of the flux hose, we can change the frequency of the SQUID. This in turn will shift the dressed frequencies of the readout resonator accordingly. Thus, we can determine the conversion between the current applied and the flux quantum in the SQUID loop. In this map, hysteresis present in the system prevents full fitting of the resonator frequencies. In the first generation of flux hoses, as shown here one flux quantum required 24.5 mA, while with the improved designs, only 5.6 mA was required per Φ_0. Measurement was performed with Lucien Québaud during an internship project.

In an initial proof of concept experiment, we compare a SQUID in two setups where we determine the flux periodicity of the system for the two generations of flux hoses. Both experiments have the same SQUID loop area and flux hose to SQUID loop distance. For the first generation flux hose, we required 24.5 mA per Φ_0 (shown in Fig. 4.2) while the new generation design only required 5.6 mA per Φ_0. This shows a factor 5 improvement in the efficiency of magnetic flux transfer. Measurements of the fast flux tuneability of the new generation design are currently ongoing.

4.2 Qubit Measurements

After measuring the resonator, we can introduce another pump tone to characterise the qubit. This frequency can be filtered out or attenuated in the output lines as we do not read out at the qubit frequency.

Qubit Spectroscopy The next set of CW measurements is probing at the low-power readout resonator resonance and including a second pump tone, known as two tone spectroscopy. When the pump tone is resonant with the qubit frequency, the resonator is shifted down by χ (Fig. 4.3). At higher pump powers we are also able to excite the two-photon transition to the $|f\rangle$ state and see a twice-shifted readout resonator. At this pump frequency, the detuning from the ground state transition is half the anharmonicity of the qubit. Similar to the CW measurements of the readout resonator, this measurement can also be done while the experimental setup is around 100 mK as we are only determining frequencies here.

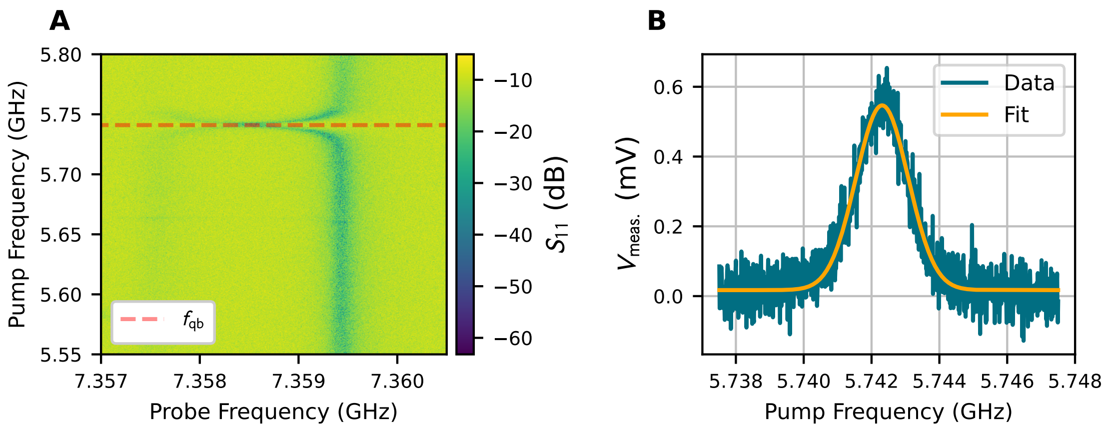

Figure 4.3: Two tone spectroscopy. (**A**) Qubit spectroscopy map. Two tone spectroscopy is done by turning on a pump tone and probing the readout resonator. By sweeping the frequency of the pump tone, we can determine the qubit frequency when the readout resonator shifts to a lower frequency. (**B**) Linecut data and fit of a single probe frequency. For a measurement in reflection, the probe frequency is at the readout resonator frequency and thus will read an increase in signal when the qubit is excited and the readout resonator is shifted.

4.2.1 Rabi

Thus far, all of the presented measurements have been CW measurements where both the probe and pump tone are always on at the same time. To do more complex experiments, the measurements have to be in the pulsed mode. This requires moving to fast AWGs and mixing setups. Between measurements, a long wait time is needed to allow the system to cool back down and initialise in the ground state. This is typically $5-10\ T_1$ of the qubit.

The first measurement is called a Rabi experiment which aims to tune up qubit pulses. In this experiment, a qubit pulse is first played followed by a measurement of the readout resonator. There are two ways to tune up qubit pulses referred to as power Rabi (Fig. 4.4A) or time Rabi (Fig. 4.4B).

For power Rabi, the qubit pulse length is kept the same while the amplitude is increased. This means the pulse has the same frequency width. However, the Stark shift due to the pulse amplitude will increase. For systems that are very susceptible to these shifts, it could be the case that the qubit is tuned in and out of resonance within the amplitude sweep. For time Rabi, the pulse length increases and becomes more selective at higher pulse lengths. It is also the case, that some AWGs can easily increase the amplitude but cannot stretch a pulse quickly without incurring additional lag time.

As we are averaging sequential experiments, the voltage that we measure is

$$\begin{aligned} V_{\text{measurement}} &= P_{\text{e}} V_{\text{e}} + P_{\text{g}} V_{\text{g}} && (4.2) \\ &= V_{\text{A}} \cos\left(2\pi A t\right) + V_{\text{offset}}. && (4.3) \end{aligned}$$

where $V_{\text{e,g}} = V_A \pm V_{\text{offset}}$ is the voltage that corresponds to measuring the qubit state in $|e\rangle$ or $|g\rangle$. P_{e} and P_{g} refer to the probability that the qubit is in the ground or excited state given by Eq. (2.62). Here, note that there is no phase component in the cosine as a zero amplitude and time qubit pulse must leave the qubit in the ground state. However, it is often the case that AWGs have a minimum pulse length and thus, the time Rabi needs to start from some minimum pulse length. For all future measurements, if there are no higher-order cross-Kerr effects from the excitation of other modes, the obtained measurement voltage should be between V_{e} and V_{g}.

We can determine the maximum applied Rabi frequency Ω. Using square pulses with a constant amplitude and thus constant applied Rabi frequency, the number of oscillations n_{osc} in a time Rabi measurement will give $\Omega/2\pi = \frac{n_{\text{osc}}}{T_{\text{pulse}}} \approx 10-80\,\text{MHz}$. This allows us to convert between the voltage we apply and the Rabi frequency on the qubit.

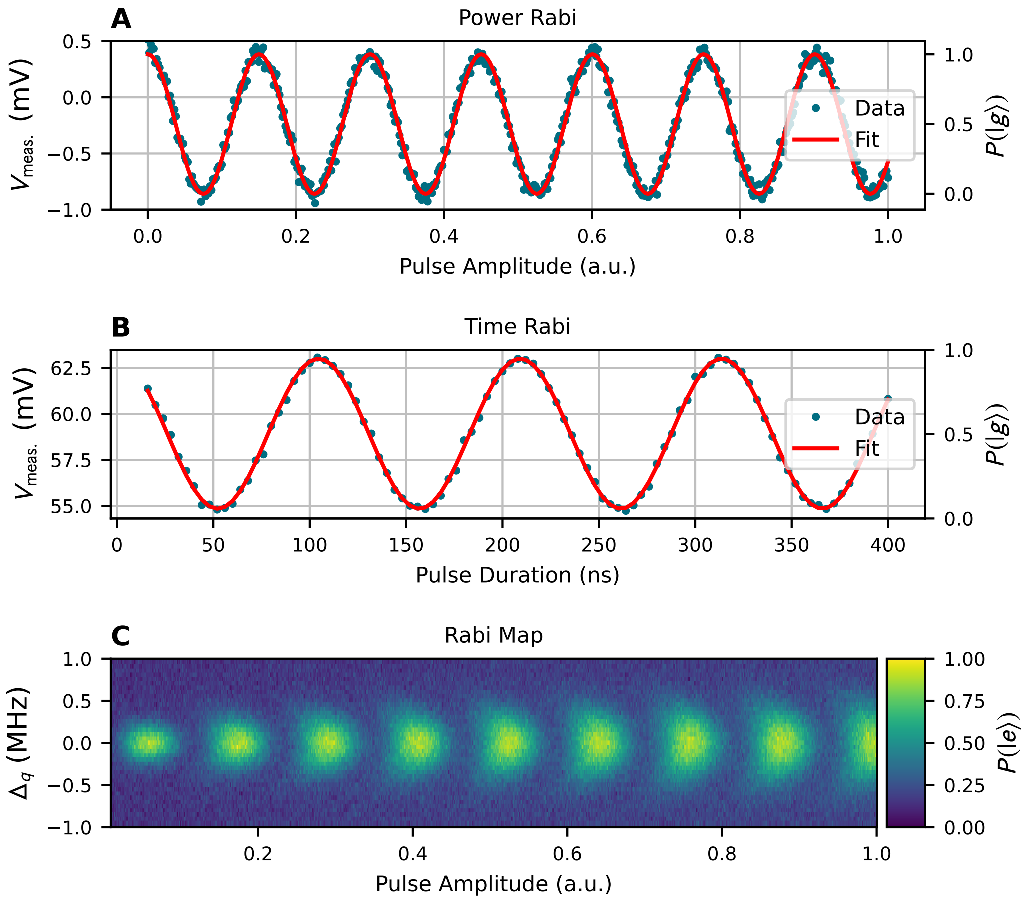

Figure 4.4: Rabi experiments. (**A**) Power and (**B**) time Rabi measurements. These measurements are done by sweeping the amplitude or length of the qubit pulse which results in Rabi flopping the qubit between the excited and ground state. The AWG used has a minimum pulse length and thus, the time Rabi needs to start from some minimum pulse length. (**C**) Rabi map. Detuned Rabi oscillations can be seen when the qubit tone is off in frequency. At detuned frequency, the qubit is not fully rotated to the excited state.

In Fig. 4.4C, the power Rabi measurement is done for a detuned qubit drive. From Eq. (2.62), we note that slightly detuned pulses will result in similar measurement results but with a smaller amplitude V_{A}. Furthermore, small pulse amplitude or time errors are also difficult to catch. This might be visible on big measurement maps of qubit detuning and pulse amplitude and doing a global map fit. However, such maps are time-intensive. A more time-efficient way to amplify such small errors is the repetition of N pulses. The errors in each pulse will add up and thus can be more easily seen. This is known as Amplified Phase Error and some measurements are shown in appendix F.1.

4.2.2 Optimising Qubit Readout

For the initial measurements, we can just pick a low-power readout resonator and measure the amplitude or phase of the resonator. To improve the readout fidelity, we can optimise the measurement pulse amplitude and time. Optimising the readout parameters will require measurement of the qubit coherence times and readout fidelities. Thus, initial measurements are first set to a longer waiting time and measurement pulse time. Unoptimised values just result in a lower measurement fidelity but still produce the results needed to optimise the measurement.

The measurement time is bounded by two limits, the external coupling rate of the readout resonator κ_c and the qubit lifetime T_1. We need to get information on the resonator photons and thus we choose the measurement time $t_m > 4(\frac{2\pi}{\kappa_c})$. A longer measurement time also allows for a longer integration of the signal and thus reduces the measurement noise. However, the qubit should not decay during the measurement time $t_m < \frac{1}{10}T_1$.

Similarly, a larger measurement pulse amplitude will give us better differentiation between the qubit in the ground or excited state voltages. However, for quantum non-demolition measurements, we need to stay under the n_{crit} limit[2].

Between each measurement, we have to allow for all qubit and cavity states to decay back to the ground state. The waiting time between measurements is limited by the longest-lived quantum element $T \approx 5 - 10\ T_1$.

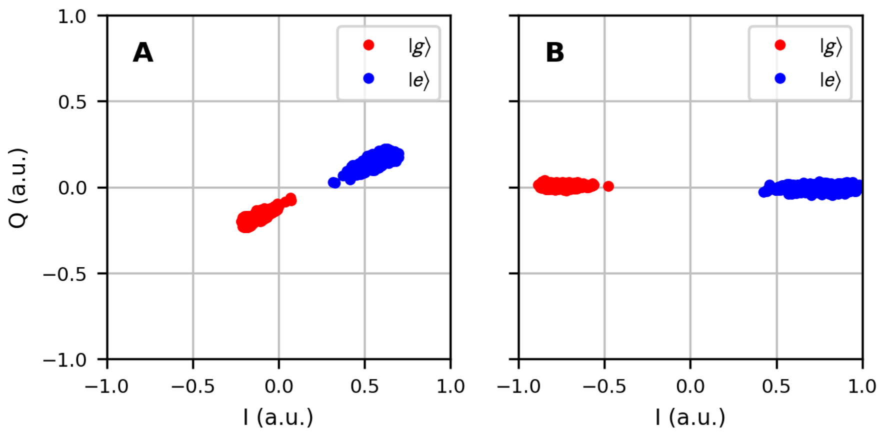

Figure 4.5: Phase space of the readout signal. (**A**) Raw data and (**B**) Rotated signal. The readout signal should be demodulated such that it is only along one quadrature. Otherwise, measurement artefacts will appear, shown in appendix F.4C. Another improvement is to remove the mean DC offset so that the readout signal can be amplified to use the full range of the digitiser.

[2]QND measurements are those where the projected qubit state after the measurement is the result of the measurement. Consecutive QND measurements will result in the same answer. A counter-example is most photon detectors, in which the measurement of the photon destroys the photon.

The readout signal can be demodulated to the I and Q components. These components can have some DC and phase offset (Fig. 4.5A). For maximum signal contrast, it is best to account for these offsets to use the maximum voltage and bit resolution of the digitised used. To maximise the measurement signal over digitiser noise, we can include low-frequency amplifiers and a bias tee with a resistor across the DC port to the ground port to remove any DC components of the noise.

The phase offset can be accounted for by applying a rotation angle on the integration weights in the demodulation process. As shown in Fig. 4.5B, this is equivalent to rotating the demodulated signal by some angle. It is best to rotate such that all the signal is only in one quadrature. In reflection configurations, this is crucial as there is a phase difference of π between the signals. This might result in some intermediate voltage parameters $|V_{\text{measured}}| < |V_e|$ or $|V_g|$. This is shown in appendix F.4A.

Low Power Readout and Active Reset

Optimal readout parameters use only one quadrature or the phase of the readout signal and are at a frequency, between both the dressed frequency and χ shifted frequency.

To optimise the readout parameters, we can repeat measurements for the qubit in the ground or excited state. Plotting the data in a histogram will allow us to obtain a state preparation and measurement (SPAM) fidelity based on the overlap between the two histograms (Fig. 4.6). In Fig. 4.6B, when the qubit is prepared in the excited state (blue line), we still see a significant population in the ground state. This is due to a low qubit T_1 which results in the decay of the qubit state during state preparation or measurement.

For active reset, two additional conditions are required. The first condition is the ability for fast single-shot QND measurement of the qubit. Fast single-shot QND measurements will require a quantum-limited parametric amplifier with a gain of $\approx 20\,\text{dB}$ to beat the HEMT noise. The second condition is initialising the readout resonator in the zero photon state. Photons in the readout resonator will cause a shift in qubit frequencies due to the dispersive interaction. The decay of resonator photons is fast due to the large external couplings, but can still be sped up by shaping the measurement pulse [135].

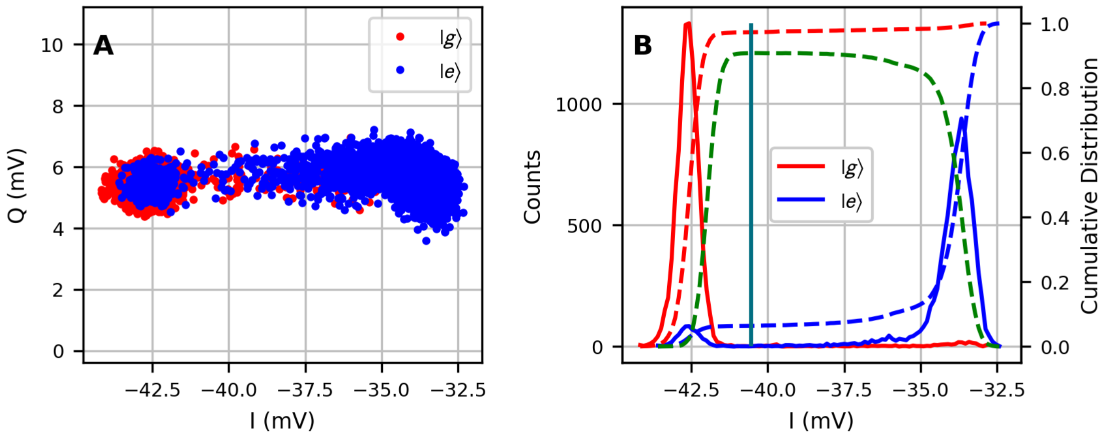

Figure 4.6: Single shot high power readout (**A**) Phase space of measurement signal and (**B**) Histogram of data along the I signal direction. The histogram determines state preparation and measurement (SPAM) errors. Data is sorted into bins and fitted to a normal distribution (solid lines). The dashed line is the cumulative distribution of the two cases. The overlap between the two normal distributions gives the error due to SPAM errors. The maximum fidelity is given by the difference between the two cumulative counts (green line). Here, the preparation and readout fidelity is 90.8%.

High Power Readout

An alternative method for readout is high-power readout, also known as Jaynes-Cumming readout [136]. This method involves high powers of the measurement pulse, giving us a larger number of signal photons and a higher signal-to-noise ratio (SNR). Depending on the relative detuning of the qubit from the resonator, the probe power is placed above or below the high power peak of the resonator. For the qubit in the excited state, the low power peak of the resonator is shifted down by χ. For a qubit frequency below the readout resonator frequency, this means that the low power peak is now closer to the high power peak. This causes a faster transition to the high-power peak. By probing with a power just below the high power peak, we will only see the readout resonator resonance if the qubit is excited. The power spectroscopy at the bare resonator frequency for different qubit initial states is shown in Fig. 4.7A. In Fig. 4.7B, the readout voltage is normalised by the input readout voltage (as larger input signals will achieve larger output signals). The normalised data will allow us to calculate the difference in normalised readout signal between the two cases for qubit ground and excited and we can choose a readout amplitude that maximises the readout contrast (green line).

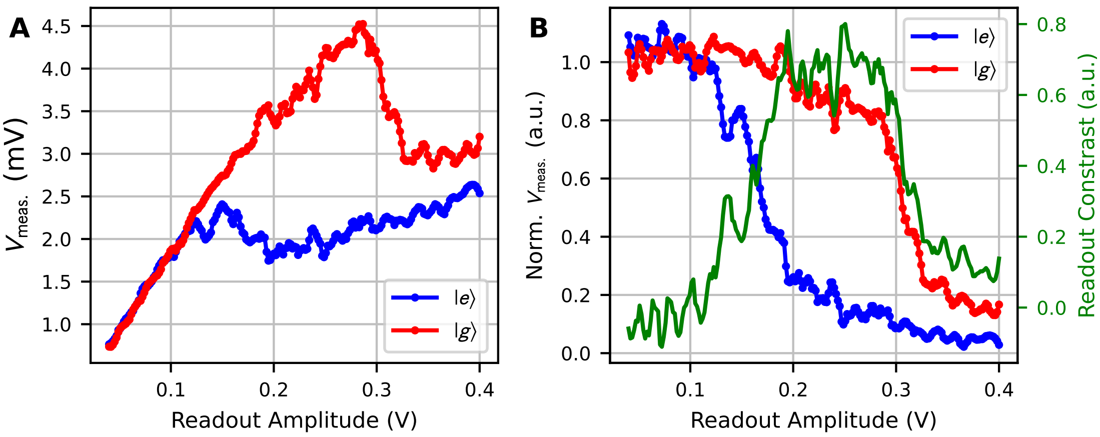

Figure 4.7: High power readout calibration. Power Spectroscopy at the $f_{\text{bare resonator}}$ frequency for the qubit initialised in the ground or excited state. (**A**) Raw data. The overall rise in V_{measured} is due to the increase in readout amplitude used. The dip in readout amplitude is due to the saturation of all qubits and two-level systems such that we see the bare resonator frequency. As the measurement is done in reflection, this results in a dip in the readout amplitude. (**B**) Normalised data. We can divide the measured readout by the readout amplitude used to normalise the data. Calculating the difference between the two curves allows us to choose a readout amplitude that maximises the readout contrast (green line).

High power readout is not a QND measurement as the qubit is excited to very high transition levels. During this readout method, the qubit and resonator become highly hybridized. Transitions between the "qubit" and the "cavity" mode occur which results in a lower measurement fidelity. High power readout also requires a longer waiting time for the qubit and readout resonator to fully decay and be reinitialised into the ground state between experiments. Thus, we cannot do feedback control with high-power readout.

Measurement fidelity aside, a high-power readout has an overall measurement time similar to that of a low-power readout with a quantum-limited amplifier. This method is especially useful in some experimental situations such as the lack of a quantum-limited parametric amplifier due to device, wiring or instrument constraints. Furthermore, in the case of high Q cavities without a technique to for fast Q switching or to empty out the photons in the high Q cavity, a long waiting time between experiments is already required. In such scenarios, high-power readout can be a middle ground between shorter measurement time and having good SNR.

4.2.3 Qubit Lifetime and Coherence Time

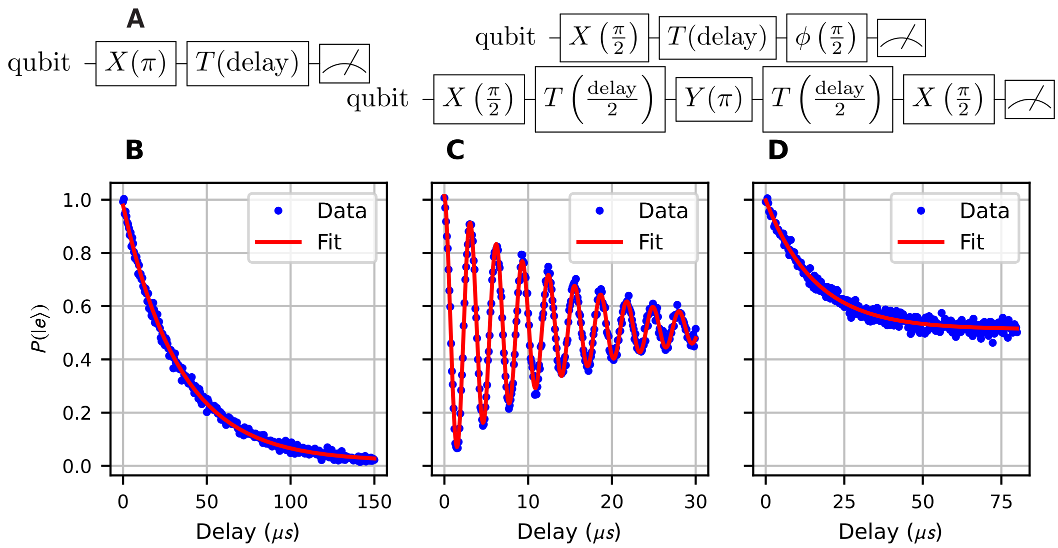

Figure 4.8: Qubit relaxation and coherence time measurements. (**A**) Pulse sequence for (left) qubit relaxation and (right) decoherence time measurements. (**b**) T_1, (**C**) T_2^*, (**D**) T_2^E measurement results. T_2^* is done by introducing controllable and artificial phase oscillations in the second $\hat{\phi}(\frac{\pi}{2})$ pulse. For T_2^E, the $\hat{Y}(\pi)$ echo pulse helps to mitigate low qubit frequency noise and small qubit pulse amplitude errors. Here, $T_1 = (33.6 \pm 0.3)\,\mu$s, $T_2^* = (13.7 \pm 0.2)\,\mu$s and $T_2^E = (15.7 \pm 0.3)\,\mu$s

For qubit T_1, a π pulse is applied on the qubit with a variable waiting time (Fig. 4.8A). The probability of finding the qubit in the excited state will decay with an exponential. $P_e(t) = e^{-t/T_1} \rightarrow V_{\text{measured}} = Ae^{-t/T1} + V_{\text{offset}}$. The total quality factor of a qubit can be calculated by $Q_{\text{tot}} = \omega_q 2T_1$.

T_2^* measures the phase coherence of the qubit by placing the qubit on the equator of the Bloch sphere. Then, after a variable waiting time, the qubit state is mapped onto the ground or excited state with another $\pi/2$ pulse (Fig. 4.8B). This is known as a T_2^* Ramsey experiment. A detuned qubit frequency will give phase oscillations in the exponential decay, the measurement map is shown in Fig. 4.9A. For small frequency detunings, the slow phase oscillation will be hard to fit on top of an exponential decay. Thus, it is better to use larger detunings or preferably to introduce artificial phase oscillations into the second $\pi/2$ pulse. This allows us to play calibrated qubit tones on resonance and the frequency of the oscillations to be changed $V_{\text{measured}}(t) = Ae^{-t/T_2^*}\cos(\delta\omega t + \phi(t)) + V_{\text{offset}}$, where $\delta\omega$ is the detuning between the qubit and the drive frequency and $\phi(t)$ is the introduced phase oscillations in the second $\pi/2$ pulse.

Another commonly done experiment is the T_2^E measurement where an additional π pulse is applied in the middle of the waiting time in a T_2^* measurement Fig. 4.8C. This is known as the spin or Hahn echo sequence [137]. The echo pulse will refocus low-frequency qubit detuning and the T_2^E will have a similar decay form to T_1. Echo pulses are designed into pulse sequences to mitigate low-frequency noise and fluctuations of the qubit frequency due to shot-to-shot photon number fluctuations. By making the echo pulse $\pi/2$ out of phase with the $\pi/2$ pulses, we can add a first-order insensitivity to pulse amplitude errors.

An extension to the echo pulses is the Carr-Purcell-Meiboom-Gill (CPMG) sequence [138, 139]. The CPMG sequence increases the number of π pulses that refocus the qubit Bloch vector after each delay time. By varying the number of pulses, we can also sample different parts of the noise spectrum of the qubit [140].

Doing repeated T_1, T_2^* and T_2^E measurements over a long time scale, we typically see fluctuations of these values and the qubit frequency to an order of 10% (Fig. 4.9B and C). The fluctuations can be due to stochastic variations in the qubit's environment leading to a change in the loss rate of the qubit such as ionising radiation from cosmic rays [141].

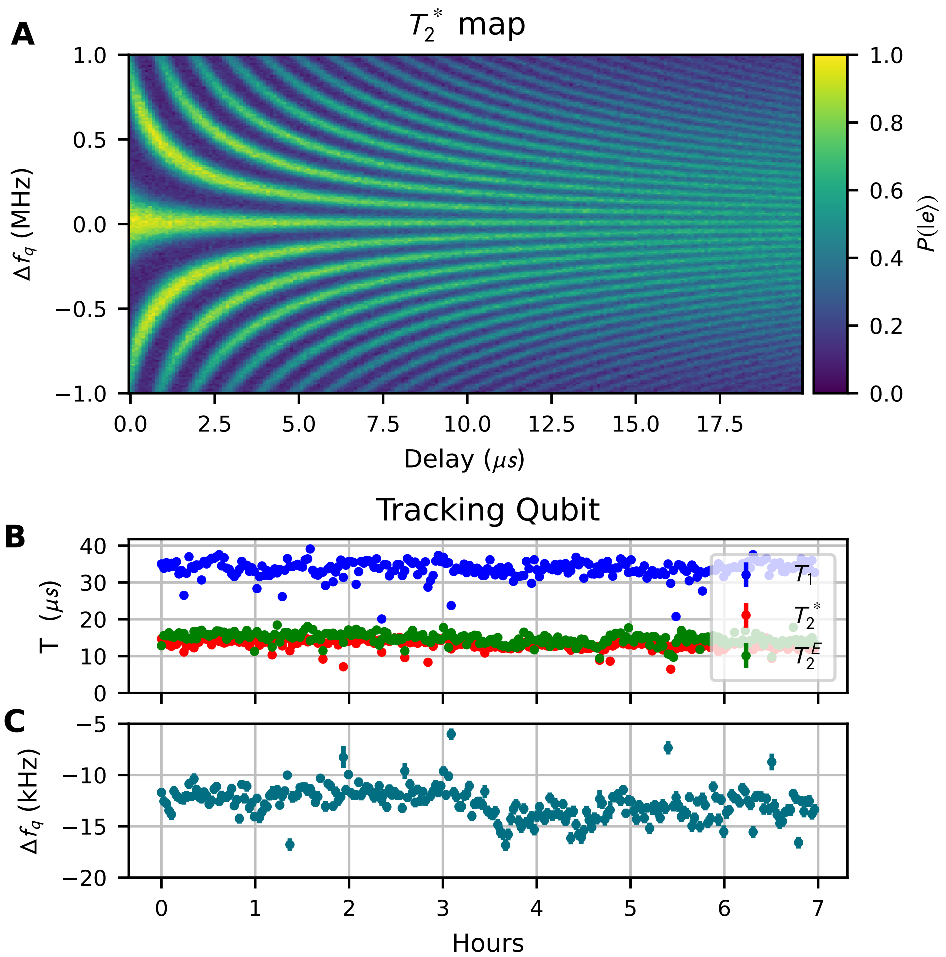

Figure 4.9: Detuned T_2^* measurement map and monitoring qubit lifetime over hours. (**A**) T_2^* measurement map with detuning of the qubit drive tone. We see phase oscillations in the measurement due to the qubit drive frequency and qubit frequency detuning. (**B** and **C**) Measurement results from repeated qubit lifetime and decoherence time experiments. Doing repeated measurements of T_1, T_2^* and T_2^E show stochastic fluctuations around 10%.

4.2.4 Qubit Anharmonicity

Transmons have a higher lying $|f\rangle$ state with a transition frequency from $|f\rangle$ to $|e\rangle$ at $\omega_q - \alpha$. This additional state can be a resource for qutrits or a problem causing higher-order effects on our quantum system. Figure 4.10A shows the pulse sequence used to determine the anharmonicity. The pulse sequence starts from the qubit in the excited state first applying a $\hat{X}_{\text{ge}}(\pi)$. A spectroscopy pulse can then be applied to determine the frequency α. Finally, we need to alter our readout scheme by either measuring the population of $|e\rangle$ at the end of the sequence or by applying another $\hat{X}_{\text{ge}}(\pi)$ pulse to transfer the remaining excited state population to ground state before reading out the ground state population. When the spectroscopy pulse is at the anharmonicity, the pulse will drive transitions between the $|e\rangle$ and the $|f\rangle$ state, thus the excited state population will decrease (Fig. 4.10B).

Similar to higher Fock states in the cavity, higher lying states in the qubit will have a reduced lifetime. For the n$^{\text{th}}$ excited state, the lifetime is $T_n = T_1/n$.

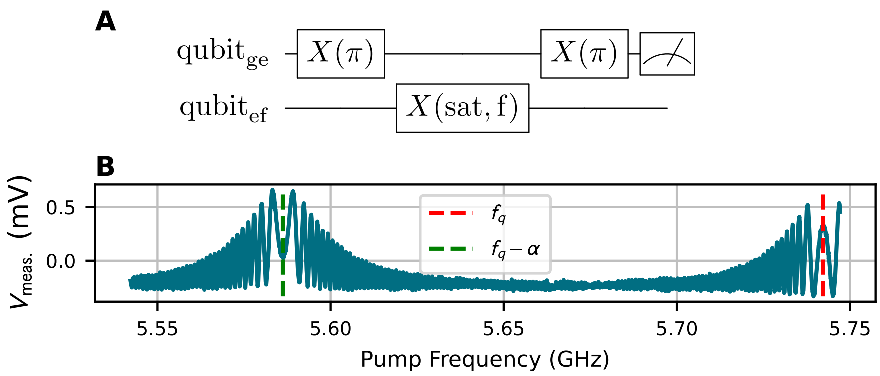

Figure 4.10: Measurement pulse sequence and results of identifying the anharmonicity of the transmon. (**A**) Pulse sequence to identify anharmonicity of the transmon. First, the qubit is placed in the $|e\rangle$ state with a π_{ge} pulse and a spectroscopy pulse is played. For readout, another π_{ge} pulse is played to determine if the qubit has left the $|e\rangle$ state due to the spectroscopy pulse. (**B**) Spectroscopy of the ef transition. Additional oscillations close to the transitions are due to off-resonant excitation of the respective transitions, this results in detuned Rabi oscillations.

4.2.5 Mode Temperatures

As mentioned in Sec. 3.7.1, due to the thermal noise coupling in via the control and measurement lines, the qubit and the cavity mode temperature will not reach the physical temperature of the base plate of the fridge. To characterise the mode temperature, we need to measure the mode population distribution. There are two methods to do so: selective Rabi oscillations [142] or spectroscopy. The measurement methods are appropriate for different regimes of mode temperature. But both can be used to determine either qubit or cavity mode temperature.

Qubit

For lower mode temperatures, we can determine the occupation of the excited state by using the $|f\rangle$ state. This is done by mapping the amplitude of Rabi oscillations between the $|e\rangle$ and $|f\rangle$ state to the populations of the ground and excited state [142]. The pulse sequence is shown in Fig. 4.11A. The measurement result is shown in Fig. 4.11B. The amplitude of the Rabi oscillations can then be used to calculate the mode temperature

$$\frac{A_{|e\rangle}}{A_{|g\rangle}} = e^{\frac{hf_q}{k_B T_q}}. \tag{4.4}$$

This equation assumes a thermal distribution with low temperature or a two-level approximation of the qubit meaning that there is no population in the $|f\rangle$.

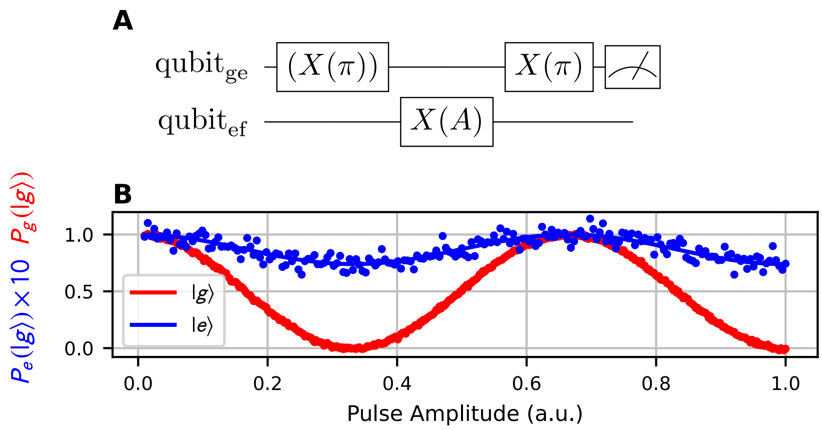

Figure 4.11: Qubit mode temperature measurement. (**A**) Pulse sequence of Rabi population measurement of the $|e\rangle$ or $|g\rangle$ state. First, the qubit is placed in the $|e\rangle$ state with a π_{ge} pulse and another Rabi pulse is played with varying amplitude. For readout, another π_{ge} pulse is played to determine if the qubit has left the $|e\rangle$ state due to the Rabi pulse. For the population measurement of $|g\rangle$, the experiment is repeated without the first π_{ge} pulse. (**B**) The amplitude of oscillations is proportional to the qubit population in each state. This measurement assumes that there is no population in the $|f\rangle$. For visibility, the amplitude of oscillation for the $|e\rangle$ (blue line) is enlarged by a factor of 10. Here the excited state population is 1.3%.

With good isolation, the qubit excited state population is 1% resulting in a qubit mode temperature of $60 - 80\,\mathrm{mK}$.

Cavity

For higher mode temperatures, qubit or cavity spectroscopy will reveal multiple peaks spaced by χ. The height of the peaks reflects the distribution of the excited state population (Fig. 4.12). However, this method is not as accurate for colder mode temperatures $n_q = \frac{A_{|e\rangle}}{A_{|g\rangle}+A_{|e\rangle}} \lessapprox 10\%$. This method is more suited for higher levels of the excited state population.

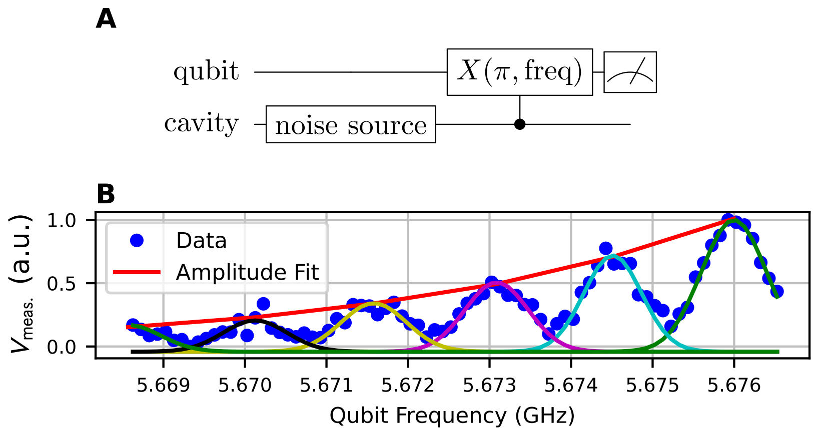

Figure 4.12: Qubit spectroscopy measurement and fit with a thermal population in the high Q cavity. (**A**) Pulse sequence of measuring with added thermal noise. First, a noise source is used to initialise the cavity to a larger thermal photon population ($n_{\text{th}} > 0.1$). Secondly, a cavity photon number selective qubit spectroscopy is performed. (**B**) Measurement result of qubit spectroscopy with cavity thermal population. The amplitude of peaks is proportional to the population in each cavity photon number. A global fit of the multiple Gaussian with peaks weighted to a common thermal photon distribution is performed. The individual Gaussians are plotted to check for fitting anomalies (colour lines), such as all Gaussians should have the same offset and the Gaussian linewidths should be limited by the pulse and not the loss given by $\gamma_{\text{q}}+n\kappa$, where γ_{q} is the decoherence rate of the qubit, n is the cavity Fock state number and κ is the loss rate of the cavity. For this measurement, $n_{\text{th}} \approx 2.4$, giving a mode temperature of $T_{\text{cavity}} = 645\,\text{mK}$.

The qubit peak distribution follows a super-Poissonion Eq. (2.17). In this distribution, the highest peak is always for $n = 0$. If the first qubit peak is lower, this points towards a leakage of a coherent signal into the cavity mode. The individual Gaussians lines are plotted to check for fitting anomalies, such as all Gaussians should have the same offset and the Gaussian linewidths should not be too different.

The mode temperature can be calculated via Eq. (3.31). The difference between this equation and Eq. (4.4), is due to the multi-level Hilbert space of the cavity.

4.2.6 SQUIDs

For SQUID measurements, at each flux point, the experiments above can be repeated. Big flux maps will require multiple recalibration of instruments or readout parameters. Fortunately, for certain parameters, we can play a few tricks to reduce the time taken to recalibrate.

For readout, low-power readout requires recalibration of the readout frequency. However, using high-power readout, the readout frequency is always at the bare resonator frequency, while the optimal readout power will change, we do not have to recalibrate the readout power as often.

For T_1 measurements, we can avoid calibrating π pulses at each flux point. We can use a fast microwave switch and a LO to saturate the qubit. There will be an equal mixed population of the $|g\rangle$ and $|e\rangle$ state. The resulting measurement will also have the same T_1 decay with half the readout contrast.

4.3 High Q Cavity

This section describes measurement methods to characterise the high Q cavity. Without a method of direct readout, we have to ask binary questions on the qubit to infer the cavity state. There are two main methods of measuring the cavity state, namely generalised Husimi-Q and parity measurement [24]. With these two techniques, we can quickly understand the concept of the other measurements in the frequency or time domain.

4.3.1 Inferring the state of the cavity

These methods work by reconstructing the cavity state via parity values at each phase space point β of the cavity. The full cavity state is reconstructed by doing a full map of $\hat{D}(\beta)$ to every phase space point.

In these measurements, the qubit and the cavity is assumed to be initialised in the ground state. Measurements with some excited state qubit population will have a reduced measurement contrast.

Generalised Husimi-Q Measurement

The first measurement technique is to do a selective $X_{\pi,n}$ pulse on the qubit conditioned on a specific cavity photon number. The pulse sequence is shown in Fig. 4.13A. The qubit state will then flip only if there are n photons in the cavity at the phase space point β. To eliminate the overall shift in readout value caused by the cross Kerr between the high Q cavity and readout resonator, we can repeat the measurement for no qubit pulse (Fig. 4.13B). The probability of reading the excited state is given by Eq. (2.20).

As plotted in Fig. 4.13C, we can use this technique to determine the displacement scaling factor A between an applied voltage β_V and the coherent state reached $\beta = \beta_V A$

$$P_n(\beta_V) \propto e^{-(\beta_V A)^2} \frac{(\beta_V A)^2}{n!}. \tag{4.5}$$

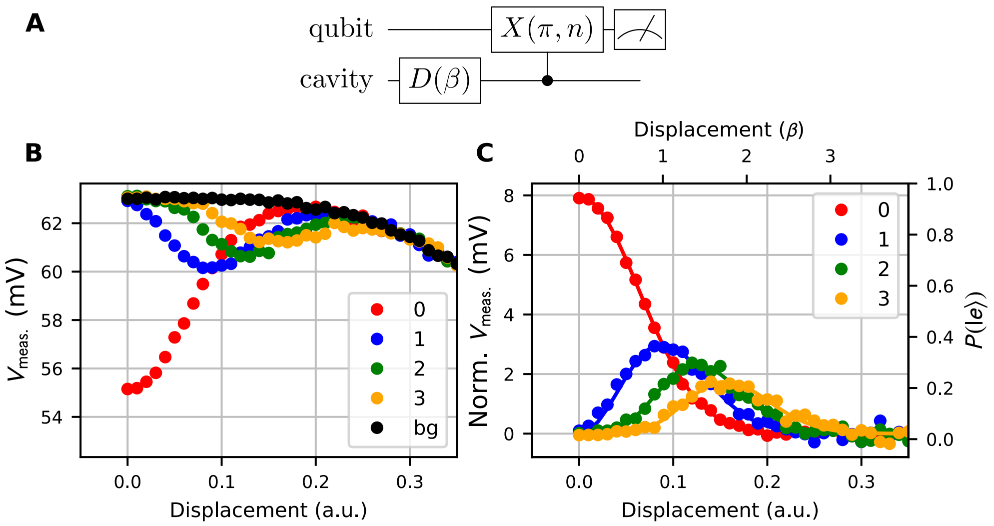

Figure 4.13: Generalised Husimi-Q measurements. (**A**) Pulse Sequence of the generalised Husimi-Q (**B**) Raw measurement data for the $n = 0, 1, 2, 3$ cavity Fock states and a background measurement (bg). The decrease in measured amplitude is due to the cross-Kerr between the high Q cavity and the readout resonator. The background measurement will take into account this cross-Kerr effect (**C**) Normalised and fitted data of the generalised Husimi-Q for the $n = 0, 1, 2, 3$ cavity Fock states [24].

For a small initial thermal state in the cavity, P_0 will not start from one and P_1 will not start from zero. Due to the distribution of Fock states present at zero displacement.

To reconstruct the Wigner map, we can just do two measurements where the qubit pulse is a frequency comb of the even or odd photon peaks. This is possible by using a DSH setup (Fig. 3.13D). The Wigner map can be reconstructed by doing $P_{\mathrm{even}} - P_{\mathrm{odd}}$ without the need for a background measurement.

Parity Measurement

The second measurement method is to map the parity of the cavity onto the qubit state [143, 144]. The pulse sequence is shown in Fig. 4.14A. An unconditional $\frac{\pi}{2}$ pulse rotates the qubit to the equator of the Bloch sphere. Due to the dispersive interaction, the Bloch vectors will evolve at different speeds given by $n\chi$. Thus, waiting a time of $T = \frac{\pi}{\chi}$, all the Bloch vectors for an even cavity photon number will have done a multiple of full rotations while the odd qubit vectors will have a half rotation. Another $\frac{\pi}{2}$ pulse will then map the parity of the state to the two different qubit states $|g\rangle$ or $|e\rangle$. The qubit evolution can be visualised in the Bloch sphere Fig. 4.14B.

As an example, for a cavity in initial state $|\alpha, g\rangle$, the evolution of the quantum state for the first 3 operations is as follows

$$\begin{aligned}
\hat{D}(\beta) :&e^{i\mathrm{Im}\{\beta\alpha^*\}} |\beta + \alpha, g\rangle \\
\hat{Y}\left(\frac{\pi}{2}\right) :&\frac{1}{\sqrt{2}} e^{i\mathrm{Im}\{\beta\alpha^*\}} |\beta + \alpha\rangle \otimes (|g\rangle + |e\rangle) = \\
&\frac{1}{\sqrt{2}} e^{i\mathrm{Im}\{\beta\alpha^*\}} e^{-\frac{|\beta+\alpha|^2}{2}} \sum_n \frac{(\beta+\alpha)^n}{\sqrt{n!}} |n\rangle \otimes (|g\rangle + |e\rangle) \\
\hat{T}\left(\frac{\pi}{\chi}\right) :&\frac{1}{\sqrt{2}} e^{i\mathrm{Im}\{\beta\alpha^*\}} e^{-\frac{|\beta+\alpha|^2}{2}} \sum_n \frac{(\beta+\alpha)^n}{\sqrt{n!}} e^{-in^2\frac{K}{2}t} |n\rangle \otimes \left(|g\rangle + e^{i\left(n\chi - n^2\chi'\right)t} |e\rangle\right) = \\
&\frac{1}{\sqrt{2}} e^{i\mathrm{Im}\{\beta\alpha^*\}} e^{-\frac{|\beta+\alpha|^2}{2}} \sum_n \frac{(\beta+\alpha)^n}{\sqrt{n!}} e^{-in^2\frac{K}{2}\frac{\pi}{\chi}} |n\rangle \otimes \left(|g\rangle + e^{i\left(n\pi - n^2\frac{\chi'}{\chi}\right)} |e\rangle\right).
\end{aligned} \tag{4.6}$$

Neglecting phase error factors $n^2\frac{\chi'}{\chi}$, separating the case for even or odd photons, $e^{i\pi n_{\text{even, odd}}} = \pm 1$, gives $|\psi\rangle \propto |n_{\text{even}}\rangle \otimes (|g\rangle + |e\rangle) + |n_{\text{odd}}\rangle \otimes (|g\rangle - |e\rangle)$. The final $\hat{Y}\left(\frac{\pi}{2}\right)$ gives

$$\hat{Y}\left(\frac{\pi}{2}\right) : \propto |n_{\text{even}}, e\rangle + |n_{\text{odd}}, g\rangle . \tag{4.7}$$

Thus, an even parity will result in the qubit in the excited state, while an odd parity will result in the qubit in the ground state. The background measurement is done by inversing the mapping of the cavity parity to the qubit state with a $-\frac{\pi}{2}$ amplitude for the second pulse. The raw measurements are shown in Fig. 4.14C. The background measurement removes the global coefficients and some higher order Hamiltonian terms.

Similar to the Generalised Husimi-Q calibration method, we can also use this measurement technique to calibrate our displacement pulses (Fig. 4.14D)

$$P(\beta) = \sum_n P_n(\beta) \langle n|\hat{\Pi}|n\rangle = \sum_n \left(e^{-|\beta|^2} \frac{|\beta|^{2n}}{n!} (-1)^n\right) = e^{-2|\beta|^2}. \tag{4.8}$$

However, this calibration method also assumes that the initial state of the cavity is in the ground state, a thermal state in the cavity will result in a larger standard deviation.

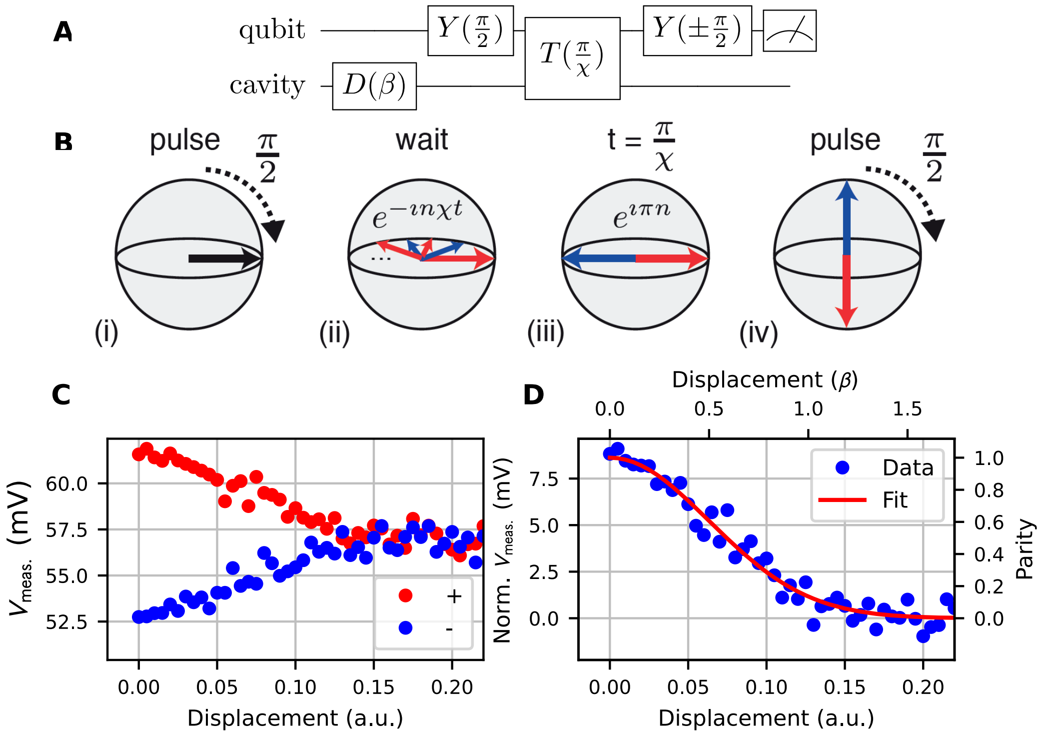

Figure 4.14: Parity measurement. (**A**) Pulse Sequence of a parity measurement. (**B**) Bloch sphere representation of the evolution of the qubit. Figure taken from [60]. (**C** and **D**) Raw and fitted data of displacement for the two mappings of the qubit to cavity state. This measurement reveals the parity of the ground state with β. Thus, by fitting the result to a Gaussian, the scaling of the standard deviation of the ground state will give the scaling of the displacement pulses [144].

Due to the higher order interaction terms, a phase error $e^{i\phi} = e^{-in^2\frac{\chi'}{\chi}}$ which results in the imperfect mapping of the parity to the ground and excited state. On the Bloch sphere, this results in the spreading of the blue and red vectors along the equator in Fig. 4.14B(iii). After the last $\frac{\pi}{2}$ pulse, the parity is not perfectly mapped into the $|g\rangle$ and $|e\rangle$ states. This error can be minimised by changing the delay between the pulses Fig. 4.19 or the phase of the second $\hat{Y}(\frac{\pi}{2})$ pulse to account for the spread of Bloch vectors. This effect also results in a reduced readout contrast for different cavity state populations.

Finally, another imperfection present is due to the non-zero cross-Kerr between the high Q cavity and the readout resonator. This means that the readout resonator will shift in frequency and thus readout contrast will be different for different cavity photon states. Measuring further out in the phase space of the cavity would mean a larger cross-Kerr shift of the readout resonator. For a system with cross-Kerr between the high Q cavity and readout resonator, a parity measurement via the qubit state will have different readout contrasts at different phase space points of the cavity qubit system.

The difference in readout contrast can be accounted for in two ways. Measurements of Fock states or displaced coherent states can be used to determine the maximum readout contrast at different phase space points. Alternatively, the Wigner measurement results can be scaled by preparing the desired quantum state and then measuring the maximum readout contrast at every phase space point. This is done by two additional measurement maps and altering the parity measurement to $\hat{D}(\beta)\hat{Y}(\pi)$ and $\hat{D}(\beta)\hat{Y}(0)$ instead. The difference between these two background maps gives the maximum readout contrast for each phase space point and can be used to scale the parity measurement maps.

4.3.2 Frequency Domain Measurements

Cavity Spectroscopy

The high Q cavity frequency can be determined by High Q cavity spectroscopy. This is done by first applying a saturation pulse on the cavity, a π pulse selective on the cavity ground state is applied to the qubit (Fig. 4.15A). The qubit will not flip when the saturation pulse is resonant with the high Q cavity frequency. By reducing the power of the saturation pulse, we can reduce the observed linewidth and allow us to measure small features such as the anharmonicity of the cavity $\frac{K}{2}$ (Fig. 4.15B and C).

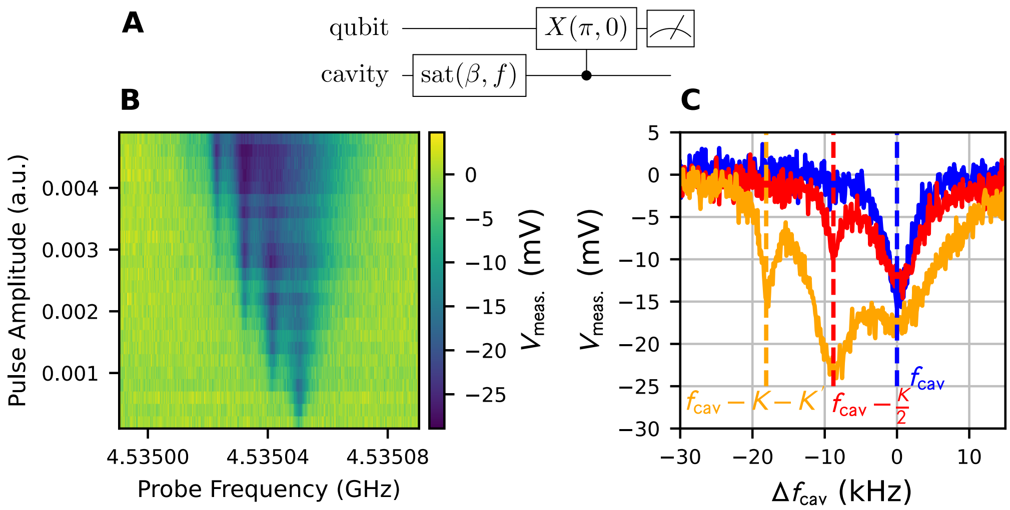

Figure 4.15: High Q cavity spectroscopy. (**A**) Pulse Sequence of a high Q cavity spectroscopy measurement. When the spectroscopy pulse is resonant with a cavity transition, the cavity is driven to some higher excited state. The selective qubit pulse, conditioned on the vacuum state of the cavity, will not be able to flip the qubit to the excited state. (**B**) Measurement map and (**C**) linecuts for different amplitudes of saturation pulse. For long saturation times and low enough powers, the linewidth of the cavity is not power broadened and small enough to see a single transition where the qubit could not be flipped to the excited state. As the power is slowly increased, we can see higher-order transitions such as the two-photon $|0\rangle$ to $|2\rangle$ or three-photon $|0\rangle$ to $|3\rangle$. Here, $\frac{K}{2}/2\pi = 8.8\,\text{kHz}$ and $K'/2\pi = 0.5\,\text{kHz}$.

Qubit Number Split Spectroscopy

The dispersive interaction between the qubit and high Q cavity can be determined by first displacing the high Q cavity and then doing a qubit spectroscopy. This is similar to doing generalised Husimi Q measurements without knowing the correct frequency spacing χ. The measurement pulse sequence, map, linecut and fit is shown in Fig. 4.16.

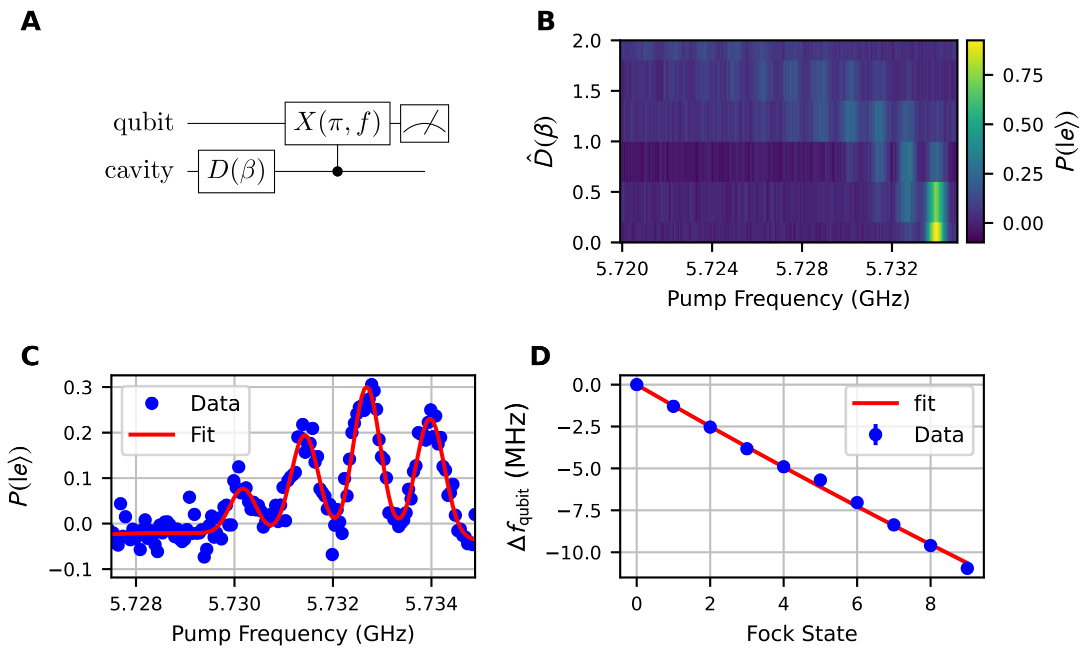

Figure 4.16: Qubit number split spectroscopy with a displaced cavity. (**A**) Pulse Sequence of the measurement. First, the cavity is displaced to some coherent state $|\beta\rangle$. A long, spectrally narrow, number selective qubit pulse is applied. The qubit state is then readout. (**B**) Measurement map with sweeping amplitude of the displacement pulse. (**C**) Single linecut data that is fitted to a multiple Gaussian with heights weighted by a cavity coherent state photon number distribution. The height of the peaks is fitted to follow the photon number distribution of a coherent state in Eq. (4.5). Here, the fit gives a coherent state $|\alpha = 1.2\rangle$. (**D**) The fit of number-split qubit frequency peaks to obtain the dispersive shift between the qubit and cavity χ and the higher order dispersive shift χ'. Here, $\chi/2\pi = 1.257\,\text{MHz}$ and $\chi'/2\pi = 19\,\text{kHz}$.

As a general rule of thumb, when the height of the n^{th} and $(n+1)^{th}$ peak is the same, the amplitude of the coherent state is approximately $|\alpha = n\rangle$. The height of the qubit peaks can be fitted and follow the photon number distribution of a coherent state in Eq. (4.5). This is another method of calibrating the displacement scaling between the pulse amplitude applied and the coherent state achieved.

Cavity-Readout Resonator Cross-Kerr

The cross-Kerr between the high Q cavity and readout resonator can be similarly determined by sweeping the readout resonator frequency. A displacement pulse is applied on the high Q cavity and a low-power readout resonator spectroscopy is done (Fig. 4.17A). By using the calibration of the displacement pulse, we relate the mean cavity photon number to the frequency shift of the readout resonator (Fig. 4.17B).

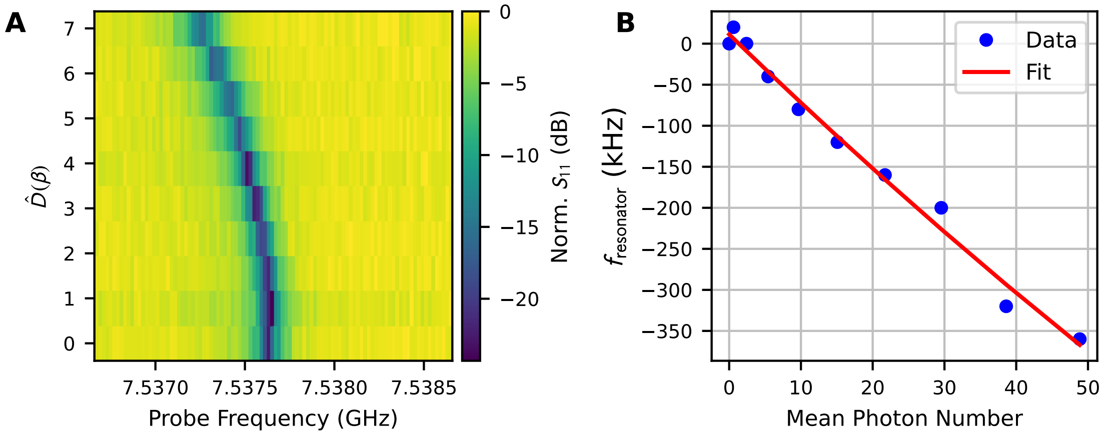

Figure 4.17: Cross-Kerr measurement between high Q cavity and readout resonator. (**A**) Measurement map data with a sweep in the displacement pulse amplitude. At each displacement amplitude, we can fit the readout resonator frequency to obtain (**B**) the extracted detuning with cavity photon number. The cross-Kerr between the high Q cavity and readout resonator can be extracted, here $\chi_{cr}/2\pi = 8.5\,\text{kHz}$.

4.3.3 Time Domain Measurements

Frequency domain measurements require small frequency steps over a large frequency range to accurately determine the Hamiltonian coefficients. For example, to measure the higher order χ', we need to measure changes of $\chi/2\pi \approx 1\text{MHz}$ to an accuracy of $\approx 1\text{kHz}$. Such measurements can be very time-intensive. Time domain techniques provide a faster method to measure such small corrections.

Cavity Revivals

Cavity revival measurements are a useful technique to determine the small higher-order terms. The pulse sequence, phase space evolution, measurement map, linecut data and global fit is shown in Fig. 4.18.

Firstly, the cavity is displaced, $\hat{D}(\beta)$ and allowed to evolve for a time $\hat{T}(t)$. Coherent states will evolve in phase space with a frequency of the cavity. To second order, this is $\omega_{\text{cav}} = \omega_{\text{cav},0} - n\frac{K}{2} - n^2\frac{K'}{6}$, where n is the mean number of photons of the coherent state. The coherent state has gained some phase $\beta(t) = \beta e^{-i\tilde{\omega}t}$. Subsequently, a second displacement with a phase difference is applied $\hat{D}(-\beta e^{i\phi})$. If the phase evolution of the coherent state matches the phase difference of the two pulses, the cavity is brought back to the ground state.

Written explicitly, the evolution of the cavity is as follows

$$\hat{D}(\beta) : |\beta\rangle \tag{4.9}$$

$$\hat{T}(t) : |\beta(t)\rangle = |\beta e^{i\tilde{\omega}t}\rangle \tag{4.10}$$

$$\hat{D}(-\beta e^{i\phi}) : \propto |\beta\left(e^{i\tilde{\omega}t} - e^{i\phi}\right)\rangle \tag{4.11}$$

Finally, a cavity ground state selective $\hat{X}(\pi, n = 0)$ pulse was applied to the qubit. The qubit state will only flip if the final state of the cavity is in the ground state. The evolution and revivals of the cavity state are governed by the cavity frequency detuning from the lab frame. The phase difference as a function of the delay time is similar to the qubit T_2 Ramsey measurements. Similarly, we can detune the cavity drive to obtain a measurement map similar to Fig. 4.9A.

The probability of finding the qubit in the ground state after the second pulse is given by

$$\begin{aligned} P_0(\beta, t) &= |\langle 0|\alpha_{\text{final}}\rangle|^2 = \left|\langle 0|\hat{D}(-\beta e^{i\phi})|\beta(t)\rangle\right|^2 \\ &= \left|\langle \beta e^{i\phi}|\beta(t)\rangle\right|^2 \\ &= e^{-|\beta e^{-i\tilde{\omega}t} - \beta e^{i\phi}|^2} = e^{-|\beta|^2(e^{i\omega t} + e^{i\phi})} \\ &= e^{-2|\beta|^2\left[1 - \cos\left(\Delta + |\beta|^2\left(\frac{K}{2} + \frac{K'}{6}\right)\right)t\right]} \end{aligned} \tag{4.12}$$

where Δ is the detuning between the induced detuning and the cavity frequency. By repeating the experiment with varying amplitudes of the displacement pulse, we can fit the frequency of revivals to obtain the higher-order parameters K and K'.

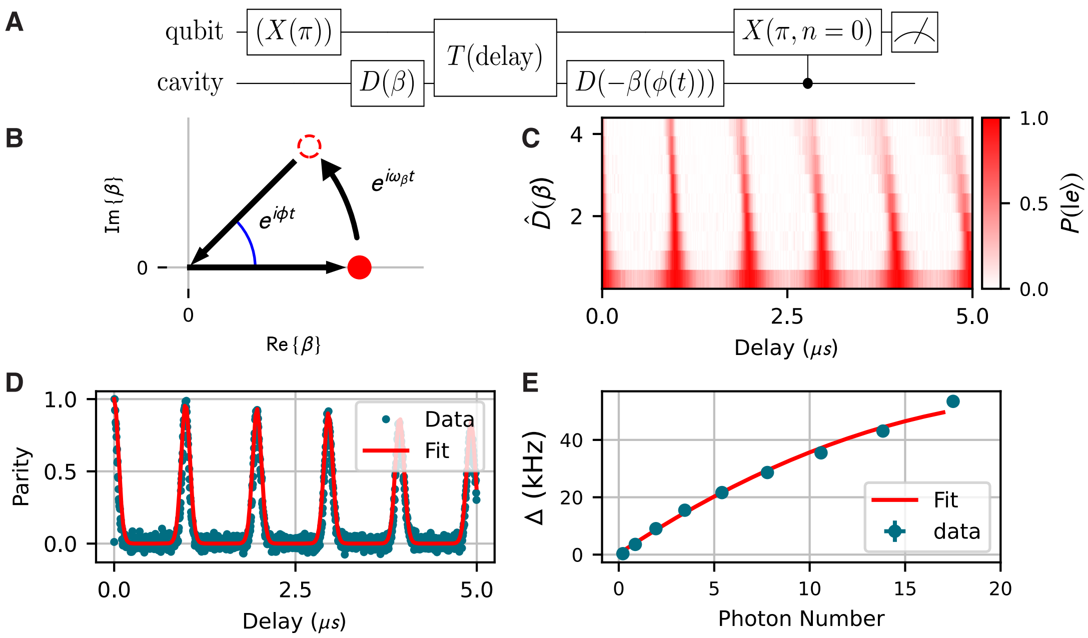

Figure 4.18: Cavity revivals measurement. (**A**) Pulse Sequence of a cavity revival sequence. Qubit is initialised in the ground or excited state. The cavity is then displaced and allowed to evolve. Artificial phase oscillations in the return displacement pulse allow for faster acquisition of cavity revivals. (**B**) Phase Space and (**C**) measurement map of the experiment. (**D**) Linecut and fit to Eq. (4.12) for a single displacement amplitude. Here, $\beta = 1.8$. (**E**) Doing the same for all linecuts and extracting the fit parameters for the entire map allows us to evaluate the cavity drive and frequency detuning, the Kerr coefficient $K/2\pi = 8.7\,\text{kHz}$ and higher order Kerr coefficient $K'/2\pi = 550\,\text{Hz}$. The measurement can be repeated for the qubit in the excited state to extract all values of the Hamiltonian.

This measurement is limited to $(n\frac{K}{2} + n^2\frac{K'}{6})t \lessapprox \frac{\pi}{2}$. To first order, the Kerr effect only causes a frequency detuning of the coherent state. However, at larger displacements or longer times, the coherent state also starts to smear out due to the Kerr effect. This is because the phase difference between Fock states grows as $n^2\frac{K}{2}t$. The collapse of the coherent state has a time scale $T_{\text{collapse}} \approx \frac{\pi}{2(n\frac{K}{2}+n^2\frac{K'}{6})}$.

Higher-Order Terms To accurately characterise the Hamiltonian of our system, we can extend the cavity revival measurement method for other initial states of the qubit. By placing the qubit in the excited state, the cavity frequency is now $\omega_{\text{cav}} - \chi$. Similarly, with increasing displacement powers, the cavity frequency will scale as $n\chi - n^2\chi'$.

For larger qubit systems, the experiment can be repeated with different combinations of excited qubit states to determine factors such as $\chi_{q_1 q_2 c}$. The measured values for an experiment consisting of two qubits and one high Q cavity system are shown in Table 3.1.

Parity Revivals

Parity revival measurements determine the time an excited state qubit takes to do a full evolution in phase space. This measurement is used to determine the correct time for the parity measurement method in Sec. 4.3.1. Figure 4.19 illustrates the pulse sequence, measurement results, linecuts and fits.

The cavity is displaced $\hat{D}(\alpha)$ and a $\hat{Y}\left(\frac{\pi}{2}\right)$ is played on the qubit. The system is allowed to evolve. One will see the difference in evolution speed as $\chi + n\chi'$. A second $\hat{Y}\left(\pm\frac{\pi}{2}\right)$ before the state of the qubit is read out (Fig. 4.19A). The order of pulses is chosen such that these measurement results can help account for any possible instrument delay when playing this particular sequence. The final state of the system is

$$|\psi\rangle_{\pm} = \frac{1}{2}\left[\left(|\alpha\rangle \mp |\alpha e^{-i\chi t}\rangle\right) \otimes |g\rangle + \left(\pm|\alpha\rangle + |\alpha e^{-i\chi t}\rangle\right) \otimes |e\rangle\right]. \tag{4.13}$$

Thus, we can determine the probability of measuring the qubit in the excited state

$$P_{\pm}(e) = \langle\psi\,|e\rangle\,\langle e|\,\psi\rangle = \frac{1}{4}\left(2 \pm \langle\alpha|\alpha e^{-i\chi t}\rangle \pm \langle\alpha|\alpha e^{-i\chi t}\rangle^{*}\right) \tag{4.14}$$

$$= \frac{1}{2}\left(1 \pm e^{|\alpha|^2(\cos\chi t - 1)}\cos\left(|\alpha|^2 \sin\chi t\right)\right). \tag{4.15}$$

Finally, including the background measurement where the mapping of the cavity parity to qubit state is reversed. We can derive the equation of the measured voltage

$$V_{\mathrm{measurement}} \propto P_{+}(e) - P_{-}(e) = e^{|\alpha|^2(\cos\chi t - 1)}\cos\left(|\alpha|^2 \sin\chi t\right). \tag{4.16}$$

Similar to the cavity revivals, the measurement is limited to the linear phase difference between Fock states and thus the experiment is accurate to $(n^2\chi')t \lessapprox \frac{\pi}{2}$.

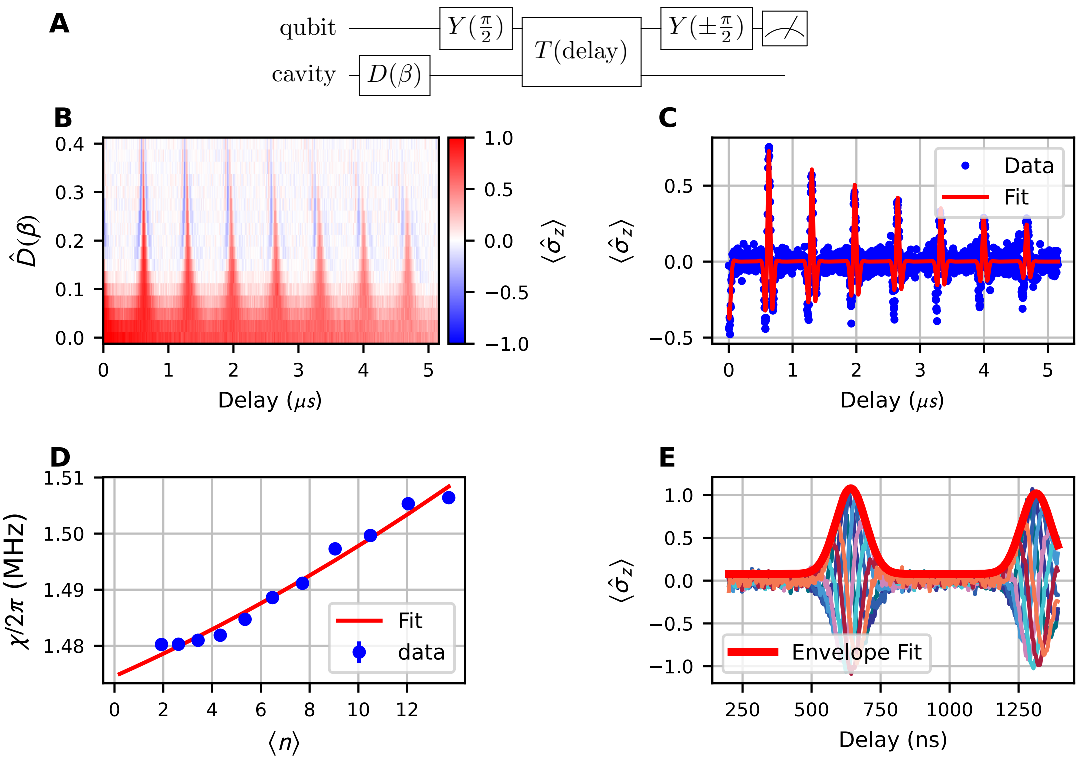

Figure 4.19: Parity revival measurement. (**A**) Pulse Sequence of a parity revival measurement. The cavity is first displaced and the qubit is placed in a superposition of $|g\rangle$ and $|e\rangle$ state on the equator of the Bloch sphere. After a delay time, another $\frac{\pi}{2}$ pulse is applied on the qubit and the qubit state is measured. The order of pulses is used to determine the hardware lag time. Measurement is repeated for a $-\frac{\pi}{2}$ amplitude for the pulse to reverse the mapping between the qubit state and the cavity parity. (**B**) Measurement map sweeping the revival time and displacement amplitude. (**C**) Linecut for a displacement amplitude, $\beta = 2.3$. Eq. (4.16) is used to fit the data and obtain appropriate parity revival time. (**D**) Fitting all the data and extracting revival time for the various displacements give $\chi/2\pi = 1.47\,\text{MHz}$ and $\chi'/2\pi = 2.8\,\text{kHz}$. (**E**) It might be difficult to fit the fast oscillations within each revival cycle. An alternative method to properly obtain the revival time for a specific cavity displacement is to sweep the phase of the second pulse. This results in a different fast phase oscillation within each cycle and the overall envelope can be used to determine the proper revival time. While this method uses more time, it is easier to fit the overall envelope.

It might be difficult to fit the fast oscillations within each revival cycle (narrow features in Fig. 4.19B). Another method to circumvent the difficulty in fitting is to sweep the phase of the second pulse. This measurement requires more time and is only done for a specific displacement pulse and is shown in Fig. 4.19E. This results in a different phase of the fast oscillations within each cycle and the overall envelope can be used to determine the proper revival time. While this method uses more time, it is easier to fit the overall envelope and can more accurately determine any lags due to hardware implementation of the pulses.

High Q Cavity Lifetime

For a high Q cavity lifetime, a displacement pulse is applied on the cavity with a variable delay time after (Fig. 4.20A). The cavity state is probed by doing generalised Husimi Q measurements. The coherent state can be seen decaying through the different Fock states (Fig. 4.20B and C). The probability of the qubit to be in the excited state is

$$P_n(e) = |\langle n|\alpha(t)\rangle|^2 = e^{-|\alpha^2 e^{-\kappa t}|}\frac{(\alpha e^{-\frac{\kappa}{2}t})^{2n}}{n!}. \tag{4.17}$$

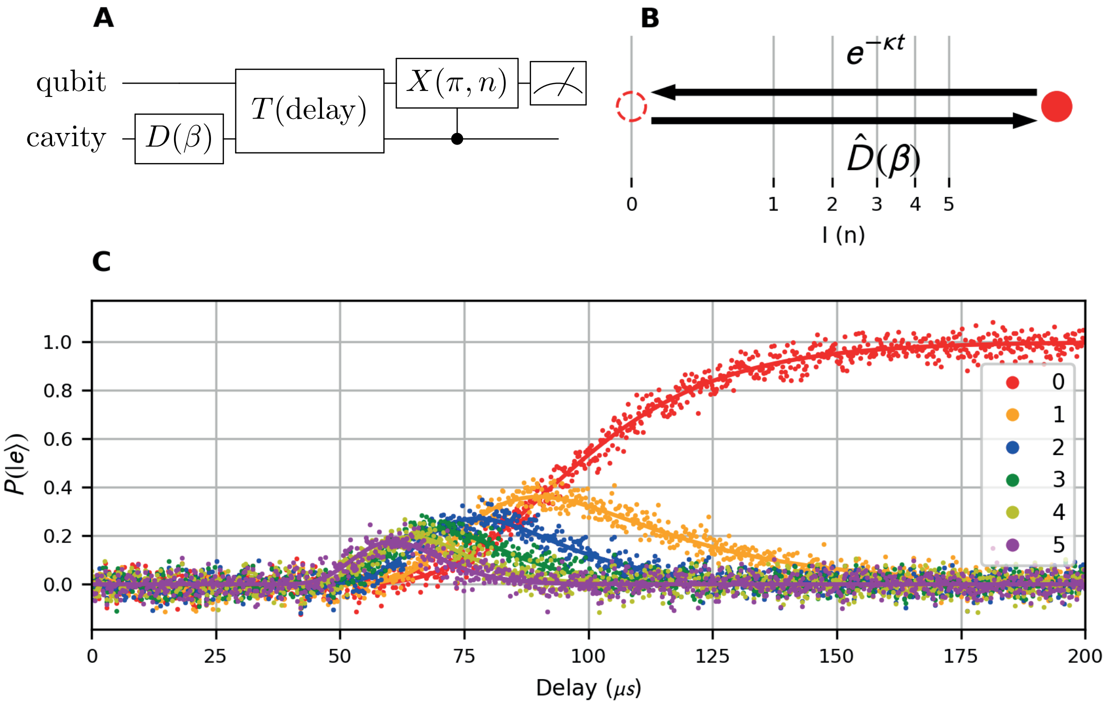

Figure 4.20: High Q cavity T_1 measurement. (**A**) Pulse Sequence of a high Q cavity T_1 measurement. The cavity is first displaced. After a delay time, a generalised Husimi-Q_n measurement is made. (**B**) Phase space evolution of the cavity. First, the cavity is displaced out $\hat{D}(\beta)$ to some coherent state $|\beta\rangle$. As the cavity decays at a rate of $e^{-\kappa t}$, the cavity will decay through the different Fock states which are denoted by n in the phase space of the cavity. $n = \sqrt{\beta}$. (**C**) Linecut and fit to Eq. (4.17) of the high Q cavity decay for each generalised Husimi-Q_n measurement up to $n = 5$, denoted by the different colours. We see the cavity state decaying and changing its Fock state distribution with time. Here, $T_{1,\mathrm{cav}} = (120 \pm 2)\,\mu$s.

4.4 Fock State Creation

Thus far, we have only worked with coherent states. Optimal control methods aside, we can also deterministically form a single Fock state in the cavity, $|1\rangle$. The first method is with Selective Number-dependent Arbitary Phase (SNAP) gates [145]. The second method is via driving the blue sideband transitions.

Such states are useful as another measurement of the cavity decay rate and can also serve as a good calibration of the Wigner tomography scaling and normalisation. These methods can also be extended to larger Fock states or more complicated superposition. Figure 4.21 are plots of a single Fock state $|1\rangle$ Wigner map and marginal distributions.

The Wigner functions can be calibrated by a Wigner measurement of single photon Fock state. The radius of the Fock state in phase space allows for the scaling of the displacement factors used in the experiment while the measurement of the central parity allows to calibrate of the Wigner measurement values.

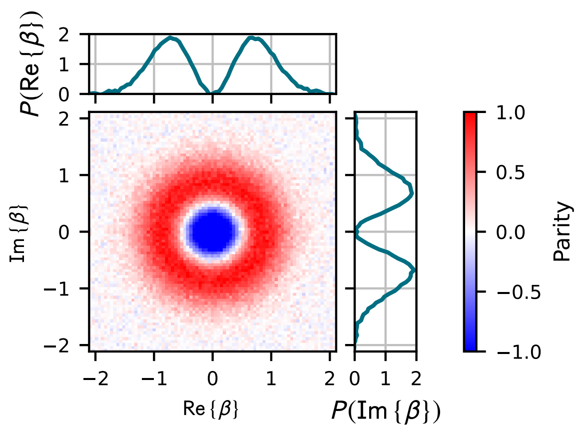

Figure 4.21: Wigner map and marginal distributions of single Fock state $|1\rangle$. The value at $W(0,0)$ reveals the parity of the state. The single Fock state data can also be used to fit the measured $W(\beta)$ values and the displacement scaling $\beta \propto \beta_V$ used in the experiment.

SNAP Gates SNAP gates work by imparting a geometric phase on some Fock states of the system [24, 60, 145]. The pulse sequence is $\hat{D}(\alpha_1) - \hat{X}(2\pi, n) - \hat{D}(\alpha_2)$. The resulting interference between all the Fock states will result in a non-trivial result that is usually numerically solved with QuTiP [146].

With SNAP gate parameters: $\alpha_1 = 1.14, n = 0, \alpha_2 = -0.56$, the resulting quantum state is $|1, g\rangle$ with a 98% preparation fidelity. To form a state with $|\psi\rangle = \frac{1}{\sqrt{2}}(|0\rangle + |1\rangle)$, we can use $\alpha_1 = 0.56, n = 0, \alpha_2 = -0.26$.

Typically, this set of pulses is limited to the time taken for a selective 2π pulse, $\sigma_f \lessapprox \chi$. Furthermore, the resulting state is sensitive to the displacement scaling factor errors.

Blue Sideband Pulses We can also form single Fock states by using the blue sideband pulses (Fig. 4.22A). This technique is similar to resolved sideband cooling techniques used in ion traps [147] or atomic arrays [148].

Driving the 2 photon transition at freqeuncy $f_{\text{bsb}} = \frac{1}{2}(f_{\text{qb}} + f_{\text{cav}})$, the quantum state will Rabi flop between $|0, g\rangle$ and $|1, e\rangle$ (Fig. 4.22B and C).

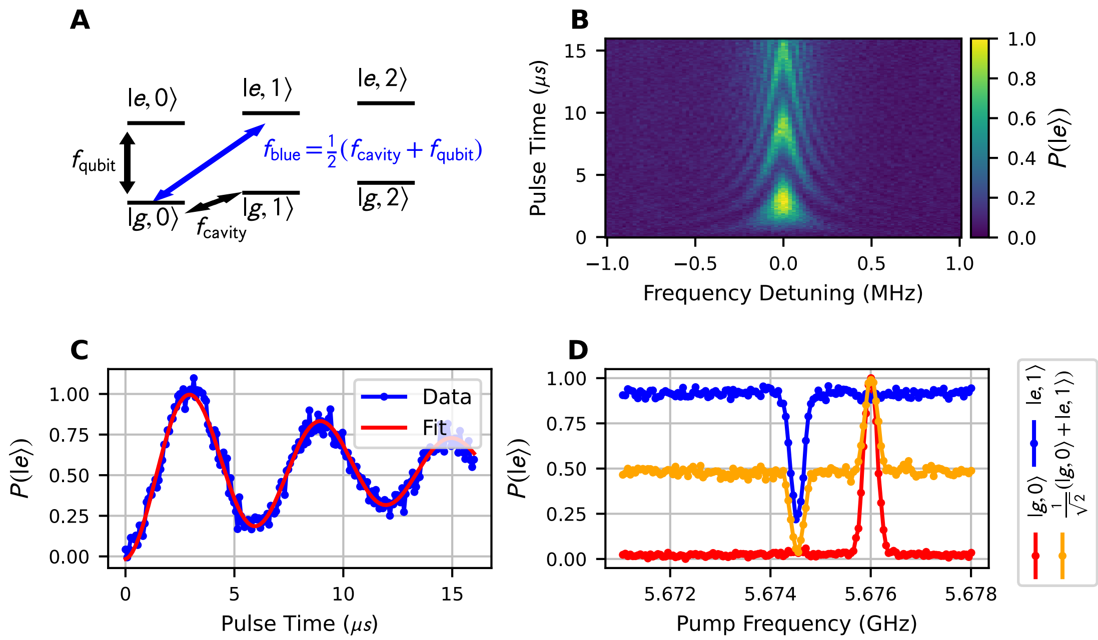

Figure 4.22: Blue sideband pulses to form Fock states in a cavity. (**A**) Energy levels of a qubit system coupled to a harmonic oscillator. The blue sideband pulse is a two-photon transition between the $|0, g\rangle$ and the $|1, e\rangle$ state. (**B**) Map of time Rabi measurements with detuning centred at the $\frac{1}{2}(f_{\text{qb}} + f_{\text{cav}})$ frequency. (**C**) Linecut and fit on resonance of the transition. The reduction in oscillation amplitude with increasing pulse length is due to an AC Stark shift of the cavity-qubit system. (**D**) Qubit spectroscopy of three different states, $|g, 0\rangle$, $|e, 1\rangle$ and $\frac{1}{\sqrt{2}}(|g, 0\rangle + |e, 1\rangle)$. Additional selective qubit pulses can be played to disentangle the qubit and cavity.

As the qubit is also Rabi flopping between $|g\rangle$ and $|e\rangle$, we can still do a usual readout of the qubit to determine the correct Rabi amplitude. However, at the end of the cavity "π" pulse, the final state is $|e, 1\rangle$ or for the case of negligible qubit preparation errors, a global $\hat{X}(\pi)$ pulse. Thus, we need to reset the qubit with a selective $\hat{X}(\pi, n = 1)$. Furthermore, this blue sideband transition requires another mixing setup to play at the correct frequency $\omega_{\text{drive}} = \frac{1}{2}(\omega_{\text{cav}} - \omega_{\text{qb}})$. With this technique, we can form the single-photon Fock state and superpositions with the cavity ground state (Fig. 4.22D).

CHAPTER 5

Cat States

The Schrödinger thought experiment and Schrödinger cat state are used to highlight the seemingly counterintuitive situation that challenges our classical intuition [1]. Until observation, the cat exists in a superposition of being both alive and dead simultaneously. The paradigmatic example of the Schrödinger cat state is the superposition of two coherent states in a bosonic mode. Such superposition states are a resource for quantum experiments and can be used in quantum error correction protocols [36] or quantum metrology [149–151]. The interference fringes in the cat state are often used as a goal to prove the generation of a quantum state in an experiment [152, 153].

In this chapter, I outline the different methods to form such Schrödinger cat states. Using the cQED toolbox, these methods realise non-unitary operations on the cavity state via unitary operations on the whole qubit-cavity system. The detailed analysis of the different protocols was done in collaboration with Thomas Agrenius from Prof. Oriol Romero-Isart group and is described in [131]. Here, I provide the gist of the protocols in an idealised setting. Section 5.3 deals with the imperfections arising from using the cQED platform with higher order terms in the Hamiltonian. Finally, in the last section, we demonstrate a closed-loop optimisation of the formation of a cat state. This work was done in collaboration with Vasilisa Usova from the Kirchmair group, Dr. Phila Rembold (now with Prof. Marcus Huber) and Marco Rossignolo from the group of Prof. Simone Montangero.

5.1 qcmap cat

The qcmap protocol is a method of deterministically forming cat states in the bosonic mode [4]. It utilises the dispersive qubit-cavity interaction $\chi\hat{c}^\dagger\hat{c}\hat{q}^\dagger\hat{q}$ to impart a qubit-state-dependent frequency shift on the cavity. The full pulse sequence is illustrated in Fig. 5.1A. The qubit is placed in a superposition with a controllable phase ϕ. After a displacement pulse on the cavity, the dispersive interaction entangles the qubit and cavity to the form $|\psi(t)\rangle = \frac{1}{\sqrt{2}}\left(|\alpha, g\rangle + e^{i\phi}\,|\alpha e^{i\chi t}, e\rangle\right)$ (Fig. 5.1B). This effectively implements a qubit-state-dependent displacement on the cavity. After an evolution time of $\hat{T}\left(\frac{\pi}{\chi}\right)$, the entangled qubit-cavity state is a Schrödinger cat state where the qubit state is entangled to a cavity displacement in phase space Eq. (5.5).

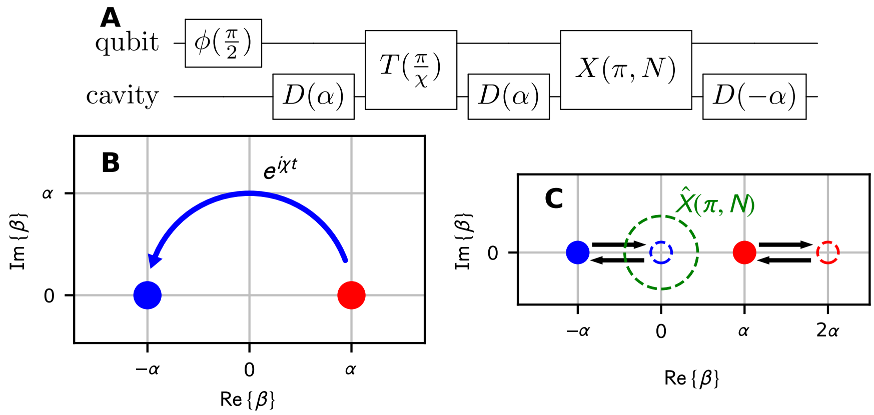

Figure 5.1: qcmap generation sequence. (**A**) Pulse sequence for generating cat states with the qcmap protocol. The phase of the first $\pi/2$ pulse determines the phase of the cat state at the end of the protocol. (**B** and **C**) Phase space representation of the qcmap pulse generation sequence. Red and blue colours represent the qubit in the ground and the excited state respectively. In **B**, the state of the qubit and cavity become entangled as only the $|\alpha, e\rangle$ will gain a phase $e^{i\chi t}$ in α with time. In **C**, the qubit is disentangled by displacing the $|-\alpha, e\rangle$ branch to the ground state and applying a selective π pulse (that only affects qubit frequencies in the green dashed circle). Finally, the cat state is brought back to $|-\alpha\rangle + |\alpha\rangle$.

We can form a cat state by disentangling the qubit from the cavity (Fig. 5.1C). First, we displace the cavity by $\hat{D}(\alpha)$. The $|g\rangle$ and $|e\rangle$ branch of the entangled state are separated in frequency due to the dispersive interaction and the cavity state in each branch ($|e, 0\rangle$ and $|g, 2\alpha\rangle$). By choosing a long disentanglement pulse, the spectral width of the disentanglement pulse is reduced, $\sigma_\mathrm{f} < \chi$, and the operation is selective on the cavity ground state. Effectively, this is choosing a maximum Fock state N that a $\hat{X}(\pi, N)$ is applied to the qubit state. The maximum Fock state N corresponds to choosing a radius in phase space of the cavity for which the qubit states are flipped (green dashed circle). Ideally, the selective pulse can be written as

$$\hat{X}(\pi, N) = \hat{X}(\pi) \otimes \sum_{n=0}^{N} |n\rangle \langle n| + \hat{\mathbb{I}} \otimes \sum_{n=N+1}^{\infty} |n\rangle \langle n| \,. \tag{5.1}$$

Finally, a displacement pulse $\hat{D}(-\alpha)$ is applied to centre the cat state about the cavity ground state.

The final state is a superposition of coherent states in the high Q cavity where the qubit is disentangled. Explicitly written, the evolution of the quantum system is as follows

$$\begin{aligned}
\hat{\phi}\left(\frac{\pi}{2}\right) :& \frac{1}{\sqrt{2}} |0\rangle \otimes \Big(|g\rangle + e^{i\phi} |e\rangle\Big) && (5.2)\\
\hat{D}(\alpha) :& \frac{1}{\sqrt{2}} |\alpha\rangle \otimes \Big(|g\rangle + e^{i\phi} |e\rangle\Big) && (5.3)\\
\hat{T}\left(\frac{\pi}{\chi}\right) :& \frac{1}{\sqrt{2}} \Big(|\alpha, g\rangle + e^{i\phi} |\alpha e^{i\chi t}, e\rangle\Big) && (5.4)\\
=& \frac{1}{\sqrt{2}} \Big(|\alpha, g\rangle + e^{i\phi} |-\alpha, e\rangle\Big) && (5.5)\\
\hat{D}(\alpha) :& \frac{1}{\sqrt{2}} \Big(|2\alpha, g\rangle + e^{i\phi} |0, e\rangle\Big) && (5.6)\\
\hat{X}(\pi, n < N_{\mathrm{max}}) :& \frac{1}{\sqrt{2}} \Big(|2\alpha, g\rangle + e^{i\phi} |0, g\rangle\Big) && (5.7)\\
\hat{D}(-\alpha) :& \frac{1}{\sqrt{2}} \Big(|\alpha, g\rangle + e^{i\phi} |-\alpha, g\rangle\Big) \,. && (5.8)
\end{aligned}$$

The idealised qcmap protocol can be written as the operator

$$\hat{S}_{\mathrm{qcmap}} \equiv \frac{1}{\sqrt{2}} \Big(1 - e^{i\phi}\hat{\Pi}\Big) \hat{D}(\alpha). \tag{5.9}$$

Effectively, this qcmap protocol applies a superposition of the identity and the parity operation on the cavity state displaced by α, including a controllable phase ϕ. The phase of the cat can be controlled via the phase of the first $\phi\left(\frac{\pi}{2}\right)$ pulse. The Wigner function corresponding to the idealised qcmap operator is

$$W(\beta) = \frac{1}{2}\left[W_0(\beta - \alpha) + W_0(-\beta - \alpha) - \frac{4}{\pi}\mathrm{Re}\left\{\mathrm{e}^{\mathrm{i}(4\alpha \mathrm{Im}\{\beta\} + \phi)}\chi_0(2\beta)\right\}\right], \tag{5.10}$$

where $\chi_0(\beta) \equiv \mathrm{Tr}\{\hat{D}(\beta)\hat{\rho_0}\}$ is the characteristic function of the initial state and W_0 is the Wigner function of the initial state $\hat{\rho_0}$. The first two terms represent a coherent superposition of the initial state and the third term characterises the quantum coherence.

When the initial state is a thermal state, the initial Wigner function is

$$W_0(\beta) = \frac{1}{2\pi}\frac{1}{2n_{\mathrm{th}} + 1} \exp\{-(n_{\mathrm{th}} + 1/2)^{-1}|\beta|^2\}, \tag{5.11}$$

and the characteristic function is $\chi_0(\beta) = \exp\{-(n_{\text{th}} + 1/2)|\beta|^2\}$. The measured Wigner function of a cat state with size $\alpha = 2$ is plotted in Fig. 5.2A. By changing the phase of the first $\pi/2$ pulse, we can change the phase of the interference fringes Fig. 5.2B.

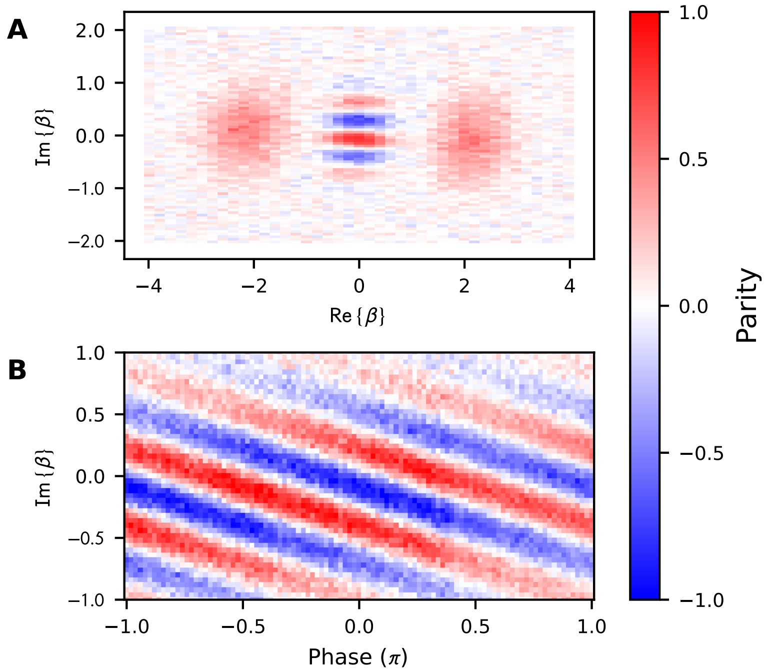

Figure 5.2: Measured Wigner function of a cat state.(**A**) Wigner Tomography of a zero-parity cat $\alpha = 2$. (**B**) The phase of the interference fringes of the cat state can be controlled by changing the phase ϕ of the first $\hat{\phi}\left(\frac{\pi}{2}\right)$ pulse. The cQED toolbox allows us to deterministically form cat states with any parity.

In addition to parity measurement inaccuracies, imperfections in the final cat state can arise. This can be due to qubit or cavity dephasing or relaxation events, the higher order Kerr effect and qubit initialisation.

Imperfections in the cat state are most noticeable at the fringes of the cat state. For even or odd parity cats, the central fringe height should be double that of the Gaussians. During the formation sequence, the cavity undergoes decoherence due to photon loss. This results in a flip in the parity of the cat state fringes. Coherent states decay at a rate of $e^{-t/T_{1,\text{cav}}}$, and the cat state fringes have a lifetime $T_{\text{cat fringes}} = \frac{T_{1,\text{cav}}}{2\alpha^2}$ [2, 23]. Thus, larger cat states have a much shorter fringe lifetime.

The Kerr effect during the time evolution and disentanglement part of the qcmap protocol will distort the shape of the two Gaussians and fringes. This effect is discussed in detail in Sec. 5.3.

Another imperfection comes from the qubit initialisation. An initial excited state will result in a cat state with the opposite parity. If the qubit is not initialised perfectly in the ground state, the fringe contrast is reduced by twice the initial excited state population.

Qubit decoherence during the formation and measurement of the cat state can also reduce the contrast of the fringes. If the qubit loses phase coherence during the time evolution of the qcmap protocol, the cat state fringes will have a random phase and thus the ensemble average will have a reduced contrast. To reduce the effect of qubit decoherence, the qcmap protocol can be modified to include an echo pulse on the qubit.

5.2 ECD cats

The echo-conditional-displacement (ECD) protocol is very similar to the qcmap protocol, except for a $\hat{Y}(\pi)$ applied on the qubit in the middle of the time evolution [154]. The echo pulse helps refocus low-frequency qubit noise. The waiting time $\hat{T}\left(\frac{\pi}{\chi}\right)$ is divided into two, with two displacements $\hat{D}(\alpha/2(-1-i))$ pulse and a $\hat{Y}(\pi)$ pulse in the middle. An additional minor change is that the disentanglement pulse is now applied to the $|-\alpha, e\rangle$ branch. The pulse sequence is illustrated in Fig. 5.3A and phase space evolution before and after the echo pulse is shown in B and C respectively.

Written without considering geometric phase factors from $\hat{D}(\alpha)|\beta\rangle = |(\alpha+\beta)e^{i\mathrm{Im}\{\alpha\beta^*\}}\rangle$, the evolution of the quantum system is as follows

$$\hat{\phi}\left(\frac{\pi}{2}\right) : \frac{1}{\sqrt{2}}|0\rangle \otimes \Big(|g\rangle + e^{i\phi}|e\rangle\Big) \tag{5.12}$$

$$\hat{D}(\alpha) : \frac{1}{\sqrt{2}}|\alpha\rangle \otimes \Big(|g\rangle + e^{i\phi}|e\rangle\Big) \tag{5.13}$$

$$\hat{T}\left(\frac{\pi}{2\chi}\right) : \frac{1}{\sqrt{2}}\Big(|\alpha, g\rangle + e^{i\phi}|\alpha i, e\rangle\Big) \tag{5.14}$$

$$\hat{D}\left(-\frac{\alpha}{2}(1+i)\right) : \frac{1}{\sqrt{2}}\Big(|\frac{\alpha}{2}(1-i), g\rangle + e^{i\phi}|\frac{\alpha}{2}(-1+i), e\rangle\Big) \tag{5.15}$$

$$\hat{Y}(\pi) : \frac{1}{\sqrt{2}}\Big(|\frac{\alpha}{2}(1-i), e\rangle + e^{i\phi}|\frac{\alpha}{2}(-1+i), g\rangle\Big) \tag{5.16}$$

$$\hat{D}\left(-\frac{\alpha}{2}(1+i)\right) : \frac{1}{\sqrt{2}}\Big(|-\alpha i, e\rangle + e^{i\phi}|-\alpha, g\rangle\Big) \tag{5.17}$$

$$\hat{T}\left(\frac{\pi}{2\chi}\right) : \frac{1}{\sqrt{2}}\Big(|\alpha, e\rangle + e^{i\phi}|-\alpha, g\rangle\Big) \tag{5.18}$$

$$\hat{D}(-\alpha) : \frac{1}{\sqrt{2}}\Big(|0, e\rangle + e^{i\phi}|-2\alpha, g\rangle\Big) \tag{5.19}$$

$$\hat{X}(\pi, n < N_{\max}) : \frac{1}{\sqrt{2}}\Big(|0, g\rangle + e^{i\phi}|-2\alpha, g\rangle\Big) \tag{5.20}$$

$$\hat{D}(-\alpha) : \frac{1}{\sqrt{2}}\Big(|\alpha, g\rangle + e^{i\phi}|-\alpha, g\rangle\Big). \tag{5.21}$$

While the final cat state is similar to the qcmap, the idealised ECD protocol implements the operator

$$\hat{S}_{\mathrm{ECD}} \equiv \frac{1}{\sqrt{2}}\Big(\hat{D}(\alpha) - e^{i(\phi+|\alpha|^2)}\hat{D}(-\alpha)\Big)\, i^{\hat{n}}. \tag{5.22}$$

The operator $\mathrm{i}^{\hat{n}}$ rotates the initial state by $\pi/4$ in phase space before displacement. This goes unnoticed because of the rotationally symmetric ground state. The extra geometric phase factor $e^{i|\alpha|^2}$ is gained from the additional displacements acting on the cavity.

The ECD protocol effectively realises a state-dependent displacement to phase space locations α and $-\alpha$. The resulting Wigner function of an idealised ECD cat state is

$$W(\beta) = \frac{1}{2}\left[W_0(\beta-\alpha) + W_0(\beta+\alpha) - 2\cos(4\alpha\mathrm{Im}\{\beta\}+\phi)W_0(\beta)\right]. \tag{5.23}$$

where W_0 is the Wigner function of the initial state $\hat{\rho}_0$. For an initial mean cavity thermal photon, the initial Wigner function is Eq. (5.11). The first two terms represent a coherent superposition of the initial state and the third term characterises the quantum coherence. The measured Wigner function of an ECD cat with $|\alpha = 3\rangle$ is plotted in Fig. 5.3D.

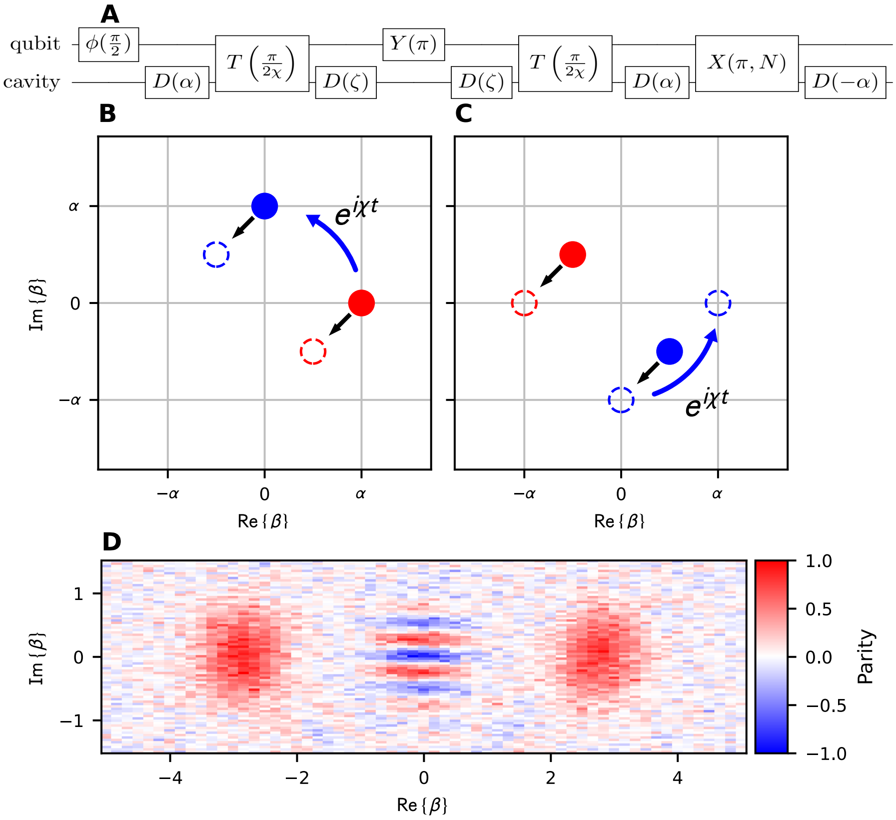

Figure 5.3: ECD cat state generation and measurement. (**A**) Pulse sequence and (**B** and **C**) phase space representation of ECD cat state generation sequence. Red and blue colours represent the qubit in the ground and the excited state respectively. In **B**, after an evolution time of $t = \frac{\pi}{2\chi}$, the cavity is brought towards the centre of the phase space by a displacement pulse $\hat{D}(\zeta) = \hat{D}\left(\frac{\alpha}{2}(-1-i)\right)$. After an unconditional echo pulse is played on the qubit. The qubit state is swapped. In **C**, after another displacement, the second half of the evolution is continued. Now, to disentangle the qubit and put it back in the ground state, the disentanglement pulse should be played on the right coherent state. (**D**) Wigner Tomography of an even-parity ECD cat state of size $\alpha = 3$.

On top of the imperfections mentioned in the qcmap protocol, an additional imperfection for the ECD cat state is due to an improper echo pulse. In Fig. 5.3D, faint parasitic fringes pointing towards the bottom of the plot can be observed. Such fringes are caused by undesired selectivity in the echo pulse that does not cover the entire qubit frequency spectrum. At the time of the echo pulse, the cavity will have a coherent state of $|\pm\frac{\alpha}{2}(1-i)\rangle$ (Eq. (5.16)). This means the qubit will have some finite frequency spread. Instrumental limitations will place a maximum pulse amplitude and minimum pulse length which results in unwanted selectivity of the pulses. The improper addressing of all possible qubit frequencies results in population at the position $(I, Q) = (0, -\alpha)$ at the end of the protocol and additional interference fringes. The effects of undesired selectivity is discussed in greater detail in Sec. 6.1.

5.3 Kerr Effect

The higher order Hamiltonian terms present will cause imperfections in the measured cat state. On top of the cross-Kerr between the high Q cavity and readout resonator causing measurement artefacts mentioned in Sec. 4.3.1, the Kerr effect will also distort the final cat state.

During the time evolution of a coherent state, the higher order terms of K and χ' will distort the Gaussian shape. This results in the bending of the fringes and the reduction of the parity of the cat state. The Kerr effect is introduced in two portions of the protocol.

Firstly, during the time evolution $\hat{T}(\frac{\pi}{\chi})$, the Kerr effect will cause a distortion proportional to $e^{i|\alpha|^2\frac{K}{2}\frac{\pi}{\chi}}$ for the cavity state in $|\alpha, g\rangle$. For the cavity state in $|\alpha, e\rangle$, the distortion is greater due to the excited state of the qubit which enhances the Kerr shift by χ'. For large χ' or K, this can result in the final cat state with very distorted coherent states and fringes that are washed out. This is shown in the Fig. 5.4. The ECD protocol divides the total error from the higher order χ' term between both left and right coherent states.

Secondly, to disentangle the qubit from the cavity, the qcmap and ECD protocol require displacements and a disentanglement pulse. In this process, part of the cavity state occupies a higher photon number $|2\alpha\rangle$ which results in a larger phase error $e^{i|2\alpha|^2\frac{K}{2}t}$. As the disentanglement pulse has to be selective on the cavity ground state, this pulse has to be long and of the order $t = \frac{\pi}{N\chi}$, where $N < |2\alpha|^2$. The finite pulse time, $t > \pi/(|2\alpha|^2\chi)$ results in a phase error $\phi > |2\alpha|^2\frac{K}{2}t = \frac{\pi}{2}\frac{K}{\chi}$ which distorts the $|2\alpha\rangle$ branch. In the experiments, limitations on pulse amplitudes will result in an even lower time limit on the disentanglement pulse and thus a larger Kerr error.

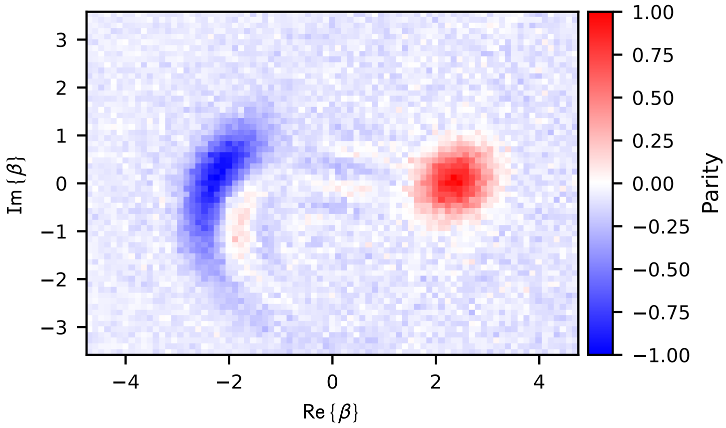

Figure 5.4: Wigner tomography of an entangled cat state formed with qcmap in a system with large Kerr effect. The enhanced Kerr effect during the evolution of $|e, \alpha\rangle$ branch results in the left coherent state being severely distorted. The Kerr effect also causes problems in the parity measurement which results in a non-zero background offset. In such situations, the generalised Husimi-Q measurement method is more suitable for cavity state tomography. In this experiment, the qubit and high Q cavity frequencies were very close together resulting in a highly hybridised system with large Kerr. Here, $f_{\mathrm{qb}} = 5.402\,\mathrm{GHz}$, $f_{\mathrm{cav}} = 4.562\,\mathrm{GHz}$, $K_q/2\pi = 207\,\mathrm{MHz}$, $K_c/2\pi = 17\,\mathrm{kHz}$, $\chi/2\pi = 4.915\,\mathrm{MHz}$ and $\chi'/2\pi = 130\,\mathrm{kHz}$.

A cat state formation protocol that circumvents this problem is with the Kerr cat [155]. This method involves displacing the cavity mode, allowing the system to evolve. With a waiting time $t = \pi/K_c$, the resulting state is a zero parity cat without the need for a disentanglement pulse. By starting in the qubit excited state, the waiting time can also be shortened to $\pi/(K + \chi')$. The evolution of the cat can then be stopped by resetting the qubit to the ground state. The Kerr cat operator is equivalent to the qcmap operator Eq. (5.9) with $\phi = \pi/2$. Details on the Kerr cat protocol are shown in appendix G.

However, this method takes a longer time to form ($t_{\pi/(K+\chi')}$ as compared to $t_{\pi/\chi}$). This method of Kerr cat formation is limited by $T_{1,\mathrm{qubit}}$ or $T_{1,\mathrm{cavity}}$. To speed up the Kerr cat formation, we can increase χ', however, this will limit our parity measurement fidelity and we have to use the Husimi-Q measurement method for full state reconstruction of our cavity state. Furthermore, as the Kerr effect is parity preserving, arbitrary cat fringe phase control is not possible. Importantly, the cat is transient and only occurs at $t = \pi/(K + \chi')$, after which the cat will continue to evolve.

5.4 Closed-Loop Optimisation of cat states

In this section, we improved the fidelity of the qcmap protocol, by optimising the first displacement value and time evolution.

Both open-loop optimisation and closed-loop optimisation approaches were used to find a set of pulses to play on the cavity and qubit to improve the final state fidelity. For the open-loop optimisation, the system was simulated with QuTiP [146] and the pulses were optimised with dCRAB [156]. These open-loop optimised pulses were used as an initial guess for the closed-loop optimisation. As a comparison, the closed-loop optimisation was also performed for an initial guess of zero amplitude pulses.

In a quantum system where the qubit is coupled to a high Q cavity, the speed of operations is usually limited by $\frac{1}{\chi}$. This factor can be reduced by using large coherent states to increase the phase space separation between different coherent states [154]. However, this requires large displacement amplitudes and will cause larger Kerr effects. Large χ will also result in dephasing errors on the qubit [52]. Conversely, faster operations by increasing χ will result in larger higher-order terms K or χ'. Together with the inaccuracies in instruments or Hamiltonian characterisation, closed-loop optimisation offers a process to gain operation speed or fidelity while accounting for these imperfections.

Closed-loop optimisation for generating a quantum state requires state tomography after each iteration. This is prohibitively expensive for bosonic modes, as it requires consideration of the entire phase space for state reconstruction. With careful consideration of the distribution of sampling points in the phase space of the bosonic mode, a figure of merit (FOM) can be constructed to serve as an approximation of the final state fidelity.

For a successful optimisation, tuning of the FOM was required. In cat states, two main features need to be accounted for: two coherent states at $|\pm\alpha\rangle$ and the interference fringes in the centre displaying the superposition of the two coherent states. Sample points around the coherent state need to be distributed such that the shape of the coherent state can be accounted for. For sample points at the fringes, we distribute the points to account for the phase and height of the fringes. A total of 29 sampling points were picked over the entire Wigner phase space shown in Fig. 5.5A. For comparison, we plot the analytical Wigner function for an ideal cat state in Fig. 5.5B.

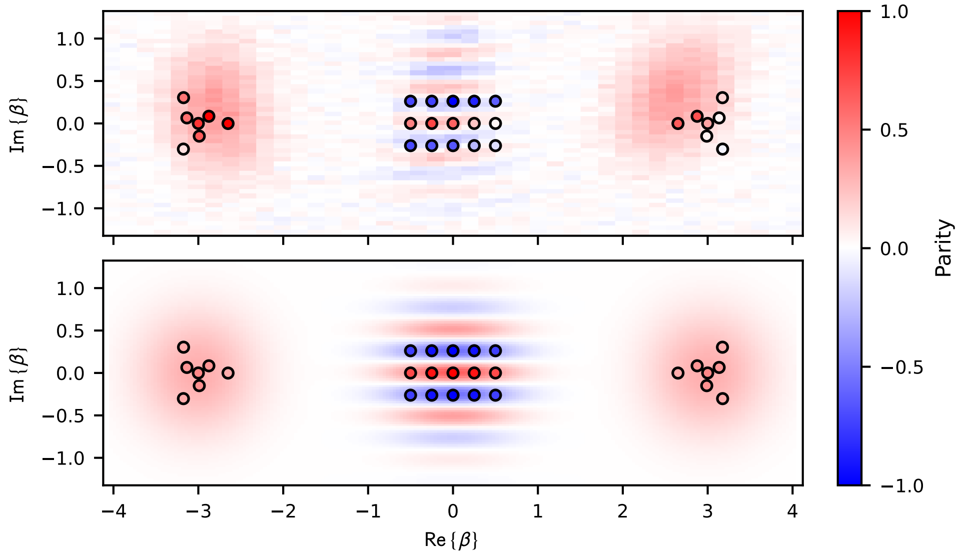

Figure 5.5: Cat state figure of merit (FOM) sample point distribution on the phase space of the system. In (**A**), the measured Wigner function of a qcmap cat state with $\alpha = 3$. This can be compared to the analytical theory in (**B**). The black circles denote the sample points and the colours denote the value at each sample point. The points are chosen to account for both the fringes and coherent state distribution of the cat state. Here, we can see the Kerr effect distorting the coherent states of the cat state. Eq. (2.69) was used as the FOM. The initial FOM over the sample points was 0.4 and the entire phase space was 0.5.

We used Eq. (2.69) to emphasise the phase coherence and size of the fringes. In the perfect scenario, the optimiser can account for the Kerr effect by correcting for the phase errors on the different cavity Fock states introduced throughout the whole qcmap protocol. Additionally, the amplitude of the first displacement was optimised, this allows the optimiser to account for imperfections of cat size due to cavity decay. The pulse sequence is shown in Fig. 5.6A, where α_0, $I_{\mathrm{q,c}}(t)$ and $Q_{\mathrm{q,c}}(t)$ was optimised.

Plotted in Fig. 5.6B is the FOM with each iteration of the optimisation. Starting at an initial FOM of 0.40, the optimiser reached a final FOM of 0.96. The big dips in FOM during the search routine are due to the changes in the parameter search basis in the dCRAB algorithm. In the dCRAB algorithm to find the global maximum, the basis of the control pulses is redefined during the searching process. This changes the FOM "landscape" [73]. Calculating the same FOM over the entire phase space of the cavity showed a FoM increase from 0.50 to 0.74 (Fig. 5.6D). The discrepancy between the FOM over the sample points and the full cavity phase space demonstrates the importance of the choice of the distribution of the sampling points. Here, the Kerr effect on both coherent states could not be completely corrected.

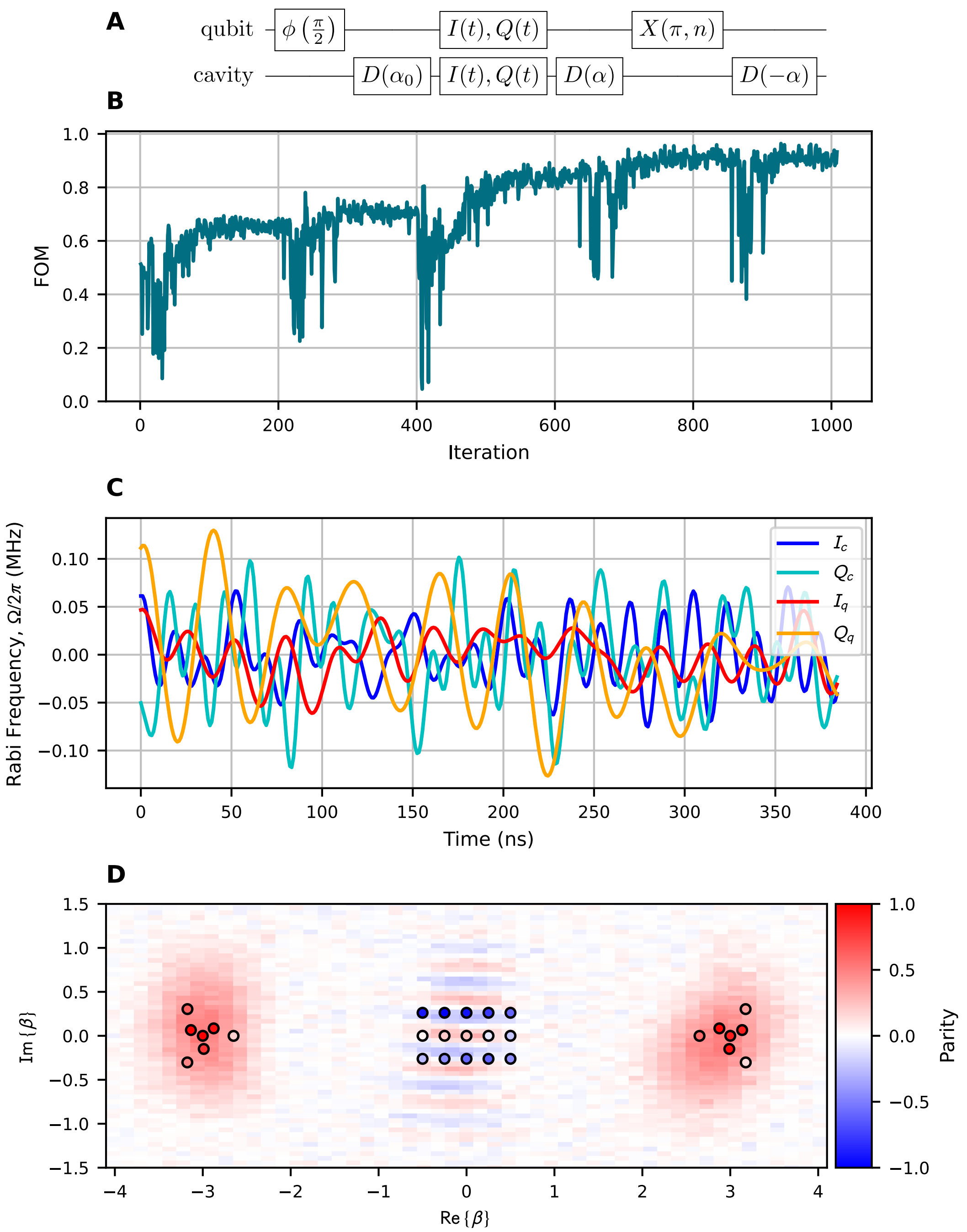

Figure 5.6: Closed-loop optimisation of a qcmap cat (**A**) Pulse sequence of the cat state generation. The optimiser is allowed to play pulses during the time evolution part of the qcmap cat state generation sequence. This was both the in-phase $I(t)$ and out-of-phase $Q(t)$ for both the qubit and cavity control fields $\mathbf{E}(t)$. An additional parameter is the amplitude of the first displacement pulse α_0. This is to account for imperfections from cavity decay. (**B**) Results of the FOM during the optimisation process. The big dips in FOM are due to the changes in the parameter search basis during the dCRAB search routine. (**C**) The optimised pulses for the protocol at the end of the optimisation sequence. These pulses can be analysed to gain a better understanding of the corrections that the optimiser is correcting for. In this optimisation, the optimised value of the first displacement is $\alpha_0 = 3.003$. (**D**) Wigner tomography map of the optimised qcmap protocol. The overall FOM increased to 0.74 and demonstrates a promising method to increase state preparation fidelities of bosonic states.

The total optimisation time for one run took ≈ 8 hour for a total of 1008 iterations. Each sample point required 1000 averages. The measurement time of a single experiment was dominated by the long waiting time in between experiments. This was set to 1 ms to ensure that the high Q cavity with a lifetime of $T_{1,\mathrm{cav}} = 150\,\mu$s was fully initialised to the ground state.

The optimisation was done over 1601 control parameters over a large set of possible values. In the experiment, the time evolution $\hat{T}(\frac{\pi}{\chi})$ was 368 ns. However, initial open-loop optimisation tests showed that the optimiser will have difficulty improving the fidelity of the cat state in such a short time. Thus, the optimised pulses were chosen to be 400 ns long. The AWG had a sampling rate of 1 GSample/s. This was done for the I and Q pulses on the qubit and cavity, and the amplitude of the first displacement pulse.

The optimisation was repeated for two search setting step sizes. First, large search steps were used to reach a faster convergence to a solution. The second search was repeated with smaller step sizes and used the first optimiser solution as an initial guess. This allowed for fine tuning of the optimised solution to improve the fidelity of the state preparation.

This proof-of-principle experiment demonstrated an improvement by $\approx 50\%$ of the original qcmap FOM. By studying the optimised pulse shape and frequency distribution, we can get a better understanding of the errors that the optimiser is trying to correct and guide us in improving our subsequent experiment setups. By going into a smaller dispersive coupling regime and improving the maximum pulse amplitude of our instrument setup, we anticipate an even greater increase in the state preparation fidelity.

The proposed method applies to any quantum platform and can be extended to more complex states. Soon, we plan to optimise states such as a large Fock, Binomial or GKP state, by selecting the corresponding FOM.

CHAPTER 6

Thermal Cats

Garfield Cat States

Work in this chapter was done with Vasilisa Usova from the Kirchmair group and a theory collaboration with Thomas Argenius from Prof. Oriol-Romero-Isart group. This resulted in a paper that is currently in the publication process [131].

The observation of quantum phenomena often necessitates sufficiently pure states, a requirement that can be challenging to achieve. In this chapter, a non-classical state was prepared originating from a mixed state. Utilising dynamics that preserve the initial purity of the state, we generate a Schrödinger's cat state with a mode temperature of up to 1.78 ± 0.04 Kelvin, which is sixty times hotter than its physical environment of $30\,\mathrm{mK}$. Our realisation of non-pure but quantum coherent superposition states could guide the preparation of similar states in other continuous-variable quantum systems.

The quantum superposition principle allows us to prepare a system in a superposition of two arbitrary states. The paradigmatic example is the superposition of two coherent states. While the superposition of coherent states is typically called a Schrödinger's Cat state, in Schrödinger's original thought experiment, the cat, which is a hot and out-of-equilibrium system, is prepared in a superposition of two mixed states dominated by classical fluctuations [1].

The superposition of coherent states has been realised with various quantum systems ranging from the motion of an ion [3], a cold cloud of atoms, molecules [157], microwave photons [158] to the motion of a mechanical oscillator [153]. A shared description of these realisations is the preparation of the superposition of coherent states in a confined bosonic mode, i.e. quantum harmonic oscillator. The state is prepared by either coherent manipulation, engineered dissipation or preparation by measurement, starting with the quantum system as pure as possible.

Low-purity states ($\mathcal{P} \lesssim 1/2$) are often thought of as classical since they typically arise from dissipative dynamics in open quantum systems. However, purity is not a necessary condition for quantum coherence in a state. In particular, mixed-state generalisations of the Schrödinger cat state where a thermal state with non-negligible temperature is put in a superposition with full quantum coherence and full-contrast interference fringes are fully consistent with quantum mechanics and have been considered on several occasions in theoretical works [159–167]. One may argue that these states are closer analogies to Schrödinger's original idea of a body-temperature cat in a quantum superposition state than the cold cat states, which raises interest in their experimental preparation. In the laboratory, quantum interference fringes have been observed from thermal clouds of atoms, both in a double-slit protocol [168] and a half-Stern–Gerlach interferometer [169]. Full state tomography, such as direct measurement of the Wigner function, of low-purity Schrödinger cat states has to our best knowledge not been previously reported.

Considering that there are at least 2 distinct mixed-state generalisations of the pure Schrödinger cat state with distinct quantum coherence properties. The preparation of superposition states from thermal states in continuous-variable systems additionally serves as proof-of-principle for proposals for thermal state quantum computing protocols [161, 163, 170].

We present the preparation of arbitrarily non-pure superposition states by generating coherent superpositions from initial thermal states, that is 'hot' Schrödinger cat states, in a high-coherence microwave cavity through coherent operations. We run the protocol with an initial thermal state of up to 7.6 ± 0.2 average photons on a cQED setup. We confirm the quantum features of the states by imaging their Wigner function. Importantly, we do not remove entropy or purify the system with measurement during these operations.

In this chapter, I begin by discussing important details when working with thermal states. Section 6.2 describes the initialisation and characterisation of a thermal state in the bosonic mode and illustrates our control of the bosonic environment. Section 6.3 and Sec. 6.4 are the Wigner measurement results of the hot Schrödinger cat states we formed. The protocols were numerically simulated and are explained in Sec. 6.5. Finally, in the last section, I describe the conclusions and outlooks of the work from this chapter.

6.1 Protocols with Thermal States

While the techniques mentioned in chapter 5 are also applicable to initial thermal states, imperfections in the final cat state become more apparent with a larger thermal population. In this section, I discuss in greater detail the differences between the qcmap and ECD protocols and the imperfections that become more apparent from the experimental implementation of the protocols when dealing with thermal states.

The cavity state is initialised by coming into equilibrium with the heat bath. The heat bath is then disconnected (to prevent it from causing decoherence) and the cat state preparation commences immediately. The state preparation and measurement protocols take up to $1.9\,\mu s$ which is instantaneous compared to the cavity relaxation time $T_{1,\mathrm{cav}} = (110 \pm 2)\,\mu\mathrm{s}$. Thus, there is no cooling nor heating of the cavity mode during the protocol.

To prepare hot cat states with this setup, we utilise the two different methods described in Sec. 5.1 and Sec. 5.2. When applied to cold cats, only the ground state of the cavity contributes significantly to the thermal mixture, so the differences between the protocols go unnoticed. While these protocols prepare equivalent cold cats, we observe that they lead to differing outcomes when applied to thermal initial states.

At $n_{\text{th}} > 0$, the coherence terms in Eq. (5.10) and Eq. (5.23) behave differently. For the qcmap Wigner function, the coherence term shrinks in phase space with increasing n_{th}, resulting in localised fringes but its maximum amplitude remains constant at $2/\pi$. Conversely, the coherence term in the ECD Wigner function has an envelope that is $2W_0(\beta)$. This means that the interference fringes grow in radius in phase space with more oscillation periods becoming visible but reduce in amplitude with increasing n_{th}.

The different outputs of the qcmap and ECD protocol can be understood when considering the formation sequence. The hot initial state of the cavity can be equivalently described as a mixture of displaced ground states. A coherent state $|\gamma\rangle = \hat{D}(\gamma)|0\rangle$ will transform under the qcmap and ECD protocols respectively as

$$\hat{S}_{\text{qcmap}}|\gamma\rangle = \frac{e^{i\text{Im}\{\alpha\gamma^*\}}}{\sqrt{2}}\Big[|\alpha+\gamma\rangle - e^{i\phi}|-\alpha-\gamma\rangle\Big], \tag{6.1}$$

$$\hat{S}_{\text{ECD}}|\gamma\rangle = \frac{1}{\sqrt{2}}\Big[e^{i\text{Re}\{\alpha\gamma^*\}}|\alpha+i\gamma\rangle - e^{i(\phi+2|\alpha|^2-\text{Re}\{\alpha\gamma^*\})}|-\alpha+i\gamma\rangle\Big]. \tag{6.2}$$

The key point is to recognise that the qcmap output state is a superposition of $|\alpha+\gamma\rangle$ and $|-(\alpha+\gamma)\rangle$, while the ECD output state is a superposition of $|\alpha+i\gamma\rangle$ and $|-\alpha+i\gamma\rangle$. The final cat state is the sum of the individual cat states that are formed and weighted by the initial distribution of the displaced coherent states.

We present a graphical version of this description, with step-by-step tracing of the state through the protocol operations to explain the outcome, in Fig. 6.1 and Fig. 6.2. The initial thermal state of the cavity is viewed as a distribution of displaced coherent states. The distribution is split into two parts, coherent states that are displaced along the I or Q axis of the cavity phase space. This is represented by the different colours.

The qcmap state is created by displacing the initial state by α and then putting it in a superposition with its image under inversion through the phase-space origin. The individual cat states out of a thermal distribution have different sizes and rotations. This results in the interference fringes overlapping and only the fringes localised in the center of the cat state will constructively interfere resulting in a maximum parity while the other fringes will be washed out.

For the ECD protocol, the state is created by first rotating the initial state by $\pi/2$ counterclockwise around the phase space origin, and then putting it in a superposition of being translated to α and $-\alpha$ respectively. The individual cat states formed will always have the same size and angle. This results in cat states with the same fringe period. Therefore, interference from the cat states on-axis (along $\text{Re}\{\beta\}$) will constructively interfere and off-axis (along $\text{Im}\{\beta\}$) cats will cancel each other out. This results in fringes that are extended across the distribution of the initial states and have amplitudes that are smaller as compared to the cold cat case.

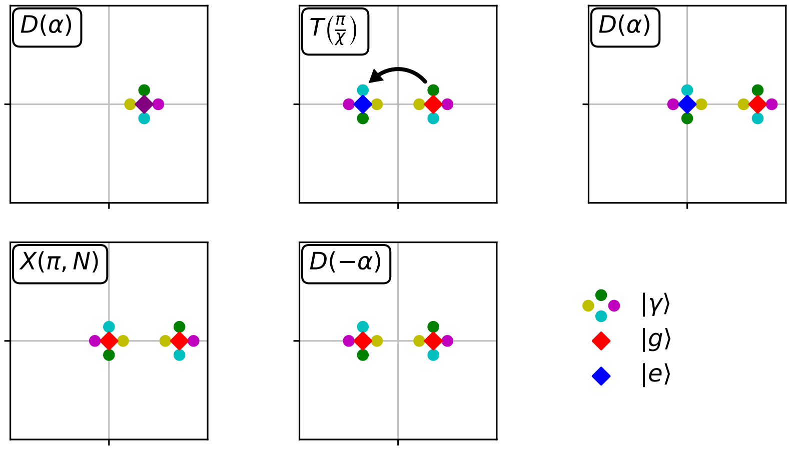

Figure 6.1: Hot Schrödinger cat state with qcmap. The different colours represent the initial displacement of the cavity $|\gamma\rangle$. The red and blue diamonds refer to the ideal qubit state $|g\rangle$ or $|e\rangle$. Depending on the initial displacement, the final Schrödinger cat state has a different size and rotation. This results in the interference fringes overlapping and only the fringes localised in the center of the Schrödinger cat state will constructively interfere resulting in a maximum parity while the other fringes will be washed out.

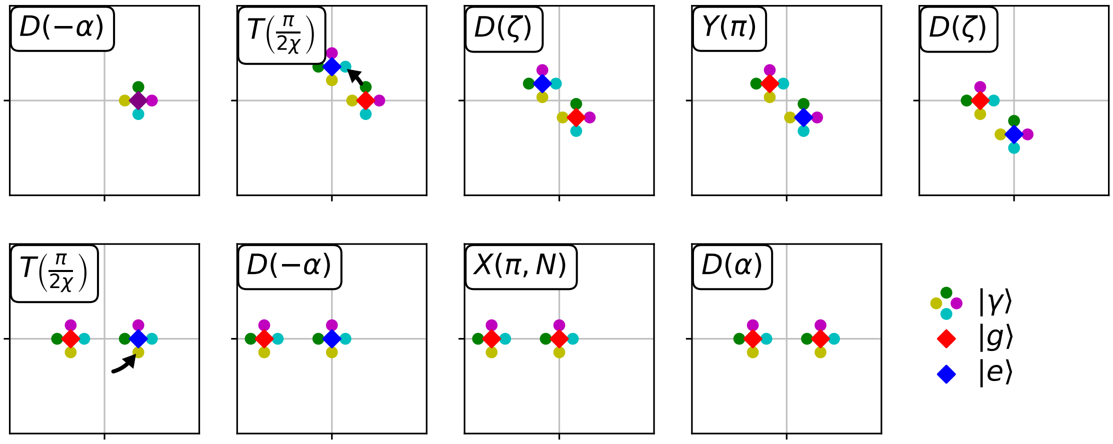

Figure 6.2: Hot Schrödinger cat state with the ECD protocol. The different colours represent the initial displacement of the cavity $|\gamma\rangle$. The red and blue diamonds refer to the ideal qubit state $|g\rangle$ or $|e\rangle$. Regardless of the initial displaced state, the final Schrödinger cat state will always have the same size and angle. This results in the same fringe period and therefore, cat states on-axis will add up and off-axis cats will destructively interfere.

6.1.1 Gaussian Pulses

In the experiment, qubit operations are implemented using Rabi pulses with a Gaussian line envelope. The Gaussian envelope has a controllable standard deviation σ_t.

The Gaussian envelope, as compared to a square pulse shape, reduces frequency components at the higher level of qubit transitions. Specifically, Fourier components at the $|e\rangle$ to $|f\rangle$ transition frequency will lead to leakage of the qubit outside the computation subspace.

The Gaussian profile of the qubit pulse leads to an n-dependent qubit $|g\rangle \leftrightarrow |e\rangle$ transition probability approximately given by $P_{g\leftrightarrow e}(n) = \exp\{-(n\chi_{\mathrm{qc}}\sigma_t)^2\}$ [171, 172]. Thus we can tune the selectivity of our pulses by tuning σ_t. The smooth decay of $P_{g\leftrightarrow e}(n)$ with n limits the maximum selectivity that we can achieve in our disentanglement pulse. Conversely, instrument implementation of the pulses limits the desired unselectivity of qubit operations.

The effects of the Gaussian line profile of our qubit pulses on the prepared cavity states can be understood by deriving the second-order Magnus approximation [171, 173] to the time-evolution operator for our total system under $\hat{H}$ when a Gaussian pulse resonant with ω_q is applied to the qubit. The resulting joint cavity-qubit operator is

$$\begin{aligned}\hat{R}_2(\theta, \phi, \sigma_t, T) \equiv \sum_{n=0}^{\infty} |n\rangle\langle n| \exp\{i[\frac{\theta}{2}\mathrm{e}^{-(\chi_{\mathrm{qc}}\sigma_t n)^2/2}\left(\cos\left(\phi_n\right)\hat{\sigma}_x + \sin\left(\phi_n\right)\hat{\sigma}_y\right) \\ - \frac{\theta^2}{4\sqrt{\pi}} F\left(\chi_{\mathrm{qc}}\sigma_t n\right)\hat{\sigma}_z]\} \exp\left\{\mathrm{i}\chi_{qc} T n\,|e\rangle\langle e|\right\}.\end{aligned} \tag{6.3}$$

Here θ is the pulse area (either π or $\pi/2$ depending on the desired operation), $T \gg \sigma_t$ is the pulse duration, $\phi_n \equiv \phi + \chi_{\mathrm{qc}} T n/2$, and $F(x)$ is the Dawson function.

In Eq. (6.3), we observe additional effects due to the Gaussian pulses. The term proportional to $\hat{\sigma}_z$ and the n dependent phase ϕ_n accounts for the detuning of the $n > 0$ Fock state. It is these term that causes different phase rotations for different cavity Fock states that result in a distortion of the final cat state and is more apparent when dealing with thermal states. The last term with exponent proportional $i\chi_{\mathrm{qc}Tn}$ accounts for the duration of the pulse.

In summary, the Gaussian pulses have three effects that cause the qubit operation to deviate from the perfect σ_x pulse. The operator in Eq. (6.3) is a 2^{nd} order approximation which captures these effects. Firstly, the n-dependent transition probability is due to the linewidth of the Gaussian pulses. This is accounted for by the exponential $e^{-(\chi_{\mathrm{qc}}\sigma_t n)^2/2}$. Secondly, the n-dependent phase that the Gaussian pulse imparts on the qubit for different cavity Fock states. This is considered for by the ϕ_n and term proportional to $\hat{\sigma}_z$. Finally, the finite duration of the Gaussian pulses causes additional rotations in the cavity-qubit system. This effect is captured by the final term in Eq. (6.3) which is proportional to $e^{i\chi_{\mathrm{qc}} n T |e\rangle\langle e|}$. In Sec. 6.5, we compare the Magnus approximation of the Gaussian pulses with numerical simulations in modelling our experimental protocol.

6.1.2 Disentanglement Pulse

Attention to the thermal mixture character of the initial state must also be paid when designing the disentanglement pulse (Fig. 6.3A). We need to apply a conditional flip operation on the qubit which is selective for the first N Fock states of the cavity (Eq. (5.1)). The choice of N is effectively the choice of a radius in the α plane within which the qubit state is flipped (Fig. 6.3B). To properly disentangle, one must choose $|\alpha|$ large enough so that the displaced $|g\rangle$ branch is not affected by the disentanglement pulse. This results in the condition that we need α such that $W_0(\alpha) = 0$, where $W_0(\beta)$ is the Wigner function of the initial state at β.

For cold initial states, it is sufficient to choose $N = 1$, which places no important restriction on α. For hot initial states, N and consequently $|\alpha|$ must be chosen to comply with $P_{n_{\text{th}}}(n)$. Experimentally, we are constrained in the choice of N and $|\alpha|$ because of instrument limitations in the maximum pulse power. The phase space radius of the thermal state is proportional to $\sqrt{n_{\text{th}} + 1/2}$, so larger n_{th} necessitates larger α. Since the cat state lifetime decreases with α as $T_{1,\text{cav}}/2\alpha^2$ [2, 174], this places stricter requirements on the experimental parameters as n_{th} increases.

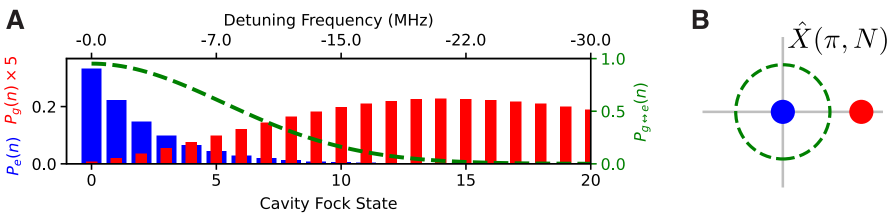

Figure 6.3: Spectral considerations for disentanglement pulse. (**A**) Plot of the qubit-conditional cavity Fock state distribution $P_q(n) = \langle n| \langle q| \hat{\rho} |n\rangle |q\rangle$, $(q \in \{g, e\})$ in the total state $\hat{\rho}$ just before the disentanglement operation $\hat{X}(\pi, n)$. The plot uses $\alpha = 2$ and $n_{\text{th}} = 2$. The colours of the bar plots correspond to the qubit in the ground state (red) and excited state (blue), with $P_g(n)$ multiplied by 5 for visibility. The green dashed line shows the probability of a Gaussian Rabi pulse resonant with ω_q and with standard deviation $\sigma_{\text{t}} = 20$ ns to flip the qubit state from $|e\rangle$ to $|g\rangle$ while the qubit is entangled with the Fock state $|n\rangle$ under the dispersive Kerr coupling. The overlap between the $|g\rangle$ and $|e\rangle$ Fock state distributions will result in incomplete disentanglement of the qubit and cavity in this scenario. This can be remedied by increasing α, which separates the distributions further. (**B**) The choice of width of the disentanglement pulse corresponds to the choice of a radius in the phase space within which the qubit state is flipped with a certain probability.

The n-dependent transition probability will result in some residual entanglement between the qubit and the cavity. Due to our Wigner function measurement method (Sec. 4.3.1), any residual entanglement causes the subsequent measurement result to output $W_{\text{measured}}(\beta) = p_g W_g(\beta) - p_e W_e(\beta)$, where the Wigner functions correspond to the cavity state operators entangled to $|g\rangle$ and $|e\rangle$, and $p_{g,e}$ are the probabilities of the qubit being in the respective state. This reduces the parity values of the measured results.

6.2 Thermal Noise

Most initial states in practice are thermal states, the purity $\mathcal{P}$ of the initial state is related to its average thermal occupation number n_{th} via $\mathcal{P} = 1/(2n_{\mathrm{th}} + 1)$, and n_{th} is in turn related to the initial temperature T via the Bose-Einstein distribution. In this section, we demonstrate control of the bosonic mode environment.

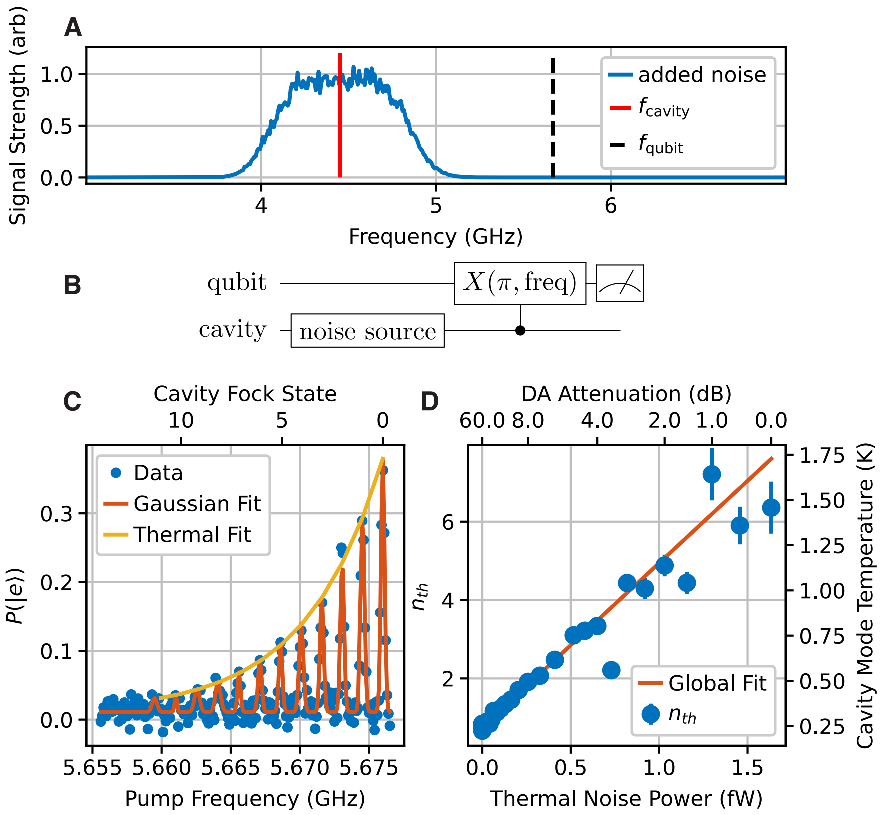

Figure 6.4: Intialisation and characterisation of thermal noise in the cavity. (**A**) The theoretical frequency spectrum of added noise. The thermal noise is only added at the cavity frequency and qubit frequencies are filtered out. The added noise level is controlled by a digital attenuator. (**B**) Pulse sequence of the thermal state measurement technique. A microwave switch was closed, adding Johnson-Nyquist noise at the cavity frequency for 1 ms. The switch was opened and a photon number selective π pulse was played on the qubit and the qubit state was measured. (**C**) Qubit spectroscopy measurement result for a single thermal state. The height in the qubit spectroscopy follows the thermal photons distribution in the cavity. Here, $n_{\mathrm{th}} = 3.3$. (**D**) The measurement was repeated for a sweep in added noise power.

In this experiment, we have experimental control of n_{th} by deliberately adding noise on top of the equilibrium thermal state via filtering and amplifying the Johnson-Nyquist noise of a 50Ω resistor (Fig. 6.4A). To determine the initial thermal state, number-split qubit spectroscopy was performed (Fig. 6.4B). We control the noise power at the cavity frequency via a variable attenuator. A switch is used to initialise the cavity into a thermal state before the switch is opened to prevent additional decoherence. The coldest thermal state can be achieved by leaving the switch open, which is a residual thermal population of $n_{\text{th}} = 0.03$.

The relative heights of the individual qubit frequency peaks are split by the presence of different numbers of photons in the cavity due to the dispersive qubit-cavity interaction (Fig. 6.4C). The distribution of these peak heights directly reflects the distribution of thermal photons within the cavity [175]. We fit the theoretical thermal photon distribution to the experimental distribution (Eq. (2.17), $P_n(n_{\text{th}}) = \frac{n_{\text{th}}^n}{(1+n_{\text{th}})^{n+1}}$), finding agreement and allowing us to relate the noise attenuation to n_{th} (Fig. 6.4D).

6.3 Hot Schrödinger Cat States

We run our experiment using both protocols for $\alpha = 3$, starting from an initial thermal state with an n_{th} from 0.75 ± 0.01 to 7.6 ± 0.2 and then apply the Wigner function measurement protocol to the resulting state. We use a disentanglement pulse width of $\sigma_t = 20\,\text{ns}$.

We present the measurement results for qcmap in Fig. 6.5 and ECD in Fig. 6.6. We also compare to the ideal Wigner function as predicted by Eq. (5.10) & Eq. (5.23) for the chosen experimental parameters.

Independently of comparison to theory, the data shows clear Wigner negativities that produce interference fringes and thus confirms the quantum nature of the prepared states with a purity starting at $\mathcal{P} = 0.400 \pm 0.003$ and going as low as $\mathcal{P} = 0.062 \pm 0.002$ (without accounting for the effects of decoherence).

For qcmap, the fringe envelope is given by the characteristic function, the variance of which shrinks with n_{th} and the height of which is saturated to the parity bound *independently* of n_{th}.

For the ECD state, the amplitude of the fringe envelope is twice the envelope of $W_0(\beta)$. Since the amplitude of $W_0(\beta)$ shrinks and its variance increases with n_{th}, the same applies to the ECD fringes. In particular, the number of visible fringes *increases* with n_{th}. The $-$i phases in the ECD cat state arguments vanish due to the rotational symmetry of the thermal state. Furthermore, the issue of unwanted selectivity in the echo pulse (mentioned in Sec. 5.2), is exacerbated by the larger spread of qubit frequencies due to the thermal state of the cavity.

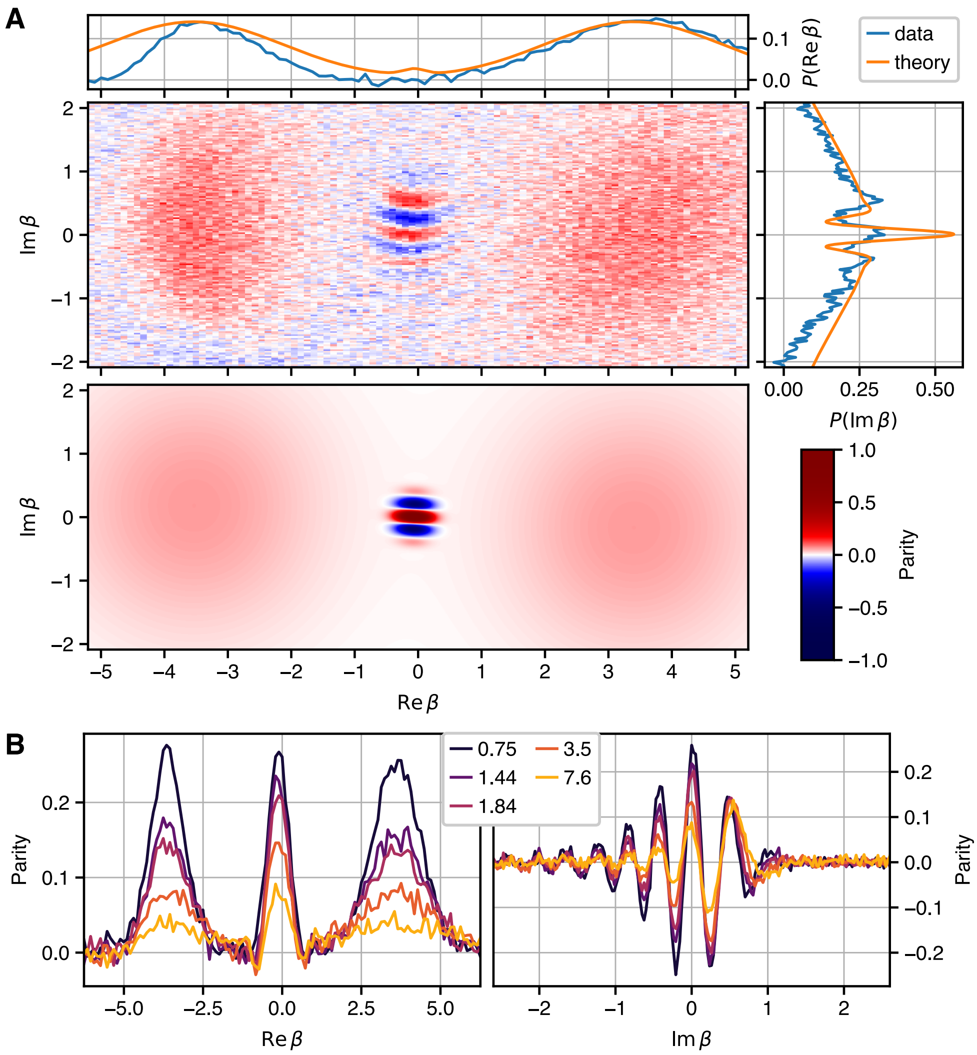

Figure 6.5: Hot Schrödinger cat state created with qcmap protocol. (**A**) Starting from an initial thermal state with $n_{\mathrm{th}} = 3.48 \pm 0.07$, the result of the Wigner function measurement on the hot Schrödinger cat state (centre) and marginal distributions (top, right) are shown. For comparison, the Wigner function $W_1(\mathrm{e}^{i\varphi}(\beta))$ ($n_{\mathrm{th}} = 3.48$, $\alpha = 3.47$, $\varphi = 0.05$, $\phi = \pi$) is shown (bottom). Note the nonlinear change of the colour brightness across the colourbar to increase the visibility of small parity values. (**B**) The experiment was repeated up to a mode temperature of 1.78 ± 0.04 Kelvin or a mean of 7.6 ± 0.2 thermal cavity photons. The colours denote the starting mean thermal cavity photon number. In all linecuts, we observe negativity in the interference fringes.

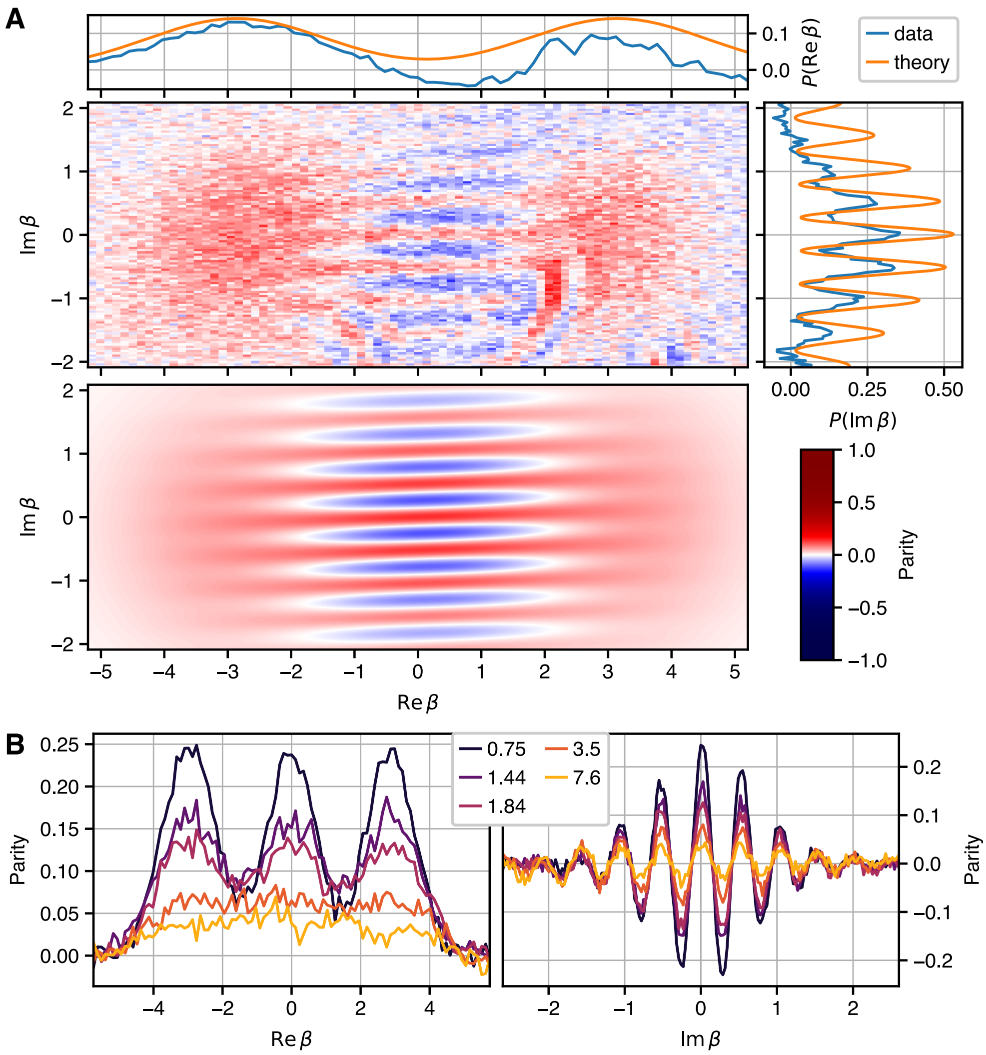

Figure 6.6: Hot Schrödinger cat state created with ECD protocol. (**A**) The result of the Wigner function measurement on the hot Schrödinger cat state (centre) and marginal distributions (top, right) are shown. For comparison, the Wigner function $W_2(e^{i\varphi}(\beta))$ ($n_{\mathrm{th}} = 3.48$, $\alpha = 3.00$, $\varphi = -0.03$, $\phi = \pi$) is shown (bottom). Note the nonlinear change of the colour brightness across the colourbar to increase the visibility of small parity values. (**B**) The experiment was repeated up to a mode temperature of 1.78 ± 0.04 Kelvin or a mean of 7.6 ± 0.2 thermal cavity photons. The colours denote the starting mean thermal cavity photon number. In all linecuts, we observe negativity in the interference fringes.

6.4 Fringe lifetime

The quantum nature of the coherence in the hot cat states is further confirmed by measuring the decay of the central fringe as the cavity undergoes decoherence due to photon loss. We first initialise the cavity to a hot thermal bath resulting in an initial thermal state with mean photons n_{th}. The hot bath is then disconnected and the cavity is only connected via residual coupling to a bath n_{b}. An interesting feature of the hot cat states is that the lifetime of the fringes is independent of the initial thermal state n_{th}. It is only dependent on the thermal bath n_{b} that the high Q cavity is connected to [2, 164, 174]. For short timescales, the fringe lifetime is

$$T_{\mathrm{fringe}} \equiv T_{1,\mathrm{cav}}/[2(2n_{\mathrm{b}}+1)|\alpha|^2] < T_{1,\mathrm{cav}} \tag{6.4}$$

where n_{b} is the bath thermal population that the cavity is connected to and $T_{1,\mathrm{cav}}$ is the lifetime of the high Q cavity. We see that T_{fringe} defines the time at which quantum coherence is lost from the system, whereas $T_{1,\mathrm{cav}}$ defines the rate at which energy dissipates out of the system. Since $T_{\mathrm{fringe}} \ll T_{1,\mathrm{cav}}$, the fringes will usually decay before $\alpha(t)$ changes noticeably from α. We then also clearly see that the quantum coherence time T_{fringe} is independent of n_{th}. So the quantum coherence time of a hot qcmap or ECD state is the same as that of a cold cat.

The fringe is measured to decay exponentially with a time constant of 3.38 ± 0.08 µs. This is consistent with the theoretical prediction of the cat lifetime 5.2 ± 0.8 µs independent of n_{th} when accounting for state preparation and measurement time of 1.9 µs. The measurements are shown in Fig. 6.7, where the fringe decay does not change significantly with increasing n_{th}.

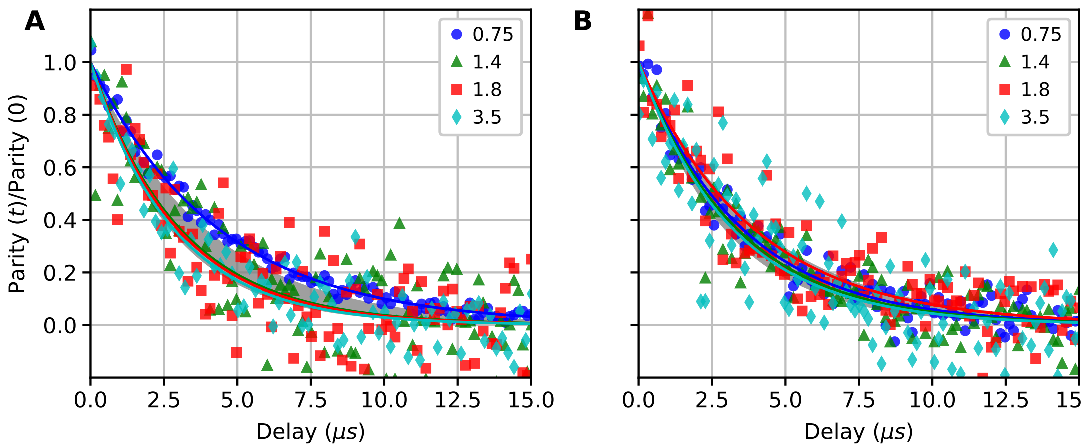

Figure 6.7: Measured central fringe lifetime. The lifetime was measured for both (**A**) qcmap and (**B**) ECD hot cat states. The labels denote the n_{th} of the initial thermal state. The data is scaled to the measured parity immediately after state preparation to emphasise the decay rate of the hot cat state fringes after preparation. The data was fitted to an exponential decay and with a mean fringe lifetime of 3.38 ± 0.08 µs which does not significantly change with an increase in n_{th}. The grey area denotes an exponential decay with the combined mean lifetime with a 3σ deviation in the time constant.

6.5 QuTiP Simulations

6.5.1 Increasing Thermal Noise

QuTiP simulations of the pulse sequence with different starting cavity thermal populations are plotted Fig. 6.8. The operations were implemented as follows: Displacement operators and thermal initial states are implemented using QuTiP's built-in functions. The qubit and cavity-conditional qubit operations are implemented using either Eq. (6.3) or a dynamical simulation of the system under a driving Hamiltonian. The time evolution operations $\hat{T}(t)$ are implemented using QuTiP's built-in mesolve function to solve the Lindblad master equations with collapse operators representing the decoherences in the system.

To test the viability of the simulation model, simulations were done with instantaneous, ideal unselective $\hat{\sigma}_{x,y}$ pulses and disentanglement pulse with linewidth $\sigma_t = 10\,\mathrm{ns}$. Here, higher order terms in the Hamiltonian such as K and χ' are neglected, and cavity and qubit decoherence terms $\Gamma_{\mathrm{q,c}}$ are set to zero.

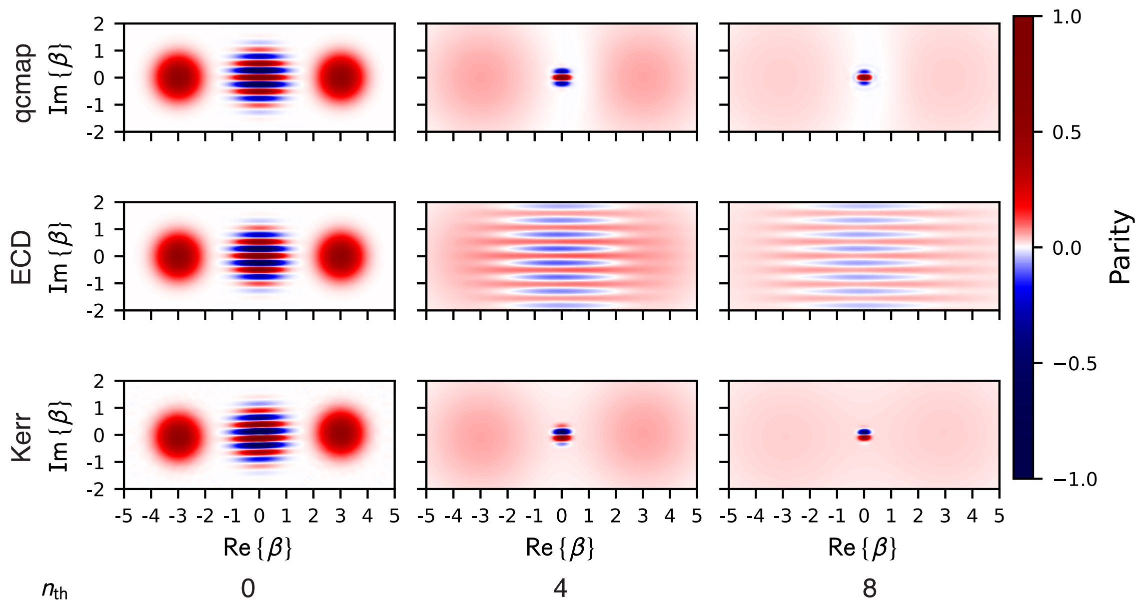

Figure 6.8: QuTiP Simulations of idealised cat state generation sequence. Hot Schrödinger cat states were simulated with an increasing thermal state population (left to right) and n_{th} for qcmap (top row), ECD (centre row) and Kerr (bottom row) sequences. To increase the visibility of small parity values, the colour brightness changes nonlinearly across the colourbar.

In all cases of the simulation, interference fringes in the Wigner function can be observed. This demonstrates the feasibility of our QuTiP simulation model when comparing the simulation results to the measured data and analytical theory. For an initial ground state of the cavity $n_{\mathrm{th}} = 0$, the three sequences result in a similar cat state. However, the results are noticeably different for higher thermal population. In the qcmap cat states, the fringes are localised to the centre while in the ECD cat states, the fringes follow the total phase space extend of the cavity state. Included in the bottom row is the Kerr cat method of forming cat states (Sec. 5.3, [155]) which results in a similar fringe structure to the qcmap ones except for a zero-parity fringe phase.

6.5.2 Comparison with Experiments

Using our experimental characterisation of the setup, we model the known imperfections in an *ab initio* numerical simulation which reproduces all the features of the measured data within the expected accuracy of the experiment.

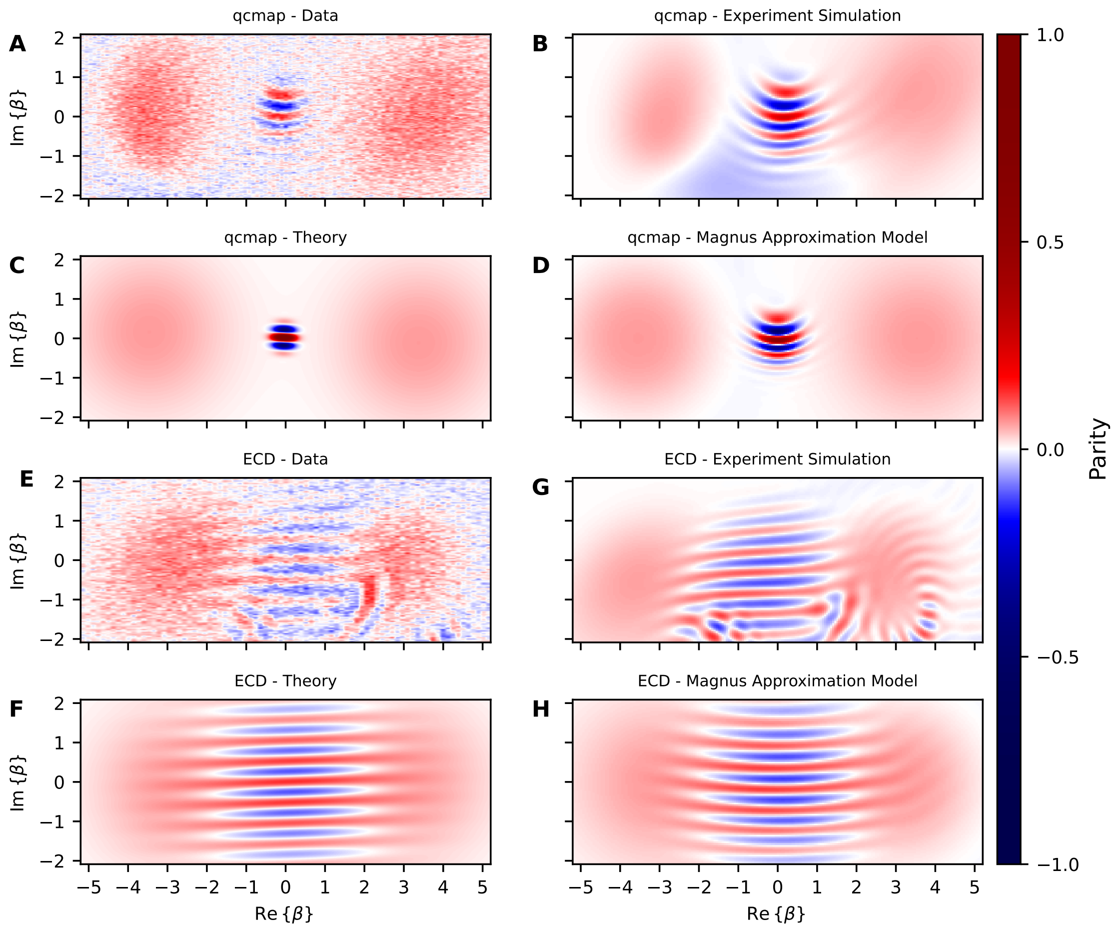

Figure 6.9: Comparison of QuTiP Simulations to measured data and analytical fit. **A** to **D** are for qcmap and **E** to **H** is for ECD. The panels correspond to (**A** and **E**) measured data, (**B** and **F**) full simulation with all the experimental parameters, (**C** and **G**) analytical fit and (**D** and **H**) simulation in a Kerr free, ideal unconditional pulses and decoherence free environment. The Magnus 2$^{\text{nd}}$ order approximation is used as the operator for the Gaussian disentanglement pulse. To increase the visibility of small parity values, the colour brightness changes nonlinearly across the colourbar.

6.5.3 Effects of Kerr, Gaussian pulses and Decoherence

To explain the different features present in the map, we plot QuTiP simulations with different effects turned on for both the qcmap (Fig. 6.10) and ECD (Fig. 6.11) protocol. These can be compared to the full experimental parameters simulation (panel A) and the Magnus approximation model (panel B) where the Magnus 2^{nd} operator (Eq. (6.3)) is used for the qubit rotations. We identify four areas that result in imperfections in the experiment (panels C to F). These are the higher-order Kerr effects (K, χ'), the undesired selectivity of the pulses (finite width of $\hat{X}(\pi)$ and $\hat{X}(\pi/2)$ pulses), the timing of the imperfect disentanglement pulse ($\hat{X}(\pi, N)$) and the qubit and the cavity decoherence and relaxation rates (Γ_{q} and Γ_{c}).

Firstly, the undesired selectivity of qubit pulses results in imperfect flipping of the qubit population for high cavity photon numbers. This results in unequal populations between the left and right cavity state distributions. For the case of ECD, comparing Fig. 6.11 panel B to C, there are additional parasitic fringes at the bottom of the map due to the undesired selectivity of the echo π pulse that results in a small population at $\beta = (0, -\alpha)$.

Secondly, the Kerr effect results in the bending of fringes due to a photon number dependent phase shift during the evolution of the the cavity state ($|n(t)\rangle = e^{in^2Kt}|n\rangle$).

Thirdly, the timing of the disentanglement pulse results in additional distortion of cavity distributions. This disentanglement pulse timing is typically a significant proportion of the waiting time required during the formation protocol ($t = \pi/\chi_{\mathrm{qc}}$). When this effect is turned on at the same time as the Kerr effect, this results in additional bending of the hot cat state interference fringes. During the disentanglement pulse, the $|2\alpha, g\rangle$ branch will occupy a larger Fock state, this results in a larger Kerr effect and bigger distortion of the coherent state.

The similarity between panels B and E illustrate the accuracy of the Magnus second-order approximation operator as an accurate description for the Gaussian pulses used. Detailed simulated linecuts are displayed in the following section.

Finally, decoherence of the cavity or qubit will result in a loss in interference fringes contrast. By comparing panels B and F, we see that our decoherence rates are so low that they can be neglected.

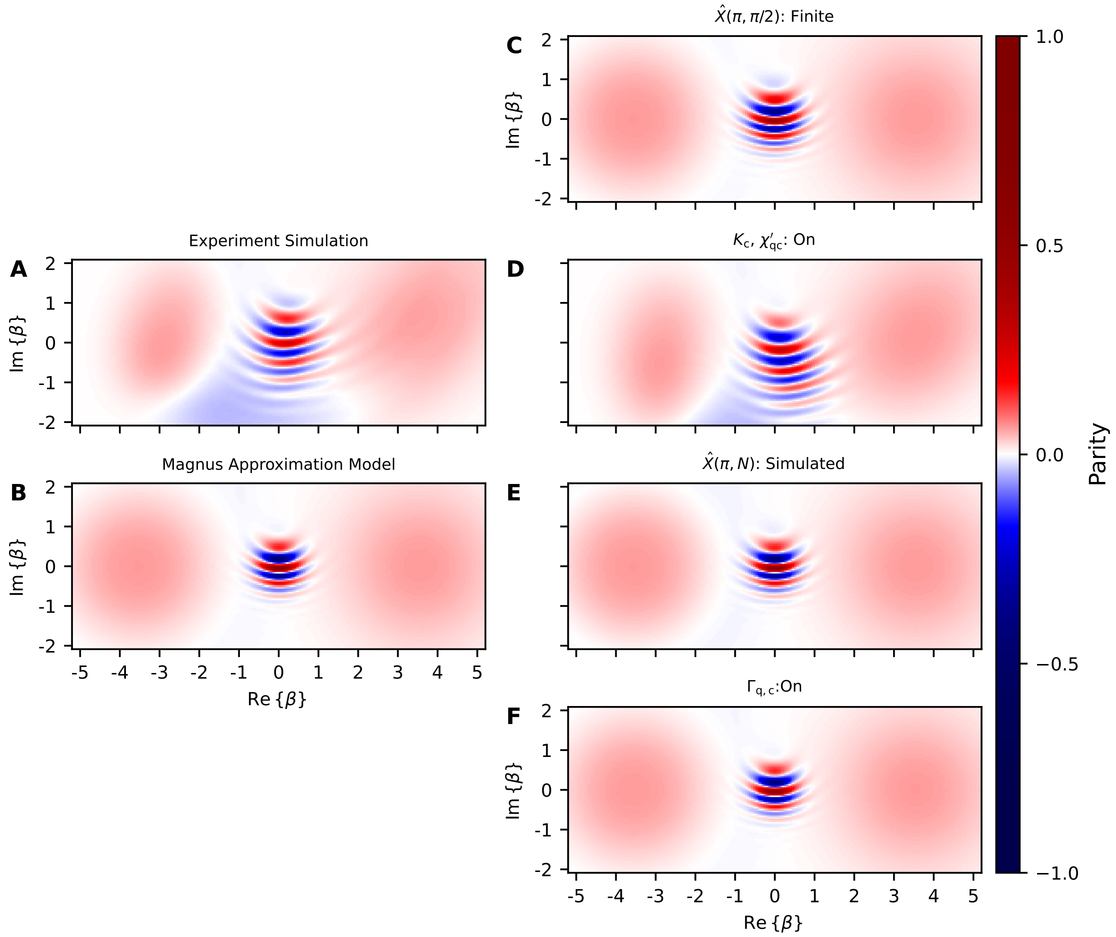

Figure 6.10: QuTiP Simulations of hot Schrödinger cat states with qcmap. Hot Schrödinger cat states were simulated with different imperfections turned on. The simulations are compared to the cases for (**A**) full experimental parameters simulation where all the imperfections are turned on and (**B**) Magnus approximation model where the Magnus 2^{nd} operator (Eq. (6.3)) is used for the qubit rotations. The imperfections are the (**C**) undesired selectivity of qubit pulses ($\hat{X}(\pi, \pi/2)$), the (**D**) higher order Kerr effect (K_c, χ'_{qc}), the (**E**) timing of the long disentanglement pulse ($\hat{X}(\pi, N)$) and (**E**) decoherence rates of the qubit and cavity ($\Gamma_{q,c}$). To increase the visibility of small parity values, the colour brightness changes nonlinearly across the colourbar.

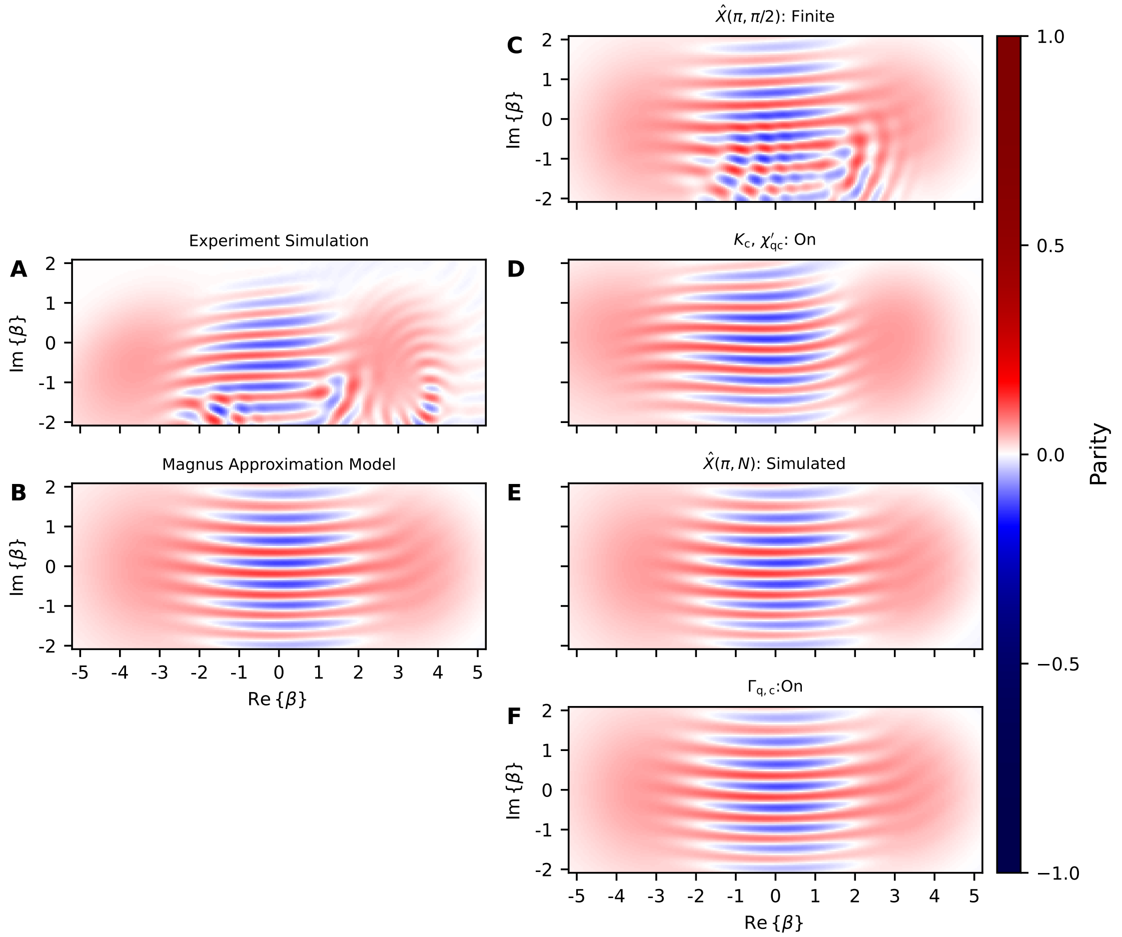

Figure 6.11: QuTiP Simulations of hot Schrödinger cat states with ECD. Hot Schrödinger cat states were simulated with different imperfections turned on. The simulations are compared to the cases for (**A**) full experimental parameters simulation where all the imperfections are turned on and (**B**) Magnus approximation model where the Magnus 2$^{\text{nd}}$ operator (Eq. (6.3)) is used for the qubit rotations. The imperfections are the (**C**) undesired selectivity of qubit pulses ($\hat{X}(\pi, \pi/2)$), the (**D**) higher order Kerr effect (K_c, χ'_{qc}), the (**E**) timing of the long disentanglement pulse ($\hat{X}(\pi, N)$) and (**E**) decoherence rates of the qubit and cavity ($\Gamma_{q,c}$). To increase the visibility of small parity values, the colour brightness changes nonlinearly across the colourbar.

Magnus Approximation Model

Importantly, we observe that calculating the final state of our protocols using $\hat{R}_2(\pi, 0, 20\,\mathrm{ns})$ in place for $\hat{X}(\pi, N)$ in the disentanglement operation, in the absence of both K, χ', and qubit and cavity relaxation and decoherence, produces a bending distortion of the coherence fringes similar to that observed in Fig. 6.5A and Fig. 6.6A. For the qcmap protocol, the qualitative behaviour of the linecuts with increasing n_{th} observed in Fig. 6.5B is also reproduced by this model (Fig. 6.12).

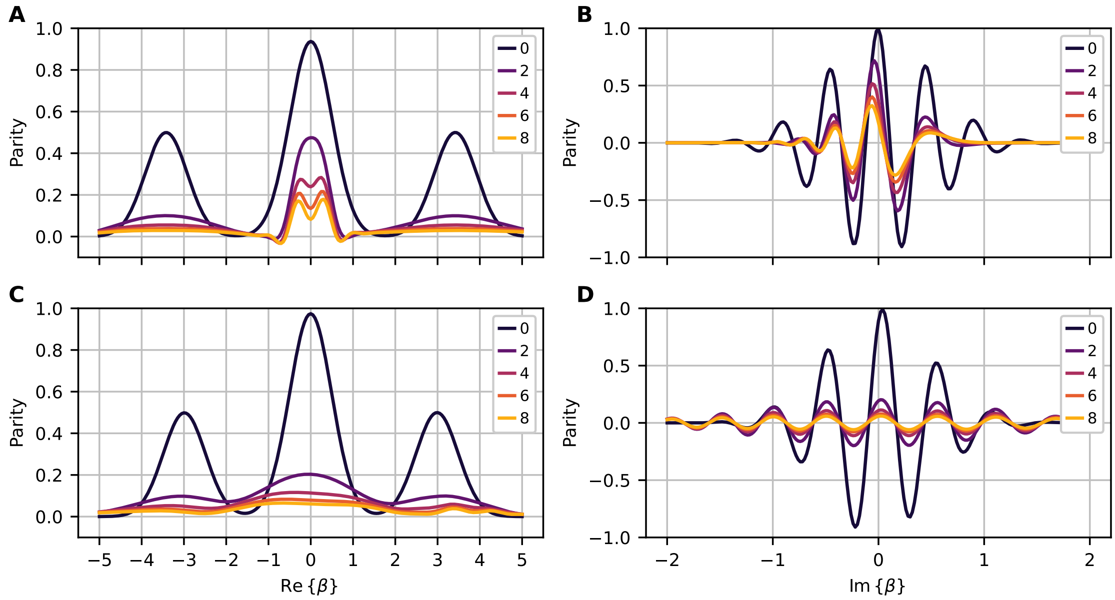

Figure 6.12: Magnus approximation model simulations. Simulated linecuts for qcmap (**A** and **B**) and ECD (**C** and **D**) across the cavity distributions (**A** and **C**) and fringes (**B** and **D**) of the hot cat state. The legend denotes the starting thermal state n_{th}. The simulations were done in a Kerr free, decoherence free and ideal unconditional qubit pulses. The simulated values of α and n_{th} are the same as the fitted experimental values in Fig. 6.5 and Fig. 6.6. The disentanglement pulse was replaced with the Magnus 2^{nd} order approximation operator for Gaussian operators, $\hat{R}_2(\pi, 0, 20\,\mathrm{ns})$. The linecuts across the (**A** and **C**) cavity distributions and (**B** and **D**) interference fringes illustrate the effect of the Gaussian pulse during the disentanglement on the final Hot Schrödinger cat state.

We note that using either the Magnus approximation model or numerical simulation of the Gaussian pulse will reach the same result.

We conclude that to prepare the interesting sharp and saturated phase-space features of $W_{\mathrm{qcmap}}(\beta)$ using the qcmap protocol, one would need to replace our Gaussian pulses with engineered pulses which achieve a disentanglement operator such as $\hat{X}(\pi, N) = \sum_{n=0}^{N} |n\rangle\langle n|\,\hat{\sigma}_x + \sum_{n=N+1}^{\infty} |n\rangle\langle n|$, in addition to minimising higher-order Kerr effects as well as decoherence.

6.6 Summary and Outlook

Our investigation proves that quantum superposition states with perfect quantum features (phase coherence, interference fringes) can be prepared from initial states of low purity (high temperature) without entropy removal up to an initial thermal photon occupation of $n_{\text{th}} = 7.6 \pm 0.2$ (cavity mode temperature $T = 1.78 \pm 0.04$ K). These values are to be compared to $\mathcal{P} = 0.9367(1)$, $n_{\text{th}} = 0.0338(7)$, $T = 63.7(4)$ mK when the cavity is in equilibrium with residual excitations in the experimental setup and the initial state can be considered pure.

The enabling feature of the demonstrated quantum state preparation protocols is the ability to imprint a deterministic phase difference between different components of the state. Purity, a global number of the quantum state, does not convey information about the presence of quantum features of a state. Rather, it is phase coherence, a non-global property of the state defined via the coherence function, which is a useful indicator of quantum features.

Although we have prepared the “hot cat states” (Garfield states) in a cQED setup, they are realisable in any continuous-variable quantum system. This holds particular relevance for systems where the quantum degree of freedom is intermittently in contact with a heat bath but where unitary dynamics otherwise take place. Examples include levitated optomechanical systems, where a laser or electric field is typically used for initialisation and measurement but turned off during quantum state preparation [166, 176–181]. Our investigation highlights that achieving a high purity of the initial state, e.g. through ground-state cooling, is not a necessary prerequisite for the preparation for a quantum state [166], but the required experimental resources and coherence time increase with the decreasing purity of the initial state.

The sharp, omnidirectional fringes in the phase space of the cavity for the hot qcmap cat state represent a distinctive feature with practical implications. These fringes exhibit a narrow width and a substantial gradient in all directions. This feature could have potential applications in force or displacement sensing. Moreover, the observation that the hot qcmap state always has fringes that take on perfect parity values might have practical advantages in quantum information processing protocols with bosonic modes. Further exploration of their utility in this context is a topic for future investigation.

The observed difference between the hot Schrödinger cat states produced by the two different protocols highlights the importance of the chosen pulse generation sequence, particularly in the presence of residual thermal photons. While echo pulses are conventionally integrated to refocus low-frequency qubit fluctuations, their impact on the cavity state should not be disregarded. This insight adds nuance to the understanding of state preparation protocols within the context of realistic experimental conditions specifically, the temperature of the bosonic mode.

Thermal noise coupling into a quantum system is unavoidable. This problem is made worse for optomechanical setups and other bosonic quantum systems. Due to the characteristic low mechanical frequencies, the mechanical modes often possess a substantial thermal population, rendering attainment of the ground state through cooling a challenging endeavour. Consequently, real-world experiments inherently possess some level of residual thermal population within the initial state.

To imprint a deterministic phase on the state, decoherence during the state preparation protocols must be limited. In our present experiments, the decoherence rates were so low that they could be neglected. It is interesting to consider how far, in terms of n_{th}, the present experimental method could be pushed. Improvements could be made by the use of a purpose-designed setup, which can mitigate imperfections from the disentanglement sequence by using larger displacements. Alternatively, the need for large displacements could be avoided by utilisation of the Kerr cat pulse generation sequence. While this method demands stronger higher-order terms in the Hamiltonian, it eliminates the necessity for a disentanglement step during the generation process.

The ‘burlesque’ character of Schrödinger’s thought experiment [1] arises in our opinion not only because of the size of the cat-box system, but also because the involved states of the cat are room temperature, highly mixed states, and the cat is strongly entangled with its environment before it is placed in a superposition. Nonetheless, quantum mechanical theory allows for quantum superposition states to be prepared from arbitrarily non-pure initial states, as long as the preparation itself is unitary. This remarkable, falsifiable assertion has hitherto received very little dedicated experimental investigation. We therefore see the preparation of increasingly hot Schrödinger cat states as a new potential direction for fundamental tests of quantum mechanics and the quantum-to-classical transition. Our reported experiment shows that this new line of investigation is immediately accessible for further laboratory investigation.

CHAPTER 7

Flexible Multi Qubit gates

Quantum algorithms' advantage over classical computers relies on the quantum properties of entanglement and superposition. In such algorithms, multi-qubit gates are a vital resource to produce such entanglement.

A proposal from Friis et. al. [71], demonstrates a scheme for implementing a flexible control unitary (Fig. 7.1). The proposed protocol allows for flexibility while retaining performance that is independent of the required control gate.

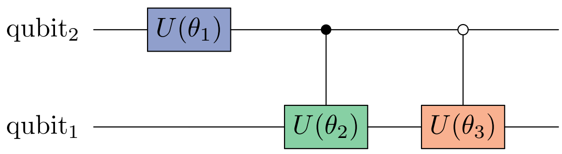

Figure 7.1: Simplified diagram of a two qubit gate protocol. Figure adapted from [71].

This scheme is modular, flexible and extendable to multiple qubits. The flexibility of the target unitary can reduce the number of pulses needed in an algorithm. The gate can be used to realise quantum switches, a novel tool that can open new fields of research explained in Sec. 7.5. Furthermore, the gate will have applications in quantum subroutines and learning algorithms [182].

In the first section, I describe the pulse sequence and technical requirements of the protocol on the superconducting circuits platform. In Sec. 7.2, I describe a modification to the protocol to account for experiment inaccuracies. Section 7.3 describes a proof of principle experiment that realises a simplified version of the full pulse protocol. Finally, I describe the imperfections in the experiment, possible improvements and some immediate applications of such gates.

7.1 Protocol

The flexible multi-qubit gate protocol uses qubits coupled via a high Q cavity acting as a quantum bus. The entire sequence is made up of fast, unselective displacement pulses on the cavity and both unconditional qubit rotations and cavity-photon number selective operations on the qubit.

The proposed protocol requires that the individual qubits are far detuned and have small direct coupling. The cavity is coupled to all qubits with a dispersive interaction between the n$^{\text{th}}$ qubit and the cavity being $\chi_{qn,c} = \frac{\chi_{1c}}{n}$. In the experiment, this can be achieved by in-situ tuning of the qubit frequency or effectively by introducing echo pulses during the time evolution.

The pulse sequence of the full gate protocol is shown in Fig. 7.2A with the phase space evolution of the system in Fig. 7.2B.

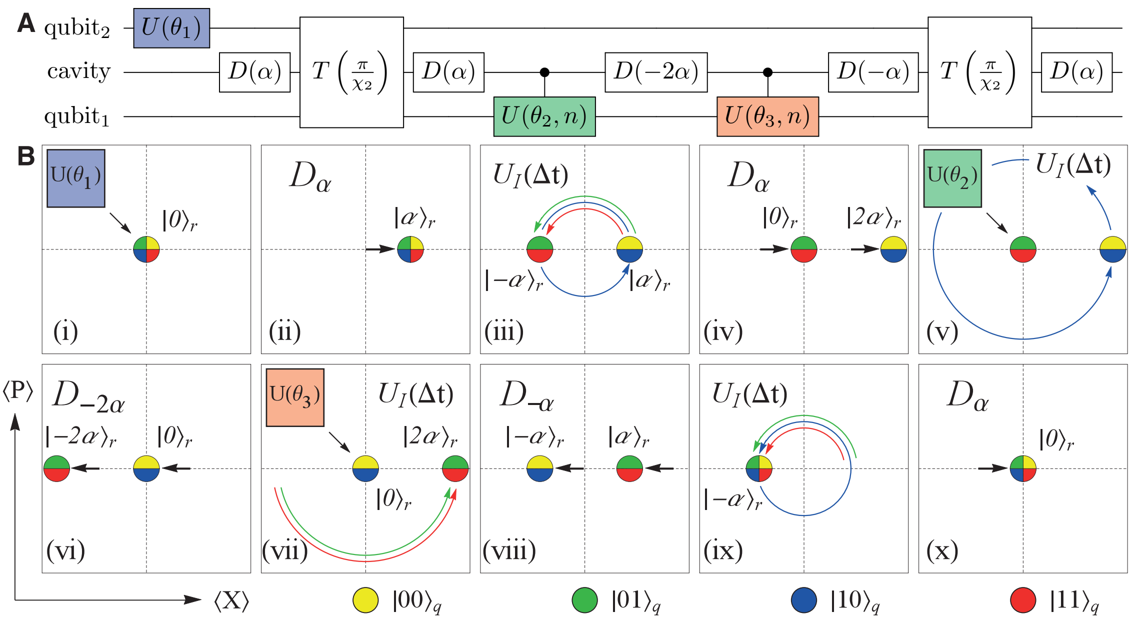

Figure 7.2: Full proposed protocol for flexible two qubit gates. (**A**) Pulse sequence of ideal two qubit gate protocol. In this protocol, the coloured gates can be any single qubit gate. The flexible two qubit gate is realised by conditioning the target single qubit gate on zero photons in the cavity. By mapping the state of one qubit onto the cavity photon state, we can effectively implement two qubit gates. (**B**) Phase space evolution of the system during gate protocol. Figure taken from [71].

Consider some initial two qubit state and the cavity in the ground state with the couplings required. Here, qubit 1 and 2 are the target and control qubits respectively. First, qubit 2's state is mapped onto the cavity photon state via a process similar to the qcmap protocol

$$
\begin{aligned}
|c, q1, q2\rangle &= |0\rangle \otimes (a\,|00\rangle + b\,|01\rangle + c\,|10\rangle + d\,|11\rangle) && (7.1)\\
\hat{D}(\alpha) &: |\alpha\rangle \otimes (a\,|00\rangle + b\,|01\rangle + c\,|10\rangle + d\,|11\rangle) && (7.2)\\
\hat{T}\left(\frac{\pi}{\chi_2}\right) &: \left(a\,|\alpha 00\rangle + b\,|\alpha e^{-i\chi_2\left(\frac{\pi}{\chi_2}\right)} 01\rangle + c\,|\alpha e^{-i\chi_1\left(\frac{\pi}{\chi_2}\right)} 10\rangle + d\,|\alpha e^{-i(\chi_1+\chi_2)\left(\frac{\pi}{\chi_2}\right)} 11\rangle\right) && (7.3)\\
&= a\,|\alpha 00\rangle + b\,|-\alpha 01\rangle + c\,|\alpha 10\rangle + d\,|-\alpha 11\rangle && (7.4)\\
&= |\alpha\rangle_c \otimes (a\,|0\rangle + c\,|1\rangle)_1 \otimes |0\rangle_2 + |-\alpha\rangle_c \otimes (b\,|0\rangle + d\,|1\rangle)_1 \otimes |1\rangle_2 && (7.5)\\
\hat{D}(\alpha) &: |2\alpha\rangle_c \otimes (a\,|0\rangle + c\,|1\rangle)_1 \otimes |0\rangle_2 + |0\rangle_c \otimes (b\,|0\rangle + d\,|1\rangle)_1 \otimes |1\rangle_2 \,. && (7.6)
\end{aligned}
$$

During the time evolution, the states with qubit 2 in the excited state, gain a phase $e^{-i\pi}$. This is equivalent to the phase of the entangled coherent state to $|-\alpha\rangle$. Thus by doing another displacement pulse, the state of qubit 2 is mapped onto the cavity state. $|\psi\rangle = |\alpha\psi_1 0\rangle + |-\alpha\psi_1 1\rangle$. Next, operations on the second qubit are applied conditioned on the cavity photons

$$
\begin{aligned}
\hat{U}(\theta_2, n < N) &: |2\alpha\rangle_c \otimes (a\,|00\rangle + v\,|10\rangle) + |0\rangle_c \otimes \left(b'\,|01\rangle + d'\,|11\rangle\right) && (7.7)\\
\hat{D}(-2\alpha) &: |0\rangle_c \otimes (a\,|00\rangle + c\,|10\rangle) + |-2\alpha\rangle_c \otimes \left(b'\,|01\rangle + d'\,|11\rangle\right) && (7.8)\\
\hat{U}(\theta_3, n < N) &: |0\rangle_c \otimes \left(a'\,|00\rangle + c'\,|10\rangle\right) + |-2\alpha\rangle_c \otimes \left(b'\,|01\rangle + d'\,|11\rangle\right) && (7.9)
\end{aligned}
$$

where we have used $\hat{U}(\theta_2, n < N)(b\,|0\rangle_1 + d\,|1\rangle_1) = b'\,|0\rangle_1 + d'\,|1\rangle_c$ and likewise for $\hat{U}(\theta_3)$. The operations $\hat{U}(\theta_2)$ and $\hat{U}(\theta_3)$ acting on qubit 2 have to be selective on the ground state. The pulse's spectral width must not exceed $\sigma_f \ll |2\alpha|^2\chi_2$. During this time, the part of the cavity state in $|2\alpha\rangle_c$ will start rotating due to the dispersive shift. This can be accounted for by choosing the length of selective operations to be $\frac{\pi}{\chi_{1c}}$ and changing the phase of the displacement pulses afterwards.

Finally, the two qubit system is disentangled from the cavity by reversing the first part of the protocol

$$
\begin{aligned}
\hat{D}(\alpha) &: |\alpha\rangle_c \otimes \left(a'\,|00\rangle + c'\,|10\rangle\right) + |-\alpha\rangle_c \otimes \left(b'\,|01\rangle + d'\,|11\rangle\right) && (7.10)\\
&= a'\,|\alpha 00\rangle + b'\,|-\alpha 01\rangle + c'\,|\alpha 10\rangle + d'\,|-\alpha 11\rangle && (7.11)\\
\hat{T}\left(\frac{\pi}{\chi_2}\right) &: a'\,|\alpha 00\rangle + b'\,|-\alpha e^{-i\pi} 01\rangle + c'\,|\alpha e^{-i2\pi} 10\rangle + d'\,|-\alpha e^{-i3\pi} 11\rangle && (7.12)\\
&= |\alpha\rangle_c \otimes \left(a'\,|00\rangle + b'\,|01\rangle + c'\,|10\rangle + d'\,|11\rangle\right) && (7.13)\\
\hat{D}(-\alpha) &: |0\rangle_c \otimes \left(a'\,|00\rangle + b'\,|01\rangle + c'\,|10\rangle + d'\,|11\rangle\right). && (7.14)
\end{aligned}
$$

These operations are effectively a controlled gate between the two qubits with the cavity acting as a quantum bus. The total time taken of the protocol is $T_{\text{gate}} \approx \frac{4\pi}{\chi_2}$ and is dominated by the waiting time $\hat{T}\left(\frac{\pi}{\chi_2}\right)$ and the time for the selective pulses $\hat{U}_2$ and $\hat{U}_3$.

7.2 Echoed Protocol

A major obstacle in the protocol is the relative qubit-cavity dispersive coupling ratio needed. This requires in-situ fine-tuning of qubit frequencies that will also introduce added noise. χ ratios that are not carefully tuned will result in evolution times that are not consumerate and residual entanglement between the qubit and the high Q cavity mode.

An alternative method is to introduce an unconditional π pulse to the qubit 1 in the middle of the time evolution Eq. (7.3) (Fig. 7.3B). Effectively, this results in a circuit shown in Fig. 7.3A. The phase space evolution of the system during the echo sequence is illustrated in Fig. 7.3C.

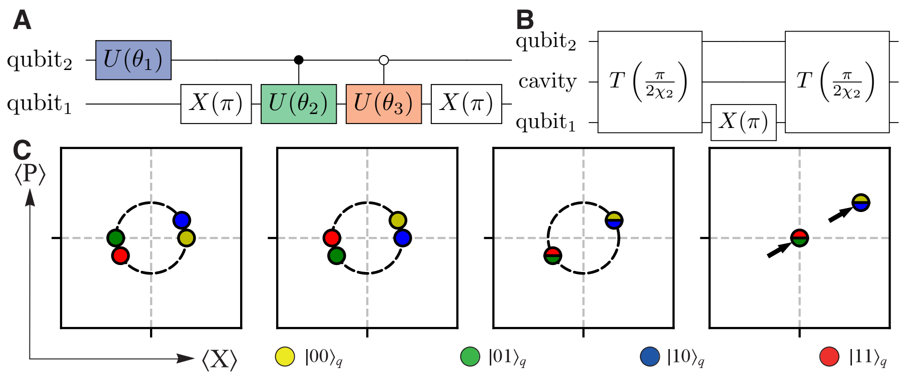

Figure 7.3: Echoed two qubit gate protocol. (**A**) Effective two qubit gate circuit of the protocol with an echo pulse. (**B**) Pulse sequence during one part of the evolution of the circuit in Eq. (7.3) where an echo pulsed is used to refocus the qubit states in the cavity phase space. (**C**) Phase space evolution of the system during echo sequence. The time evolution is split into two parts and an echo pulse is played on the target qubit. This will refocus the qubit states in phase space with only an overall phase term in the cavity state.

Written without considering geometric phase factors from $\hat{D}(\alpha)\,|\beta\rangle = |(\alpha+\beta)e^{i\mathrm{Im}\{\alpha\beta^*\}}\rangle$, the quantum system will evolve as follows

$$\hat{T}\left(\frac{\pi}{2\chi_2}\right) : a\,|\alpha 00\rangle + b\,|\alpha e^{-i\pi/2} 01\rangle + c\,|\alpha e^{-i\pi\frac{\chi_1}{2\chi_2}} 10\rangle + d\,|\alpha e^{-i\pi\frac{\chi_1+\chi_2}{2\chi_2}} 11\rangle \tag{7.15}$$

$$\hat{X}_1(\pi) : a\,|\alpha 10\rangle + b\,|\alpha e^{-i\pi/2} 11\rangle + c\,|\alpha e^{-i\pi\frac{\chi_1}{2\chi_2}} 00\rangle + d\,|\alpha e^{-i\pi\frac{\chi_1+\chi_2}{2\chi_2}} 01\rangle \tag{7.16}$$

$$\hat{T}\left(\frac{\pi}{2\chi_2}\right) : a\,|\alpha e^{-i\pi\frac{\chi_1}{2\chi_2}} 10\rangle + b\,|\alpha e^{-i\pi/2} e^{-i\pi\frac{\chi_1+\chi_2}{2\chi_2}} 11\rangle \tag{7.17}$$

$$+ c\,|\alpha e^{-i\pi\frac{\chi_1}{2\chi_2}} 00\rangle + d\,|\alpha e^{-i\pi\frac{\chi_1+\chi_2}{2\chi_2}} e^{-i\pi/2} 01\rangle \tag{7.18}$$

$$= a\,|\alpha e^{-i\pi\frac{\chi_1}{2\chi_2}} 10\rangle + b\,|\alpha e^{-i\pi/2} e^{-i\pi\frac{\chi_1+\chi_2}{2\chi_2}} 11\rangle \tag{7.19}$$

$$+ c\,|\alpha e^{-i\pi\frac{\chi_1}{2\chi_2}} 00\rangle + d\,|\alpha e^{-i\pi\frac{\chi_1+\chi_2}{2\chi_2}} e^{-i\pi/2} 01\rangle \tag{7.20}$$

$$= a\,|\alpha' 10\rangle + b\,|-\alpha' 11\rangle + c\,|\alpha' 00\rangle + d\,|-\alpha' 01\rangle \tag{7.21}$$

$$= \left[|\alpha'\rangle_c \otimes (a\,|1\rangle + c\,|0\rangle)_1 \otimes |0\rangle_2 + |-\alpha'\rangle_c \otimes (b\,|1\rangle + d\,|0\rangle)_1 \otimes |1\rangle_2\right] \tag{7.22}$$

where the global phase on the high Q cavity state has been included in $|\alpha'\rangle = |\alpha e^{-i\pi\frac{\chi_1}{2\chi_2}}\rangle$. This phase factor can be accounted for by a simple rotation of the cavity frame. These phase factors do not change the important dynamics of the gate and can be accounted for by a change in the phase of the cavity or qubit pulse. The echo pulse will refocus the evolution of the cavity-qubit states. This echo pulse has to be used during the steps that take a longer time such as both time evolution steps and both $\hat{U}(\theta_2)$ and $\hat{U}(\theta_3)$ gates.

7.3 Simplified Experiment

In a proof-of-principle experiment, the pulse sequence up to the first conditional $\hat{U}(\theta_2)$ pulse was carried out. The experiment was repeated for different initial qubit states and the different amplitudes of the target unitary. This results in a final state given by $|\psi\rangle = \hat{X}(\pi)\hat{X}(\pi)\,|\psi\rangle_1 \otimes |0\rangle_2 + \hat{X}(\pi)\hat{U}(\theta_2)\hat{X}(\pi)\,|\psi\rangle_1 \otimes |1\rangle_2$.

To understand the action of the two qubit gate, we can limit the target unitary and consider the different initial states of the two qubits. This is presented as a logic table table 7.1

Initial State		$\hat{U}(\theta_2)$	$\|\psi\rangle_f$
$\|\text{target}\rangle_i$	$\|\text{control}\rangle_i$		
$\|0\rangle$	$\|0\rangle$	$\hat{X}$	$\|00\rangle$
$\|0\rangle$	$\|1\rangle$	$\hat{X}$	$\|11\rangle$
$\|1\rangle$	$\|0\rangle$	$\hat{X}$	$\|10\rangle$
$\|1\rangle$	$\|1\rangle$	$\hat{X}$	$\|01\rangle$
$\|0\rangle$	$\|\pm\rangle$	$\hat{X}$	$\|\Phi^{\pm}\rangle$
$\|1\rangle$	$\|\pm\rangle$	$\hat{X}$	$\|\psi^{\pm}\rangle$

Table 7.1: Two qubit gate logic table. In this example, the target unitary is an $\hat{X}$ gate that implements a CNOT gate.

Here, the chosen target unitary is a $\hat{U}(\theta_2) = \hat{X}$. The strength of the protocol is that the target unitary is not fixed to any specific single qubit gate unitary. Thus, we can easily do any controlled Rabi oscillation on the target qubit without adding or changing any other of the qubit or the cavity pulses.

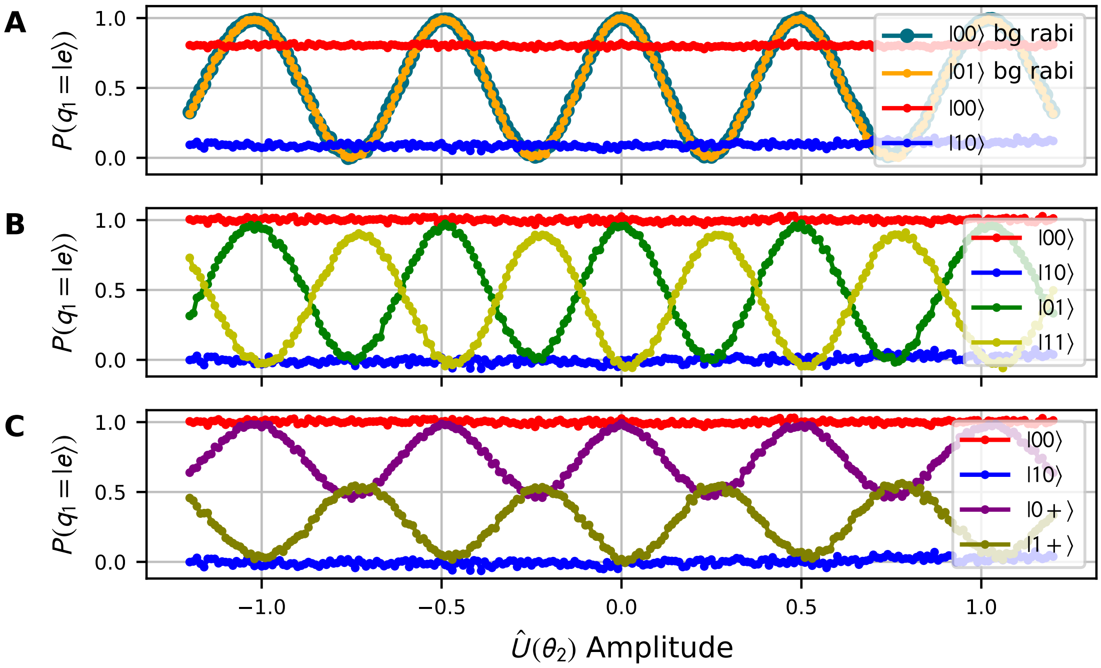

Figure 7.4: Flexible target unitary through controlled Rabi oscillations. The legend labels represent the initial state of the two qubit system $|\text{target}, \text{control}\rangle$. (**A**) Background Rabi oscillations on qubit 1 for different initial qubit 2 states. The offset between $|00\rangle$ and the maximum of the background Rabi measurements are due to residual entanglement between the high Q cavity and the qubit. This results in additional cross-Kerr to the readout resonator and a different readout contrast. These measurements are used to scale and account for the difference in readout contrast in the other measurements with the same initial qubit 2 state. (**B** and **C**) Controlled Rabi oscillations on qubit 1 for different initial states. The red and blue lines in the different plots serve as a visual guide as the two qubit gate has no action on these initial states. The green and yellow lines show full Rabi oscillations of qubit 1 when qubit 2 is excited. Similarly, for qubit 2 in the $|+\rangle$ eigenstate, the Rabi oscillations only have half the amplitude. At $\hat{U}(\theta_2) = 0.25$, the state is $\frac{1}{\sqrt{2}}(|00\rangle + |11\rangle)$.

Fig. 7.4A shows the background measurements used to scale the subsequent measurements. Normal Rabi oscillations are done on qubit 1 for different initial states of qubit 2. There is a small difference in readout levels due to cross-Kerr terms between qubit 2 and the readout resonator for qubit 1. These levels are used to scale and account for the difference in readout contrast for the measurements according to the initial state of qubit 2. For the qubit system in $|\psi_1 0\rangle$, the two qubit gate does not have any action on the qubits. The difference in readout level is due to the imperfect disentanglement between the high Q cavity and the qubit system. Photons in the high Q cavity, through the cross-Kerr effect, will shift the optimal readout point for the readout resonator.

Fig. 7.4B and C show Rabi oscillations with amplitudes that follow the truth table. This demonstrates the realisation of the flexible target unitary. The green and yellow lines show full Rabi oscillations of qubit 1 when qubit 2 is excited. Similarly, for qubit 2 in the $|+\rangle$ eigenstate, the Rabi oscillations only have half the amplitude. At $\hat{U}(\theta_2) = 0.25$, the state is $\frac{1}{\sqrt{2}}(|00\rangle + |11\rangle)$.In the next section, imperfections in the experiment and possible improvements are discussed.

7.4 Imperfections and Improvements

Imperfections arise from residual cavity photons that cause incomplete disentanglement between the qubit and cavity states. This can be due to the cavity self-Kerr effect or the qubit-qubit coupling.

To first order, the Kerr effect will be a detuning of the cavity frequency and can be accounted for with a phase change of the cavity frame, $\phi \approx \frac{nK}{2\chi_2}$. However, the full Kerr effect and higher-order terms such as χ' cannot be easily accounted for and require additional correction pulses.

The unwanted terms, K, χ' and qubit-qubit coupling χ_{q1q2} scale with the dispersive shift χ. For a larger χ, the qubit gate operation is faster while a small χ will cause the higher order effects to reduce. A balance must be found between the qubit coherence time and interactions due to higher-order effects. We can compare the speed of operations, bounded by χ to the higher-order terms parameterised by K. Using Eq. (3.11), we can calculate the relative ratio $\frac{\chi}{K}$ for a particular coupling strength g and qubit anharmonicity α. Thus, to reduce the unwanted interaction terms, we can use a regime of smaller χ.

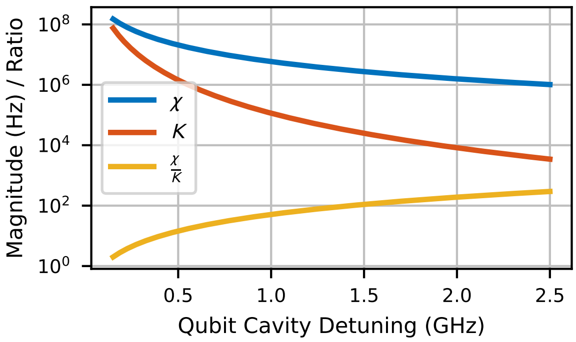

Figure 7.5: Comparision of χ and K magnitudes. Plot of magnitudes of χ (blue) which determines the speed of the operation and K (red) which determines the unwanted terms against qubit-cavity detuning. We want to maximise the χ/K ratio (yellow) while not being limited by qubit relaxation time or decoherence time. Not accounted for in the plot is the effect of χ' which is a comparable effect to the Kerr effect. Here, $\alpha/2\pi = 150\,\mathrm{MHz}$ and $g/2\pi = 150\,\mathrm{MHz}$.

Another improvement is to use optimal control for the state transfer during the evolution times of the protocol. A closed-loop routine can account for such higher order unwanted terms. However, the optimiser needs to work on a state transfer and not a state preparation. This means that the optimised gate must work on all possible input states and their superpositions. While this increases the complexity of the optimisation process, methods used in Sec. 5.4 can be adapted to improve the fidelity of the state transfer.

Currently, two qubit gates can have a gate fidelity benchmark by doing process tomography [72, 183] or interleaved randomised benchmarking [184]. Process tomography is done by initialising all possible input states and for every input state, do state tomography of the output state of the target gate. This method is very resource-intensive to determine the gate fidelity. Interleaved randomised benchmarking involves applying random pulses to the qubit system that are interleaved with the two qubit gate. The decay of coherence with the number of gates applied is a proxy function of the gate fidelity.

The flexibility of the controlled unitary gate places a question on the difficulty of placing a fidelity of the controlled gate. The strength of the scheme is its possibility to do any controlled unitary. While it is possible to determine the gate fidelity for a particular target gate, there has yet to be a defined metric on the fidelity on the set of all possible two qubit gates that can be applied.

7.5 Summary and Outlook

With qubit coherence improvements and an experimental parameter regime with lower higher order effects, the complete multi-qubit gate protocol can be realised with small errors. The gate is fundamentally different as it can realise all possible controlled single qubit gate unitary. Thus, a simple gate or process fidelity does not capture the full capability of the realised flexible gate. A new method of benchmarking such flexible gates should be considered.

One immediate application of a flexible target unitary is the operation of a quantum switch [185, 186]. In quantum mechanics, it is possible to use a time-like superposition of quantum gates. This means a coherent control of the order of a quantum circuit applied to one qubit conditioned on the state of another qubit.

The order of gates $\hat{U}_1$ and $\hat{U}_2$ are controlled by another qubit. For a two qubit system, the operator implements the gate $|\psi_{\mathrm{control}}\psi_{\mathrm{target}}\rangle = \alpha\hat{U}_1\hat{U}_2\,|0\psi_t\rangle + \beta\hat{U}_2\hat{U}_1\,|1\psi_t\rangle$. This can be implemented by the flexible multi-qubit gate protocol shown in Fig. 7.1 by choosing $\hat{U}(\theta_1) = \hat{U}_1\hat{U}_2$ and $\hat{U}(\theta_2) = \hat{U}_2\hat{U}_1$.

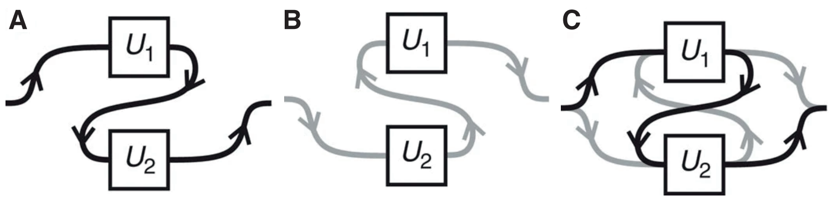

Figure 7.6: Working principle of the quantum switch. The order of gates $\hat{U}_1$ and $\hat{U}_2$ are controlled by another qubit. For a two qubit system, the operator implements the gate $|\psi_{\mathrm{control}}\psi_{\mathrm{target}}\rangle = \alpha\hat{U}_1\hat{U}_2\,|0\psi_t\rangle + \beta\hat{U}_2\hat{U}_1\,|1\psi_t\rangle$. This can be realised with the flexible multi-qubit gate protocol shown in Fig. 7.1, by choosing $\hat{U}(\theta_1) = \hat{U}_1\hat{U}_2$ and $\hat{U}(\theta_2) = \hat{U}_2\hat{U}_1$. Figure from [187].

This novel resource is a useful tool to open new research avenues such as in fundamental science in studying quantum causal structures [185, 186], quantum error mitigation protocols [188], quantum communication [189–191], quantum computation [187, 192].

An exciting use case is for quantum error mitigation [188]. The protocol considers the operator in which $\hat{U}(\theta_1) = \hat{U}(\theta_2)$, the action of the two qubit gate will split the quantum system into two possible quantum channels. The recombination of the two channels allows for constructive or destructive interference of errors that occur in the quantum system. Thus, allows for the study of possible phase differences between the two quantum channels.

CHAPTER 8

Conclusions and Outlook

In this thesis, I have introduced a setup for fundamental quantum physics research with bosonic modes. The platform was built to realise vastly different experiments. This was possible with the help of many internal and external collaborators. In the following paragraphs, I outline the anticipated results in the near future and pose some further research questions.

Part 1: Concept and Characterisation. In chapter 2, 3 and 4, I introduced and outlined the working principles of the superconducting circuits with high Q cavities platform and characterisation of experiments. I improved on key areas for the next generation development of the platform. This includes a more efficient superconducting flux hose design (Sec. 4.1) and a modular Purcell filter with an integrated SMA pin for 3D architectures (Sec. 3.6). Finally, the ongoing efforts in optimisation of qubit fabrication and adopting Tantalum qubits with longer lifetimes will improve the experiment results.

Part 2: Quantum Superpositions. In chapter 5, I demonstrate the different ways to form Schrödinger cat states in a bosonic mode. These cat states are a useful quantum resource and are the basis of many other experiments such as quantum error correction protocols and quantum meteorology. To improve the preparation of such cat states, I used closed-loop optimisation on a bosonic mode. However, measuring the bosonic mode is resource-intensive due to the fundamental problem of enormous Hilbert space. Thus, a figure of merit was carefully chosen as a proxy for the state fidelity of the bosonic state. With closed-loop optimisation, state preparation fidelity was improved and the optimised pulses can be used to understand the imperfections of the system. While the optimisation was done on a cat state, the novel and general method can also be used for optimising the preparation of many other complex states and platforms.

Part 3: Quantum Superpositions of Thermal States. In chapter 6, I explore the fundamental question of forming quantum superpositions of a mixed state. The results show that thermal states with low purity can still be used to form states with quantum features and high visibility. The formation of quantum superpositions of low purity states demonstrates that coherence, rather than purity, is the crucial ingredient for the "quantum-ness" of a state.

The existence of the hot cat state poses many follow-up research directions:

We can consider if such hot cat states can be a resource for quantum computation and quantum meteorology. The results show that there are at least 2 types of hot cat states and that they have the same lifetime as their cold counterparts. Furthermore, the sharp features of the hot qcmap cat state could be used for highly sensitive displacement measurements. This also poses a more fundamental question of how increasing the noise of the system might improve the sensitivity of the state.

While these experiments were performed on a cQED setup, the results can be applied to any bosonic system. Such as in optomechanics setups, where a big challenge is the cooling of the quantum system to the ground state. The existence of hot cat states shows that reaching the ground state is not a strict condition for quantum features. Thus, this alleviates the obstacles to forming a cat state with mechanical systems.

Fundamentally, the theoretical results do not place a fundamental limit on how hot the thermal state can be. The experimental results were limited only by instrumental constraints. With the setup used, we could reach a cavity mode temperature of 1.8 K which is sixty times larger than its physical temperature. Given an improved experimental setup of smaller coupling ratios χ, we can explore what is the hottest thermal state superposition achievable.

Part 4: Flexible Multi-qubit Gate. Finally, in chapter 7, based on the gate protocol in [71], I demonstrate a proof of principle experiment to achieve a flexible multi-qubit gate. This method uses the high Q cavity as a quantum bus for flexible conditional qubit operations.

The gate is fundamentally different with respect to other fixed two-qubit gates as it can realise any possible controlled single-qubit gate unitary. Thus, a simple gate or process fidelity does not capture the full capability of the realised flexible gate. A new method of benchmarking such flexible gates should be considered.

The most exciting application is the quantum switch gate [185, 186]. The superposition of the order of quantum gates is a novel tool that opens new research areas. The possible application covers a wide area which includes fundamental studies in quantum causality [185], quantum communication [191], quantum computation [187, 192], and quantum error mitigation [188].

Final Remarks The large Hilbert space of bosonic modes allows for investigating complex quantum phenomena while being hardware-efficient. The coherence and controllability of bosonic modes are unique to superconducting circuits. The field of using bosonic modes in quantum computing has many possible research directions and it is still possible to find novel and exciting fundamental research or expand the rich circuit QED toolbox.

Bibliography

[1] E. Schrödinger, "Die gegenwärtige Situation in der Quantenmechanik", Naturwissenschaften **23**, 807 (1935).

[2] S. Deléglise, I. Dotsenko, C. Sayrin, J. Bernu, M. Brune, J.-M. Raimond, and S. Haroche, "Reconstruction of non-classical cavity field states with snapshots of their decoherence", Nature **455**, 510 (2008).

[3] C. Monroe, D. M. Meekhof, B. E. King, and D. J. Wineland, "A "schrödinger cat" superposition state of an atom", Science **272**, 1131 (1996).

[4] Z. Leghtas, G. Kirchmair, B. Vlastakis, M. H. Devoret, R. J. Schoelkopf, and M. Mirrahimi, "Deterministic protocol for mapping a qubit to coherent state superpositions in a cavity", Physical Review A **87**, 042315 (2013).

[5] P. W. Shor, "Polynomial-time algorithms for prime factorization and discrete logarithms on a quantum computer", SIAM Journal on Computing **26**, 1484 (1997).

[6] A. Ambainis, K. Balodis, J. Iraids, M. Kokainis, K. Prūsis, and J. Vihrovs, in *Proceedings of the 2019 Annual ACM-SIAM Symposium on Discrete Algorithms (SODA)* (2019) pp. 1783–1793.

[7] N. Moll, P. Barkoutsos, L. S. Bishop, J. M. Chow, A. Cross, D. J. Egger, S. Filipp, A. Fuhrer, J. M. Gambetta, M. Ganzhorn, A. Kandala, A. Mezzacapo, P. Müller, W. Riess, G. Salis, J. Smolin, I. Tavernelli, and K. Temme, "Quantum optimization using variational algorithms on near-term quantum devices", Quantum Science and Technology **3**, 030503 (2018).

[8] "The quantum state of affairs", Nature Physics **19**, 605 (2023).

[9] Google Quantum AI, R. Acharya, I. Aleiner, R. Allen, T. I. Andersen, M. Ansmann, F. Arute, K. Arya, A. Asfaw, J. Atalaya, R. Babbush, D. Bacon, J. C. Bardin, J. Basso, A. Bengtsson, S. Boixo, G. Bortoli, A. Bourassa, J. Bovaird, L. Brill, M. Broughton, B. B. Buckley, D. A. Buell, T. Burger, B. Burkett, N. Bushnell, Y. Chen, Z. Chen, B. Chiaro, J. Cogan, R. Collins, P. Conner, W. Courtney, A. L. Crook, B. Curtin, D. M. Debroy, A. Del Toro Barba, S. Demura, A. Dunsworth, D. Eppens, C. Erickson, L. Faoro, E. Farhi, R. Fatemi, L. Flores Burgos, E. Forati, A. G. Fowler, B. Foxen, W. Giang, C. Gidney, D. Gilboa, M. Giustina, A. Grajales Dau, J. A. Gross, S. Habegger, M. C. Hamilton, M. P. Harrigan, S. D. Harrington, O. Higgott, J. Hilton, M. Hoffmann, S. Hong, T. Huang, A. Huff, W. J. Huggins, L. B. Ioffe, S. V. Isakov, J. Iveland, E. Jeffrey, Z. Jiang, C. Jones, P. Juhas, D. Kafri, K. Kechedzhi, J. Kelly, T. Khattar, M. Khezri, M. Kieferová, S. Kim, A. Kitaev, P. V. Klimov, A. R. Klots, A. N. Korotkov, F. Kostritsa, J. M. Kreikebaum, D. Land-

huis, P. Laptev, K.-M. Lau, L. Laws, J. Lee, K. Lee, B. J. Lester, A. Lill, W. Liu, A. Locharla, E. Lucero, F. D. Malone, J. Marshall, O. Martin, J. R. McClean, T. McCourt, M. McEwen, A. Megrant, B. Meurer Costa, X. Mi, K. C. Miao, M. Mohseni, S. Montazeri, A. Morvan, E. Mount, W. Mruczkiewicz, O. Naaman, M. Neeley, C. Neill, A. Nersisyan, H. Neven, M. Newman, J. H. Ng, A. Nguyen, M. Nguyen, M. Y. Niu, T. E. O'Brien, A. Opremcak, J. Platt, A. Petukhov, R. Potter, L. P. Pryadko, C. Quintana, P. Roushan, N. C. Rubin, N. Saei, D. Sank, K. Sankaragomathi, K. J. Satzinger, H. F. Schurkus, C. Schuster, M. J. Shearn, A. Shorter, V. Shvarts, J. Skruzny, V. Smelyanskiy, W. C. Smith, G. Sterling, D. Strain, M. Szalay, A. Torres, G. Vidal, B. Villalonga, C. Vollgraff Heidweiller, T. White, C. Xing, Z. J. Yao, P. Yeh, J. Yoo, G. Young, A. Zalcman, Y. Zhang, and N. Zhu, "Suppressing quantum errors by scaling a surface code logical qubit", Nature **614**, 676 (2023).

[10] Y. Kim, A. Eddins, S. Anand, K. X. Wei, E. Van Den Berg, S. Rosenblatt, H. Nayfeh, Y. Wu, M. Zaletel, K. Temme, and A. Kandala, "Evidence for the utility of quantum computing before fault tolerance", Nature **618**, 500 (2023).

[11] Q. Xu, J. K. Iverson, F. G. S. L. Brandão, and L. Jiang, "Engineering fast bias-preserving gates on stabilized cat qubits", Phys. Rev. Res. **4**, 013082 (2022).

[12] M. Dupont, B. Evert, M. J. Hodson, B. Sundar, S. Jeffrey, Y. Yamaguchi, D. Feng, F. B. Maciejewski, S. Hadfield, M. S. Alam, Z. Wang, S. Grabbe, P. A. Lott, E. G. Rieffel, D. Venturelli, and M. J. Reagor, "Quantum-enhanced greedy combinatorial optimization solver", Science Advances **9**, eadi0487 (2023).

[13] C. Berdou, A. Murani, U. Réglade, W. Smith, M. Villiers, J. Palomo, M. Rosticher, A. Denis, P. Morfin, M. Delbecq, T. Kontos, N. Pankratova, F. Rautschke, T. Peronnin, L.-A. Sellem, P. Rouchon, A. Sarlette, M. Mirrahimi, P. Campagne-Ibarcq, S. Jezouin, R. Lescanne, and Z. Leghtas, "One hundred second bit-flip time in a two-photon dissipative oscillator", PRX Quantum **4**, 020350 (2023).

[14] V. V. Sivak, A. Eickbusch, B. Royer, S. Singh, I. Tsioutsios, S. Ganjam, A. Miano, B. L. Brock, A. Z. Ding, L. Frunzio, S. M. Girvin, R. J. Schoelkopf, and M. H. Devoret, "Real-time quantum error correction beyond break-even", Nature **616**, 50 (2023).

[15] Z. Ni, S. Li, X. Deng, Y. Cai, L. Zhang, W. Wang, Z.-B. Yang, H. Yu, F. Yan, S. Liu, C.-L. Zou, L. Sun, S.-B. Zheng, Y. Xu, and D. Yu, "Beating the break-even point with a discrete-variable-encoded logical qubit", Nature **616**, 56 (2023).

[16] C. S. Wang, J. C. Curtis, B. J. Lester, Y. Zhang, Y. Y. Gao, J. Freeze, V. S. Batista, P. H. Vaccaro, I. L. Chuang, L. Frunzio, L. Jiang, S. M. Girvin, and R. J. Schoelkopf, "Efficient multiphoton sampling of molecular vibronic spectra on a superconducting bosonic processor", Phys. Rev. X **10**, 021060 (2020).

[17] K. S. Chou, J. Z. Blumoff, C. S. Wang, P. C. Reinhold, C. J. Axline, Y. Y. Gao, L. Frunzio, M. H. Devoret, L. Jiang, and R. J. Schoelkopf, "Deterministic teleportation of a quantum gate between two logical qubits", Nature **561**, 368 (2018).

[18] D. M. Pozar, “Microwave engineering”, 4th ed. (Wiley, Hoboken, NJ, 2012).

[19] S. Casulleras, C. Gonzalez-Ballestero, P. Maurer, J. J. García-Ripoll, and O. Romero-Isart, “Remote Individual Addressing of Quantum Emitters with Chirped Pulses”, Physical Review Letters **126**, 103602 (2021).

[20] M. Zanner, R. Albert, E. I. Rosenthal, S. Casulleras, I. Yang, C. M. F. Schneider, K. W. Lehnert, O. Romero-Isart, and G. Kirchmair, “Spatial addressing of qubits in a dispersive waveguide” (2024), unpublished.

[21] M. A. Nielsen and I. L. Chuang, “Quantum computation and quantum information”, 10th ed. (Cambridge University Press, Cambridge ; New York, 2010).

[22] M. Fox, “Quantum optics: An introduction”, Oxford Master Series in Physics (OUP Oxford, 2006).

[23] S. Haroche and J.-M. Raimond, “Exploring the quantum: Atoms, cavities, and photons” (Oxford University Press, 2006).

[24] B. M. Vlastakis, “Controlling coherent state superpositions with superconducting circuits”, Ph.D. thesis, Yale University, Yale (2015).

[25] C. M. F. Schneider, “Magnetic Coupling between Superconducting Circuits and a Cantilever”, Ph.D. thesis, University of Innsbruck (2021).

[26] O. Gargiulo, “Superconducting 3D transmons”, Ph.D. thesis, University of Innsbruck (2021).

[27] I. Yang, “Flux bias control in a coaxial superconducting qubit architecture”, Master thesis, Oxford University (2019).

[28] A. Blais, A. L. Grimsmo, S. M. Girvin, and A. Wallraff, “Circuit quantum electrodynamics”, Rev. Mod. Phys. **93**, 025005 (2021).

[29] U. Fano, “Description of states in quantum mechanics by density matrix and operator techniques”, Rev. Mod. Phys. **29**, 74 (1957).

[30] S. Cao, M. Bakr, G. Campanaro, S. D. Fasciati, J. Wills, D. Lall, B. Shteynas, V. Chidambaram, I. Rungger, and P. Leek, “Emulating two qubits with a four-level transmon qudit for variational quantum algorithms” (2023), arXiv:2303.04796.

[31] D. J. Griffiths and D. F. Schroeter, “Introduction to quantum mechanics”, 3rd ed. (Cambridge University Press, 2018).

[32] L. Hu, Y. Ma, W. Cai, X. Mu, Y. Xu, W. Wang, Y. Wu, H. Wang, Y. P. Song, C.-L. Zou, S. M. Girvin, L.-M. Duan, and L. Sun, “Quantum error correction and universal gate set operation on a binomial bosonic logical qubit”, Nature Physics **15**, 503 (2019).

[33] N. Lu, “Effects of dissipation on photon statistics and the lifetime of a pure number state”, Phys. Rev. A **40**, 1707 (1989).

[34] H. Wang, M. Hofheinz, M. Ansmann, R. C. Bialczak, E. Lucero, M. Neeley, A. D. O’Connell, D. Sank, J. Wenner, A. N. Cleland, and J. M. Martinis, “Measurement of the decay of fock states in a superconducting quantum circuit”, Phys. Rev. Lett. **101**, 240401 (2008).

[35] E. Schrödinger, “Der stetige Übergang von der mikro- zur makromechanik”, Naturwissenschaften **14**, 664 (1926).

[36] N. Ofek, A. Petrenko, R. Heeres, P. Reinhold, Z. Leghtas, B. Vlastakis, Y. Liu, L. Frunzio, S. M. Girvin, L. Jiang, M. Mirrahimi, M. H. Devoret, and R. J. Schoelkopf, “Extending the lifetime of a quantum bit with error correction in superconducting circuits”, Nature **536**, 441 (2016).

[37] J. Sakurai and J. Napolitano, “Modern quantum mechanics” (Cambridge University Press, 2020).

[38] D. F. Walls and G. J. Milburn, “Quantum optics”, 2nd ed. (Springer, Berlin, 2008).

[39] A. Royer, “Wigner function as the expectation value of a parity operator”, Phys. Rev. A **15**, 449 (1977).

[40] M. H. Michael, M. Silveri, R. T. Brierley, V. V. Albert, J. Salmilehto, L. Jiang, and S. M. Girvin, “New class of quantum error-correcting codes for a bosonic mode”, Phys. Rev. X **6**, 031006 (2016).

[41] M. Tinkham, “Introduction to Superconductivity”, 2nd ed. (Dover Publications Inc., New York, 2004).

[42] J. Annett, “Superconductivity, superfluids and condensates”, Oxford Master Series in Physics (OUP Oxford, 2004).

[43] M. Devoret, B. Huard, R. Schoelkopf, and L. F. Cugliandolo, “Ecole de physique des houches 2011 - quantum machines: Measurement control of engineered quantum systems” (2011).

[44] B. Josephson, “Possible new effects in superconductive tunnelling”, Physics Letters **1**, 251 (1962).

[45] B. D. Josephson, “The discovery of tunnelling supercurrents”, Rev. Mod. Phys. **46**, 251 (1974).

[46] D. G. Atanasova, “Fabrication and Characterization of a Dimer Josephson Junction Array Amplifier”, Master thesis, University of Innsbruck (2020).

[47] V. Bouchiat, D. Vion, P. Joyez, D. Esteve, and M. H. Devoret, "Quantum coherence with a single cooper pair", Physica Scripta **1998**, 165 (1998).

[48] M. Metcalfe, E. Boaknin, V. Manucharyan, R. Vijay, I. Siddiqi, C. Rigetti, L. Frunzio, R. J. Schoelkopf, and M. H. Devoret, "Measuring the decoherence of a quantronium qubit with the cavity bifurcation amplifier", Phys. Rev. B **76**, 174516 (2007).

[49] A. A. Houck, J. Koch, M. H. Devoret, S. M. Girvin, and R. J. Schoelkopf, "Life after charge noise: recent results with transmon qubits", Quantum Information Processing **8**, 105 (2009).

[50] J. Koch, T. M. Yu, J. Gambetta, A. A. Houck, D. I. Schuster, J. Majer, A. Blais, M. H. Devoret, S. M. Girvin, and R. J. Schoelkopf, "Charge-insensitive qubit design derived from the cooper pair box", Phys. Rev. A **76**, 042319 (2007).

[51] A. Somoroff, Q. Ficheux, R. A. Mencia, H. Xiong, R. Kuzmin, and V. E. Manucharyan, "Millisecond coherence in a superconducting qubit", Phys. Rev. Lett. **130**, 267001 (2023).

[52] J. Gambetta, A. Blais, D. I. Schuster, A. Wallraff, L. Frunzio, J. Majer, M. H. Devoret, S. M. Girvin, and R. J. Schoelkopf, "Qubit-photon interactions in a cavity: Measurement induced dephasing and number splitting", Physical Review A **74**, 10.1103/PhysRevA.74.042318 (2006).

[53] E. Jaynes and F. Cummings, "Comparison of quantum and semiclassical radiation theories with application to the beam maser", Proceedings of the IEEE **51**, 89 (1963).

[54] J. Majer, J. M. Chow, J. M. Gambetta, J. Koch, B. R. Johnson, J. A. Schreier, L. Frunzio, D. I. Schuster, A. A. Houck, A. Wallraff, A. Blais, M. H. Devoret, S. M. Girvin, and R. J. Schoelkopf, "Coupling superconducting qubits via a cavity bus", Nature **449**, 443 (2007).

[55] J. Clarke and A. I. Braginski, "The SQUID Handbook" (Wiley-VCH, 2004).

[56] J. Braumüller, L. Ding, A. P. Vepsäläinen, Y. Sung, M. Kjaergaard, T. Menke, R. Winik, D. Kim, B. M. Niedzielski, A. Melville, J. L. Yoder, C. F. Hirjibehedin, T. P. Orlando, S. Gustavsson, and W. D. Oliver, "Characterizing and optimizing qubit coherence based on squid geometry", Phys. Rev. Appl. **13**, 054079 (2020).

[57] E. M. Purcell, "Proceedings of the american physical society", Phys. Rev. **69**, 674 (1946).

[58] A. A. Houck, J. A. Schreier, B. R. Johnson, J. M. Chow, J. Koch, J. M. Gambetta, D. I. Schuster, L. Frunzio, M. H. Devoret, S. M. Girvin, and R. J. Schoelkopf, "Controlling the spontaneous emission of a superconducting transmon qubit", Phys. Rev. Lett. **101**, 080502 (2008).

[59] D. T. Sank, “Fast, Accurate State Measurement in Superconducting Qubits”, Ph.D. thesis, University of California, Santa Barbara (2014).

[60] M. J. Reagor, “Superconducting Cavities for Circuit Quantum Electrodynamics”, Ph.D. thesis, Yale University, Yale (2015).

[61] M. D. Reed, B. R. Johnson, A. A. Houck, L. DiCarlo, J. M. Chow, D. I. Schuster, L. Frunzio, and R. J. Schoelkopf, “Fast reset and suppressing spontaneous emission of a superconducting qubit”, Applied Physics Letters **96**, 203110 (2010).

[62] E. Jeffrey, D. Sank, J. Y. Mutus, T. C. White, J. Kelly, R. Barends, Y. Chen, Z. Chen, B. Chiaro, A. Dunsworth, A. Megrant, P. J. J. O’Malley, C. Neill, P. Roushan, A. Vainsencher, J. Wenner, A. N. Cleland, and J. M. Martinis, “Fast accurate state measurement with superconducting qubits”, Phys. Rev. Lett. **112**, 190504 (2014).

[63] H. Yan, X. Wu, A. Lingenfelter, Y. J. Joshi, G. Andersson, C. R. Conner, M.-H. Chou, J. Grebel, J. M. Miller, R. G. Povey, H. Qiao, A. A. Clerk, and A. N. Cleland, “Broadband bandpass purcell filter for circuit quantum electrodynamics”, Applied Physics Letters **123**, 134001 (2023).

[64] N. T. Bronn, Y. Liu, J. B. Hertzberg, A. D. Córcoles, A. A. Houck, J. M. Gambetta, and J. M. Chow, “Broadband filters for abatement of spontaneous emission in circuit quantum electrodynamics”, Applied Physics Letters **107**, 172601 (2015).

[65] Y. Liu and A. A. Houck, “Quantum electrodynamics near a photonic bandgap”, Nature Physics **13**, 48 (2017).

[66] Y. Sunada, S. Kono, J. Ilves, S. Tamate, T. Sugiyama, Y. Tabuchi, and Y. Nakamura, “Fast readout and reset of a superconducting qubit coupled to a resonator with an intrinsic purcell filter”, Phys. Rev. Appl. **17**, 044016 (2022).

[67] I. Iakoupov and K. Koshino, “Saturable purcell filter for circuit quantum electrodynamics”, Phys. Rev. Res. **5**, 013148 (2023).

[68] Y. Sunada, K. Yuki, Z. Wang, T. Miyamura, J. Ilves, K. Matsuura, P. A. Spring, S. Tamate, S. Kono, and Y. Nakamura, “Photon-noise-tolerant dispersive readout of a superconducting qubit using a nonlinear purcell filter” (2023), arXiv:2309.04315 .

[69] S. H. Autler and C. H. Townes, “Stark effect in rapidly varying fields”, Phys. Rev. **100**, 703 (1955).

[70] D. I. Schuster, A. Wallraff, A. Blais, L. Frunzio, R.-S. Huang, J. Majer, S. M. Girvin, and R. J. Schoelkopf, “ac stark shift and dephasing of a superconducting qubit strongly coupled to a cavity field”, Phys. Rev. Lett. **94**, 123602 (2005).

[71] N. Friis, A. A. Melnikov, G. Kirchmair, and H. J. Briegel, “Coherent controlization using superconducting qubits”, Scientific Reports **5**, 18036 (2015).

[72] I. L. Chuang and M. A. Nielsen, “Prescription for experimental determination of the dynamics of a quantum black box”, Journal of Modern Optics **44**, 2455 (1997).

[73] P. Rembold, N. Oshnik, M. M. Müller, S. Montangero, T. Calarco, and E. Neu, “Introduction to quantum optimal control for quantum sensing with nitrogen-vacancy centers in diamond”, AVS Quantum Science **2**, 024701 (2020).

[74] P. Reinhold, “Controlling Error-Correctable Bosonic Qubits”, Ph.D. thesis, Yale University (2019).

[75] N. Khaneja, T. Reiss, C. Kehlet, T. Schulte-Herbrüggen, and S. J. Glaser, “Optimal control of coupled spin dynamics: design of nmr pulse sequences by gradient ascent algorithms”, Journal of Magnetic Resonance **172**, 296 (2005).

[76] N. Rach, M. M. Müller, T. Calarco, and S. Montangero, “Dressing the chopped-random-basis optimization: A bandwidth-limited access to the trap-free landscape”, Phys. Rev. A **92**, 062343 (2015).

[77] M. M. Müller, R. S. Said, F. Jelezko, T. Calarco, and S. Montangero, “One decade of quantum optimal control in the chopped random basis”, Reports on Progress in Physics **85**, 076001 (2022).

[78] S. Rosi, A. Bernard, N. Fabbri, L. Fallani, C. Fort, M. Inguscio, T. Calarco, and S. Montangero, “Fast closed-loop optimal control of ultracold atoms in an optical lattice”, Phys. Rev. A **88**, 021601 (2013).

[79] A. Omran, H. Levine, A. Keesling, G. Semeghini, T. T. Wang, S. Ebadi, H. Bernien, A. S. Zibrov, H. Pichler, S. Choi, J. Cui, M. Rossignolo, P. Rembold, S. Montangero, T. Calarco, M. Endres, M. Greiner, V. Vuletić, and M. D. Lukin, “Generation and manipulation of schrödinger cat states in rydberg atom arrays”, Science **365**, 570 (2019).

[80] P. Horowitz and W. Hill, “The art of electronics”, 2nd ed. (Cambridge University Press, Cambridge [England] ; New York, 1989).

[81] P. Krantz, M. Kjaergaard, F. Yan, T. P. Orlando, S. Gustavsson, and W. D. Oliver, “A Quantum Engineer’s Guide to Superconducting Qubits”, Applied Physics Reviews **6**, 021318 (2019).

[82] J. Blumoff, “Multiqubit experiments in 3D circuit quantum electrodynamics”, Ph.D. thesis, Yale University (2017).

[83] M. Zanner, “Coherent Control of Multi-Qubit Dark States in Waveguide Quantum Electrodynamics”, Ph.D. thesis, University of Innsbruck (2022).

[84] C. Wang, C. Axline, Y. Y. Gao, T. Brecht, L. Frunzio, M. H. Devoret, and R. J. Schoelkopf, “Surface participation and dielectric loss in superconducting qubits”, Applied Physics Letters **107**, 162601 (2015).

[85] H. Paik, D. I. Schuster, L. S. Bishop, G. Kirchmair, G. Catelani, A. P. Sears, B. R. Johnson, M. J. Reagor, L. Frunzio, L. Glazman, S. M. Girvin, M. H. Devoret, and R. J. Schoelkopf, "Observation of high coherence in Josephson junction qubits measured in a three-dimensional circuit QED architecture", Physical Review Letters **107** (2011).

[86] T. Brecht, Y. Chu, C. Axline, W. Pfaff, J. Z. Blumoff, K. Chou, L. Krayzman, L. Frunzio, and R. J. Schoelkopf, "Micromachined integrated quantum circuit containing a superconducting qubit", Phys. Rev. Appl. **7**, 044018 (2017).

[87] B. Aune, R. Bandelmann, D. Bloess, B. Bonin, A. Bosotti, M. Champion, C. Crawford, G. Deppe, B. Dwersteg, D. A. Edwards, H. T. Edwards, M. Ferrario, M. Fouaidy, P.-D. Gall, A. Gamp, A. Gössel, J. Graber, D. Hubert, M. Hüning, M. Juillard, T. Junquera, H. Kaiser, G. Kreps, M. Kuchnir, R. Lange, M. Leenen, M. Liepe, L. Lilje, A. Matheisen, W.-D. Möller, A. Mosnier, H. Padamsee, C. Pagani, M. Pekeler, H.-B. Peters, O. Peters, D. Proch, K. Rehlich, D. Reschke, H. Safa, T. Schilcher, P. Schmüser, J. Sekutowicz, S. Simrock, W. Singer, M. Tigner, D. Trines, K. Twarowski, G. Weichert, J. Weisend, J. Wojtkiewicz, S. Wolff, and K. Zapfe, "Superconducting tesla cavities", Phys. Rev. ST Accel. Beams **3**, 092001 (2000).

[88] A. Romanenko, R. Pilipenko, S. Zorzetti, D. Frolov, M. Awida, S. Belomestnykh, S. Posen, and A. Grassellino, "Three-dimensional superconducting resonators at $t = 20$ mk with photon lifetimes up to $\tau = 2$ s", Phys. Rev. Appl. **13**, 034032 (2020).

[89] L. Krayzmann, "Thin-film 3d resonators for superconducting quantum circuits", Ph.D. thesis, Yale University (2022).

[90] M. Reagor, W. Pfaff, C. Axline, R. W. Heeres, N. Ofek, K. Sliwa, E. Holland, C. Wang, J. Blumoff, K. Chou, M. J. Hatridge, L. Frunzio, M. H. Devoret, L. Jiang, and R. J. Schoelkopf, "Quantum memory with millisecond coherence in circuit qed", Phys. Rev. B **94**, 014506 (2016).

[91] S. Chakram, A. E. Oriani, R. K. Naik, A. V. Dixit, K. He, A. Agrawal, H. Kwon, and D. I. Schuster, "Seamless high-q microwave cavities for multimode circuit quantum electrodynamics", Phys. Rev. Lett. **127**, 107701 (2021).

[92] P. Heidler, C. M. F. Schneider, K. Kustura, C. Gonzalez-Ballestero, O. Romero-Isart, and G. Kirchmair, "Non-Markovian Effects of Two-Level Systems in a Niobium Coaxial Resonator with a Single-Photon Lifetime of 10 milliseconds", Physical Review Applied **16**, 034024 (2021).

[93] P. Heidler, "Improving the quality factor of coaxial quarterwave resonators", Master thesis, University of Innsbruck (2019).

[94] R. M. Foster, "A reactance theorem", Bell System Technical Journal **3**, 259 (1924).

[95] S. E. Nigg, H. Paik, B. Vlastakis, G. Kirchmair, S. Shankar, L. Frunzio, M. H. Devoret, R. J. Schoelkopf, and S. M. Girvin, “Black-box superconducting circuit quantization”, Physical Review Letters **108**, 240502 (2012).

[96] K. S. Chou, “Teleported operations between logical qubits in circuit”, Ph.D. thesis, Yale University (2018).

[97] S. Rasmussen, K. Christensen, S. Pedersen, L. Kristensen, T. Bækkegaard, N. Loft, and N. Zinner, “Superconducting circuit companion—an introduction with worked examples”, PRX Quantum **2**, 040204 (2021).

[98] Z. K. Minev, Z. Leghtas, S. O. Mundhada, L. Christakis, I. M. Pop, and M. H. Devoret, “Energy-participation quantization of Josephson circuits”, npj Quantum Information **7**, 131 (2021).

[99] J. M. Chow, “Quantum Information Processing with Superconducting Qubits”, Ph.D. thesis, Yale University (2010).

[100] J. M. Martinis, “Surface loss calculations and design of a superconducting transmon qubit with tapered wiring”, npj Quantum Information **8**, 26 (2022).

[101] D. Zöpfl, “Characterisation of stripline resonators in a waveguide”, Master thesis, University of Innsbruck (2017).

[102] V. Ambegaokar and A. Baratoff, “Tunneling between superconductors”, Phys. Rev. Lett. **10**, 486 (1963).

[103] Y. Y. Gao, M. A. Rol, S. Touzard, and C. Wang, “Practical guide for building superconducting quantum devices”, PRX Quantum **2**, 040202 (2021).

[104] L. J. Zeng, S. Nik, T. Greibe, P. Krantz, C. M. Wilson, P. Delsing, and E. Olsson, “Direct observation of the thickness distribution of ultra thin AlO_x barriers in Al/AlO_x /Al Josephson junctions”, Journal of Physics D: Applied Physics **48**, 395308 (2015).

[105] A. Osman, J. Fernández-Pendás, C. Warren, S. Kosen, M. Scigliuzzo, A. Frisk Kockum, G. Tancredi, A. Fadavi Roudsari, and J. Bylander, “Mitigation of frequency collisions in superconducting quantum processors”, Phys. Rev. Res. **5**, 043001 (2023).

[106] A. Bilmes, S. Volosheniuk, A. V. Ustinov, and J. Lisenfeld, “Probing defect densities at the edges and inside Josephson junctions of superconducting qubits”, npj Quantum Information **8**, 24 (2022).

[107] I. M. Pop, T. Fournier, T. Crozes, F. Lecocq, I. Matei, B. Pannetier, O. Buisson, and W. Guichard, “Fabrication of stable and reproducible submicron tunnel junctions”, Journal of Vacuum Science and Technology B **30**, 010607 (2012).

[108] J. Wenner, R. Barends, R. C. Bialczak, Y. Chen, J. Kelly, E. Lucero, M. Mariantoni, A. Megrant, P. J. J. O'Malley, D. Sank, A. Vainsencher, H. Wang, T. C. White, Y. Yin, J. Zhao, A. N. Cleland, and J. M. Martinis, "Surface loss simulations of superconducting coplanar waveguide resonators", Applied Physics Letters **99**, 113513 (2011).

[109] A. P. Read, B. J. Chapman, C. U. Lei, J. C. Curtis, S. Ganjam, L. Krayzman, L. Frunzio, and R. J. Schoelkopf, "Precision measurement of the microwave dielectric loss of sapphire in the quantum regime with parts-per-billion sensitivity", Phys. Rev. Appl. **19**, 034064 (2023).

[110] G. Marchegiani, L. Amico, and G. Catelani, "Quasiparticles in superconducting qubits with asymmetric junctions", PRX Quantum **3**, 040338 (2022).

[111] A. P. M. Place, L. V. H. Rodgers, P. Mundada, B. M. Smitham, M. Fitzpatrick, Z. Leng, A. Premkumar, J. Bryon, S. Sussman, G. Cheng, T. Madhavan, H. K. Babla, B. Jaeck, A. Gyenis, N. Yao, R. J. Cava, N. P. de Leon, and A. A. Houck, "New material platform for superconducting transmon qubits with coherence times exceeding 0.3 milliseconds", Nature Communications **12**, 1779 (2021).

[112] K. D. Crowley, R. A. McLellan, A. Dutta, N. Shumiya, A. P. M. Place, X. H. Le, Y. Gang, T. Madhavan, M. P. Bland, R. Chang, N. Khedkar, Y. C. Feng, E. A. Umbarkar, X. Gui, L. V. H. Rodgers, Y. Jia, M. M. Feldman, S. A. Lyon, M. Liu, R. J. Cava, A. A. Houck, and N. P. de Leon, "Disentangling losses in tantalum superconducting circuits", Phys. Rev. X **13**, 041005 (2023).

[113] M. Kudra, J. Biznárová, A. Fadavi Roudsari, J. J. Burnett, D. Niepce, S. Gasparinetti, B. Wickman, and P. Delsing, "High quality three-dimensional aluminum microwave cavities", Applied Physics Letters **117**, 070601 (2020).

[114] J. Verjauw, A. Potočnik, M. Mongillo, R. Acharya, F. Mohiyaddin, G. Simion, A. Pacco, T. Ivanov, D. Wan, A. Vanleenhove, L. Souriau, J. Jussot, A. Thiam, J. Swerts, X. Piao, S. Couet, M. Heyns, B. Govoreanu, and I. Radu, "Investigation of microwave loss induced by oxide regrowth in high-q niobium resonators", Phys. Rev. Appl. **16**, 014018 (2021).

[115] J. Lee, Z. Mao, K. He, Z. H. Sung, T. Spina, S.-I. Baik, D. L. Hall, M. Liepe, D. N. Seidman, and S. Posen, "Grain-boundary structure and segregation in nb3sn coatings on nb for high-performance superconducting radiofrequency cavity applications", Acta Materialia **188**, 155 (2020).

[116] L. DiCarlo, J. M. Chow, J. M. Gambetta, L. S. Bishop, B. R. Johnson, D. I. Schuster, J. Majer, A. Blais, L. Frunzio, S. M. Girvin, and R. J. Schoelkopf, "Demonstration of two-qubit algorithms with a superconducting quantum processor", Nature **460**, 240 (2009).

[117] W. Meissner and R. Ochsenfeld, "A new effect when superconductivity occurs.", Natural Sciences **21**, 787 (1933).

[118] O. Gargiulo, S. Oleschko, J. Prat-Camps, M. Zanner, and G. Kirchmair, “Fast flux control of 3d transmon qubits using a magnetic hose”, Applied Physics Letters **118**, 012601 (2021).

[119] S. Oleschko, “Fast Flux Control Of A Transmon Qubit In A Three-Dimensional Cavity Architecture”, Master thesis, University of Innsbruck (2017).

[120] A. Sanchez and N. Bort-Soldevila, “Shaping magnetic fields with zero-magnetic-permeability media”, Journal of Applied Physics **130**, 163901 (2021).

[121] J.-S. Hong and M. J. Lancaster, “Microstrip filters for RF/microwave applications” (Wiley, New York, 2001) OCLC: 52368006.

[122] W. Commons, “File:sketch of helium dilution refrigerator.svg — wikimedia commons, the free media repository” (2023).

[123] J. B. Johnson, “Thermal agitation of electricity in conductors”, Phys. Rev. **32**, 97 (1928).

[124] H. Nyquist, “Thermal agitation of electric charge in conductors”, Phys. Rev. **32**, 110 (1928).

[125] A. Borgognoni, “Mode temperature analysis of a readout resonator”, Master thesis, University of Innsbruck (2020).

[126] A. A. Clerk and D. W. Utami, “Using a qubit to measure photon-number statistics of a driven thermal oscillator”, Phys. Rev. A **75**, 042302 (2007).

[127] R. Barends, J. Wenner, M. Lenander, Y. Chen, R. C. Bialczak, J. Kelly, E. Lucero, P. O’Malley, M. Mariantoni, D. Sank, H. Wang, T. C. White, Y. Yin, J. Zhao, A. N. Cleland, J. M. Martinis, and J. J. A. Baselmans, “Minimizing quasiparticle generation from stray infrared light in superconducting quantum circuits”, Applied Physics Letters **99**, 113507 (2011).

[128] L. Salerno and P. Kittel, “Thermal contact conductance”, NASA technical memorandum (NASA, Ames Research Center, 1997).

[129] R. Berman, “Some Experiments on Thermal Contact at Low Temperatures”, Journal of Applied Physics **27**, 318 (2004).

[130] J. Herrmann, C. Hellings, S. Lazar, F. Pfäffli, F. Haupt, T. Thiele, D. C. Zanuz, G. J. Norris, F. Heer, C. Eichler, and A. Wallraff, “Frequency up-conversion schemes for controlling superconducting qubits” (2022), arXiv:2210.02513 [quant-ph] .

[131] I. Yang, T. Agrenius, V. Usova, O. Romero-Isart, and G. Kirchmair, “Hot schrödinger cat states” (2024), unpublished.

[132] D. Rieger, S. Günzler, M. Spiecker, A. Nambisan, W. Wernsdorfer, and I. Pop, "Fano interference in microwave resonator measurements", Phys. Rev. Appl. **20**, 014059 (2023).

[133] H. Wang, M. Hofheinz, J. Wenner, M. Ansmann, R. C. Bialczak, M. Lenander, E. Lucero, M. Neeley, A. D. O'Connell, D. Sank, M. Weides, A. N. Cleland, and J. M. Martinis, "Improving the coherence time of superconducting coplanar resonators", Applied Physics Letters **95**, 233508 (2009).

[134] P. Macha, S. H. W. van der Ploeg, G. Oelsner, E. Il'ichev, H.-G. Meyer, S. Wünsch, and M. Siegel, "Losses in coplanar waveguide resonators at millikelvin temperatures", Applied Physics Letters **96**, 062503 (2010).

[135] D. T. McClure, H. Paik, L. S. Bishop, M. Steffen, J. M. Chow, and J. M. Gambetta, "Rapid driven reset of a qubit readout resonator", Phys. Rev. Appl. **5**, 011001 (2016).

[136] M. D. Reed, L. DiCarlo, B. R. Johnson, L. Sun, D. I. Schuster, L. Frunzio, and R. J. Schoelkopf, "High-fidelity readout in circuit quantum electrodynamics using the jaynes-cummings nonlinearity", Phys. Rev. Lett. **105**, 173601 (2010).

[137] E. L. Hahn, "Spin echoes", Phys. Rev. **80**, 580 (1950).

[138] H. Y. Carr and E. M. Purcell, "Effects of diffusion on free precession in nuclear magnetic resonance experiments", Phys. Rev. **94**, 630 (1954).

[139] S. Meiboom and D. Gill, "Modified spin-echo method for measuring nuclear relaxation times", Review of Scientific Instruments **29**, 688 (2004).

[140] J. Bylander, S. Gustavsson, F. Yan, F. Yoshihara, K. Harrabi, G. Fitch, D. G. Cory, Y. Nakamura, J.-S. Tsai, and W. D. Oliver, "Noise spectroscopy through dynamical decoupling with a superconducting flux qubit", Nature Physics **7**, 565 (2011).

[141] T. Thorbeck, A. Eddins, I. Lauer, D. T. McClure, and M. Carroll, "Two-level-system dynamics in a superconducting qubit due to background ionizing radiation", PRX Quantum **4**, 020356 (2023).

[142] X. Y. Jin, A. Kamal, A. P. Sears, T. Gudmundsen, D. Hover, J. Miloshi, R. Slattery, F. Yan, J. Yoder, T. P. Orlando, S. Gustavsson, and W. D. Oliver, "Thermal and residual excited-state population in a 3d transmon qubit", Phys. Rev. Lett. **114**, 240501 (2015).

[143] P. Bertet, A. Auffeves, P. Maioli, S. Osnaghi, T. Meunier, M. Brune, J. M. Raimond, and S. Haroche, "Direct measurement of the wigner function of a one-photon fock state in a cavity", Phys. Rev. Lett. **89**, 200402 (2002).

[144] B. Vlastakis, G. Kirchmair, Z. Leghtas, S. E. Nigg, L. Frunzio, S. M. Girvin, M. Mirrahimi, M. H. Devoret, and R. J. Schoelkopf, "Deterministically Encoding Quantum Information Using 100-Photon Schrödinger Cat States", Science **342**, 607 (2013).

[145] R. W. Heeres, B. Vlastakis, E. Holland, S. Krastanov, V. V. Albert, L. Frunzio, L. Jiang, and R. J. Schoelkopf, "Cavity state manipulation using photon-number selective phase gates", Phys. Rev. Lett. **115**, 137002 (2015).

[146] J. Johansson, P. Nation, and F. Nori, "Qutip 2: A python framework for the dynamics of open quantum systems", Computer Physics Communications **184**, 1234 (2013).

[147] F. Diedrich, J. C. Bergquist, W. M. Itano, and D. J. Wineland, "Laser cooling to the zero-point energy of motion", Phys. Rev. Lett. **62**, 403 (1989).

[148] S. E. Hamann, D. L. Haycock, G. Klose, P. H. Pax, I. H. Deutsch, and P. S. Jessen, "Resolved-sideband raman cooling to the ground state of an optical lattice", Phys. Rev. Lett. **80**, 4149 (1998).

[149] W. Wang, Y. Wu, Y. Ma, W. Cai, L. Hu, X. Mu, Y. Xu, Z.-J. Chen, H. Wang, Y. P. Song, H. Yuan, C.-L. Zou, L.-M. Duan, and L. Sun, "Heisenberg-limited single-mode quantum metrology in a superconducting circuit", Nature Communications **10**, 4382 (2019).

[150] M. Tatsuta, Y. Matsuzaki, and A. Shimizu, "Quantum metrology with generalized cat states", Phys. Rev. A **100**, 032318 (2019).

[151] X. Deng, S. Li, Z.-J. Chen, Z. Ni, Y. Cai, J. Mai, L. Zhang, P. Zheng, H. Yu, C.-L. Zou, S. Liu, F. Yan, Y. Xu, and D. Yu, "Heisenberg-limited quantum metrology using 100-photon fock states" (2023), arXiv:2306.16919 [quant-ph] .

[152] C. Wang, Y. Y. Gao, P. Reinhold, R. W. Heeres, N. Ofek, K. Chou, C. Axline, M. Reagor, J. Blumoff, K. M. Sliwa, L. Frunzio, S. M. Girvin, L. Jiang, M. Mirrahimi, M. H. Devoret, and R. J. Schoelkopf, "A schrödinger cat living in two boxes", Science **352**, 1087 (2016).

[153] M. Bild, M. Fadel, Y. Yang, U. Von Lüpke, P. Martin, A. Bruno, and Y. Chu, "Schrödinger cat states of a 16-microgram mechanical oscillator", Science **380**, 274 (2023).

[154] A. Eickbusch, V. Sivak, A. Z. Ding, S. S. Elder, S. R. Jha, J. Venkatraman, B. Royer, S. M. Girvin, R. J. Schoelkopf, and M. H. Devoret, "Fast universal control of an oscillator with weak dispersive coupling to a qubit", Nature Physics **18**, 1464 (2022).

[155] G. Kirchmair, B. Vlastakis, Z. Leghtas, S. E. Nigg, H. Paik, E. Ginossar, M. Mirrahimi, L. Frunzio, S. M. Girvin, and R. J. Schoelkopf, "Observation of quantum state collapse and revival due to the single-photon Kerr effect", Nature **495**, 205 (2013).

[156] M. Rossignolo, T. Reisser, A. Marshall, P. Rembold, A. Pagano, P. J. Vetter, R. S. Said, M. M. Müller, F. Motzoi, T. Calarco, F. Jelezko, and S. Montangero, "Quocs: The quantum optimal control suite", Computer Physics Communications **291**, 108782 (2023).

[157] S. Gerlich, S. Eibenberger, M. Tomandl, S. Nimmrichter, K. Hornberger, P. J. Fagan, J. Tüxen, M. Mayor, and M. Arndt, "Quantum interference of large organic molecules", Nature Communications **2**, 263 (2011).

[158] A. Ourjoumtsev, H. Jeong, R. Tualle-Brouri, and P. Grangier, "Generation of optical 'Schrödinger cats' from photon number states", Nature **448**, 784 (2007).

[159] K. Zhu, H. Tang, C. Li, D. Huang, X. Li, and X. Li, "The quantum statistical properties of superposition coherent states with thermal noise", Journal of Modern Optics **43**, 323 (1996).

[160] G. Huyet, S. Franke-Arnold, and S. M. Barnett, "Superposition states at finite temperature", Physical Review A **63**, 043812 (2001).

[161] H. Jeong and T. C. Ralph, "Transfer of Nonclassical Properties from a Microscopic Superposition to Macroscopic Thermal States in the High Temperature Limit", Phys. Rev. Lett. **97**, 100401 (2006).

[162] S.-B. Zheng, "Macroscopic superposition and entanglement for displaced thermal fields induced by a single atom", Phys. Rev. A **75**, 032114 (2007).

[163] H. Jeong and T. C. Ralph, "Quantum superpositions and entanglement of thermal states at high temperatures and their applications to quantum-information processing", Phys. Rev. A **76**, 042103 (2007).

[164] H. Jeong, J. Lee, and H. Nha, "Decoherence of highly mixed macroscopic quantum superpositions", JOSA B **25**, 1025 (2008).

[165] F. Nicacio, R. N. P. Maia, F. Toscano, and R. O. Vallejos, "Phase space structure of generalized Gaussian cat states", Physics Letters A **374**, 4385 (2010).

[166] M. Scala, M. S. Kim, G. W. Morley, P. F. Barker, and S. Bose, "Matter-Wave Interferometry of a Levitated Thermal Nano-Oscillator Induced and Probed by a Spin", Phys. Rev. Lett. **111**, 180403 (2013).

[167] X.-g. Meng, H.-S. Goan, J.-s. Wang, and R. Zhang, "Nonclassical thermal-state superpositions: Analytical evolution law and decoherence behavior", Optics Communications **411**, 15 (2018).

[168] D. E. Miller, J. R. Anglin, J. R. Abo-Shaeer, K. Xu, J. K. Chin, and W. Ketterle, "High-contrast interference in a thermal cloud of atoms", Phys. Rev. A **71**, 043615 (2005).

[169] M. Keil, S. Machluf, Y. Margalit, Z. Zhou, O. Amit, O. Dobkowski, Y. Japha, S. Moukouri, D. Rohrlich, Z. Binstock, Y. Bar-Haim, M. Givon, D. Groswasser, Y. Meir, and R. Folman, in *Molecular Beams in Physics and Chemistry*, edited by B. Friedrich and H. Schmidt-Böcking (Springer, Cham, 2021) pp. 263–301.

[170] K. Marshall, D. F. V. James, A. Paler, and H.-K. Lau, "Universal quantum computing with thermal state bosonic systems", Phys. Rev. A **99**, 032345 (2019).

[171] G. F. Thomas, "Validity of the Rosen-Zener conjecture for Gaussian-modulated pulses", Physical Review A **27**, 2744 (1983).

[172] I. S. Mihov and N. V. Vitanov, "Pulse shape effects in qubit dynamics demonstrated on an IBM quantum computer. arXiv:2301.10004" (2023).

[173] W. Magnus, "On the exponential solution of differential equations for a linear operator", Communications on Pure and Applied Mathematics **7**, 649 (1954).

[174] M. S. Kim and V. Bužek, "Schrödinger-cat states at finite temperature: Influence of a finite-temperature heat bath on quantum interferences", Physical Review A **46**, 4239 (1992).

[175] D. I. Schuster, A. A. Houck, J. A. Schreier, A. Wallraff, J. M. Gambetta, A. Blais, L. Frunzio, J. Majer, B. Johnson, M. H. Devoret, S. M. Girvin, and R. J. Schoelkopf, "Resolving photon number states in a superconducting circuit", Nature **445**, 515 (2007).

[176] M. O. Brown, S. R. Muleady, W. J. Dworschack, R. J. Lewis-Swan, A. M. Rey, O. Romero-Isart, and C. A. Regal, "Time-of-flight quantum tomography of an atom in an optical tweezer", Nature Physics **19**, 569 (2023).

[177] M. Roda-Llordes, A. Riera-Campeny, D. Candoli, P. T. Grochowski, and O. Romero-Isart, "Macroscopic Quantum Superpositions via Dynamics in a Wide Double-Well Potential", Physical Review Letters **132**, 023601 (2024).

[178] L. Neumeier, M. A. Ciampini, O. Romero-Isart, M. Aspelmeyer, and N. Kiesel, "Fast quantum interference of a nanoparticle via optical potential control", Proceedings of the National Academy of Sciences **121**, e2306953121 (2024).

[179] L. Dania, D. S. Bykov, F. Goschin, M. Teller, and T. E. a. Northup, "Ultra-high quality factor of a levitated nanomechanical oscillator. arXiv:2304.02408" (2023).

[180] D. S. Bykov, L. Dania, F. Goschin, M. Teller, and T. E. Northup, in *2023 Conference on Lasers and Electro-Optics Europe & European Quantum Electronics Conference (CLEO/Europe-EQEC)* (2023) pp. 1–1.

[181] E. Bonvin, L. Devaud, M. Rossi, A. Militaru, L. Dania, D. S. Bykov, O. Romero-Isart, T. E. Northup, L. Novotny, and M. Frimmer, "State Expansion of a Levitated Nanoparticle in a Dark Harmonic Potential. arXiv:2312.13111" (2023).

[182] V. Dunjko, N. Friis, and H. J. Briegel, "Quantum-enhanced deliberation of learning agents using trapped ions", New Journal of Physics **17**, 023006 (2015).

[183] G. M. D'Ariano and P. Lo Presti, "Quantum tomography for measuring experimentally the matrix elements of an arbitrary quantum operation", Phys. Rev. Lett. **86**, 4195 (2001).

[184] E. Magesan, J. M. Gambetta, B. R. Johnson, C. A. Ryan, J. M. Chow, S. T. Merkel, M. P. da Silva, G. A. Keefe, M. B. Rothwell, T. A. Ohki, M. B. Ketchen, and M. Steffen, "Efficient measurement of quantum gate error by interleaved randomized benchmarking", Phys. Rev. Lett. **109**, 080505 (2012).

[185] O. Oreshkov, F. Costa, and C. Brukner, "Quantum correlations with no causal order", Nature Communications **3**, 1092 (2012).

[186] G. Chiribella, G. M. D'Ariano, P. Perinotti, and B. Valiron, "Quantum computations without definite causal structure", Phys. Rev. A **88**, 022318 (2013).

[187] L. M. Procopio, A. Moqanaki, M. Araújo, F. Costa, I. Alonso Calafell, E. G. Dowd, D. R. Hamel, L. A. Rozema, C. Brukner, and P. Walther, "Experimental superposition of orders of quantum gates", Nature Communications **6**, 7913 (2015).

[188] J. Miguel-Ramiro, Z. Shi, L. Dellantonio, A. Chan, C. A. Muschik, and W. Dür, "Superposed quantum error mitigation", Phys. Rev. Lett. **131**, 230601 (2023).

[189] Y. Guo, X.-M. Hu, Z.-B. Hou, H. Cao, J.-M. Cui, B.-H. Liu, Y.-F. Huang, C.-F. Li, G.-C. Guo, and G. Chiribella, "Experimental transmission of quantum information using a superposition of causal orders", Phys. Rev. Lett. **124**, 030502 (2020).

[190] A. A. Abbott, J. Wechs, D. Horsman, M. Mhalla, and C. Branciard, "Communication through coherent control of quantum channels", Quantum **4**, 333 (2020).

[191] K. Wei, N. Tischler, S.-R. Zhao, Y.-H. Li, J. M. Arrazola, Y. Liu, W. Zhang, H. Li, L. You, Z. Wang, Y.-A. Chen, B. C. Sanders, Q. Zhang, G. J. Pryde, F. Xu, and J.-W. Pan, "Experimental quantum switching for exponentially superior quantum communication complexity", Phys. Rev. Lett. **122**, 120504 (2019).

[192] J. Miguel-Ramiro, Z. Shi, L. Dellantonio, A. Chan, C. A. Muschik, and W. Dür, "Enhancing quantum computation via superposition of quantum gates", Phys. Rev. A **108**, 062604 (2023).

[193] N. H. Balshaw, "Practical Cryogenics - Oxford Instruction Manual" (2016).

[194] D. C. Mattis and J. Bardeen, "Theory of the anomalous skin effect in normal and superconducting metals", Phys. Rev. **111**, 412 (1958).

[195] C. Schlager, "Fabrication and characterization of superconducting microwave resonators featuring new vacuum-gap structures", Master thesis, University of Innsbruck (2022).

Publication list

[1] I. Yang, T. Agrenius, V. Usova, O. Romero-Isart, and G. Kirchmair, “Hot schrödinger cat states” (2024), unpublished.

[2] M. Zanner, R. Albert, E. I. Rosenthal, S. Casulleras, I. Yang, C. M. F. Schneider, K. W. Lehnert, O. Romero-Isart, and G. Kirchmair, “Spatial addressing of qubits in a dispersive waveguide” (2024), unpublished.

APPENDIX A

Useful Relations

A.1 Coherent states

Some useful relations that are used in this thesis

- $\hat{D}^{\dagger}(\alpha) = \hat{D}(-\alpha)$
- $\hat{D}(\alpha)\hat{D}(\beta) = \hat{D}(\alpha + \beta)e^{i\mathrm{Im}(\alpha\beta^*)}$
- $\langle\beta|\alpha\rangle = \langle 0|\hat{D}^{\dagger}(\beta)D(\alpha)|0\rangle = e^{-\frac{1}{2}(|\alpha|^2+|\beta|^2)+\alpha\beta^*)}$
- $|\langle\beta|\alpha\rangle|^2 = e^{-|\alpha-\beta|^2}$
- $\langle\alpha|\alpha e^{\pm i\chi t}\rangle = e^{|\alpha|^2(\cos\chi t-1)}\left(\cos|\alpha|^2 \pm i\sin|\alpha|^2\right)\sin(\chi t)$

A.2 Wigner Coordinates Normalisation

Considering the generalised dimensionless position $\hat{X}$ and momentum $\hat{P}$ operators, we have a choice of writing these coordinate operators as the raising $\hat{a}^\dagger$ and lowering $\hat{a}$ operators

$$\hat{X} = \frac{1}{N}(\hat{a}^\dagger + \hat{a}) \tag{A.1}$$

$$\hat{P} = \frac{i}{N}(\hat{a}^\dagger - \hat{a}) \tag{A.2}$$

where the raising and lowering operator obey the commutator relation $[\hat{a}, \hat{a}^\dagger] = \hat{a}\hat{a}^\dagger - \hat{a}^\dagger\hat{a} = 1$ and N is our choice of normalisation factor. Equivalently, the raising and lowering operators can be written as $\hat{a}^\dagger = \frac{N}{2}(\hat{X} - i\hat{P})$ and $\hat{a} = \frac{N}{2}(\hat{X} + i\hat{P})$.

Consider the commutator relation of the dimensionless position and momentum operators

$$\begin{aligned} [\hat{X}, \hat{P}] =& \frac{i}{N^2}[(\hat{a}^\dagger + \hat{a})(\hat{a}^\dagger - \hat{a}) - (\hat{a}^\dagger - \hat{a})(\hat{a}^\dagger + \hat{a})] \\ =& \frac{2i}{N^2}. \end{aligned} \tag{A.3}$$

As a result, the choice of N will affect the commutator relation. The commutator relation is used in many equations. For example, the uncertainty relation obeys

$$\Delta\hat{X}\Delta\hat{P} \geq \frac{1}{2}|[\hat{X}, \hat{P}]| = \frac{1}{N^2}. \tag{A.4}$$

This means that the ground state with the minimum uncertainty will have a size $\Delta\hat{X}_{\text{vac}} = \Delta\hat{P}_{\text{vac}} = \frac{1}{N}$.

Similarly, the choice of N will have a scaling factor in the displacement operator: $\hat{D}(\alpha) = e^{\alpha\hat{a}^\dagger - \alpha^*\hat{a}} = e^{\frac{N}{2}\left(\alpha(\hat{X} - i\hat{P}) - \alpha^*(\hat{X} + i\hat{P})\right)} = e^{\frac{N}{2}\left((\alpha - \alpha^*)\hat{X} - i(\alpha + \alpha^*)\hat{P}\right)}$. When working with numerical methods to calculate the Wigner function over the phase space, these factors will need to be accounted for. Knowledge of the normalisation used and its impacts on the functions are essential for avoiding confusion. For example, in qutip, the default scaling factor is $\hat{a} = \frac{1}{\sqrt{2}}(\hat{X} + i\hat{P})$ which results in displacements looking smaller than anticipated.

In this thesis, we use $N = 2$. Thus, we expect the ground state to have an uncertainty of $\frac{1}{2}$.

APPENDIX B

Optimisation and Searching Algorithms

The optimisation problem and search routine used to find the ideal $\mathbf{E}_{\text{cavity}}(t)$ and $\mathbf{E}_{\text{qubit}}(t)$ is outlined here. For a more in-depth discussion, the following sources provide a good description [73, 74].

The target unitary defined in Eq. (2.66) is split into a piecewise function with N steps with length δt for a total time $T = N \times \delta t$

$$\hat{U}_{QOC}(t, \mathbf{E}) = \hat{U}_N \hat{U}_{N-1} ... \hat{U}_1, \tag{B.1}$$

$$\hat{U}_i = e^{-i\frac{\delta t}{\hbar}\hat{H}(\mathbf{E}(i\delta t)}. \tag{B.2}$$

Instrument limitations will impose some constraints on the search space. This includes the voltage resolution of the Digital-Analog-Converter (DAC) used or the sampling rate of the Arbitrary Waveform Generator (AWG). Such experimental limits can be placed on the objective function by introducing constraints on the fidelity.

Open-loop Optimisation In open-loop optimisation, an objective function with the proper constraint functions needs to be defined to properly construct the optimisation problem Sec. 2.3.3. There is some finesse in choosing the multiplier values correctly and will require a few trials. However, the constraint functions can be carefully designed based on experimental requirements, such as giving a linear or non-linear cost to the objective function. In this subsection, I outline some examples of constraint functions.

The AWG has some maximum voltage where instruments are still linear. Or one might want to limit the power sent into the fridge that is proportional to the integrated power. Such constraints can be accounted for by including

$$g_{\text{amplitude linear cost}}(\mathbf{E}) = \sum_i (|E_i|^2)$$

where E_i is the control field applied at time interval i.

Importantly, the optimised pulse might contain quickly oscillating terms, which break RWA and result in complex system dynamics and a departure from the dispersive Hamiltonian. Thus, it is important to use the correct Hamiltonian or limit the bandwidth of the pulses

$$g_{\text{bandwidth linear cost}}(\mathbf{E}) = \sum_i (|E_i - E_{i-1}|^2).$$

We can penalise the occupation of higher cavity photon numbers by introducing

$$g_{\text{cavity photon occupation}} = \sum_{i}^{N} |\langle n_{\max}|\psi(i)\rangle|^2$$

where $|\psi(i)\rangle$ is the state vector of the system at time interval i.

Other than experimental limitations, one can also reward certain properties of the pulses. Such as robustness under Hamiltonian variation by optimising under different Hamiltonians $\mathcal{F} = \frac{1}{N}\sum_{i}^{N} \mathcal{F}(\hat{H})$.

Search Methods For N elements, with I and Q voltages, we have $N_{elements} \times 2 \times N_{steps}$ parameters in a large search space of voltage parameters. In many cases, the number of possible parameters is too large to calculate every single possible trajectory. The number of parameters can be reduced by allowing for some degrees of freedom in the search routine.

One simple degree of freedom is the global phase invariance of the desired gate $\hat{U}_{QOC} \equiv e^{i\phi}\hat{U}'_{QOC}$. Some techniques do not optimise a full pulse but only some parameterised amplitudes of applied gates [154].

We require a search algorithm that can reduce the number of parameters we need to calculate. Some common search methods include:

- Newton: Searching the parameter space and calculating second derivatives to find the global maxima
- Trust region: searching a local parameter space and then updates the region center and radius to find new local maxima
- Gradient: search in a direction given by the gradient of the objective function
- Randomised basis: A gradient-based search of the parameter space in a randomised basis

The Newton search method requires finding the second derivative of the objective function and is very computationally expensive. However, the other methods might not always find the global maximum. To avoid this, the optimisation is repeated for different random starting points. With enough iterations, the optimisation routine will then converge on the global maxima.

The randomised basis search defines the control pulse in a basis with the coefficients of the basis being optimised for. In a variant of this search method, the dressed Chopped Randomised Basis (dCRAB) algorithm changes the basis of the pulse after the optimization reaches a plateau in the objective function [76, 77]. This will redefine the objective function "landscape" and allow the optimisation routine to search for a global maximum or minimum without having to repeat the optimisation for different starting points.

APPENDIX C

Black Box Quantisation Expansions

Consider the case of a single qubit coupled to a cavity. The phase through the junction can be written as

$$\hat{\phi} = \hat{\phi}_c + \hat{\phi}_q = \phi_c(\hat{c}^\dagger + \hat{c}) + \phi_q(\hat{q}^\dagger + \hat{q}). \tag{C.1}$$

The fourth-order expansion in the cosine in Eq. (3.8) results in $\hat{\phi}^4 = \hat{\phi}_c^4 + 4\hat{\phi}_c^3\hat{\phi}_q + 6\hat{\phi}_c^2\hat{\phi}_q^2 + 4\hat{\phi}_c\hat{\phi}_q^3 + \hat{\phi}_q^4$. We can expand and drop the non-energy-conserving terms.

The first and fifth term results in the anharmonicity of the cavity and qubit mode respectively: $\hat{\phi}_m \approx \phi_m^4(6\hat{m}^\dagger\hat{m}^\dagger\hat{m}\hat{m} + 12\hat{m}^\dagger\hat{m} + 3)$. The coefficients are not trivial due to the commutation relation of the raising and lowering operators. Immediately, one can note some effects due to the introduction of the junction. The zero point energy is shifted by $\frac{3}{4!}\frac{E_J}{\phi_0^4}(\phi_c^2 + \phi_q^2)^2$. Each mode m will have an eigenfrequency shift due to its coupling to the other mode n, $\frac{12}{4!}\frac{E_J}{\phi_0^4}\phi_m^2(1 + \phi_n^2)$. Finally, all modes will inherit some non-linearity $\frac{K_m}{2} = \frac{1}{4!}6\frac{E_J}{\phi_0^4}\phi_m^4$.

The second and fourth term results in: $\hat{\phi}_m^3\hat{\phi}_n \approx 4\phi_m^3\phi_n(3\hat{m}^\dagger\hat{m}^\dagger\hat{m}\hat{n} + 3\hat{m}^\dagger\hat{m}\hat{m}\hat{n}^\dagger + 3\hat{m}\hat{n}^\dagger + 3\hat{m}^\dagger\hat{n})$. All these Rabi-like terms are fast oscillations that are dropped with the RWA. Similarly, all odd powers of the flux operator are also dropped.

Finally, the third term results in $\hat{\phi}_c^2\hat{\phi}_q^2 \approx 6\phi_c^2\phi_q^2(\hat{c}^\dagger\hat{c}^\dagger\hat{q}\hat{q} + 4\hat{c}^\dagger\hat{c}\hat{q}^\dagger\hat{q} + \hat{c}\hat{c}\hat{q}^\dagger\hat{q}^\dagger + 2\hat{c}^\dagger\hat{c} + 2\hat{q}^\dagger\hat{q} + 1)$. Likewise, with RWA, many terms will drop and we arrive at the Hamiltonian

$$\begin{aligned}\hat{H}_{\text{up to fourth order}} = &\left(1 - \frac{E_J}{8\phi_0^4}(\phi_c^2 + \phi_q^2)^2\right) \\ &+ \left(\hbar\omega_c - \frac{E_J}{2\phi_0^4}(\phi_c^4 + \phi_c^2\phi_q^2)\right)\hat{c}^\dagger\hat{c} - \left(\hbar\omega_q + \frac{E_J}{2\phi_0^4}(\phi_q^4 + \phi_q^2\phi_c^2)\right)\hat{q}^\dagger\hat{q} \\ &- \frac{E_J}{4\phi_0^4}\phi_c^4\hat{c}^\dagger\hat{c}^\dagger\hat{c}\hat{c} - \frac{E_J}{4\phi_0^4}\phi_q^4\hat{q}^\dagger\hat{q}^\dagger\hat{q}\hat{q} - \frac{E_J}{\phi_0^4}\phi_c^2\phi_q^2\hat{c}^\dagger\hat{c}\hat{q}^\dagger\hat{q}.\end{aligned} \tag{C.2}$$

We arrive at the same dispersive Hamiltonian as using the frame transformation Eq. (2.49).

To find higher-order interaction effects, one can carry the expansion to the sixth order: $\hat{\phi}^6 \approx \hat{\phi}_c^6 + 15\hat{\phi}_c^4\hat{\phi}_q^2 + 15\hat{\phi}_c^2\hat{\phi}_q^4 + \hat{\phi}_c^6$. After working it out, we find higher-order correction terms proportional to lower-order operators. Importantly, we find new terms in the Hamiltonian

$$\begin{aligned}\hat{H}_{\text{sixth order}} &= \frac{E_J}{36\phi_0^6}\sum_m \phi_m^6 \hat{m}^\dagger\hat{m}^\dagger\hat{m}^\dagger\hat{m}\hat{m}\hat{m} \\ &+ \frac{E_J}{6\phi_0^6}\phi_c^4\phi_q^2\hat{c}^\dagger\hat{c}^\dagger\hat{c}\hat{c}\hat{q}^\dagger\hat{q} \\ &+ \frac{E_J}{6\phi_0^6}\phi_q^4\phi_c^2\hat{c}^\dagger\hat{c}\hat{q}^\dagger\hat{q}^\dagger\hat{q}\hat{q}.\end{aligned} \tag{C.3}$$

1 cavity, 2 qubits Doing the fourth order expansion for a quantum system with one cavity and two qubits, we arrive at the Hamiltonian

$$\begin{aligned}\hat{H}_{1\text{ cavity, 2 qubits}} &= \hbar\omega_{q_1}\hat{q}_1^\dagger\hat{q}_1 + \hbar\omega_{q_2}\hat{q}_2^\dagger\hat{q}_2 + \hbar\omega_c\hat{c}^\dagger\hat{c} \\ &- \frac{1}{4}\left(\frac{E_{J1}}{\phi_0^4}\phi_{11}^4 + \frac{E_{J2}}{\phi_0^4}\phi_{12}^4\right)\hat{q}_1^\dagger\hat{q}_1^\dagger\hat{q}_1\hat{q}_1 \\ &- \frac{1}{4}\left(\frac{E_{J1}}{\phi_0^4}\phi_{21}^4 + \frac{E_{J2}}{\phi_0^4}\phi_{22}^4\right)\hat{q}_2^\dagger\hat{q}_2^\dagger\hat{q}_2\hat{q}_2 \\ &- \frac{1}{4}\left(\frac{E_{J1}}{\phi_0^4}\phi_{c1}^4 + \frac{E_{J2}}{\phi_0^4}\phi_{c2}^4\right)\hat{c}^\dagger\hat{c}^\dagger\hat{c}\hat{c} \\ &- \left(\frac{E_{J1}}{\phi_0^4}\phi_{11}^2\phi_{c1}^2 + \frac{E_{J2}}{\phi_0^4}\phi_{12}^2\phi_{c2}^2\right)\hat{q}_1^\dagger\hat{q}_1\hat{c}^\dagger\hat{c} \\ &- \left(\frac{E_{J1}}{\phi_0^4}\phi_{21}^2\phi_{c1}^2 + \frac{E_{J2}}{\phi_0^4}\phi_{22}^2\phi_{c2}^2\right)\hat{q}_2^\dagger\hat{q}_2\hat{c}^\dagger\hat{c} \\ &- \left(\frac{E_{J1}}{\phi_0^4}\phi_{11}^2\phi_{21}^2 + \frac{E_{J2}}{\phi_0^4}\phi_{12}^2\phi_{22}^2\right)\hat{q}_1^\dagger\hat{q}_1\hat{q}_2^\dagger\hat{q}_2.\end{aligned} \tag{C.4}$$

The first 3 terms are the usual Harmonic oscillator modes. The next 3 terms are the respective mode anharmonicities. Now, each term has contributions from each junction, the mode anharmonicity is now due to the inherited anharmonicity of both junctions. Similarly, the dispersive interaction between both modes has terms from both junctions. The Hamiltonian coefficient is the sum of contributions from both qubits $K_{mn} = \sum_r K_{mn,r}$, where K_{mm} is the respective mode anharmonicity.

APPENDIX D

Fabrication and Etching Recipes

In this appendix chapter, I summarise the details of the recipes I used for fabrication and etching of the samples in the thesis.

D.1 Aluminium Qubits

Step	Equipment/Chemical	Description
Piranha Cleaning	$H_2SO_4 : H_2O_2 = 3 : 1$	Cleaned for 5min Cleaned with H_2O Blow Dry with N_2
Resist Static Spinning	MMA (8.5) EL13	1500 rpm for 100 s Baked at 200°C for 5 min Thickness of 1122 nm
	950 PMMA A4	1500 rpm for 100 s Baked at 200°C for 5 min Thickness of 268 nm
Gold Sputtering	Cressington 108auto Sputter Coater	Current of 40 mA for 50 s
e-beam Lithography	Raith eLINE Plus 30 kV	Base dose = 80 μCcm^{-2} Dose Factors:
	Aperture: 10 μm Step Size: 5 nm Writefield size: 200 μm	undercut: 1.7 undercut proximity: 1.2 small structures: 5 junction trenches: 7
	Aperture: 120 μm Step Size: 40 nm Writefield size: 1000 μm Zoom factor: $\times$1.01	large structures: 4 chip cut lines: 3
Gold Etching	Solution of I_2, KI and H_2O 5%Lugold : H_2O = 2 ml : 30 ml	Etch for 10 s Quench reaction with H_2O H_2O rinse in first beaker H_2O rinse in second beaker Blow Dry with N_2

Development	IPA : $H_2O = 3 : 1$	1 min45 s at 6°C Quench reaction with H_2O Blow Dry with N_2
Evaporation	Plassys Bestek MEB 550S	**Pump Overnight** Loadlock: $1.0e^{-7}$ mbar Chamber: $2.2e^{-8}$ mbar
	Descum V_{beam}: 200 V V_{acc}: 50 V I_{beam}: 5 mA Ar flow: 10 sccm O_2 flow: 5 sccm Sample: Rotating Duration: 3 min	
	Gattering Crucible: Ti Rate: 0.2 nms^{-1} Duration: 2 min	
	First layer Crucible: Al Rate: 1 nms^{-1} Angle: 25° Thickness: 25 nm	
	Oxidation Pressure: 5 mbar Time: 5.5 min	
	Second layer Crucible: Al Rate: 1 nms^{-1} Angle: −25 ° Thickness: 50 nm	
	Capping Layer Pressure: 30 mbar Time: 5 min	
Laser Dicing	Coherent 430 Laser Parameters Peak Power: 340 W Pulse Width: 0.2 ms Burst Frequency: 600 Hz Average Power: 40 W Pulse Energy: 68 mJ	Structure facing down Bridge size: 300 μm
Liftoff	Acetone at 40°C for 4 + hour	
Ultrasonic Cleaning	Power: 40% Frequency: 135 kHz	Acetone at 40°C for 10 min IPA at 40°C for 5 min

Table D.1: Aluminium Qubit Fabrication Process

D.2 Tantalum Pads Fabrication

Step	Equipment/Chemical	Description
Ultrasonic Solvent Cleaning	Power: 40% Frequency: 135 kHz	Acetone at 40°C for 10 min IPA at 40°C for 5 min
Resist Static Spinning	Ma-N 2403	1000 rpm for 45 s Baked at 90°C for 1 min Thickness of 590 nm
e-beam Lithography	Raith eLINE Plus 30kV Aperture: 120 μm Step Size: 40 nm Writefield size: 1000 μm Zoom factor: $\times$1.01	Base dose = 80 μCcm^{-2} Dose Factor: 3
Development	Ma – D525	1 min30 s Quench reaction with H_2O Blow Dry with N_2
Post Bake		Baked at 100°C for 5 min
Etching	Sentech ICP SI 500	**Chamber Preconditioning** Pressure: 2 Pa O_2 flow: 50 sccm RF Power: 5 W ICP Power: 400 W Time: 10 min
	Soft O_2 Cleaning Pressure: 10 Pa O_2 flow: 60 sccm RF Power: 40 W ICP Power: 0 W Duration: 30 s	
	Tantalum Etching Pressure: 1 Pa O_2 flow: 2 sccm CF_4 flow: 20 sccm RF Power: 50 W ICP Power: 50 W Duration: 5 min + 30 s over-etching	

Table D.2: Tantalum Qubit Pads Fabrication Process

D.3 Purcell Filter

Here, I present the in-house fabrication recipe for the Purcell Filter that was developed by Stefan Oleschko.

Step	Equipment/Chemical	Description
Backside Gold sputtering	AJAA ATC1800-HY	
	Argon Ion Milling Pressure: 10 sccm V_{beam} : 400 V V_{acc} : 80 V I_{beam} : 400 W Sample : Rotation 10 rpm Time: 3 min	
	First Layer Crucible: Ti Rate: 0.1 $\mathrm{nms^{-1}}$ Thickness: 5 nm	
	Second Layer Crucible: Au Rate: 0.1 $\mathrm{nms^{-1}}$ Thickness: 5 nm	
Resist Static Spinning	Adhesion Promoter, AR3000-80	6000 rpm for 60 s Baked at 180°C for 2 min
	AR-P-5350	4000 rpm for 60 s Baked at 105°C for 4min
	AR-P-3740	4000 rpm for 60 s Baked at 100°C for 4 min
Optical Lithography	Microtech 405nm Gallium Nitride laser Optical Lens: 3 D-step: 4 Gain: 9.2 Filter: 30% Dose: 111 $\mathrm{mJcm^{-2}}$	
Development	$\mathrm{Ar} - 300 - 35 : \mathrm{H_2O} = 4 : 1$	1 min Quench reaction with H_2O Blow Dry with N_2
	$\mathrm{Ar} - 300 - 47 : \mathrm{H_2O} = 2 : 3$	1 min Quench reaction with H_2O Blow Dry with N_2
Evaporation	Plassys Bestek MEB 550S	**Pump** Time: 3 hour

	Descum V_{beam}: 200 V V_{acc}: 50 V I_{beam}: 5 mA Ar flow: 10 sccm O_2 flow: 5 sccm Sample: Rotating Duration: 3 min	
	Gattering Crucible: Ti Rate: 0.2 nms^{-1} Duration: 2 min	
	Aluminium layer Crucible: Al Rate: 1 nms^{-1} Thickness: 50 nm	
	Capping Layer Pressure: 30 mbar Time: 5 min	
Liftoff	Acetone at 40°C	
Ultrasonic Cleaning	Power: 40% Frequency: 135 kHz	Acetone at 40°C for 10 min IPA at 40°C for 5 min
Resist Static Spinning	AZ-1505	4000 rpm for 100 s Baked at 100°C for 50 s
Optical Lithography	Microtech 405nm Gallium Nitride laser Optical Lens: 3 D-step: 4 Gain: 25 Filter: 10% Dose: 100 $mJcm^{-2}$	
Development	AZdeveloper : $H_2O = 4 : 1$	1 min Quench reaction with H_2O Blow Dry with N_2
Contact Pads Gold Evaporation	AJAA ATC1800-HY	
	Argon Ion Milling Pressure: 10 sccm V_{beam} : 400 V V_{acc} : 80 V I_{beam} : 400 W Sample : Rotation 10 rpm Time: 3 min	
	First Layer Crucible: Ti Rate: 0.1 nms^{-1} Thickness: 5 nm	
	Second Layer Crucible: Au Rate: 0.1 nms^{-1} Thickness: 5 nm	

Liftoff	Acetone at 40°C	
Ultrasonic Cleaning	Power: 40% Frequency: 135 kHz	Acetone at 40°C for 10 min IPA at 40°C for 5 min

Table D.3: Purcell Filter Fabrication Process

D.4 Aluminium cavities

Step	Description
Ultrasonic Solvent Cleaning	Power: 40% Frequency: 135 kHz Acetone at 40°C for 10 min IPA at 40°C for 5 min
Aluminium Etching	Duration: 2 hour Temperature: 50°C Rate: 10 nms^{-1}
H_2O Rinse	Multiple Rinsing cycles Blow Dry with N_2
Aluminium Etching	Duration: 2 hour Temperature: 50°C Rate: 10 nms^{-1}
H_2O Rinse	Multiple Rinsing cycles Blow Dry with N_2

Table D.4: Aluminium Cavity Etching Process

D.5 Niobium cavities

Step	Description
Ultrasonic Solvent Cleaning	Power: 40% Frequency: 135 kHz Acetone at 40°C for 10 min IPA at 40°C for 5 min
Niobium Etching	Duration: 1 hour Temperature: 6°C Chemicals: HF : HNO_3 : H_3PO_4 Ratio: 1:1:1
Niobium Polishing	Duration: 1 hour Temperature: 6°C Chemicals: HF : HNO_3 : H_3PO_4 Ratio: 1:1:2
H_2O Rinse	Multiple Rinsing cycles Blow Dry with N_2

Table D.5: Niobium Cavity Etching Process

APPENDIX E

Cryostat

The cryogenic fridge operates with two cooling methods. A good overview of cryogenic considerations can be found in [193].

The first cooling system is a pulse tube refrigerator which compresses helium that undergoes adiabatic expansion at the cold plate to provide the cooling. This allows the fridge to reach a temperature of 4 K.

The second cooling system is a ^{3}He/^{4}He mixture that undergoes a phase transition at the base plate. This mixture separates between a fermi liquid ^{3}He and a superfluid ^{4}He. ^{3}He going through a phase transition between concentrated and dilute phases provides cooling power. The mixture concentration needs to be chosen so that the phase boundary is in the mixing chamber and below the still plate.

The operation cryostat has many finer details such as pre-cooling of the mixture so as not to bring too high a thermal load to the base plate or the need for liquid N_2 cold traps to capture any contaminants to avoid plugging the lines.

In the past decades, cryogenic systems in research labs have been automated to a large degree such that experimentalists can almost just push a full cooldown button. This allows for more time available to spend on experiments and other instrument problems. However, with many experiments that try to push the instrumental limits, one needs to understand what the cryostat can do. For example, the mechanical decoupling of the pulse tube to reduce vibrations in the cryostat.

E.1 Heat Load

Adding cables and sending signals to the experiments will result in a heat load on the different cryostat plates. This is the thermal conduction between plates through the cables and the dissipation of the signal and room temperature noise in attenuators at each plate. We can account for the thermal conduction from the cables with

$$P_{\text{thermal conductance}} = \frac{\sigma A \Delta K}{L}. \tag{E.1}$$

where σ is the thermal conductivity of the wire used. A and L are the cross-sectional area and length of the wire respectively. ΔK is the temperature difference across the wire. The thermal conductivity for the different wires used, taking into account the cross-sectional area of the SMA cable is, $\sigma_{\text{CuN}}A_{\text{SMA}} = 2.18e^{-4}$ WcmK^{-1}, $\sigma_{\text{SS}}A_{\text{SMA}} = 4.3e^{-5}$ WcmK^{-1} [1].

Due to the lower cooling powers of the bottom plates of the cryostat, we cannot add all the attenuators to the base plate. One must take care of the heat load on each plate. In addition to the power dissipated from the incoming drive signal, using Eq. (3.27), we can calculate the total power dissipated from Johnson-Nyquist noise

$$\begin{aligned} P_{\text{Thermal noise dissipation}} &= \int_0^\infty \frac{V_{\text{RMS}}^2}{R} df = \int_0^\infty 4hfn_{\text{th}}(f,T)df \\ &= \frac{4k_BT}{h}(k_BT)\int_0^\infty \frac{\frac{hf}{k_BT}}{e^{\frac{hf}{k_BT}}-1} d\left(\frac{hf}{k_BT}\right) = \frac{4(k_BT)^2}{h}\left(\frac{\pi^2}{6}\right) \\ &= \frac{\pi}{3\hbar}k_B^2T^2 \end{aligned} \tag{E.2}$$

which is the one-dimensional analogue of the Stefan Boltzmann law. In electronic circuits, the classical limit $hf \ll k_BT$ approximates $hfn_{\text{th}}(f,T) \approx k_BT$. This recovers the typical condition that the total Johnson-Noise is k_BT [2]. The blackbody radiation from hotter plates irradiating the colder plates is also enough to heat the lower plates which prevents the base plate from reaching colder temperatures. Thus, line-of-sight ports must be closed to reduce the absorption of thermal radiation.

In the following simplistic scenario, an input drive power $1\,\mu$W is sent into the cryostat with a reflection configuration. This means that the thermal photons from the input and output lines add up. The power level is derived from the usual case where most of the power sent to the fridge is the readout pulse which is around ≈ 1 mW with an effective duty cycle of $\approx 0.1\%$. A table of the wiring scheme and the resulting cavity photons and heat load per line on each plate is shown in table E.1. The main contribution is the thermal conduction through each line.

Plate	Cooling Power	Thermal Conduction		Input Line (4 K, 100 mK, Base)		
		SS	CuNi	20-10-20	20-10-30/40	20-0-10
50 K	40 W	0.7 mW	4 mW	-	-	-
4 K	1 W	0.1 mW	0.8 mW	1.5 μW	1.5 μW	1.5 μW
1 K	10 mW	8.6 μW	-	-	-	-
100 mK	10 μW	2.6 μW	-	13.9 nW	13.9 nW	-
20 mK	1 μW	0.2 μW	-	1.5 nW	1.5 nW	15 nW

Table E.1: Table showing the heat load and attenuation in the cryostat. The second column is the nominal cooling power of the cryostat. The third column shows the heat load due to thermal conduction through the lines. Finally, the other columns show the heat load due to the dissipation of a signal plus the thermal dissipation. For these calculations, the input power is $1\,\mu$W.

[1] These values are measured values at 4 K obtained from the supplier Coax Co for the SC-219/50-SCN-CN and SC-219/50-SS-SS models. We do not consider the superconducting NbTi (SC-219/50-NbTi-NbTi).

[2] In some cases, the factor 4 in $S_{VV}(f,T)$ is dropped as the maximum power that a resistor can transmit is when the resistor is impedance matched with another Thevenin equivalent resistor. This means only half the voltage is dropped across the first resistor and the maximum power that one can measure is k_BT.

APPENDIX F

Diagnostic Toolbox

In experiments, many problems can arise. Thus to be able to properly diagnose different types of possible problems (instrument, qubit system, experimental setup), it is useful to know more techniques to figure out the exact cause of the measurement problems [1]. Additional examples of common problems in measurements can be found in [103].

F.1 Amplified Phase Error (APE) Calibration

Small errors in pulses can be difficult to detect. By repeating the pulse several times, small errors can be amplified and can be detected. Such a measurement can tune up the qubit pulse amplitude more accurately as compared to a simple Rabi experiment.

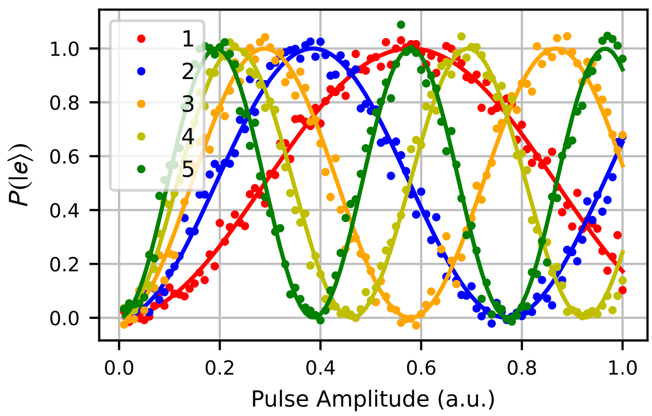

Figure F.1: Measurement data of an APE calibration experiment. Multiples of the same pulse are repeated for different pulse amplitudes (coloured lines 1 to 5). Such a measurement can tune up the qubit pulse amplitude more accurately. In this case, the oscillation period does not increase linearly with the number of pulses played. This signals a problem with the qubit pulses such as leakage of some signal or a shortening of the played pulses.

[1] In the lab, I call these obvious problems. Problems that become obvious once the solution is known.

F.2 Phase Ramsey

A phase Ramsey is similar to a qubit T_2 Ramsey experiment. Two $\frac{\pi}{2}$ pulses and the phase of the second pulse is swept. Such a measurement can reveal errors in the implementation phase or frequency of the pulses used. The errors can arise from hardware or wiring issues.

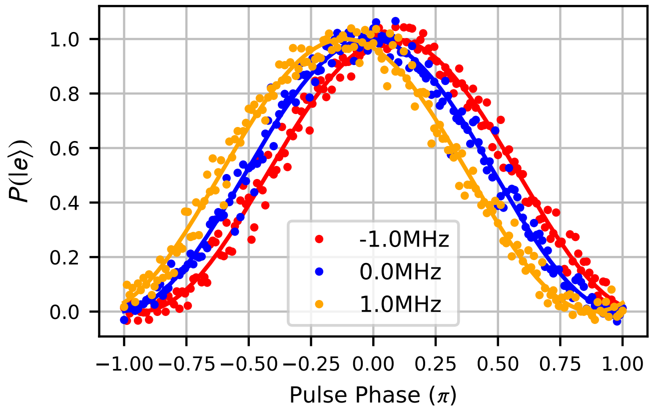

Figure F.2: Measurement data of a phase Ramsey experiment. Two $\frac{\pi}{2}$ pulses and the phase of second pulse is swept. Such a measurement can reveal errors in the phase or frequency of the pulse used.

A fixed time delay can be added between the pulses. The amplitude of the oscillations will represent the decay of coherence of the qubit.

F.3 High Q Cavity Lifetime

Additional measurements of the lifetime of the high Q cavity can be obtained. Forming a Fock state in the cavity and measure its decay via a cross-Kerr interaction to a readout resonator or a generalised Husimi Q measurement with a qubit.

Another quick way to measure the high Q cavity lifetime can be found in [92]. In this measurement, a square pulse with some duty cycle is sent to the high Q cavity. The reflected signal is analysed with time (in this case a spectrum analyser set to zero span and on resonance with the drive tone). Based on the ring up and down of the reflected signal, we can fit the reflected power and obtain the coupling quality factors and the lifetime of the cavity.

An example of a trace is shown in Fig. F.3.

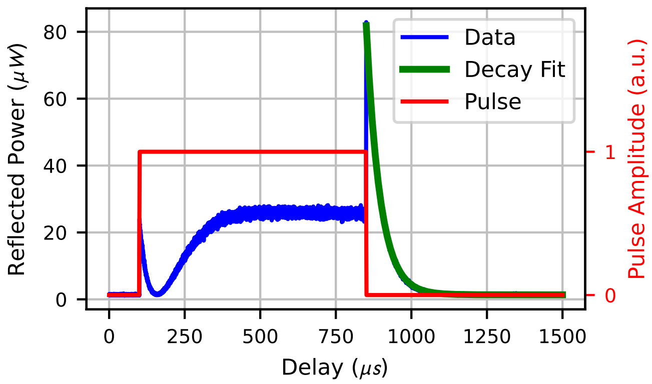

Figure F.3: High Q cavity lifetime measurement via the measurement of a reflected signal of the cavity. A square pulse with some duty cycle is sent to the high Q cavity. The reflected signal can be fitted to obtain the coupling quality factors and decay lifetime [92].

F.4 Readout Errors

To infer the state of the qubit, we need to probe the resonator. Thus, we need to measure the amplitude and phase response of the probe signal. The readout circuit can be done in a reflection or transmission configuration.

Due to instrument imperfections, the digitised signal is often at some arbitrary angle and has some DC offset in I or Q Fig. F.4A. If we do not account for these imperfections properly, they will result in measurement artefacts in the measurement result. For example in Fig. F.4C, shows the case where the signal is not properly rotated. The figure shows a Rabi measurement where the qubit flops between the $|g\rangle$ and $|e\rangle$ state. However, looking at the Q or absolute of the signal, we see a reduced contrast or worse, the qubit having small oscillations near the ground state. This occurs due to the separation of the readout signal for the qubit in $|g\rangle$ and $|e\rangle$, being close to a readout value of 0.

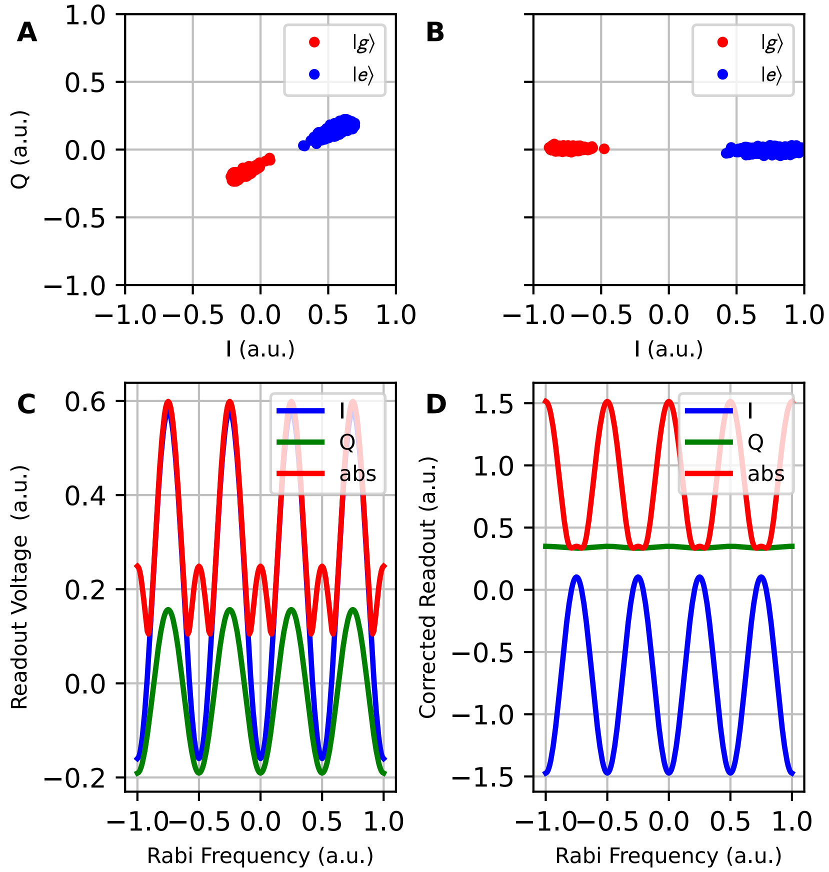

Figure F.4: Measurement artefacts due to improper readout calibration. (**A** and **B**) Phase space plots of the probe signal for different initial states of the qubit. (**C** and **D**) calculated Rabi measurement values for the readout case **A** and **B** respectively. In an experiment, depending on the qubit population, the readout value can be anywhere between the two distributions of the qubit in the ground and excited state. In **A**, the data that is not properly rotated to one of the quadratures. This results in reduced readout contrast in the quadratures and measurement artefacts in the absolute of the signal shown in **C**. In **B** and **D**, the probe signal is properly treated such that all the information is along the I quadrature. Thus, the Rabi measurement has maximum readout contrast and we can just look at the I quadrature.

By properly rotating the signal to get contrast only in I or Q, we can maximise the readout contrast and avoid any readout artefacts.

Other readout errors can also occur due to improper calibration of the readout signal. Unaccounted cross-Kerr terms can result in a shift in the frequency of the readout signal. This will affect the amplitude and phase of the probe signal when the other elements are populated. Thus, it is crucial to account for such differences by doing background measurements. For example, a comparison between two protocols where the qubit is excited or left in the ground state.

F.5 Other Methods

For other measurement artefacts, it is often difficult to pinpoint the exact cause of the underlying problem. In this section, I write a few actions that can be taken to help figure out the source of errors.

The first check is usually the operating conditions of instruments, amplifiers, and switches. This includes loose cables or power supplies that may have a broken cable due to improper soldering.

Pulse Tube Off. The operation of the cryostat requires the pulse tube to be on. However, the cryostat can still operate without the pulse tube for 15 min. The pulse tube causes mechanical vibrations in the fridge. If the qubit chip is loosely clamped or pushed against a surface, these pulse tube vibrations can adversely impact the qubit coherence and lifetime. A quick check would be to turn off the pulse tube and do fast measurements of qubit T_1, T_2^* and T_2^E and only requires 45 min for the cryostat to cool back down to normal operating range.

Retightening of cables and clamps. If clamps are loose, qubit position can change resulting in a different coupling or greater losses. In our experience, after 2 to 3 cooldowns, the clamps and SMA cables should be checked for tightness.

Changing Frame of Reference. Instrument errors can be checked by changing the frame of reference used. For example, the qubit state could be read out by probing the readout resonator at $f_{\mathrm{res},|g\rangle}$ or $f_{\mathrm{res},|e\rangle}$. The measurement result should be the opposite (that is, obtaining the measurement results $P_{|g\rangle}$ or $P_{|e\rangle} = 1 - P_{|g\rangle}$).

Similarly, high Q cavity displacement pulses can be changed to on resonant with the cavity for the qubit in the ground state f_{cav} or the excited state $f_{\mathrm{cav}} - \chi_{\mathrm{qc}}/2\pi$. Evolutions of the cavity qubit system in phase space will reflect the change in frequency.

This test is illustrated in the plots in Fig. F.5. When the qubit is in the ground state, the cavity will not evolve for the drive f_{cav}. For this drive frequency, the qubit being in the excited state will mean the cavity frequency is detuned below by the drive tone by $\chi_{\mathrm{qc}}/2\pi$. This results in a counter-clockwise evolution at rate χ_{qc}.

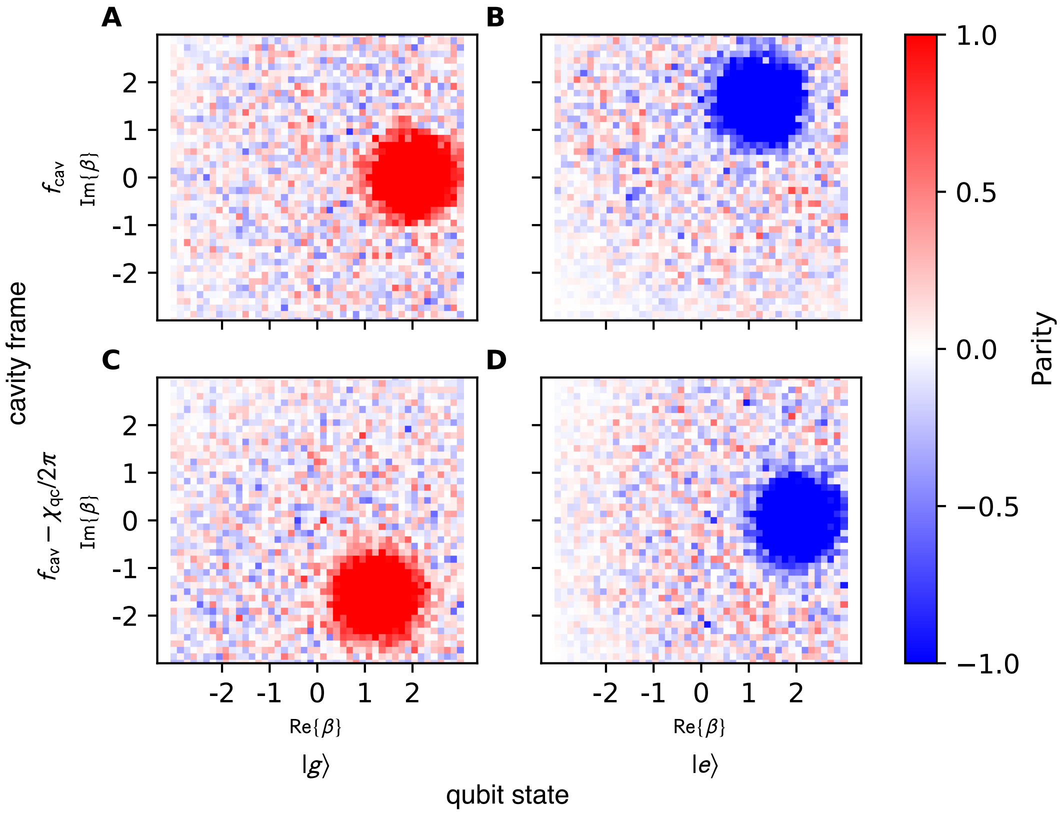

Figure F.5: Measurement results from different cavity drive frequencies and initial qubit state. In these measurements, the qubit is initialised in the ground (**A** and **C**) or excited (**B** and **D**) state. Then, the cavity is displaced with $\hat{D}(\alpha = 2)$. Finally, the cavity-qubit system is allowed to evolve for a time of $\hat{T}\left(\frac{\pi}{4\chi_{\mathrm{qc}}}\right) = 80\,\mathrm{ns}$. This experiment is done at two cavity drive frequencies; on resonance with the qubit in the ground state, f_{cav} (**A** and **B**) and similar for the qubit in the excited state, $f_{\mathrm{cav}} - \chi_{\mathrm{qc}}/2\pi$ (**C** and **D**).

These checks allow for testing of the instruments in frequency up and down conversion and digitisation of the signals.

Thermal Cycling and Temperature Ramps of Cryostat. We can also consider cycling the cryostat above T_C and back down to the base temperature. This causes the redistribution of frequency of lossy two-level systems (TLS) or changes in qubit frequencies. The new distribution of frequencies might lead to a smaller coupling to lossy TLS. The thermal cycling to 10 K and back to base will only take a night to cool back down to base temperature of the cryostat. This is shorter in comparison to the $50 - 60$ hours needed for a full cooldown from room temperature.

Temperature ramps to 10 K can also be considered. The behaviour of different resonators with temperature depends on the distribution of TLS or the non-linear inductance present in the resonators. This will allow for the identification of the different loss models of the resonators [92] or different resonators in the experiment.

An example of results from a thermal sweep of cavity spectroscopy is shown in Fig. F.6. According to the Mattis-Bardeen theory [194], an increasing temperature leads to Cooper pair breaking and the formation of quasiparticles, which results in a change in kinetic inductance and a decrease in the quality factor of the cavity [195].

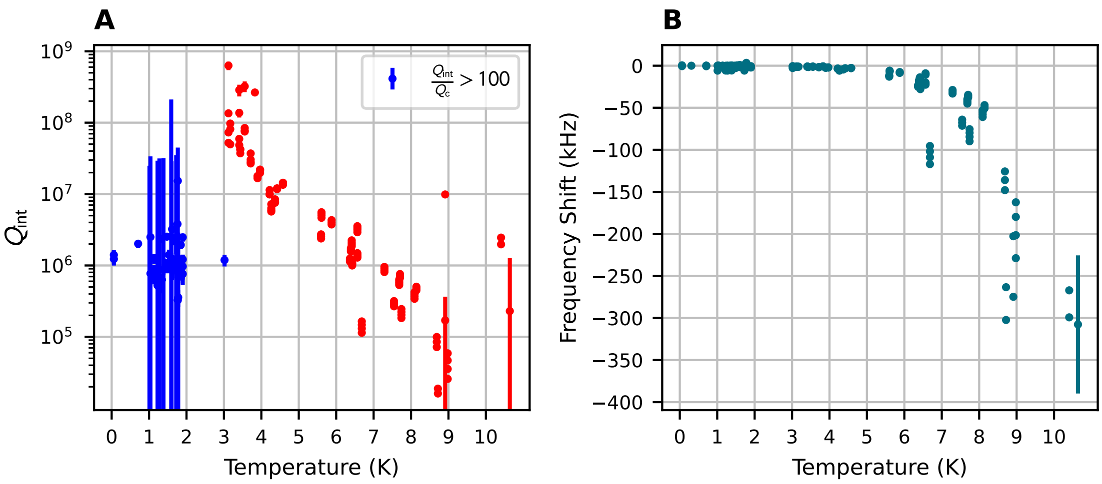

Figure F.6: Fiting results from cavity spectroscopy done across a sweep of base plate temperature. (**A**) The internal quality factor with the base plate temperature is plotted. At temperatures below 3 K, the internal quality factor has risen above the ratio of $\frac{Q_{\text{int}}}{Q_c} > 100$. This results in the circle fit routine being inaccurate and cannot properly extract the internal quality factors as the cavity is too overcoupled. At higher temperatures, an increase in quasiparticle population in the superconductor will result in higher loss and thus a lower internal quality factor. In this regime, we can properly determine the internal quality factor. (**B**) In the same thermal sweep, the frequency of the cavity will be shifted down due to a higher kinetic inductance as described by the Mattis Barden theory [194].

APPENDIX G

Kerr Cat State

The Kerr cat state can be formed by displacing the cavity state and allowing the system to evolve

$$\hat{X}(\pi) : |0, e\rangle \tag{G.1}$$

$$\hat{D}(\alpha) : |\alpha, e\rangle \tag{G.2}$$

$$\hat{T}\left(\frac{\pi}{K+\chi'}\right) : e^{\frac{-|\alpha|^2}{2}} \sum_n \frac{\alpha^n}{\sqrt{n!}} e^{i\left(\chi n + n^2 \frac{K+\chi'}{2}\right)t} |n\rangle \tag{G.3}$$

$$= e^{\frac{-|\alpha|^2}{2}} \sum_n \frac{\left(\alpha e^{i\frac{\chi}{K+\chi'}\pi}\right)^n}{\sqrt{n!}} e^{i(n^2 \frac{\pi}{2})t} |n\rangle \,. \tag{G.4}$$

We can spilt the final state into two parts with $e^{in^2\frac{\pi}{2}} |n\rangle = |n_{even}\rangle + i\,|n_{odd}\rangle$. Writing $\theta = \pi\frac{\chi}{K+\chi'}$, we can simplify the final state by writing

$$\begin{aligned} |\psi\rangle =& e^{\frac{-|\alpha|^2}{2}} \left[\sum_{n_{\text{even}}} \frac{\alpha e^{i\theta}}{\sqrt{n!}} |n\rangle + i \sum_{n_{\text{odd}}} \frac{\alpha e^{i\theta}}{\sqrt{n!}} |n\rangle\right] \\ =& e^{\frac{-|\alpha|^2}{2}} \sum_n \frac{(1+i)(\alpha e^{i\theta})^n + (1-i)(-(\alpha e^{i\theta})^n)}{\sqrt{n!}} |n\rangle \\ =& \frac{1}{\sqrt{2}} \left(e^{i\frac{\pi}{4}} |\alpha e^{i\theta}\rangle + e^{-i\frac{\pi}{4}} |-\alpha e^{i\theta}\rangle\right) \\ =& \frac{1}{\sqrt{2}} e^{i\frac{\pi}{4}} \left(|\alpha e^{i\theta}\rangle + e^{-i\frac{\pi}{2}} |-\alpha e^{i\theta}\rangle\right) \end{aligned} \tag{G.5}$$

where we have used $n_{\text{even/odd}} : (\alpha e^{i\theta})^n = \frac{1}{2}\left[(\alpha e^i\theta)^n \pm (-\alpha e^{i\theta})^n\right]$. The final state is thus a zero parity cat at an angle of θ.

For a system where we have in-situ control of the strength of Kerr terms $K + \chi'$, one can envision turning on and off these interactions to do a gate.

The Kerr cat state implements a similar operator to the qcmap protocol Eq. (5.9) with a $\phi = \pi/2$ phase.

Acknowledgements

Like many other PhD adventures, I too have plenty of people to thank. There are just so many aspects of the experiments and I would no doubt forget to thank somebody important. But know that this PhD was only possible because of many people and is the culmination of many scientific collaborations. This 4+ year journey was an amazing project and I am glad to meet many world class scientists.

Firstly, I like to thank my supervisor, **Prof. Gerhard Kirchmair** for the advice and supervision in research and the opportunity to do research in his lab. This was truly an enriching experience. Through our countless discussions, many back and forth, and asking the RIGHT questions, I learnt so much about the scientific world and just adulting in general. The number of projects and collaborations I had the privilege of having was only made possible by the vast knowledge you have and the relations you have built up over the years. Over the many random things I do and side projects I had, I hope that my work in the lab has had a net positive impact. I still don't know how you do it, but as I move onto my next career path, I will strive to "just be more efficient".

I am fortunate to stand on the metaphorical shoulders of those who laid the foundational works in the lab. Without the old guard, I definitely would have struggled much more. **Dr. Christian Schneider** who I still bug and ask questions to this day. I model much of my work ethic from how helpful you were. **Dr. Maximilian Zanner** who did so much of the grunt work and established a working cleanroom recipe such that I could just come in and get qubit fabrication going so smoothly. I see the world differently because of your views on life. Together with you two, I thoroughly "enjoyed" the opportunity to learn and develop the fabrication of Ta qubits. I shall continue to strive to strongly violate Murphy's law in the cleanroom.

Dr. Oscar Gargiulo and **Stefan Oleschko** who inducted me into the group with the coding, input lines soldering and installation of the fridge. I learnt so much both in and out of the lab. I will remember my first trip to Italy and the pizzas in Naples very fondly. **Dr. David Zöpfl**, sunset coffee! Although I didn't join as many as I should have. The few that I did was a well needed pause in the daily work routine. Thank you for always helping whenever I ask and keeping an eye out on my wellbeing.

While I did not have as much scientific overlap with **Dr. Phani Muppalla**, **Dr. Mathieu Juan**, **Dr. Aleksei Sharafiev** and **Alvise Borgognoni**, I enjoyed our small discussions and thank you for helping with even the small little things I asked for. When I entered the lab, you guys welcomed me with open arms.

To the high Q cavity team in the group, it is great to have such a huge overlap between the projects. The destination was great, I enjoyed the ride through the ups and downs of research. I will always remember our late night experiments and discussions while everyone else has gone home. I am extremely proud of the work we have done and the results we achieved together. **Desislava Atanasova**, I hope that I have been as helpful to you as others have been to me. I truly admire your relentless dedication through the countless experimental difficulties and I look forward to the scientific career you will build for yourself. **Vasilisa Usova**: It was a pleasure finishing the projects together. You showed me that we should be strong in both mathematical rigour and experimental fundamentals. **Dr. Teresa Hönigl-Decrinis**, who came in and took on so many responsibilities in the lab. I am very grateful that you were able to handle so much and took a big workload off me. **Lucien Québaud**, the newest addition to the high Q team. I am sure that many of our unfinished projects will be brought to greater heights. I am excited to see what you can do with the platform the team has built.

Dr. Romain Albert, it was a pleasure learning so much and sitting beside you. Your straight advice and "strong" opinions have made me a much better scientist. Our many one-on-one discussions in Vienna and USA have brought a mature and balanced perspective on life. It is amazing how much you know about so many random things. **Lukas Deeg**: seeing you go from learning from the seniors to spearheading the Mechanics team has been inspiring. I will remember our dinners and the many conversations and similar viewpoints we share. **Julian Daser**, who never says no to whatever I ask for. I am glad to have learnt together with a person with such high drive and a "can do" attitude. I know your project will be successful. **Christian Schlager** who is also now leading side projects and taking care of students. Thank you for answering my many small questions and for your pivotal inputs in the lab chats.

To the new blood, I mean bright-eyed and bushy-tailed, people in the group, **Dr. Bhargava Thyagarajan**, **Raamamurthy Sathyanarayanan**, **Christian Dejaco** and **Filip**, I hope I have helped out and eased the introduction into the group. Please keep your enthusiastic drive and enjoy the process. Alternatively, hopefully, Stockholm syndrome kicks in soon. I am just jealous that you guys make me look like an old dinosaur. May your research be fruitful and engaging.

It is no secret that I enjoy looking after students. To the internship/Bachelor/Masters students I had the fortune of mentoring, **Julian Daser**, **David**, **Jennifer**, **Hannah**, **Nikolai**, **Julian**, **Adrien**, **Daniela**, **Giacomo** and **Lucien Québaud**: It was fun learning together with you and showing you a little bit of my research world. Hopefully, you can find some part of your work in this thesis or others from the group. A special mention to the first and last minions, I am truly overjoyed that you decided to take up a PhD position in the lab (and reassured of my ways). I know that you guys will have plenty of results to write about and please enjoy the research way of life.

I would not have been able to cover so many projects without the successful external collaborations I had the privilege of having. To **Thomas Argenius** and **Prof. Oriol Romero-Isart** for the Garfield cat states project, I enjoyed the engaging discussions on cat states. I believe we make an effective team and look forward to more discussions about science and life in general. I will forever remember the countless, painful but rewarding times we tried to push one final time to finish the project. For the closed-loop optimisation of a cat state in a bosonic mode, I would like to thank **Dr. Phila Rembold** and **Macro Rossingnolo** in the group of **Prof. Simone Montangero**. It was an eye-opening insight into the world of optimisation. I believe our upcoming results will only be the first of many to come. For the etching of the Niobium high Q cavity, **Lubuna Shafeek** and **Prof. Johannes Fink** without which, I would not need to worry about my high Q cavity $T_{1,\text{cav}}$. For the 3D modular Purcell filter and second generation of the flux hose project, I would like to thank **Dr. Arman Alizadeh**, **Prof. Iman Mirzaei** and **Dr. Natanael Bort-Soldevila** for running the simulations and starting the design process. It was a great opportunity to build something new together.

An often overlooked aspect of research is the surrounding supporting systems in place to help ease the workload of PhD students. My research progress was made possible because of the assistance I had. A big shout-out goes out to the administrative secretaries **Claudia Mevenkamp**, **Elisabeth Huck**, **Elke Wölflmaier** and **Klaus Falschlunger** who helped so much with my many requests. Especially for a non-German-speaking foreigner getting used to living in Innsbruck, the small discussions and wholehearted advice helped make my life much easier. Thanks for making paperwork less painful. I am grateful for the one-man army IT support, **David Jordan**, who is behind the big lab network and allowed us to remote control our systems before it was mainstream. I believe that the University of Innsbruck and IQOQI mechanical workshop is truly one of a kind. Thanks to **Andreas Strasser**, **Bernhard Öttl**, **David Arnold** and **Gerhard Hendl**. I said it multiple times, if it is not possible in this workshop, it will not be easily possible anywhere in Europe.

Outside the lab and working environment, I am lucky to have a big support structure. As many other PhD students can attest to, mental health is probably not focused on as much as it should. These families from "older times" were necessary to keep this "old" guy sane. My **VS**, **VJC** and **Oxford** friends who may not understand what I do but have nonetheless always given a listening ear. There are way too many of you guys to list for way too many things you have helped me with. There will be more meals and parties to come. While most of us are on different life paths now, it has been and will be a pleasure growing up and facing the world together. I look forward to collecting more stories and doing silly/stupid things together.

I am very thankful to **Dr. Daniel Haxell** who is on a very similar life path as I am and has seen my PhD trials as I have yours, not to mention all versions of my PhD thesis. Your way of framing my thoughts and being an outlet for me has been invaluable. I will try to keep my commitment to visit every city you live in.

I have to thank my family. My parents, **pa** and **ma**, who have never asked this Asian kid to come back home and gave truly unconditional support. My siblings, **Wayne**, **Ryan** and **Joan**, I think it was in 2006 that we last stayed together for an extended period. I believe it was the chaotic household that helped me embrace the mess that is experimental research.

My largest gratitude is for **Ng Yu Hui** whose unwavering support has pushed me on. A lot of time was put into this thesis and even on holidays, you didn't ask me to spend more time with you. Remarkably, you are always behind the scenes in all that I do and are my strongest pillar of support. Reflecting back, I owe you so much. You and I have a long life together. My hope is that you know how grateful I am for your presence. Everything in this thesis is possible because of you. (: